University of Oxford

Department of Chemistry

Layered double hydroxide based materials for carbon dioxide capture



Doy Why Justin Leung

Balliol College

This thesis is submitted in partial fulfilment of the requirement for the degree of Doctor of Philosophy at the University of Oxford

Preface

The work described in this thesis was carried out in the Chemistry Research Laboratory at the University of Oxford between October 2017 and June 2021 under the supervision of Professor Dermot O'Hare. All the work was performed by the author unless otherwise stated and no part has been previously submitted for any other degree.

Part of the work contained in this thesis has been published in the following journal paper.

D. W. J. Leung, C. Chen, J. C. Buffet and D. O'Hare, *Dalton. Trans.*, 2020, **49**, 9306–9311.

Abstract

Layered double hydroxide based materials for carbon dioxide capture

Doy Why Justin Leung **DPhil Thesis**

Balliol College **Trinity Term 2020**

This thesis discusses the development of layered double hydroxides (LDHs), layered double oxides (LDOs) and their composites for use in CO_2 capture.

Chapter One introduces LDHs, providing a background into their flexible composition and versatile application. A brief description of core@shell materials is also provided. Materials used in CO_2 capture in research and industry are discussed and compared. A background to the polyurethane (PU) curing process is also introduced.

Chapter Two investigates the acidity and basicity of solvent treated LDHs and LDOs (aqueous miscible organic (AMO) and aqueous immiscible organic (AIM) solvents). Their Brønsted and Lewis acidities and basicities are probed using titration, *in situ* fourier transformed infrared spectroscopy and temperature programmed desorption (TPD) respectively. Solid state NMR (ssNMR) is used to probe both the composition and surface sites, and a novel hypothesis regarding solvent interactions upon calcination is proposed. The CO_2 adsorption of solvent treated LDOs are tested to determine the optimal solvent for the process.

Chapter Three focuses on determining both the chemical and process parameters that affect the CO_2 capture performance of Mg_xAl LDH/LDOs in CO_2 capture. Process parameters, such as calcination temperature, calcination time and heating ramp rate, are investigated. Spectroscopic techniques, including ssNMR, TPD and surface hydroxyl titration, are used to observe the differences in the materials in order to determine the physicochemical factors that control CO_2 capture performance. By combining the result from Chapters Two and Three, an Mg_xAl LDH optimised for CO_2 capture is synthesised.

Chapter Four describes the synthesis of carbon@Mg_2Al LDH core@shell materials. The effects of varying LDH composition upon the morphology and growth of the core@shells are investigated. The series of materials is explored for synergy with regards to CO_2 capture with minimal pre-treatment. Calcination parameters for carbon@Mg_2Al LDH are varied and optimised for the CO_2 capture. Different carbon-based core materials are investigated in order to improve the overall CO_2 capacities of the core@shell composites. Post-synthesis modifications, such as solvent and ammonia treatment, are also investigated for potential improvement on CO_2 capture.

Chapter Five is a preliminary study of use of LDH-based materials during the curing of polyurethanes (PUs), with the ultimate goal of reducing curing time and eliminating CO_2 production during the curing.

Chapter Six includes the experimental details of the work described in this thesis. Lastly, the findings of the work of this thesis is summarised in Chapter Seven. Any supplementary information and other data referred to in the main text are found in the Appendices.

Acknowledgements

Firstly, I would like to thank Prof Dermot O'Hare for having me in his group. I would also like to thank JC for his supervision and useful chats, and the big supply drops of Earl Grey which fuelled my borderline addiction to caffeine (why did you leave me in my final hour…? And I think after this writing up period, there is nothing borderline about my love for caffeine anymore…). Chunping's enormous and never-ending support could not go unmentioned either. Your guidance, supervision and chats were invaluable over the years and I am pretty sure this thesis and project would have probably fallen apart around page 3 without your input and help. I would also like to thank Jingfang for starting me on my research journey all those years back as my part II supervisor. Zoe, thank you for all those speedy corrections, they were absolute life-savers.

To Maureen and Meng, my fellow finishers: WE'RE finally at the end of the tunnel, can't believe this ALL started 4 very long years ago. I'm pretty sure none of us actually realised the mess we were getting ourselves IN back then. But for better or worse, we finally made it. Thanks for putting up with THIS guy constantly complaining and just distracting you on an hourly basis. I am glad we got to do this TOGETHER! Told you guys I would squeeze the lyrics in somehow.

Philly Phil-Phil, go put on a phew Phil specials and take a couple of Phil days, philled with plenty Aldi knockoffs and lots of phun. You probably deserve it after having to essentially hydraulically press my samples into the rotor in the glovebox… Rebecca, thanks for introducing me to the concept of POETS day, the structure of my week will never be the same again. Clem, thanks for being the only other person in the lab who actually enjoys Earl Grey, definitely brought the sophistication level of the lab up a lot. Justin, continue to enjoy your bird watching, may the occasional glider sighting forever cheer you up that much. Gabi, hope this acknowledgment bit makes up for the lack of your mention in a certain other (Pt II) thesis… Peace, your occasional savage comments have absolutely made my days, hope you don't have to stick around for too long. Matt, I am glad you turn out to be much better company in person than you original photo would suggest. Sam, just simply **wh-tssshhh**. And if I didn't thank Katie for running some hydroxyl numbers for me, my life would be in danger whenever I'm near a bus, so thanks Bean!

Outside of the lab, the number of people I have to thank is probably endless and will in itself make up another thesis, so I will try and be brief. Thanks to Dr Player (sorry couldn't resist using his fantastic title) for putting up with me as a housemate for years, who knew the creepy stalker back in interviews in 2012 will end up being your housemate (for 3 years!!)… To everyone who has been part of the many iterations of the short sprints squad over the better part of a decade (most lit squad anywhere, #skwad4lyfe), you guys have been awesome and are absolutely fantastic company, many a bad lab day has been turned around by even the worst of the lactic horrors we had to go through together. To everyone still in my undergrad group of friends, thanks for keeping me sane with video calls and TTS throughout the many lockdowns (how many have we had now?).

Obviously, last but not least, I have to thank my family for their endless support of me through my studies. This would not have been possible without you.

Abbreviations

ºC	Degrees Celsius
Å	Angstrom (10^{-10} m)
µmol	Micromol ($\times 10^{-6}$ mol)
1-H	Hexan-1-ol
A	Acetone
a.u.	Arbitrary units
AIM-LDH	Aqueous immiscible organic layered double hydroxide
AMO-LDH	Aqueous miscible organic layered double hydroxide
BET	Brunauer-Emmett-Teller
CDL	Crystal domain length
CPMAS	Cross polarisation magic-angle spinning
D.I.	Deionised
DPMAS	Direct polarisation magic-angle spinning
E	Ethanol
EA	Ethyl acetate
FTIR	Fourier transform infrared
FWHM	Full width half maximum
g	Gram
g_{LDH}^{-1}	Per gram of layered double hydroxide
H	Hexane
h	Hour(s)

ICP-MS	Inductively coupled plasma mass spectrometry
IPA	Isopropyl alcohol
LDH	Layered double hydroxide
LDO	Layered double oxide
M^{2+}	Divalent metal ion
M^{3+}	Trivalent metal ion
MAS	Magic angle spinning (54.74º)
Mg_xAl	An LDH or LDO with Mg^{2+} and Al^{3+} as metal ions
min	Minute(s)
mmol	Millimol ($\times 10^{-3}$ mol)
µmol	Micromol ($\times 10^{-6}$ mol)
MMT	Montmorillonite
nm	Nanometre ($\times 10^{-9}$ m)
O	Octane
O_h	Octahedral
ppm	Parts per million
PU	Polyurethane
rpm	Rotations per minute
S	Solvent
SEM	Scanning electron microscopy
SEM-EDS	Scanning electron microscopy energy dispersive X-ray spectroscopy
ssNMR	Solid state nuclear magnetic resonance
T	Toluene

T_d	Tetrahedral
TEM	Transmission electron microscopy
TGA	Thermogravimetric analysis
TPD	Temperature programmed desorption
W	Water
wt%	Weight percentage
XRD	X-ray diffraction

Table of Contents

Chapter One - Introduction 1

1.1 Layered double hydroxides (LDHs) 1

1.1.1 Structure and composition 1

1.1.2 Thermal stability 2

1.1.3 Synthesis methods 4

1.1.4 Solvent treatment methods 6

1.2 Core@shell materials 8

1.2.1 Synthesis of core@LDH 9

1.3 Applications of LDHs and LDH core@shells 12

1.3.1 Waste treatment 12

1.3.2 UV absorption 12

1.3.3 Catalysis 13

1.3.4 Gas phase CO_2 capture 14

1.3.5 Application of LDH core@shells 22

1.4 CO_2 capture in polyurethane curing 23

1.5 Acidity and basicity of solids 25

1.6 Scope of thesis 31

1.7 References 32

Chapter Two - Experimental details 43

2.1 Analytical methods 43

2.1.1 CO_2 capture values 43

2.1.2 Elemental analysis 43

2.1.3 Fourier transform infrared (FTIR) spectroscopy 43

2.1.4 Inductively coupled plasma mass spectrometry (ICP-MS) 43

2.1.5 Polyurethane mixing 44

2.1.6 Powdered X-ray diffraction (XRD) 44

2.1.7 Scanning electron microscopy (SEM) 44

2.1.8 Solid state NMR spectroscopy 45

2.1.9 Surface area and pore size distribution 45

2.1.10 Tap density 45

2.1.11 Temperature programmed desorption (TPD) 45

2.1.12 Transmission electron microscopy (TEM) 46

2.1.13 Thermogravimetric analysis (TGA) 46

2.1.14 Zeta potential 46

2.2 Starting materials and chemicals 46

2.3 Experimental details for Chapter Six 47

2.3.1 Mixing of Desmoseal M280 47

Chapter Three- Studies of the acidity and basicity of LDHs 52

3.1 Introduction 52

3.2 Experimental details 53

3.2.1 Synthesis $Mg_{2.5}Al\ CO_3$ W LDH (LDH W) 53

3.2.2 Synthesis of solvent treated LDHs 54

3.2.3 Brønsted basicity titrations 54

3.2.4 In situ FTIR for Lewis basicity 55

3.2.5 TPD measurements for Lewis acidity and basicity 55

3.2.6 CO_2 capture values 55

3.3 Characterisation of LDHs 56

3.4 Basicity study of solvent treated LDHs 59

3.5 Basicity study of dehydrated solvent treated LDHs 62

3.6 Basicity and acidity studies of solvent treated LDOs 66

3.7 CO_2 adsorption on LDOs 78

3.8 Conclusions 82

3.9 Outlook 83

3.10 References 84

Chapter Four- A study of the CO_2 capture performance of Mg_xAl LDHs and LDOs 86

4.1 Introduction 86

4.2 Experimental details 87

4.2.1 Synthesis of Mg_xAl W LDHs 87

4.2.2 Synthesis of ethanol treated LDHs 88

4.2.3 Surface OH number titration 89

4.2.4 CO_2 measurements 89

4.3 Varying calcination temperature 89

4.4 Varying the heating ramp rate 94

4.5 Varying calcination time 108

4.6 Varying Mg^{2+}/Al^{3+} ratio 117

4.7 Optimised Mg_xAl LDO for CO_2 capture 132

4.8 Conclusions 135

4.9 References 136

Chapter Five - Design of Carbon@LDH core@shell materials for CO2 capture 139

5.1 Introduction 139

5.2 Nomenclature 140

5.3 Experimental details 141

5.3.1 Synthesis of $Mg_2Al\ CO_3$ W 141

5.3.2 Synthesis of Cabot@Mg_2Al LDH 141

5.3.3 Synthesis of solvent treated Cabot@Mg_2Al LDH 142

5.3.4 Calcination of core@shell material 142

5.3.5 Synthesis of AC, MAX and TPK core@shell materials 142

5.3.6 Ammonia treatment of carbon@LDH core@shells 143

5.4 Characterisation of carbon materials 143

5.5 Synthesis of carbon@LDH hybrid materials 148

5.6 Synthesis and characterisation of Cabot@LDH core@shell materials 150

5.7 Application of Cabot@Mg_2Al W core@shell materials in CO_2 capture 161

5.7.1 Cabot@Mg_2Al W LDH for CO_2 capture 161

5.7.2 Ethanol treatment of Cabot@Mg_2Al W core@shells 164

5.7.3 Cabot@Mg_2Al W (53) LDO for CO_2 capture 167

5.7.4 Rate of CO_2 adsorption of Cabot@Mg_2Al W core@shells 175

5.8 Carbon core@shells with other carbon materials 179

5.8.1 Synthesis and characterisation of new carbon@LDH core@shells 180

5.8.2 CO_2 adsorption of new carbon@Mg_2Al W LDO core@shell 188

5.9 NH_3 treatment of carbon@LDH materials 192

5.10 Conclusion 193

5.11 References 194

Chapter Six - Study of CO_2 capture during polyurethane synthesis 196

6.1 Introduction 196

6.2 Experimental details 199

6.3 Effects of LDH on the curing process of MCPU 200

6.4 Effects of water on the curing process of MCPU 203

6.5 Solution phase CO_2 capture of LDOs in PU matrices 206

6.6 Improvement of curing time 210

6.7 Conclusion 211

6.8 Outlook 212

6.9 References 213

Chapter Seven - Conclusion 215

7.1 Conclusion 215

7.2 References 219

Appendix A - Appendices for Chapter Three A1

A.1 TGA of LDH samples A1

A.2 N_2 adsorption-desorption isotherms of LDHs and LDOs A2

A.3 Pore size distributions of LDHs and LDOs A3

A.4 Titration data A4

A.5 Deconvolution of TPD data A6

A.6 ^{1}H and ^{27}Al ssNMR spectra of LDH samples A18

A.7 CO_2 adsorption profiles of LDO samples A19

Appendix B - Appendices for Chapter Four B1

B.1 N_2 adsorption-desorption isotherms of Mg_xAl LDHs and LDOs B1

B.2 Pore size distributions of Mg_xAl LDHs and LDOs B4

B.3 Deconvolution of TPD data B7

B.4 CO_2 adsorption profiles of LDO samples B29

Appendix C - Appendices for Chapter Five C1

C.1 N_2 adsorption-desorption isotherms of carbon and carbon@LDH materials C1

C.2 Pore size distributions of carbon and carbon@LDH core@shell materials C3

C.3 CO_2 breakthrough curves C5

C.4 Pseudo-second-order kinetic model fitting of Cabot samples C8

C.5 Pseudo-second-order kinetic model fitting of Mg_2Al W samples C11

C.6 Pseudo-second-order kinetic model fitting of Cabot@Mg_2Al W (53) samples C14

Chapter One - Introduction

1.1 Layered double hydroxides (LDHs)

1.1.1 Structure and composition

LDHs were first discovered in 1842 in their naturally occurring form of hydrotalcite.[1] Also known as anionic clays, they are a family of inorganic layered materials with the general formula $[M^{z+}_{1-x}M^{y+}_{x}(OH)_2]^{a+}(A^{n-})_{a/n} \cdot mH_2O$. Although z can be 1, 2 is the more common value; $y = 3$ or 4; a is the overall cationic charge of the layers and n is the charge of the interlayer anion. LDHs exhibit a layered structure with A as the interlayer species.[2] More common metals that have been incorporated into LDHs include Mg^{2+}, Al^{3+} and first row transition metals, such as Fe^{3+}, Ni^{2+} and Zn^{2+},[3–7] although other less common metals, such as In^{3+} and the lanthanides, have seen increasing use in LDHs.[8–15] For an LDH where M^{2+} and M^{3+} are Mg^{2+} and Al^{3+} respectively, pure LDH phases only exist for $0.2 \leq x \leq 0.33$.[16] They have a structure similar to that of brucite ($Mg(OH)_2$) with edge sharing octahedra of metal hydroxides.[17]

The interlayer anions are intercalated to balance the net positive charges of the hydroxide sheets resulting from the partial substitution of divalent ions with trivalent ones.[18] A wide range of anions have been intercalated into the LDH structure, from inorganic anions[19] (e.g. halides, nitrate and sulfate), transition metal complexes[20] to various organic molecules, including drugs and amino acids.[2,21,22] Water molecules are also incorporated into the interlayer region during the synthesis procedure and form hydrogen bonds to the hydroxyl groups on the surface of the cationic layers as well as the interlayer anions. This

stabilises the layered structure, linking the individual cationic sheets together,[23] while still maintaining their translational mobility.[24]

LDHs exist naturally in two polymorphic forms: hexagonal and rhombohedral. The hexagonal structure has a repeating ABAB sequence, while the rhombohedral structure presents as an ABCABC sequence. For the former, the lattice parameter *c*, is twice the thickness of the layer consisting of a cationic sheet and interlayer spacing, whereas for the latter, it is three times that distance (Figure 1.1).[2] The different polytypes can be distinguished using systematic absences of X-ray diffraction (XRD) reflections. Rhombohedral structures only present reflection peaks of $-h + k + l = 3n$. For hexagonal structures, peaks will be present when $-h + k + l \neq 3n$.[25]

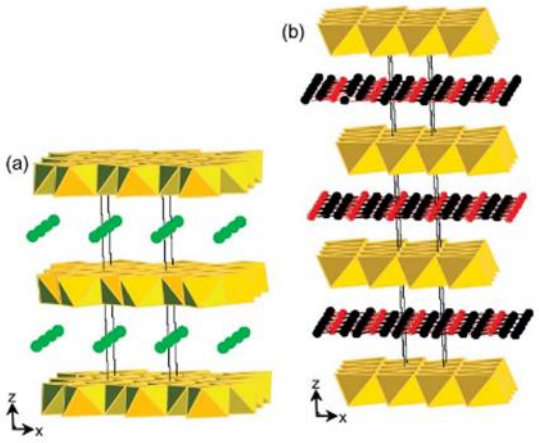


Figure 1.1 - LDH structures in (a) hexagonal and (b) rhombohedral form.[2]

1.1.2 Thermal stability

As temperature increases, an LDH undergoes thermal decomposition which leads to a change in composition and the formation of different products. Factors, such as the nature of cations and anions, and also the ratio of the metals in the structures, can affect the thermal decomposition process of the LDH.[3,26] but as the majority of this work will be focused on Mg^{2+} and Al^{3+} containing LDHs (Mg_xAl-LDHs), the following will focus more

on the specific decomposition of this family of LDHs. The first decomposition arises from the dehydration of Mg_xAl-LDHs. This usually occurs between 70–190 °C, resulting in a dehydrated LDH (Figure 1.2). Surface water molecules are removed from the structure prior to the removal of interlayer water. This is due to the interlayer water experiencing a stronger interaction by *ca* 12 kJ mol^{-1}.[27] The loss of interlayer water molecules is also accompanied by a decrease in interlayer spacing of *ca* 1 Å.[28]

When calcined at high temperatures, usually between 200 and 700 °C, some anions, as well as the hydroxide groups on the cationic layers, are removed.[23,29,30] For Mg_xAl-LDHs, the onset of dehydroxylation of the layers occurs *ca* 200 °C, as demonstrated by solid state nuclear magnetic resonance (ssNMR), XRD and other techniques carried out by Yang *et al.*.[31] Changes in the Al^{3+} environment coordination are observed as a result of the migration of Al^{3+} from octahedral sites to tetrahedral sites on the surface of the layered sheets. These Al^{3+} sites share 3 oxygens with the layer and one apical oxygen.[32] The loss of OH from the Mg^{2+} sites occurs at a slightly higher temperature, *ca* 280 °C. The change in coordination, coupled with the migration of Al^{3+} ions, leads to the creation of defects which could affect the basicity of the surrounding atoms, and therefore overall structure.[33] The loss of hydroxyl groups and migration of Al^{3+} sites lead to the neutralisation of the cationic sheets and therefore no longer require interlayer anions to balance out the excess of charge. In the case of a CO_3^{2-}-intercalated materials, the loss of anion is carried out through the liberation of CO_2. In the case of Mg_xAl-LDHs, the resulting material has the bulk structure of a crystalline periclase MgO, with an amorphous alumina. The resulting layered double oxides (LDOs) display a "structural memory effect", in which upon the reintroduction of an aqueous solution of anions, the layered structure of the LDH is rebuilt by intercalating anions in a process called reconstruction.[34] This allows for the uptake of

anions that were deemed difficult to incorporate via a direct synthesis method. However, when the samples are calcined at temperatures above 550 °C, this process becomes increasingly difficult.[35] At temperatures > 800 °C, the spinel structure is formed and the LDH structure cannot be reformed completely regardless of the length of reconstruction time due to the migration of ions within the structure during the formation of the spinel phase.[36] These spinel materials have shown basic catalytic behaviour for condensation and polymerisation reactions.[35,37–39]

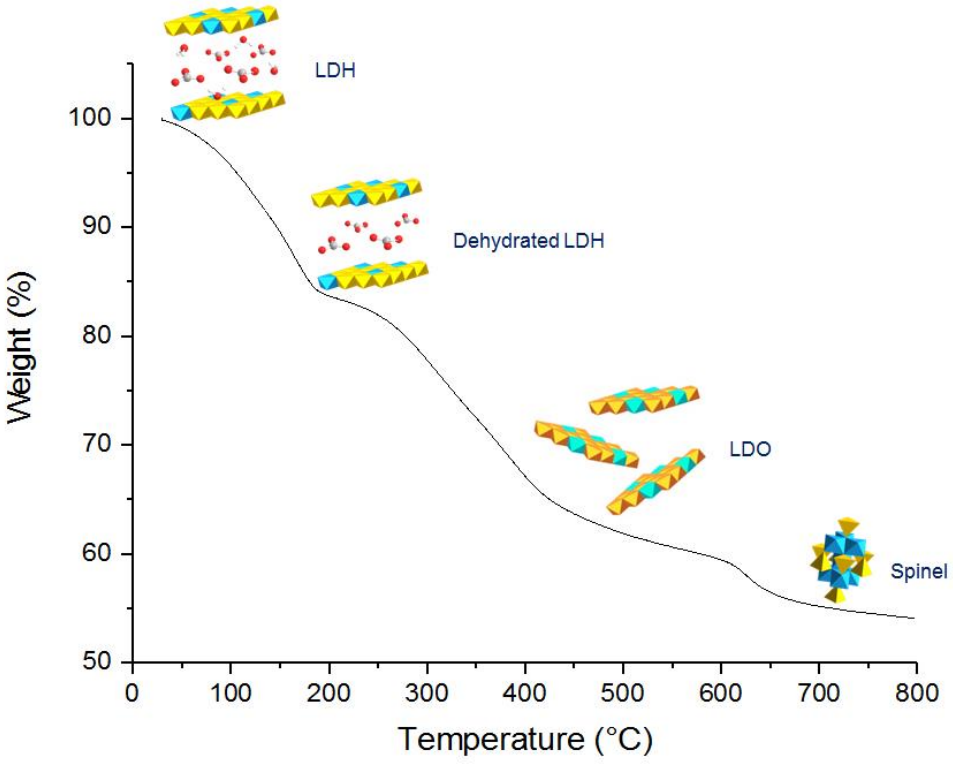


Figure 1.2 - TGA and graphic representation of the structural changes upon thermal treatment of a typical LDH.

1.1.3 Synthesis methods

The co-precipitation method is one of the most common ways of synthesising an LDH. This method, first reported by Feitknecht in 1942,[40] involves the addition of an aqueous solution of metal salts, in their desired ratio, to a basic solution of the target anion. The anions being intercalated must have a high affinity to bond to the cationic layers, otherwise

the anions from the original metal salts can be intercalated and contaminate the sample.[41] Depending on the synthesis conditions, the co-precipitation method can give different morphologies and size of LDH particles. It has been shown that changing conditions, such as pH of the mixture, ageing temperature, ageing time and stirring speed,[42] can have an effect on the morphology of the LDH. Due to the nucleation and growth taking place simultaneously, the co-precipitation method usually results in the particles having a wide size distribution.[43]

Another method is the homogeneous precipitation method, the urea method specifically, which was first reported by Constantino *et al.*.[44] Urea hydrolysis forms ammonium cyanate in the rate determining step, followed by rapid hydrolysis of ammonium cyanate to ammonium carbonate.[45] Ammonium carbonate gets further converted to ammonia and hydrogen carbonate, which results in the pH of the solution being 8.5–9 which is ideal for a lot of LDHs synthesis.[46] LDHs synthesised via this method possess a large hexagonal platelets (> 1 μm) with good crystallinity, but usually result in lower surface areas (< 100 m^2 g^{-1}) with respect to LDHs synthesised via the co-precipitation method.[47,48]

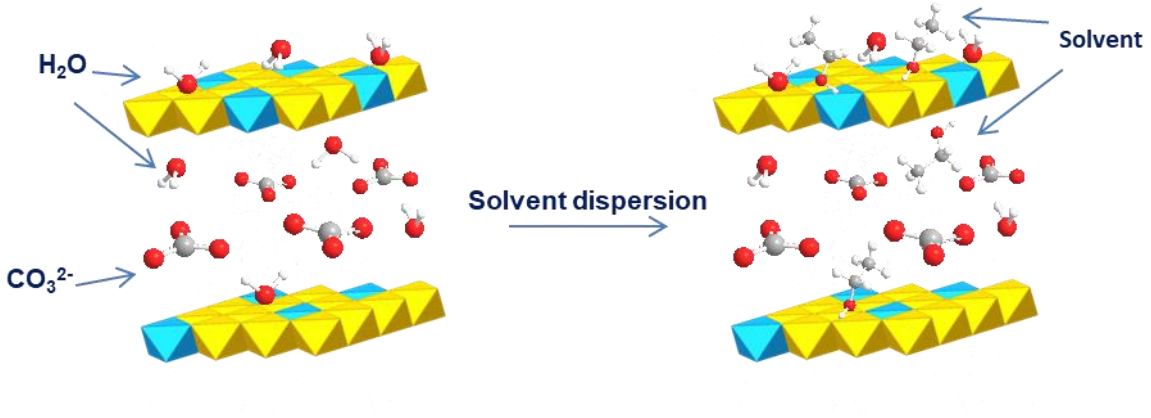
Anion exchange,[23,41,49] which relies on electrostatic interactions between the anions and the cationic sheet, is also particularly useful if the target anion is unstable in alkaline solution. The LDH is dispersed in a neutral solution with a large excess of the targeted anion. This method relies on electrostatic interactions, and hence the higher the charge density is of the anion, the better it is at replacing the existing interlayer anion.[50]

Other LDH synthesis methods include the reverse miscelle method[51] and the reconstruction (rehydration) method.[41]

1.1.4 Solvent treatment methods

During the post synthesis work up of an LDH, water is often used to wash the product until pH 7 and dried. This causes particles to aggregate by strong hydrogen bonding network between the platelets and water molecules, resulting in low surface areas, large agglomerates and a hydrophobic nature.[52] This hydrophilicity severely limits their usage as catalysts in organic reactions despite their highly tuneable compositions and properties.[53] To enhance the organophilicity of the materials, O'Hare *et al.* have developed post treatment methods to create delaminated LDH nanosheets by using aqueous miscible organic (AMO)[54] and aqueous immiscible organic (AIM) solvents.[55] The proposed mechanism of this method, as demonstrated by Erastova *et al.* using molecular dynamics, was, depending factors such as the solvent's geometry, ability to mix with water and its efficiency at disrupting the local hydrogen bonding network, the solvent penetrates the interlayer region to varying extent and removes water in the process.[56] The solvent molecules are shown to have a preferred orientation where the polar functional group aligns towards the LDH sheets while the non-polar area points into the interlayer region, disrupting the hydrogen bonding network.[56] The nature of the solvent determines the proximity of the solvent molecules to the LDH platelets. AMO solvents, such as ethanol and acetone, have shown the ability to penetrate and mix with the first hydration shell. However, AIM solvents, due to their reduced miscibility with water compared to AMO solvents, cannot penetrate as close to the LDH surface, but still retains a strong alignment of the polar functional group.[55] This weakens the interlayer interactions, allowing the cationic layers to be delaminated and prevents re-stacking during the drying process, resulting in a 'fluffy' product with high surface area and large pore volume (Scheme 1.1).[55–57] It is important to note that this facile method leaves the overall structure of the LDH untouched, with no change to metal ratios or distribution.[55,58,59] The interlayer

spacing also does not show any noticeable difference despite reducing and interrupting the interlayer hydrogen-bonding network. However, a broadening of the (00*l*) Bragg reflections in their XRDs can be observed and this indicates a reduction in the stacking of the nanosheets.



Scheme 1.1 - Proposed mechanism for solvent treatment in LDHs.

By using solvent treated LDHs in place of traditional water washed LDH, an increase in catalytic activity in esterification reactions can also be observed, similar to that achieved by increasing the basicity of LDHs. Kuljiraseth *et al*. demonstrated an increase in conversion and yield of the esterification of benzoic acid and 2-ethyl hexanol when comparing the AMO-LDH with its water washed counterpart.[60] These newly discovered LDH families have also been used as solid supports for ethylene polymerisation.[61,62] Compared to non-LDH supported polymerisation catalysts, an increase of 230% in activity can be observed when a 1-hexanol treated Mg_3Al LDH was used as a support. This increase in activity is currently being attributed to a change in Lewis acidity of the LDHs, but no research has been carried out to further investigate this effect.[62] When used as solid supports, the LDHs were heated to remove solvent molecules, therefore the difference in activities are solely due to their inherent chemical and physical properties.

1.2 Core@shell materials

Core@shells are defined as a family of materials which are composed of two or more constituents, usually consisting an inner and outer layer, although variations such as yolk shell and hollow shell materials also exist (Figure 1.3).[63] The constituent components may be organic or inorganic in nature. Organic components are usually polymers, such polystyrene[64,65] and poly(ethylene oxide),[66] whereas inorganic materials used can range from metals, such as Au, Pt and Pd,[67–69] to metal oxides, carbon and silica.[70–72]

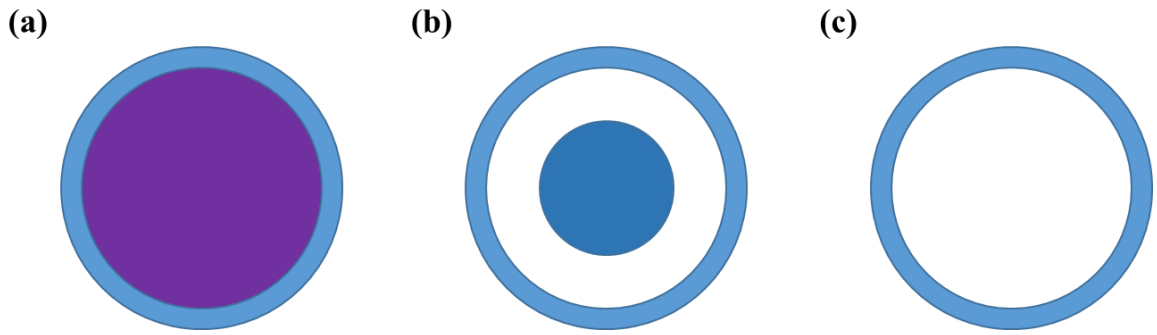


Figure 1.3 - Graphic representations of (a) core@shell, (b) yolk-shell and (c) hollow-shell hybrid materials.

These families of materials have not only been of interest in the field of chemistry, but have also gained increasing attention in biomedical, electronics and pharmaceuticals applications.[73–78] There are a large set of parameters which can be modified, such as materials and core:shell ratio, the specific properties of a synthesised core@shell can be finely tuned for the precise application.[79] There are several benefits of utilising a core@shell material over either parent material or simply a physical mixture of both. By creating a core@shell material, the properties of both core and shell materials can be altered, such as their dispersibility in a particular medium. The core material can also provide a scaffold on which the shell material can be grown in a more favourable orientation, leading to exposure of more active sites and therefore increasing their catalytic

abilities. Furthermore, the interface at which the two materials meet can cause defects in the materials. This can allow the creation of unsaturated centres with enhanced reactivities, causing a synergistic effect not observed in a physical mixture. For example, Han *et al.* reported a synergistic effect in a ZIF-8-C@NiAl LDH core@shell where the core@shell displayed a lowered resistance compared to the parent materials due to the carbon present allowing for a good conductive pathway between the materials.[80] As core@shell materials is a very wide field of research, this introduction will focus more solely on LDH-based core@shells.

1.2.1 Synthesis of core@LDH

Due to the tunable size of LDH platelets, they can act as both core and shell materials in the synthesis of a core@shell. With LDH acting as the core material, the shell materials have ranged from polymers, organic modifiers, to proteins and silica,[81–83] but this is still a relatively new and emerging field. However, due to the wider range of core materials available, such as silica, carbon, zeolites and metal oxides,[84–88] use of LDHs as a shell material has experienced more attention in comparison. Core@LDH materials are most commonly synthesised via the *in situ* co-precipitation method. This is usually a facile method which can result in a one-pot synthesis.[89–93] The growth of LDH platelets is carried out by applying an *in situ* ageing method or hydrothermal treatment.[91]

Another method is the sol-gel method, first demonstrated in 2010 by Zhao *et al.*.[94] They carried out the process by depositing $Al(O^iPr)_3$ on to the core material which hydrolysed to provide a surface coated with boehmite (AlOOH). This Al^{3+} source was the then used to grow the subsequent LDH *in situ* (Figure 1.4). This method was then developed and adopted by multiple others to create silica@LDH core@shells.[95,96] A third method is direct deposition. This method requires the separate synthesis of the two parent materials which

are then mixed together to form a core@shell via self-assembly.[97,98] This method has been adapted to be utilised in layer-by-layer core@shell synthesis. This modified method has been used to achieve multi-layered LDH core@shells by Li and Sasaki *et al.*.[99,100] The direct deposition method usually relies on a physical adhesion between LDH and core, this results in a few drawbacks, such as weaker core/shell interactions and limits on the core material.[101,102]

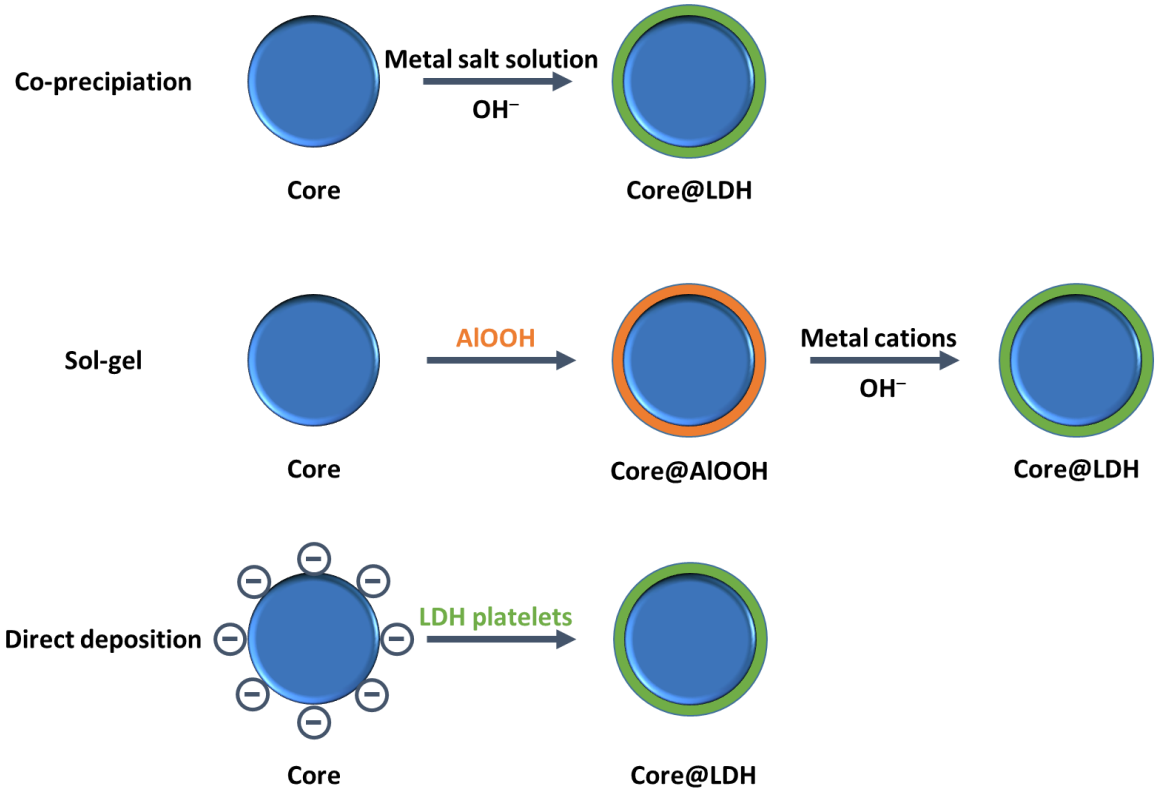


Figure 1.4 - Graphical illustration of co-precipitation, sol-gel and direct deposition core@LDH synthesis methods.

There are usually two common types of interactions for growth of LDHs on the core material.[103,104] The more simple interaction is the electrostatic attraction between the LDH and core material. An LDH platelet naturally possesses a positive surface charge, which allows them to form favourable interactions with a negatively charged surface, such as SiO_2 and activated carbon. Another interaction is by forming chemical bonds between the

LDH and support material through the oxygen of either materials, resulting in an M-O-X bonding interface. Kwok *et al.*, alongside other researchers, have demonstrated this interaction between the materials.[88,105] Kwok *et al.* first deposited a concentrated solution of $Al(NO_3)_3$ onto the surface of SiO_2, similar to the sol-gel synthesis method, followed by a heat treatment. This allowed for the formation of an aluminium oxide species which was the foundation for the LDH growth on the surface which was observed using FTIR. They demonstrated that tetrahedral Al^{3+} centres are formed in the LDH species, as shown by NMR spectroscopy. Typically in a pure LDH, only octahedral centres can be observed. The tetrahedral centres are believed to arise from the Si-O-Al interface.[106]

As an LDH is a 2D structure, the orientation of platelet growth on the core material surface is an important parameter. LDHs can grow both perpendicularly and parallel to the surface (Figure 1.5). Due to the more unsaturated centres located on the edges of an LDH, the edge of the platelet should be more reactive, and therefore the vertical growth of LDHs, perpendicular to the core surface should be more favourable than parallel growth.[104] Yet the parallel growth of LDHs in core@shell materials is still observed. It has been hypothesised that the growth orientation of LDH platelets is dependent on the concentration of metal solution. When the concentration of metal salts is high, the preferred orientation of growth is vertical, while a parallel growth to the surface is preferential when the concentration is low. This is due to factors such as nucleation rate and growth space on the core surface.[107] Gu *et al.* hypothesised when the nucleation rate is fast, the LDH nuclei are more compacted on the surface of the core, therefore due to the limited horizontal growth space, vertical growth along the (110) plane is preferred, leading to the formation of platelets growing perpendicularly to the core. However, when the

nucleation rate is slow, LDH nuclei are less compacted on the surface, which provides more freedom for horizontal growth, resulting in platelets parallel to the core.[107]

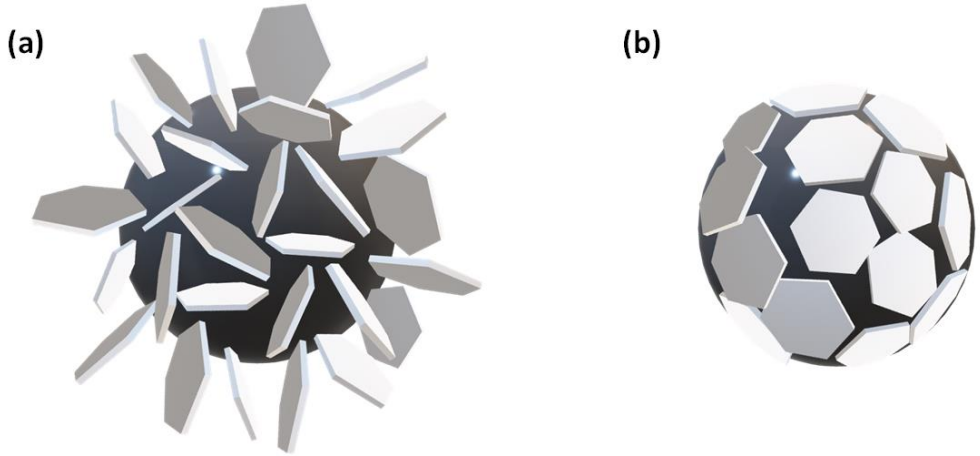


Figure 1.5 - Graphical representation of LDHs growing (a) perpendicular and (b) parallel to the core material.

1.3 Applications of LDHs and LDH core@shells

1.3.1 Waste treatment

Due to their highly tuneable compositions and properties, LDHs have seen a wide range of applications. Firstly, due to their high affinity for intercalating anions into their structure, whether through the anion exchange or reconstruction method, they have been shown to effectively absorb contaminants from wastewater and other aqueous industrial waste. Mg_xAl-LDHs have been shown to remove harmful contaminants, such as fluorides and arsenates.[108–113]

1.3.2 UV absorption

By incorporating different elements into the structure, the application for an LDH can also be widened. Lanthanide-doped LDHs have been shown to be effective as bio-imaging as well as drug delivery materials.[114] The deployment of UV absorbing metals, such as Ni^{2+}, Zn^{2+} and Ti^{4+}, has allowed for their usage as UV blocking and photocatalytic materials.[115–

[119] By adjusting the composition of the LDHs, the band gap can be fine-tuned and therefore allows for their customisation for individual reactions. LDHs have also seen use as electrode materials as they benefit from having increased surface area compared to simple oxide materials.[120] Since 2007, LDH materials with different sizes, ratios and compositions have also been used as supercapacitors.[121–124] Transition metal containing LDHs have seen use as materials in a lithium ion battery due to their ability to display high surface area and pore volumes, as well as their highly tuneable electronic properties due to their flexible chemical composition.[125,126]

1.3.3 Catalysis

Both LDHs and LDOs have been used as heterogeneous catalysts due to their natural basicity, flexible composition and uniform active site distribution.[127] They also benefit from being a solid which allows for a facile separation and recycling process post deployment. LDHs have been shown to be excellent catalysts for organic reactions such as C-C bond formation reactions and transesterifications.[128–135] Simply by changing their composition, they can also catalyse other reactions. The introduction of Y^{3+} was shown to increase catalytic activity towards certain epoxidation reactions.[136] By incorporating transition metals into the structure, they can be used in electrocatalysis of organic reactions such as oxidation reactions.[137–141] Efforts have also been made to increase their basicity in order to amplify their catalytic behaviours by doping with various cations into the structure or impregnating on the surface. For example, potassium has been impregnated onto the surface of LDHs and has seen large improvement in catalytic activity.[142,143] The increase in activity is suggested to be linked to the increase in basicity of the LDH.

1.3.4 Gas phase CO_2 capture

CO_2 is a greenhouse gas and a major contributor to climate change. Every year, CO_2 emissions are on the rise, leading to an estimated 37.1 billion tons emitted in 2018 (Figure 1.6). This is a 2.7% increase year on year, compared to the 1.6% in previous years.[144] On the current projection, the planet temperature is set to rise by 3–5 °C in the next few years. Efforts have been made around the world to decrease global emissions to try to combat this effect. Countries have pledged to reduce their carbon footprints and be less reliant on fossil fuels, but even with this change, factories and power plants are still one of the biggest contributions to the global CO_2 emission.[145] Flue gas usually has a CO_2 composition of < 15%, and due to the combustion of hydrocarbons, H_2O is also produced and exhausted as part of the composition of the flue gas. Although there are means, such as an air separation plant, to isolate CO_2 for post-combustion capture, these techniques are usually expensive, therefore a tolerance towards CO_2 greatly increases the viability and value of the sorbent materials.[146]

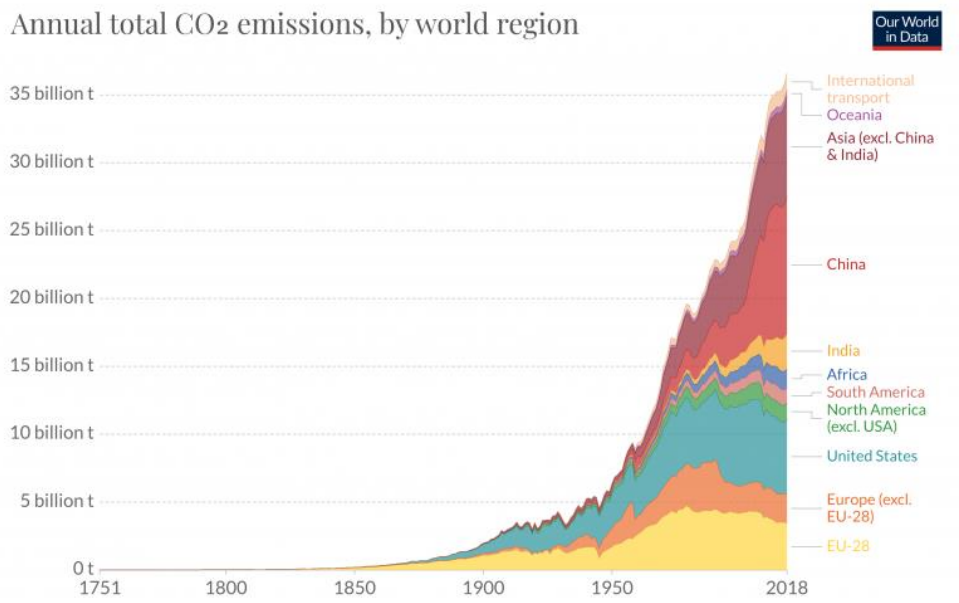


Figure 1.6 - Breakdown of global emissions of CO_2 in 2018 into individual regions and countries with data presented by Carbon Dioxide Information Analysis Centre (CDIAC).[144]

Regenerative amine capture solutions have been widely used in recent years as chemical absorbents, utilising an absorber and stripper system where the absorbent is thermally regenerated.[147–149] A majority of flue gas have operation pressures and temperatures at 1 bar and 40–60 °C / 120–140 °C (absorber/stripper) respectively for the purpose of absorption and regeneration of amine solutions. Methanol and poly(ethylene glycol) are also used as liquid phase absorption materials.[150–152] CO_2 capture values for aqueous amine systems usually range between 0.3–1.3 mol_{CO2} mol_{amine}^{-1}.[153] There are several drawbacks to the use of aqueous amine, such as low contact area between liquid and gas and severe absorbent degradation, therefore alternative materials are being explored.[154] Apart from solution phase absorption, CO_2 can also be removed by solid sorbents by way of physisorption and/or chemisorption by using porous materials. Materials, such as activated carbon and zeolites, have been widely studied for use of removing CO_2 from flue gas via physisorption while metal oxides adsorb via chemisorption.[155–164] An ideal material for CO_2 capture should be measured by the following parameters: 1) CO_2 capture capacity, 2) optimal adsorption and desorption temperatures, 3) fast adsorption kinetics, 4) ease of regeneration, and 5) ability to tolerate other contaminants in the flue gas composition.[146] The advantages and drawbacks of the materials introduced in this section are summarised in Table 1.1.

Zeolites have shown promising results with regards to CO_2 capture performances, with Na-Y demonstrating one of the highest adsorption values of 4.9 mmol g^{-1} at relatively low pressures and temperatures (0.1 bar and 273 K).[165] Other zeolites have also displayed outstanding CO_2 adsorption performances, ranging between 1–4 mmol g^{-1} at 295 K and 1 bar pressure.[166] However, similar to other materials, the CO_2 capture performance decreases when the adsorption temperature increases.[167] Furthermore, with the introduction

of H_2O into the gas mixture, the CO_2 capacity of the materials drastically decreases. This is attributed to the competition between CO_2 and H_2O for the adsorption sites on the surface of the materials. The highly polar water molecules, compared to the linear CO_2 molecules, adsorbs more favourably onto the cations in the zeolite structures, leading to a reduced availability of active sites for CO_2 to adsorb onto.[168] The regeneration of the heterogeneous adsorption materials is usually carried out using pressure swing adsorption (PSA) or temperature swing adsorption (TSA). PSA is a method using changes in pressure to separate gases whereas TSA achieves the same result via a change in temperature. It has been observed that the CO_2 capacity of zeolites decreases over the repeating regeneration cycles. This is due to a portion of the adsorbed CO_2 molecules being chemisorbed on the surface in the form of carboxylates or carbonates, and therefore blocking off active sites, reducing the CO_2 capacity.[166,168,169] Siriwardane *et al.* reported a decrease in CO_2 capacity by *ca* 15–20% over 10 cycles of regeneration.[170] In order to remove these chemisorbed CO_2 molecules, the regeneration temperature needs to be increased to 200 °C. Due to physisorption constituting the majority of adsorption, zeolites are very sensitive towards adsorption temperature. As adsorption temperature increases, CO_2 adsorption has been shown to decrease drastically.[171] Efforts have been made to improve the CO_2 adsorption of zeolites by impregnating the surface with metal hydroxides to improve their basicity.[172]

Another family of materials that have been of interest on the industrial scale is activated carbon. This is due to their relatively low cost of synthesis compared to other materials as a result of the wide range of raw materials they could be produced from. These materials range from lignocellulosic materials, to wood, bone and coal. Prior to activation, the raw materials are exposed to temperatures < 700 °C in an atmosphere without O_2, leading to the formation of a carbonised material.[173–175] There are two general methods of activation:

physical and chemical (Figure 1.7). Physical activation is more environmentally friendly and inexpensive compared to the chemical activation method, but has the drawback of high energy consumption due to the long heating time.[173,175–177]

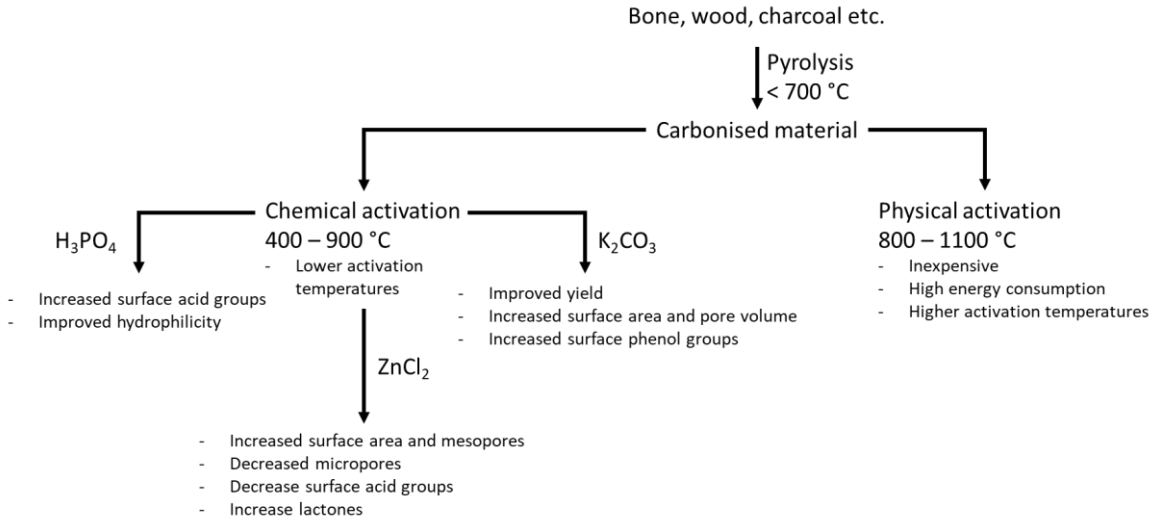


Figure 1.7 - Properties of activated carbon synthesised under different conditions.

For the chemical activation path, a variety of reagents and condition can be used, which result in a drastic changes to the physical and chemical properties of the activated carbon. The reagents can cause changes in surface area, pore sizes, and even surface functional groups.[178–194]

This wide range of synthesis parameters leads to a host of different physical and chemical properties.[195,196] This tuneable nature allows activated carbons to possess a range of CO_2 capacities, from 0.5–3.0 mmol g^{-1}.[197] Similar to zeolites, an increase in adsorption temperature, as well as the introduction of H_2O, leads to a decrease in CO_2 uptake of activated carbons.[198,199] An increase in CO_2 pressure results in an increase in CO_2 capacity of these materials.[170,196] They are also shown to display adsorption strengths that are not too strong at low pressures.[198,200] The enthalpy of adsorption, as determined by Chue *et al.*, is shown to be 30 kJ mol^{-1} for activated carbons. This is less than that of a zeolite, which

was determined to be 36 kJ mol^{-1}.[155] This is a very desirable quality due to the fact that it results in an easier, milder regeneration process, which results in a less expensive process on the industrial scale. It was shown that using identical PSA systems, activated carbons were demonstrated to completely regenerate over multiple cycles, while zeolites displayed decreasing CO_2 capture values over successive cycles.[167] Enhancements to CO_2 capture performances have also been carried out on activated carbons, usually by amine or ammonia modification.[201–203] The impregnation method is often used in the synthesis of these materials, but this method has been shown to lead to the blocking of surface pores. A promising high temperature ammonia modification method was discovered by Przepiórski *et al*..[204] This method replaces the oxygen functional groups with nitrogen-containing functional groups which improves the surface basicity of the material. This process resulted in a material with an optimal CO_2 adsorption performance at 400 °C (Figure 1.8). Increasing the temperature above 400 °C leads to a decrease in CO_2 capture capacity which is believed to be the result of pore blocking by the ammonia molecules.

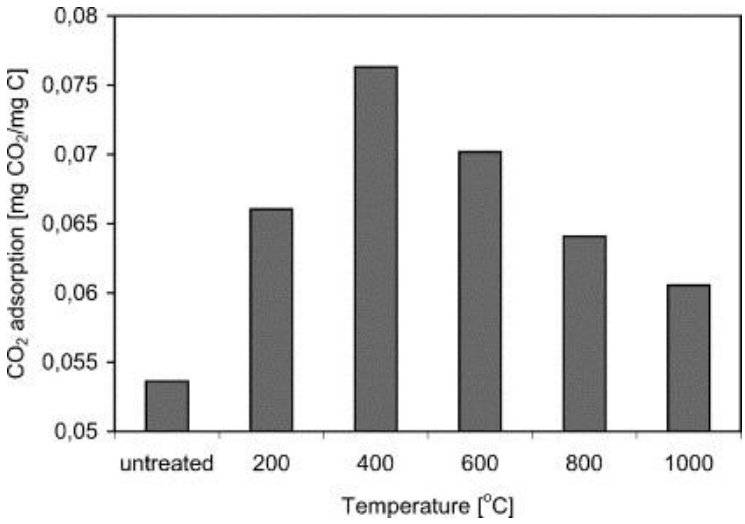
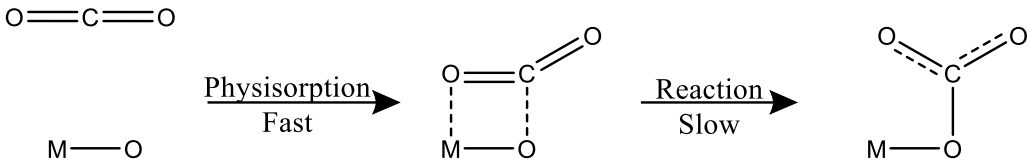


Figure 1.8 - CO_2 adsorption of activated carbons treated with ammonia at different temperatures for 2 h.[204]

Due to their inherent basicity, significant amounts of research has been carried out on the deployment of alkali and alkali earth metal oxides, as well as transition metal oxides, as

CO_2 capture materials.[205–214] Their basicity leads to the adsorption of CO_2 being weighted more towards chemisorption. The change in adsorption nature strongly affects the rate of adsorption. Most metal oxides adsorb CO_2 into their structure through firstly surface adsorption, followed by a reaction on the surface interface to form MCO_3 species.[215–217] While the first step is usually rapid, the second step is much slower and therefore limits the overall the adsorption kinetics (Scheme 1.2). Due to the chemical reaction that occurs upon adsorbing CO_2, this leads to a more difficult desorption process when attempting to regenerate the sorbent.



Scheme 1.2 - Adsorption mechanism of CO_2 on the surface of a metal oxide.

LDHs and LDOs have also been investigated as a suitable material for CO_2 capture due to their highly tuneable nature.[218–226] By altering the cations and anions, variations in particle size, pore volume, surface area, interlayer spacing and metal ratios can be accomplished in a relatively facile manner. This leads to a drastic change in CO_2 capture abilities, ranging from *ca* 0.3 to 2.5 mmol g^{-1}.[223,227–230] Veerabhadrappa *et al*. reported a CO_2 capture value of 2.14 mmol g^{-1} using Mg_xAl LDOs, which is within the range of CO_2 capture values of other materials mentioned in previous sections.[231] As sorbent materials, they are effective in their LDH forms as well as their calcined LDO derivatives. The ability to enhance CO_2 uptake upon the introduction of H_2O distinguishes LDHs as a unique adsorption material, as other sorbents, such as zeolites and activated carbons, have displayed inabilities to tolerate the presence of H_2O. This improvement in CO_2 capture has been observed in both LDHs and LDOs.[232,233] For LDOs, the introduction of water allows for CO_2 to be CO_3^{2-}

while reconstructing the LDOs to their parent LDH form. Torres-Rodriguez *et al.* showed increasing humidity led to an increase in CO_2 capture of Mg_3Al LDOs, with the optimal CO_2 adsorption value of 2.13 mmol g^{-1}.[234] The mechanism by which the LDH improves is yet to be determined. The regeneration process of LDHs/LDOs is also unique, in which they display a weaker surface interaction compared to metal oxides, such as CaO, but stronger than materials like zeolite.[235–237] Therefore they present as an intermediate material in terms of regenerative properties, demonstrating excellent retention of CO_2 capture abilities. Zhu *et al*. demonstrated that, even after 20 cycles of regeneration, the CO_2 capacity only reduced from 1.5 mmol g^{-1} to *ca* 1.4 mmol g^{-1} for a surface modified MgAl LDO.[238] This is a significant improvement upon the regenerative properties of comparable zeolites mentioned.

Improvements to LDHs can be carried in a variety of manners due to their flexible compositions and highly functionalisible surfaces. By varying the identity of M^{2+} between Mg^{2+}, Ca^{2+} and Co^{2+}, Wang *et al.* reported a $Ca_{1.5}Co_{1.5}Al$ LDO possessing the best CO_2 capture ability of 1.39 mmol g^{-1} for mid temperature adsorption (200–400 °C).[239] It was also reported for the binary LDOs, Mg_3Al LDO possessed the highest CO_2 capture value compared to Ca_3Al and Co_3Al LDOs. This is proposed to be affected by available actives and CO_2 affinity: while Ca-based oxides usually possess a strong affinity towards binding CO_2 through the formation of $CaCO_3$, Ca_3Al LDO was discovered to possess some $CaCO_3$ species, therefore reducing the available active sites for CO_2 binding. Meanwhile, Co_3Al compared to the other systems is shown to possess a lower affinity for CO_2.[239]

The effects of changing the trivalent metal have also been reported by Wang *et al.*. Al^{3+}, Ga^{3+}, Fe^{3+} and Mn^{3+} containing Mg-LDHs were tested for CO_2 capture between the temperatures of 200–400 °C and the best result was obtained by Mg_3Fe CO_3 LDH calcined

at 300 °C for 2 h (0.46 mmol g^{-1}), although Mg_3Al and Mg_3Mn LDOs also displayed similar CO_2 uptake (0.41 and 0.42 mmol g^{-1} respectively).[240] However, regardless of calcination temperature, Mg_3Ga LDO showed relatively low CO_2 capture values, with a maximum of 0.27 mmol g^{-1}. By varying adsorption temperature, the amorphous phase of LDOs was determined to mainly adsorb CO_2 via physisorption while crystalline metal oxide phase adsorbs via chemisorption, similar to a pure metal oxide material.[240]

Table 1.1 - Summary of sorption type, advantages and disadvantages of different materials for CO_2 sorption.

	Sorption type	Advantages	Disadvantages
Amine solution	Absorption	- Most common CO_2 sorbent - Compact absorber column	- Absorbent corrosion - Low CO_2 capacity - Energy intensive regeneration process
Zeolite	Physisorption	- High CO_2 capacity - Highly tuneable composition	- Intolerant to H_2O in flue gas - Reduction of CO_2 capacity post-regeneration
Activated carbon	Physisorption	- High CO_2 capacity - Ease of regeneration	- Intolerant to H_2O in flue gas - Energy intensive synthesis methods
Metal oxide	Chemisorption	- High CO_2 capacity	- Slow rate of adsorption - Difficult desorption process due to strong chemisorption
LDH/LDO	Physisorption and chemisorption	- Retention of CO_2 capacity over multiple cycles - Good tolerance to H_2O in flue gas	- Relatively low CO_2 capacity

The LDO surface can also be modified through impregnation with alkali and alkali earth metal oxides to enhance their inherent basicities.[226,236,241] Oliveira *et al.* demonstrated a 760% increase from 0.10 mmol g^{-1} to 0.76 mmol g^{-1} by impregnating commercial Mg_xAl LDOs with potassium. This improvement is believed to be due to the potassium enhancing the basicity of the LDO. LDHs and LDOs can also be altered by acting as supports for other materials or by growing on other particles, which results in core@shell materials (described in Section 1.2).

1.3.5 Application of LDH core@shells

LDH core@shells have been deployed in a multitude of applications, such as capacitors and CO_2 capture. TiO_2 based core-shells have been synthesised to enhance the overall photocatalytic abilities of the two families of materials. The first TiO_2@LDH core-shell was synthesised in 2009 by Yang *et al.*.[242] Since then, CeO_2-based core@shells have also been developed for similar uses. Magnetic core@shells have also been of interest as this allows for the utilisation of a magnetic core by functionalising the surface with an active LDH shell. This could allow for more efficient separation and recycling of catalysts post-deployment.[101,243]

Carbon@LDH core-shells, have been used in lithium batteries and superapacitors.[87,244] The synergy between carbon and LDHs have shown increased capacitance and reusability. In a study, upon repeated cycles, there was no noticeable decrease in capacitance. This family of core-shells have also seen usage as hydrogenation catalysts.[245,246] By substituting the carbon core with graphene oxide, graphene oxide/Mg_xAl hybrids have been developed as CO_2 adsorption materials. This material has an alternating layered structure. While this material experienced an increase in CO_2 capacity (*ca* 0.45 mmol g^{-1} at 300 °C and

$P(CO_2)$ = 0.2 bar), it suffers from a low surface area.[247] Carbon nanotubes have also been used as support for carbon@LDH in CO_2 capture.[248]

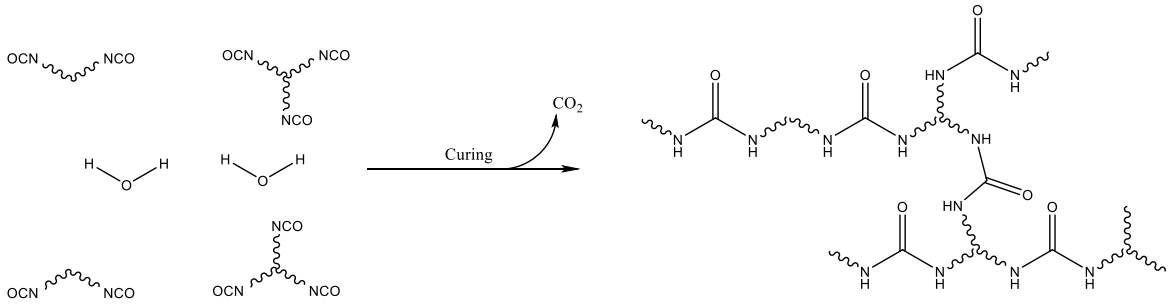
1.4 CO_2 capture in polyurethane curing

While CO_2 capture in the gas phase has been explored extensively, the use of heterogeneous material in solution phase CO_2 capture is yet to be studied. Polyurethane (PU) is a class of polymers where a monomer containing isocyanate N=C=O functional groups react with NH or OH to form urea or urethane bonding moieties respectively. PU was first discovered by Bayer *et al.* in 1937 with the initial purpose of exploiting the areas of polymer classes not covered by a patent for polyamides and nylon.[249] The resulting linkages, as well as the monomer block, contribute to the internal hydrogen bonding network. The strength of the hydrogen bonding within the polymer matrix is important in determining the properties.[250–252] This produces physical crosslinking which can improve the strength of the polymer. The curing process can be facilitated by the presence of UV light or a catalyst.[253,254]

One class of PU is the moisture curing polyurethanes (MCPUs). This family contains a one component pre-polymer with isocyanate groups.[255] However, instead of reacting with other NH or OH containing organic co-monomer, the curing process is carried out by atmospheric water. This causes urea linkages to form instead of a urethane bonding moiety. This process releases CO_2 as a by-product which ideally should escape the matrix (Scheme 1.3). The curing process of MCPUs is usually determined by the rate of diffusion of moisture through the polymer matrix and so can result in a longer curing time. Compared to other classes of PUs, this family possesses improved hardness, strength and flexibility.[256–258] Their ability to polymerise by only requiring moisture allows them to be

very effectively and efficiently deployed as sealants and adhesives as they can form strong bonds in damp, tight gaps. However, some issues arise when using MCPUs. Firstly, MCPUs have a tendency to form side products during storage. This can reduce the shelf life of the product and lead to altering of the physical properties of the polymer matrix. This could be greatly reduced by adding moisture scavengers, usually in the form of monoisocyanates.[259] Secondly, they possess a relatively long curing time when compared to other PU systems.[145]

To improve the curing process of MCPUs, catalysts, such as amines, have been used.[260] As the rate of curing is determined by moisture, additional water can also be added to the reaction. While this process decreases the curing time, it could result in the formation of CO_2 air pockets within and on the surface of the polymer matrix. This effect could prove detrimental in their deployment as adhesives and sealants due to the reduced contact with the bonding surfaces by the formation of air pockets. Therefore, efficient CO_2 capture during the MCPU curing process could lead to a significant increase in adhesive performance.



Scheme 1.3 - Curing process of MCPUs.

Nanomaterials have recently been incorporated into PUs to improve their structural properties. High surface area materials introduce more surface/polymer interactions.[261] a range of inorganic materials have been used as “fillers”, such as SiO_2, montmorillonite, as

well as other oxides, such as Fe_2O_3 and TiO_2, have been introduced to increase the thermostability of PU. Incorporating SiO_2 produced a glass transition at higher temperatures.[262] The glass transition temperature is the temperature at which the amorphous phase in a material starts to change from a rigid structure to a more flexible state.[263] This phenomenon of the elevation in glass transition temperature was attributed to the different PU environments being bound around the SiO_2 nanoparticles.[264] Layered materials, such as montmorillonites (aluminosilicates), have also been incorporated into the structure to improve properties like gas barrier, strength and reduction of weight.[265–274,275]

LDHs/LDOs have been incorporated into polymer matrices in recent years. Yu *et al.* displayed excellent dispersibility and incorporation of LDH platelets into poly(vinyl alcohol) (PVA) matrices via the reconstruction method.[276,277] This property could allow them to be very successful additives and fillers in MCPUs as they have shown excellent CO_2 capture materials. Furthermore, their layered structure with highly tuneable properties could potentially allow them to be utilised in a similar way as other nanomaterials.

1.5 Acidity and basicity of solids

The surface chemistry of solid materials, especially their acidity and basicity, is vital in determining their performances in catalytic reactions such as redox reactions and adsorption.[278,279] It has also been shown that doping LDHs and LDOs with potassium enhances their basicity which leads to an increase in CO_2 uptake.[226,280] There are 2 main definitions for acids and bases. Firstly, the Brønsted definition involves protons. A Brønsted acid is a proton donor while a Brønsted base is a proton acceptor.[281] For the Lewis definition, an acid is a lone pair acceptor while a base is a lone pair donor (Figure

1.9).[282] Several different techniques have been developed and utilised in the past decades to probe a material's acid base properties. While each technique presents with individual merits, each one also has associated disadvantages.

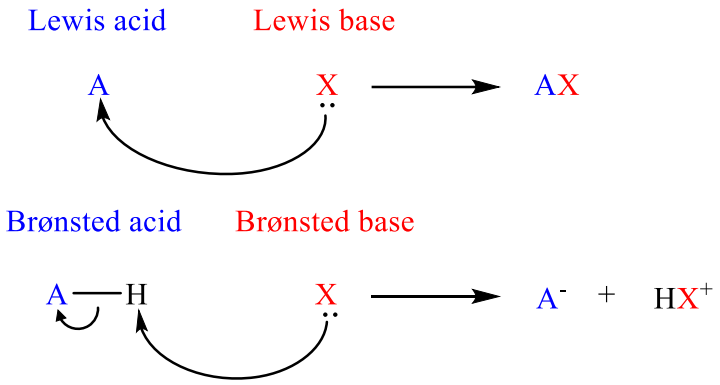


Figure 1.9 - Definition of Lewis and Brønsted acids and bases.

Hammett indicators were first developed for use in liquid or aqueous phase reactions, but has slowly been transferred for use in probing the acid base properties of solid systems.[283,284] This method utilises the colour change in the chosen indicator which occurs at given pH values. Due to the colour changes being a result of a proton transfer reaction in the indicator, this method is used to probe a material's Brønsted properties. The use of different indicators can lead to the examination of acid/base sites of different strengths.[285] Combining this technique with the titration method could result in very informative results of number of basic or acidic sites at different strengths. However, the values obtained from this method are less accurate due to the limitations of the usage of Hammett indicators in a heterogeneous system, such as the dispersibility of the solid in the solvent and that the solvent could be absorbed onto the active sites. For layered materials, further limitations could be present, depending on the ability of the indicator to penetrate the interlayer regions. The results obtained, therefore, show more of a qualitative trend.[286]

Temperature Programmed Desorption (TPD) is one of the more common ways of measuring the surface Lewis basicity and acidity of a solid.[287–289] The technique works by first pre-treating at a chosen temperature the sample in order to remove any impurities on the surface during transportation and storage. Then probe molecules of choice, usually CO_2 for basicity and NH_3 or CO for acidity, are flowed over the sample, allowing them to fully saturate and adsorb onto the active sites of the sample. An inert carrier gas (N_2 or He) is then flowed over the sample to remove any physisorbed molecules. The sample is finally heated and the chemisorbed gas is released and measured.[286,290–292] The desorption profile can be deconvoluted into different bonding modes which provides insights into the strength of the active sites (Figure 1.10). It is assumed that the adsorbed probe molecules only occupies one site and do not interact with other adsorbed molecules.[293] The accuracy of this technique is very dependent on the thermal stability of the materials.[286] The machine is only capable of measuring the amount of gas given off and cannot differentiate between different gases. Hence, this method cannot be used for materials that decompose and release gas within the testing temperature range. The final reading and results are also shown to depend on parameters such as temperature range, ramp rate of heating process and adsorption temperature.[294]

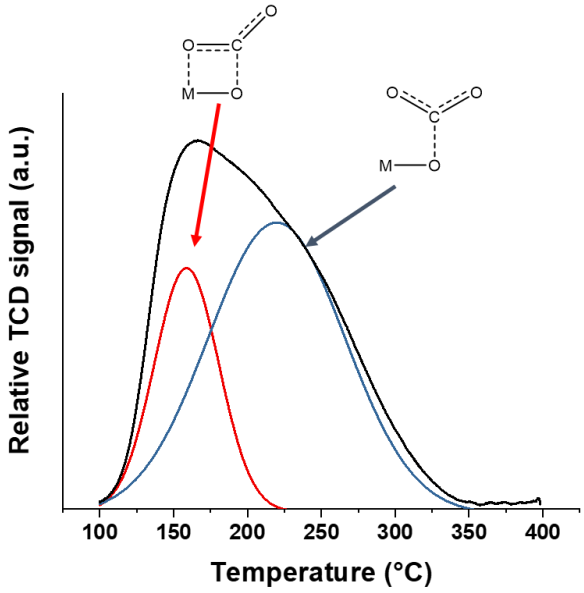


Figure 1.10 - Deconvolution of CO_2 desorption on a Mg_xAl LDO surface.[295]

In situ Fourier transform infrared spectroscopy (*in situ* FTIR) is a very well developed technique for probing the surface basicity and acidity of a surface.[241,296–298] The probe molecule is adsorbed onto the surface in a manner similar to that used in a TPD measurement. For basic sites, CO_2 or SO_2 are the common probe molecules of choice, while CO, NH_3 or pyridine is used for acidic sites.[299] This method is very useful in determining how probe molecules bond to the active sites on the surface. Extensive studies have been carried out on the bonding modes of CO_2 on a metal oxide surface and the correlating basic sites they are bonded to (Figure 1.11).[296,300,301] By combining this method with TPD, the different bonding modes of NH_3 on a surface have also been identified.[297] Both these studies have allowed for a more insightful investigation of solids. Studies have also shown that pyridine exhibits different stretching frequencies for Brønsted and Lewis sites.[302] The stretching frequencies have also shown direction correlation to basicity of a material.[303] This is due to the stronger basic sites would lead to a stronger bond to molecules, like CO_2. This would lead to a weakening of the C-O bonds which is reflected

in a decrease in stretching frequency. The disadvantage of this technique is the inability to accurately determine the number sites in a material.

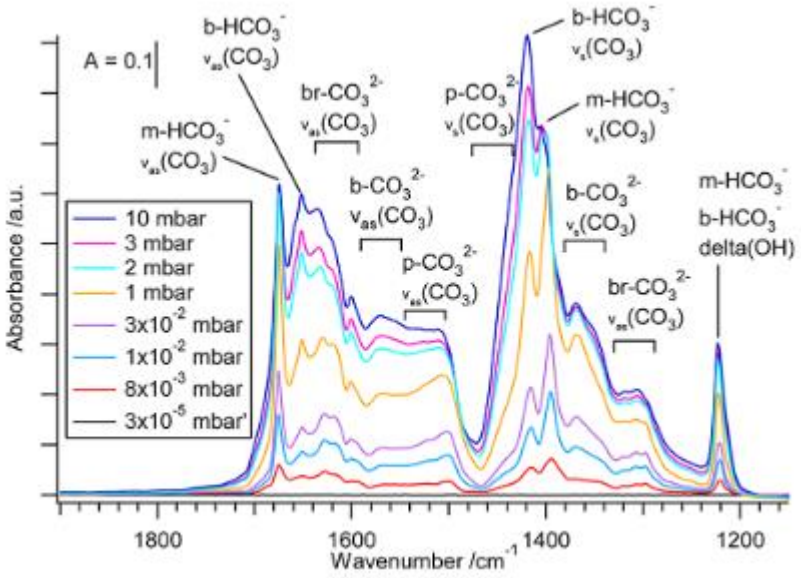


Figure 1.11 - Infrared absorbance signal of CO_2 on Y_2O_3 at different pressures.[300]

Finally, NMR has been used to probe surface chemistry by using various spin active nuclei, such as ^{1}H, ^{13}C and ^{31}P.[304,305] This method has been used to probe the environment of hydroxyl groups in zeolite materials. ^{13}C ssNMR has been shown to be a useful tool in determining the basicity of zeolites.[306–308] By adsorbing methanol or methyl iodide onto the surface of the solid, the C nuclei of the adsorbed species experience a different level of shielding based on the basicity of the surface oxygen it is bonded to. This in turn affects the chemical shift of the nuclei and has shown to correlate very well with the basicity of a zeolite (Figure 1.12).[308] Protons of the methoxy groups have also been observed to follow this trend, though fewer studies have been done on those.

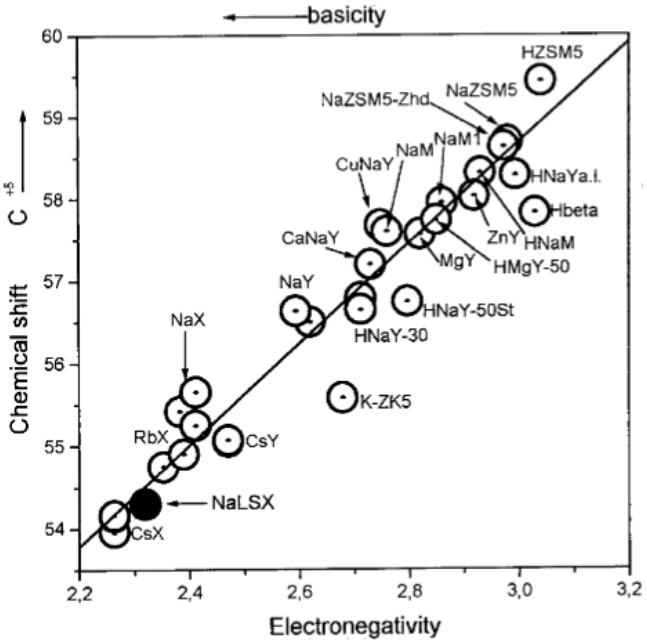


Figure 1.12 - Chemical shift dependence of surface methoxy groups on electronegativity of zeolites.[308]

Pyridine, phosphine or phosphine oxides have also been used in determining acidity in zeolites and other materials.[309,310] Trimethylphosphine (TMP) has been used extensively to probe the surface acidity of solids. Lewis and Brønsted acidic sites interact differently with the adsorbed molecule, therefore produce distinct chemical shift values (δ = –20 to –58 ppm and δ = –2 to –5 ppm respectively).[311–313] The signal attributed to the Brønsted acidic sites is the result of a "$TMPH^+$" species from TMP interacting with a proton on the surface of a material. The chemical shift value for the Lewis acidic sites have been shown to correlate to the strength of the acid site, with a stronger acid site leading to a more positive value. Furthermore, this method can also quantify the different acid sites in a material due to the quantitative nature of NMR.[312] However, this technique was shown to be not effective on LDH materials as the only signal observable in the ^{31}P NMR spectrum displays a chemical shift value of $\delta \approx 40$ ppm, which more readily corresponds to the signal observed in an adsorbed trimethylphosphine oxide (TMPO) molecule. This has been attributed to the potential oxidation of TMP by the LDH material.[314]

1.6 Scope of thesis

The scope of this thesis is to explore the use of LDH and LDH-based materials for CO_2 capture. Although MgFe LDHs have been shown to display the best CO_2 capture abilities,[240] Mg_xAl LDHs are more widely available and studied and can be made from cheaper raw materials. Therefore this body of work will focus on Mg_xAl LDHs. A study of the acidity and basicity of solvent treated Mg_xAl LDHs and LDOs will be thoroughly examined as they have shown enhanced chemical properties in various applications, and their use as CO_2 sorbent materials will be explored in Chapter Two. Various attempts to optimise LDHs/LDOs for CO_2 capture have been carried out,[229,315] however none have successfully correlated the performances to the changes in the physical and chemical properties of the resulting material, therefore more in-depth work should be done to fully understand these materials. To this extent, Chapter Three discusses the optimisation of Mg_xAl LDOs as CO_2 adsorption materials. Calcination parameters and the metal ratios are varied and the resulting physical and chemical properties are characterised. The underlying driving force for improved CO_2 capture abilities is then extrapolated and an optimised Mg_xAl LDO for CO_2 capture is described. As discussed in previous sections, core@shell materials have the potential to display synergistic effects. To that end, the synthesis and development of carbon@LDH core@shell materials is presented in Chapter Four. The carbon material is varied and the effects of varying LDH wt% on CO_2 capture is showcased and the improvement of rate of CO_2 capture of LDH materials is explored, as it has been shown that LDHs/LDOs possess slower rates of capture compared to materials such as zeolites and activated carbons. Finally, a preliminary study of LDHs as CO_2 capture materials for MCPU curing is carried out in Chapter Five as solution phase CO_2

capture is a relatively unexplored field with huge potential. The dispersibility and solution phase adsorption ability of the layered materials are discussed.

1.7 References

1 X. Duan and D. G. Evans, *Layered Double Hydroxides*, Springer, 2006.
2 A. I. Khan and D. O'Hare, *J. Mater. Chem.*, 2002, **12**, 3191–3198.
3 G. M. Lombardo, G. C. Pappalardo, F. Costantino, U. Costantino and M. Sisani, *Chem. Mater.*, 2008, **20**, 5585–5592.
4 A. Vyalikh, D. Massiot and U. Scheler, *Solid State Nucl. Magn. Reson.*, 2009, **36**, 19–23.
5 Y. Zhao, G. Chen, T. Bian, C. Zhou, G. I. N. Waterhouse, L.-Z. Wu, C.-H. Tung, L. J. Smith, D. O'Hare and T. Zhang, *Adv. Mater.*, 2015, **27**, 7824–7831.
6 T.-H. Kim, J.-A. Lee, S.-J. Choi and J.-M. Oh, *Int. J. Mol. Sci.*, 2014, **15**, 22563–79.
7 J. Li, S. Zhang, Y. Chen, T. Liu, C. Liu, X. Zhang, M. Yi, Z. Chu and X. Han, *RSC Adv.*, 2017, **7**, 29051–29057.
8 Y. Chen, S. Zhou, F. Li, J. Wei, Y. Dai and Y. Chen, *J. Fluoresc.*, 2011, **21**, 1677–1682.
9 Y. Chen, F. Li, S. Zhou, J. Wei, Y. Dai and Y. Chen, *J. Solid State Chem.*, 2010, **183**, 2222–2226.
10 T. Stumpf, H. Curtius, C. Walther, K. Dardenne, K. Ufer and T. Fanghänel, *Environ. Sci. Technol.*, 2007, **41**, 3186–3191.
11 Y. Liao, F. Li, X. Dai, N. Zhao and F. Xiao, *Chinese J. Catal.*, 2017, **38**, 1860–1869.
12 Y. Chen, K. Zhang, X. Wang and F. Zheng, *J. Fluoresc.*, 2017, 1–10.
13 M. Zhang, Y. Zhao, Q. Liu, L. Yang, G. Fan and F. Li, *Dalton Trans.*, 2016, **45**, 1093–1102.
14 S. Li, H. Qin, R. Zuo and Z. Bai, *Tribol. Int.*, 2015, **91**, 60–66.
15 K. Iqbal, A. Iqbal, A. M. Kirillov, B. Wang, W. Liu and Y. Tang, *J. Mater. Chem. A*, 2017, **5**, 6716–6724.
16 S. Miyata, *Clays Clay Miner.*, 1980, 50--56.
17 D. Tichit and B. Coq, *CATTECH*, 2003, **7**, 206–217.
18 W. K. and W. J. L. Pesic, S. Salipurovic, V. Markovic, D. Vucelic, *J. Mater. Chem.*, 1992, **2**, 1069–1073.
19 J. T. Kloprogge, D. Wharton, L. Hickey and R. L. Frost, *Am. Mineral.*, 2002, **87**, 623–629.
20 E. P. Giannelis, D. G. Nocera and T. J. Pinnavaia, *Inorg. Chem.*, 1987, **26**, 203–205.
21 H. Nakayama, N. Wada and M. Tsuhako, *Int. J. Pharm.*, 2004, **269**, 469–478.
22 S. Aisawa, S. Takahashi, W. Ogasawara, Y. Umetsu and E. Narita, *J. Solid State Chem.*, 2001, **162**, 52–62.
23 F. Cavani, F. Trifirò and A. Vaccari, *Catal. Today*, 1991, **11**, 173–301.
24 G. Marcelin, N. J. Stockhausen, J. F. M. Post and A. Schutz, *J. Phys. Chem.*, 1989, **93**, 4646–4650.
25 V. Rives, *Layered Double Hydroxides: Present and Future*, Nova Science Publishers, 1999.

26 G. Yu, Y. Zhou, R. Yang, M. Wang, L. Shen, Y. Li, N. Xue, X. Guo, W. Ding and L. Peng, *J. Phys. Chem. C*, 2015, **119**, 12325–12334.
27 L. Pesic, S. Salipurovic, V. Markovic, D. Vucelic, W. Kagunya and W. Jones, *J. Mater. Chem.*, 1992, **2**, 1069–1073.
28 F. Millange, R. I. Walton and D. O'Hare, *J. Mater. Chem.*, 2000, **10**, 1713–1720.
29 M. Ogawa and K. Inomata, *Chem. Lett.*, 2005, **34**, 810–811.
30 K. L. Erickson, T. E. Bostrom and R. L. Frost, *Mater. Lett.*, 2005, **59**, 226–229.
31 W. Yang, Y. Kim, P. K. T. Liu, M. Sahimi and T. T. Tsotsis, *Chem. Eng. Sci.*, 2002, **57**, 2945–2953.
32 M. Bellotto, B. Rebours, O. Clause, J. Lynch, D. Bazin and E. Elkaïm, *J. Phys. Chem.*, 1996, **100**, 8535–8542.
33 H. Kawakami and S. Yoshida, *J. Chem. Soc. Faraday Trans. 2 Mol. Chem. Phys.*, 1984, **80**, 921–932.
34 K. Chibwe and W. Jones, *J. Chem. Soc. Chem. Commun.*, 1989, 926–927.
35 F. Rey, V. Fornés, J. M. Rojo and J. M. Serratosa, *J. Chem. Soc., Faraday Trans.*, 1992, **88**, 2233–2238.
36 J. Rocha, M. del Arco, V. Rives and M. A. Ulibarri, *J. Mater. Chem.*, 1999, **9**, 2499–2503.
37 W. Reichle, *J. Catal.*, 1985, **94**, 547–557.
38 E. Suzuki and Y. Ono, *Bull. Chem. Soc. Jpn.*, 1988, **61**, 1008–1010.
39 T. Nakatsuka, H. Kawasaki, S. Yamashita and S. Kohjiya, *Bull. Chem. Soc. Jpn.*, 1979, **52**, 2449–2450.
40 W. Feitknecht and M. Gerber, *Helv. Chim. Acta*, 1942, **25**, 131–137.
41 S. P. Newman and W. Jones, *New J. Chem.*, 1998, **22**, 105–115.
42 S. Zeng, X. Xu, S. Wang, Q. Gong, R. Liu and Y. Yu, *Mater. Chem. Phys.*, 2013, **140**, 159–167.
43 Y. Zhao, F. Li, R. Zhang, A. D. G. Evans and D. Xue, 2002, **14**, 4286–4291.
44 U. Constantino, F. Marmottini, M. Nocchetti and R. Vivani, *Eur. J. Inorg. Chem.*, 1998, **10**, 1439–1446.
45 W. H. R. Shaw and J. J. Bordeaux, *J. Am. Chem. Soc.*, 1955, **77**, 4729–4733.
46 V. R. L. Constantino and T. J. Pinnavaia, *Inorg. Chem.*, 1995, **34**, 883–892.
47 A. Faour, V. Prévot and C. Taviot-Gueho, *J. Phys. Chem. Solids*, 2010, **71**, 487–490.
48 M. Adachi-Pagano, C. Forano, J.-P. Besse, G. G. Aloisi, F. Elisei and L. Latterini, *J. Mater. Chem.*, 2003, **13**, 1988–1993.
49 S. Carlino, *Solid State Ionics*, 1997, **98**, 73–84.
50 S. Miyata, *Clays Clay Miner.*, 1983, **31**, 305–311.
51 G. R. Williams and D. O'Hare, *J. Mater. Chem.*, 2006, **16**, 3065–3074.
52 Q. Wang and D. O'Hare, *Chem. Commun.*, 2013, **49**, 6301–6303.
53 Q. Wang, X. Zhang, C. J. Wang, J. Zhu, Z. Guo and D. O'Hare, *J. Mater. Chem.*, 2012, **22**, 19113–19122.
54 C. Chen, M. Yang, Q. Wang, J.-C. Buffet and D. O'Hare, *J. Mater. Chem. A*, 2014, **2**, 15102–15110.
55 K. Ruengkajorn, V. Erastova, J.-C. Buffet, H. C. Greenwell and D. O'Hare, *Chem. Commun.*, 2018, **54**, 4394–4397.
56 V. Erastova, M. T. Degiacomi, D. O'Hare and H. C. Greenwell, *RSC Adv.*, 2017, **7**, 5076–5083.
57 K. Ruengkajorn, University of Oxford, 2017.
58 M. Yang, O. McDermott, J.-C. Buffet and D. O'Hare, *RSC Adv.*, 2014, **4**, 51676–

51682.
59 C. Chen, A. Wangriya, J.-C. Buffet and D. O'Hare, *Dalton Trans.*, 2015, **44**, 16392–16398.
60 J. Kuljiraseth, A. Wangriya, J. M. C. Malones, W. Klysubun and S. Jitkarnka, *Appl. Catal. B Environ.*, 2019, **243**, 415–427.
61 J.-C. Buffet, Z. R. Turner, R. T. Cooper and D. O'Hare, *Polym. Chem.*, 2015, **6**, 2493–2503.
62 G. E. Hickman, C. M. R. Wright, A. F. R. Kilpatrick, Z. R. Turner, J.-C. Buffet and D. O'Hare, *Mol. Catal.*, 2019, **468**, 139–147.
63 R. Ghosh Chaudhuri and S. Paria, *Chem. Rev.*, 2012, 112, 2373–2433.
64 S. Kirsch, A. Doerk, E. Bartsch, H. Sillescu, K. Landfester, H. W. Spiess and W. Maechtle, *Macromolecules*, 1999, **32**, 4508–4518.
65 Y. Lu, A. Wittemann, M. Ballauff and M. Drechsler, *Macromol. Rapid Commun.*, 2006, **27**, 1137–1141.
66 V. Atanasov, V. Sinigersky, M. Klapper and K. Müllen, *Macromolecules*, 2005, **38**, 1672–1683.
67 J.-W. Hu, J.-F. Li, B. Ren, D.-Y. Wu, S.-G. Sun and Z.-Q. Tian, *J. Phys. Chem. C*, 2006, **111**, 1105–1112.
68 S. Kumar and S. Zou, *Langmuir*, 2007, **23**, 7365–7371.
69 R. Güzel, Z. Üstündağ, H. Ekşi, S. Keskin, B. Taner, Z. G. Durgun, A. A. I. Turan and A. O. Solak, *J. Colloid Interface Sci.*, 2010, **351**, 35–42.
70 X. Sun and Y. Li, *Langmuir*, 2005, **21**, 6019–6024.
71 J. C. Bauer, G. M. Veith, L. F. Allard, Y. Oyola, S. H. Overbury and S. Dai, *ACS Catal.*, 2012, **2**, 2537–2546.
72 Y. H. Gao, N. C. Zhang, Y. W. Zhong, H. H. Cai and Y. L. Liu, *Appl. Surf. Sci.*, 2010, **256**, 6580–6585.
73 F. Caruso, *Adv. Mater.*, 2001, **13**, 11–22.
74 C. F. Hoener, K. A. Allan, A. J. Bard, A. Campion, M. A. Fox, T. E. Mallouk, S. E. Webber and J. M. White, *J. Phys. Chem.*, 1992, **96**, 3812–3817.
75 L. Qi, J. Ma, H. Cheng and Z. Zhao, *Colloids Surfaces A Physicochem. Eng. Asp.*, 1996, **111**, 195–202.
76 A. R. Kortan, R. Hull, R. L. Opila, M. G. Bawendi, M. L. Steigerwald, P. J. Carroll and L. E. Brus, *J. Am. Chem. Soc.*, 1990, **112**, 1327–1332.
77 V. Salgueiriño-Maceira and M. A. Correa-Duarte, *Adv. Mater.*, 2007, **19**, 4131–4144.
78 S. Laurent, D. Forge, M. Port, A. Roch, C. Robic, L. Vander Elst and R. N. Muller, *Chem. Rev.*, 2008, **108**, 2064–2110.
79 M.-C. Daniel and D. Astruc, , DOI:10.1021/cr030698.
80 B. Han, G. Cheng, E. Zhang, L. Zhang and X. Wang, *Electrochim. Acta*, 2018, **263**, 391–399.
81 X. Guo, L. Zhao, L. Zhang and J. Li, *Appl. Surf. Sci.*, 2012, **258**, 2404–2409.
82 Z. An, S. Lu, J. He and Y. Wang, *Langmuir*, 2009, **25**, 10704–10710.
83 H. Bao, J. Yang, Y. Huang, Z. P. Xu, N. Hao, Z. Wu, G. Qing, M. Lu and D. Zhao, *Nanoscale*, 2011, **3**, 4069–4073.
84 X. Chen, H. Yuzhi, L. Hui, S. Bae, L. Ang, Z. Wang, K. S. Hui, K. N. Hui and E. Z. Nezhad, *J. Mater. Sci. Mater. Electron. 2018 303*, 2018, **30**, 2419–2430.
85 J. Chen, H. Liu, X. Wan, Y. Xue, J. Zhang, Y. Liu, X. Guo, Q. Kong and A. Yuan, *J. Nanoparticle Res. 2019 2110*, 2019, **21**, 1–10.
86 C. Megías-Sayago, R. Bingre, L. Huang, G. Lutzweiler, Q. Wang and B. Louis,

Front. Chem., 2019, **7**, 551.
87 A. Malak-Polaczyk, C. Vix-Guterl and E. Frackowiak, *Energy & Fuels*, 2010, **24**, 3346–3351.
88 W. L. J. Kwok, D. G. Crivoi, C. Chen, J. C. Buffet and D. O'Hare, *Dalton Trans.*, 2018, **47**, 143–149.
89 C. Chen, L. K. Yee, H. Gong, Y. Zhang and R. Xu, *Nanoscale*, 2013, **5**, 4314–4320.
90 G. B. B. Varadwaj and V. O. Nyamori, *Nano Res.*, 2016, 9, 3598–3621.
91 C. Chen, P. Wang, T. T. Lim, L. Liu, S. Liu and R. Xu, *J. Mater. Chem. A*, 2013, **1**, 3877–3880.
92 H. Zhang, D. Pan and X. Duan, *J. Phys. Chem. C*, 2009, **113**, 12140–12148.
93 H. Zhang, D. Pan, K. Zou, J. He and X. Duan, *J. Mater. Chem.*, 2009, **19**, 3069–3077.
94 Y. Zhao, S. He, M. Wei, D. G. Evans and X. Duan, *Chem. Commun.*, 2010, **46**, 3031–3033.
95 F. Ning, M. Shao, C. Zhang, S. Xu, M. Wei and X. Duan, *Nano Energy*, 2014, **7**, 134–142.
96 M. Shao, F. Ning, J. Zhao, M. Wei, D. G. Evans and X. Duan, *J. Am. Chem. Soc.*, 2012, **134**, 1071–1077.
97 D. Li, Y. T. Zhang, M. Yu, J. Guo, D. Chaudhary and C. C. Wang, *Biomaterials*, 2013, **34**, 7913–7922.
98 A. N. Ay, D. Konuk and B. Zümreoğlu-Karan, *Mater. Sci. Eng. C*, 2011, **31**, 851–857.
99 R. Ma and T. Sasaki, *Adv. Mater.*, 2010, **22**, 5082–5104.
100 L. Li, R. Ma, N. Iyi, Y. Ebina, K. Takada and T. Sasaki, *Chem. Commun.*, 2006, 3125–3127.
101 L. Li, Y. Feng, Y. Li, W. Zhao and J. Shi, *Angew. Chemie - Int. Ed.*, 2009, **48**, 5888–5892.
102 L. Huang, D. Chen, Y. Ding, S. Feng, Z. Lin Wang and M. Liu, *Nano Lett*, 2013, **13**, 3135–3139.
103 H. Zhang, R. Qi, D. G. Evans and X. Duan, *J. Solid State Chem.*, 2004, **177**, 772–780.
104 H. Zhang, K. Zou, H. Sun and X. Duan, *J. Solid State Chem.*, 2005, **178**, 3485–3493.
105 C. Chen, R. Felton, J. C. Buffet and D. O'Hare, *Chem. Commun.*, 2015, **51**, 3462–3465.
106 W. L. J. Kwok, DPhil thesis, University of Oxford, 2020.
107 Z. Gu, J. J. Atherton and Z. P. Xu, *Chem. Commun.*, 2015, **51**, 3024–3036.
108 K. H. Goh, T. T. Lim and Z. Dong, *Water Res.*, 2008, 42, 1343–1368.
109 J. Das, B. S. Patra, N. Baliarsingh and K. M. Parida, *Appl. Clay Sci.*, 2006, **32**, 252–260.
110 C. Chen, P. Gunawan and R. Xu, *J. Mater. Chem.*, 2011, **21**, 1218–1225.
111 L. Lv, J. He, M. Wei, D. G. Evans and X. Duan, *Water Res.*, 2006, **40**, 735–743.
112 S. J. Palmer and R. L. Frost, *Ind. Eng. Chem. Res.*, 2010, **49**, 8969–8976.
113 T. Hongo, T. Iemura and A. Yamazaki, *J. Fac. Sci. Tech. Seikei Univ.*, 2009, **46**, 47–51.
114 L. Wang, H. Xing, S. Zhang, Q. Ren, L. Pan, K. Zhang, W. Bu, X. Zheng, L. Zhou, W. Peng, Y. Hua and J. Shi, *Biomaterials*, 2013, **34**, 3390–3401.
115 H. Burrows, MChem thesis, University of Oxford, 2018.
116 K. Cermelj, DPhil thesis, University of Oxford, 2020.

117 W. J. Youngblood, S. H. A. Lee, K. Maeda and T. E. Mallouk, *Acc. Chem. Res.*, 2009, **42**, 1966–1973.
118 X. Chen and S. S. Mao, *Chem. Rev.*, 2007, 107, 2891–2959.
119 C. G. Silva, R. Juá rez, T. Marino, R. Molinari and H. García, *J. Am. Chem. Soc.*, 2011, **133**, 595–602.
120 Q. Wang and D. O'Hare, *Chem. Rev.*, 2012, **112**, 4124–4155.
121 J. Wang, G. Zhang, L. Ren, L. Kang, Z. Hao, Z. Lei and Z. H. Liu, *Cryst. Growth Des.*, 2014, **14**, 5626–5633.
122 W. Shi, Y. Jia, S. Xu, Z. Li, Y. Fu, M. Wei and S. Shi, *Langmuir*, 2014, **30**, 12916–12922.
123 Q. He, T. Yuan, X. Zhang, X. Yan, J. Guo, D. Ding, M. A. Khan, D. P. Young, A. Khasanov, Z. Luo, J. Liu, T. D. Shen, X. Liu, S. Wei and Z. Guo, *J. Phys. Chem. C*, 2014, **118**, 24784–24796.
124 Y. Liu, N. Wang, J. H. Pan, F. Steinbach and J. Caro, *J. Am. Chem. Soc.*, 2014, **136**, 14353–14356.
125 R. Zhang, Z. Xue, J. Qin, M. Sawangphruk, X. Zhang and R. Liu, *J. Energy Chem.*, 2020, **50**, 143–153.
126 H. Liu, T. Yu, D. Su, Z. Tang, J. Zhang, Y. Liu, A. Yuan and Q. Kong, *Ceram. Int.*, 2017, **43**, 14395–14400.
127 W. Kagunya, Z. Hassan and W. Jones, *Inorg. Chem.*, 1996, **35**, 5970–5974.
128 M. J. Campos-Molina, J. Santamaría-Gonźalez, J. Ḿerida-Robles, R. Moreno-Tost, M. C. G. Albuquerque, S. Bruque-Ǵamez, E. Rodríguez-CastelÍon, A. Jiḿenez-Ĺopez and P. Maireles-Torres, *Energy and Fuels*, 2010, **24**, 979–984.
129 L. Gao, G. Teng, J. Lv and G. Xiao, *Energy and Fuels*, 2010, **24**, 646–651.
130 Y. Xi and R. J. Davis, *J. Catal.*, 2008, **254**, 190–197.
131 D. G. Cantrell, L. J. Gillie, A. F. Lee and K. Wilson, *Appl. Catal. A Gen.*, 2005, **287**, 183–190.
132 S. Abelló, S. Dhir, G. Colet and J. Pérez-Ramírez, *Appl. Catal. A Gen.*, 2007, **325**, 121–129.
133 S. K. Sharma, P. A. Parikh and R. V. Jasra, *J. Mol. Catal. A Chem.*, 2007, **278**, 135–144.
134 J. Červený, J. Šplíchalová, P. Kačer, F. Kovanda, M. Kuzma and L. Červený, *J. Mol. Catal. A Chem.*, 2008, **285**, 150–154.
135 B. M. Choudary, M. Lakshmi Kantam, C. R. Venkat Reddy, K. Koteswara Rao and F. Figueras, *J. Mol. Catal. A Chem.*, 1999, **146**, 279–284.
136 O. D. Pavel, B. Cojocaru, E. Angelescu and V. I. Pârvulescu, *Appl. Catal. A Gen.*, 2011, **403**, 83–90.
137 Z. Lu, W. Xu, W. Zhu, Q. Yang, X. Lei, J. Liu, Y. Li, X. Sun and X. Duan, *Chem. Commun.*, 2014, **50**, 6479–6482.
138 X. Zou, A. Goswami and T. Asefa, *J. Am. Chem. Soc.*, 2013, **135**, 17242–17245.
139 Y. Wang, D. Zhang, W. Peng, L. Liu and M. Li, *Electrochim. Acta*, 2011, **56**, 5754–5758.
140 Z. Zhu, L. Qu, Y. Guo, Y. Zeng, W. Sun and X. Huang, *Sensors Actuators, B Chem.*, 2010, **151**, 146–152.
141 Z. Yin, J. Wu and Z. Yang, *Biosens. Bioelectron.*, 2011, **26**, 1970–1974.
142 S. J. Park, H. A. Ahn, I. J. Heo, I.-S. Nam, J. H. Lee, Y. K. Youn and H. J. Kim, *Top. Catal.*, 2010, **53**, 57–63.
143 J. Zhao, J. Xie, C.-T. Au and S.-F. Yin, *Appl. Catal. A Gen.*, 2013, **467**, 33–37.
144 H. Ritchie and M. Roser, CO_2 and Greenhouse Gas Emissions,

https://ourworldindata.org/co2-and-other-greenhouse-gas-emissions.
145 O. Gaffney, Global carbon dioxide emissions projected to rise after three stable years, https://futureearth.org/2017/11/13/global-carbon-dioxide-emissions-projected-to-rise-after-three-stable-years/.
146 S. Choi, J. H. Drese and C. W. Jones, *ChemSusChem*, 2009, **2**, 796–854.
147 A. L. Kohl and R. B. Nielsen, *Gas purification.*, Gulf Pub, 1997.
148 G. Astarita, D. W. Savage and A. Bisio, *Gas treating with chemical solvents*, John Wiley, New York, 1983.
149 J. M. Campbell, *Gas Conditioning and Processing* , John R. Campbell, Norman, OK, 4th edn., 1998, vol. 4.
150 S. Sircar, *Ind. Eng. Chem. Res.*, 2006, **45**, 5435–5448.
151 P. V. Danckwerts, *Chem. Eng. Sci.*, 1979, **34**, 443–446.
152 S.-W. Park, J.-W. Lee, B.-S. Choi and J.-W. Lee, *J. Ind. Eng. Chem.*, 2005, **11**, 202–209.
153 N. El Hadri, D. V. Quang, E. L. V. Goetheer and M. R. M. Abu Zahra, *Appl. Energy*, 2017, **185**, 1433–1449.
154 C.-H. Yu, C.-H. Huang and C.-S. Tan, *Aerosol Air Qual. Res.*, 2012, **12**, 745–769.
155 K. T. Chue, J. N. Kim, Y. J. Yoo, S. H. Cho and R. T. Yang, *Ind. Eng. Chem. Res.*, 1995, **34**, 591–598.
156 G. Calleja, A. Jimenez, J. Pau, L. Domínguez and P. Pérez, *Gas Sep. Purif.*, 1994, **8**, 247–256.
157 D. Ko, R. Siriwardane and L. T. Biegler, *Ind. Eng. Chem. Res.*, 2003, **42**, 339–348.
158 F. Dong, H. Lou, A. Kodama, M. Goto and T. Hirose, *Sep. Purif. Technol.*, 1999, **16**, 159–166.
159 S. Cavenati, C. A. Grande and A. E. Rodrigues, *J. Chem. Eng. Data*, 2004, **49**, 1095–1101.
160 N. N. A. H. Meis, J. H. Bitter and K. P. de Jong, *Ind. Eng. Chem. Res.*, 2010, **49**, 1229–1235.
161 F. Foeth, M. Andersson, H. Bosch, G. Aly and T. Reith, *Sep. Sci. Technol.*, 1994, **29**, 93–118.
162 M. M. Maroto-Valer, Z. Tang and Y. Zhang, *Fuel Process. Technol.*, 2005, **86**, 1487–1502.
163 M. Radosz, X. Hu, K. Krutkramelis and Y. Shen, *Ind. Eng. Chem. Res.*, 2008, **47**, 3783–3794.
164 R. Van Der Vaart, C. Huiskes, H. Bosch and T. Reith, *Adsorption*, 2000, **6**, 311–323.
165 J. A. Michelena, G. Peeters, E. F. Vansant and P. de Bièvre, *Recl. des Trav. Chim. des Pays-Bas*, 1977, **96**, 121–124.
166 P. J. E. Harlick and F. H. Tezel, *Can. J. Chem. Eng.*, 2001, **79**, 236–245.
167 R. V. Siriwardane, M. S. Shen, E. P. Fisher and J. Losch, *Energy and Fuels*, 2005, **19**, 1153–1159.
168 L. Bertsch and H. W. Habgood, *J. Phys. Chem.*, 1963, **67**, 1621–1628.
169 J. W. Ward and H. W. Habgood, *J. Phys. Chem.*, 1966, **70**, 1178–1182.
170 R. V. Siriwardane, M. S. Shen, E. P. Fisher and J. A. Poston, *Energy and Fuels*, 2001, **15**, 279–284.
171 Q. Wang, J. Luo, Z. Zhong and A. Borgna, *Energy Environ. Sci.*, 2011, **4**, 42–55.
172 E. Díaz, E. Muñoz, A. Vega and S. Ordóñez, *Ind. Eng. Chem. Res.*, 2008, **47**, 412–418.
173 M. A. Yahya, Z. Al-Qodah and C. W. Z. Ngah, *Renew. Sustain. Energy Rev.*, 2015,

46, 218–235.
174 F. C. Huang, C. K. Lee, Y. L. Han, W. C. Chao and H. P. Chao, *J. Taiwan Inst. Chem. Eng.*, 2014, **45**, 2805–2812.
175 N. Byamba-Ochir, W. G. Shim, M. S. Balathanigaimani and H. Moon, *Appl. Surf. Sci.*, 2016, **379**, 331–337.
176 C. Bouchelta, M. S. Medjram, O. Bertrand and J. P. Bellat, *J. Anal. Appl. Pyrolysis*, 2008, **82**, 70–77.
177 J. Pallarés, A. González-Cencerrado and I. Arauzo, *Biomass and Bioenergy*, 2018, **115**, 64–73.
178 Z. Heidarinejad, M. H. Dehghani, M. Heidari, G. Javedan, I. Ali and M. Sillanpää, *Environ. Chem. Lett.*, 2020, **18**, 393–415.
179 I. Demiral and C. Aydin Şamdan, *Anadolu Univ. J. Sci. Technol. Appl. Sci. Eng.*, 2016, **17**, 1.
180 T. S. Hui and M. A. A. Zaini, *Carbon Lett.*, 2015, 16, 275–280.
181 M. A. Chayid and M. J. Ahmed, *J. Environ. Chem. Eng.*, 2015, **3**, 1592–1601.
182 L. Zuo, J. Ai, H. Fu, W. Chen, S. Zheng, Z. Xu and D. Zhu, *Environ. Pollut.*, 2016, **211**, 425–434.
183 A. F. Abbas and M. J. Ahmed, *J. Water Process Eng.*, 2016, **9**, 201–207.
184 T. Budinova, N. Petrov, J. Parra and V. Baloutzov, *J. Environ. Manage.*, 2008, **88**, 165–172.
185 T. Horikawa, Y. Kitakaze, T. Sekida, J. Hayashi and M. Katoh, *Bioresour. Technol.*, 2010, **101**, 3964–3969.
186 T. Tay, S. Ucar and S. Karagöz, *J. Hazard. Mater.*, 2009, **165**, 481–485.
187 M. Y. Abdelnaeim, I. Y. El Sherif, A. A. Attia, N. A. Fathy and M. F. El-Shahat, *Int. J. Miner. Process.*, 2016, **157**, 80–88.
188 A. Martínez De Yuso, B. Rubio and M. T. Izquierdo, *Fuel Process. Technol.*, 2014, **119**, 74–80.
189 S. M. Yakout and G. Sharaf El-Deen, *Arab. J. Chem.*, 2016, **9**, S1155–S1162.
190 Z. Y. Zhong, Q. Yang, X. M. Li, K. Luo, Y. Liu and G. M. Zeng, *Ind. Crops Prod.*, 2012, **37**, 178–185.
191 Q. S. Liu, T. Zheng, P. Wang and L. Guo, *Ind. Crops Prod.*, 2010, **31**, 233–238.
192 C. Saka, *J. Anal. Appl. Pyrolysis*, 2012, **95**, 21–24.
193 A. Gundogdu, C. Duran, H. B. Senturk, M. Soylak, M. Imamoglu and Y. Onal, *J. Anal. Appl. Pyrolysis*, 2013, **104**, 249–259.
194 J. Donald, Y. Ohtsuka and C. C. Xu, *Mater. Lett.*, 2011, **65**, 744–747.
195 P. Davini, *Carbon N. Y.*, 2002, **40**, 1973–1979.
196 S. Sircar, T. C. Golden and M. B. Rao, *Carbon N. Y.*, 1996, **34**, 1–12.
197 A. Samanta, A. Zhao, G. K. H. Shimizu, P. Sarkar and R. Gupta, *Ind. Eng. Chem. Res.*, 2012, 51, 1438–1463.
198 B. K. Na, K. K. Koo, H. M. Eum, H. Lee and H. K. Song, *Korean J. Chem. Eng.*, 2001, **18**, 220–227.
199 L. B. Adams, C. R. Hall, R. J. Holmes and R. A. Newton, *Carbon N. Y.*, 1988, **26**, 451–459.
200 E. S. Kikkinides, R. T. Yang and S. H. Cho, *Ind. Eng. Chem. Res.*, 1993, **32**, 2714–2720.
201 C. Pevida, M. G. Plaza, B. Arias, J. Fermoso, F. Rubiera and J. J. Pis, *Appl. Surf. Sci.*, 2008, **254**, 7165–7172.
202 J. A. Menéndez, J. Phillips, B. Xia and L. R. Radovic, *Langmuir*, 1996, **12**, 4404–4410.

203 M. G. Plaza, C. Pevida, A. Arenillas, F. Rubiera and J. J. Pis, *Fuel*, 2007, **86**, 2204–2212.
204 J. Przepiórski, M. Skrodzewicz and A. W. Morawski, *Appl. Surf. Sci.*, 2004, **225**, 235–242.
205 Y. Pan, C. J. Liu and Q. Ge, *Langmuir*, 2008, **24**, 12410–12419.
206 Z. Yong, V. Mata and A. E. Rodrigues, *J. Chem. Eng. Data*, 2000, **45**, 1093–1095.
207 O. Seiferth, K. Wolter, B. Dillmann, G. Klivenyi, H. J. Freund, D. Scarano and A. Zecchina, *Surf. Sci.*, 1999, **421**, 176–190.
208 S. Hadenfeldt, C. Benndorf, A. Stricker and M. Töwe, *Surf. Sci.*, 1996, **352**–**354**, 295–299.
209 T. Seyller, D. Borgmann and G. Wedler, *Surf. Sci.*, 1998, **400**, 63–79.
210 H. M. Ismail, D. A. Cadenhead and M. I. Zaki, *J. Colloid Interface Sci.*, 1997, **194**, 482–488.
211 J. Tai, Q. Ge, R. J. Davis and M. Neurock, *J. Phys. Chem. B*, 2004, **108**, 16798–16805.
212 T. Zhao, E. Ochoa-Fernández, M. Rønning and D. Chen, *Chem. Mater.*, 2007, **19**, 3294–3301.
213 R. V. Siriwardane, C. Robinson, M. Shen and T. Simonyi, *Energy and Fuels*, 2007, **21**, 2088–2097.
214 I. Alcérreca-Corte, E. Fregoso-Israel and H. Pfeiffer, *J. Phys. Chem. C*, 2008, **112**, 6520–6525.
215 D. Mess, A. F. Sarofim and J. P. Longwell, *Energy and Fuels*, 1999, **13**, 999–1005.
216 W. G. Oakeson and I. B. Cutler, *J. Am. Ceram. Soc.*, 1979, **62**, 556–558.
217 S. K. Bhatia and D. D. Perlmutter, *AIChE J.*, 1983, **29**, 79–86.
218 S. Shang, A. Hanif, M. Sun, Y. Tian, Y. S. Ok, I. K. M. Yu, D. C. W. Tsang, Q. Gu and J. Shang, *J. Hazard. Mater.*, 2019, **373**, 285–293.
219 U. Sharma, B. Tyagi and R. V. Jasra, *Ind. Eng. Chem. Res.*, 2008, **47**, 9588–9595.
220 K. Coenen, F. Gallucci, G. Pio, P. Cobden, E. van Dijk, E. Hensen and M. van Sint Annaland, *Chem. Eng. J.*, 2017, **314**, 554–569.
221 S. Kim, S. G. Jeon and K. B. Lee, *ACS Appl. Mater. Interfaces*, 2016, **8**, 5763–5767.
222 S. Ishihara, P. Sahoo, K. Deguchi, S. Ohki, M. Tansho, T. Shimizu, J. Labuta, J. P. Hill, K. Ariga, K. Watanabe, Y. Yamauchi, S. Suehara and N. Iyi, *J. Am. Chem. Soc.*, 2013, **135**, 18040–18043.
223 E. L. G. Oliveira, C. A. Grande and A. E. Rodrigues, *Sep. Purif. Technol.*, 2008, **62**, 137–147.
224 A. D. Ebner, S. P. Reynolds and J. A. Ritter, *Ind. Eng. Chem. Res.*, 2006, **45**, 6387–6392.
225 S. Walspurger, P. D. Cobden, O. V. Safonova, Y. Wu and E. J. Anthony, *Chem. – A Eur. J.*, 2010, **16**, 12694–12700.
226 K. B. Lee, A. Verdooren, H. S. Caram and S. Sircar, *J. Colloid Interface Sci.*, 2007, **308**, 30–39.
227 N. D. Hutson, S. A. Speakman and E. A. Payzant, *Chem. Mater.*, 2004, **16**, 4135–4143.
228 Y. Ding and E. Alpay, *Process Saf. Environ. Prot.*, 2001, **79**, 45–51.
229 H. T. J. Reijers, S. E. A. Valster-Schiermeier, P. D. Cobden and R. W. Van Den Brink, *Ind. Eng. Chem. Res.*, 2006, **45**, 2522–2530.
230 M. K. Ram Reddy, Z. P. Xu, G. Q. (Max) Lu and J. C. Diniz da Costa, *Ind. Eng. Chem. Res.*, 2006, **45**, 7504–7509.

231 M. G. Veerabhadrappa, M. M. Maroto-Valer, Y. Chen and S. Garcia, *ACS Appl. Mater. Interfaces*, 2021, **13**, 11805–11813.
232 M. K. Ram Reddy, Z. P. Xu, G. Q. (Max) Lu and J. C. Diniz da Costa, *Ind. Eng. Chem. Res.*, 2008, **47**, 2630–2635.
233 J. R. Hufton, S. Mayorga and S. Sircar, *AIChE J.*, 1999, **45**, 248–256.
234 D. A. Torres-Rodríguez, E. Lima, J. S. Valente and H. Pfeiffer, *J. Phys. Chem. A*, 2011, **115**, 12243–12250.
235 G. Grasa, B. González, M. Alonso and J. C. Abanades, *Energy and Fuels*, 2007, 21, 3560–3562.
236 E. L. G. Oliveira, C. A. Grande and A. E. Rodrigues, *Sep. Purif. Technol.*, 2008, **62**, 137–147.
237 Y. Wang, S. Lin and Y. Suzuki, *Energy and Fuels*, 2007, **21**, 3317–3321.
238 X. Zhu, T. Ge, F. Yang, M. Lyu, C. Chen, D. O'Hare and R. Wang, *J. Mater. Chem. A*, 2020, **8**, 16421–16428.
239 X. P. Wang, J. J. Yu, J. Cheng, Z. P. Hao and Z. P. Xu, *Environ. Sci. Technol.*, 2008, **42**, 614–618.
240 Q. Wang, H. H. Tay, D. J. W. Ng, L. Chen, Y. Liu, J. Chang, Z. Zhong, J. Luo and A. Borgna, *ChemSusChem*, 2010, **3**, 965–973.
241 K. Coenen, F. Gallucci, B. Mezari, E. Hensen and M. van Sint Annaland, *J. CO_2 Util.*, 2018, **24**, 228–239.
242 Y. Xuzhuang, D. Yang, Z. Huaiyong, L. Jiangwen, W. N. Martins, R. Frost, L. Daniel and S. Yuenian, *J. Phys. Chem. C*, 2009, **113**, 8243–8248.
243 H. Zhang, G. Zhang, X. Bi and X. Chen, *J. Mater. Chem. A*, 2013, **1**, 5934–5942.
244 X. Liu, C. Wang, Y. Dou, A. Zhou, T. Pan, J. Han and M. Wei, *J. Mater. Chem. A*, 2014, **2**, 1682–1685.
245 J. Nai, Y. Tian, X. Guan and L. Guo, *J. Am. Chem. Soc.*, 2013, **135**, 16082–16091.
246 X. Lv, Z. Chen, Y. Wang, F. Huang and Z. Lin, *ACS Appl. Mater. Interfaces*, 2013, **5**, 11271–11275.
247 A. Garcia-Gallastegui, D. Iruretagoyena, V. Gouvea, M. Mokhtar, A. M. Asiri, S. N. Basahel, S. A. Al-Thabaiti, A. O. Alyoubi, D. Chadwick and M. S. P. Shaffer, *Chem. Mater.*, 2012, **24**, 4531–4539.
248 M. De Marco, R. Menzel, S. M. Bawaked, M. Mokhtar, A. Y. Obaid, S. N. Basahel and M. S. P. Shaffer, *Carbon N. Y.*, 2017, **123**, 616–627.
249 O. Bayer, *Angew. Chemie*, 1947, **59**, 257–272.
250 A. K. Mishra, D. K. Chattopadhyay, B. Sreedhar and K. V. S. N. Raju, *Prog. Org. Coatings*, 2006, **55**, 231–243.
251 C. P. Christenson, M. A. Harthcock, M. D. Meadows, H. L. Spell, W. L. Howard, M. W. Creswick, R. E. Guerra and R. B. Turner, *J. Polym. Sci. Part B Polym. Phys.*, 1986, **24**, 1401–1439.
252 L. H. Sperling, S. L. Cooper and A. V. Tobolsky, *J. Appl. Polym. Sci.*, 1966, **10**, 1725–1735.
253 J. W. Britain and P. G. Gemeinhardt, *J. Appl. Polym. Sci.*, 1960, **4**, 207–211.
254 W. Dzierża, *J. Appl. Polym. Sci.*, 1978, **22**, 1331–1342.
255 United States Patent, US6825376B2, 2004.
256 D. K. Chattopadhyay, P. S. R. Prasad, B. Sreedhar and K. V. S. N. Raju, *Prog. Org. Coatings*, 2005, **54**, 296–304.
257 D. K. Chattopadhyay, B. Sreedhar and K. V. S. N. Raju, *J. Appl. Polym. Sci.*, 2005, **95**, 1509–1518.
258 H. Ni, A. D. Skaja, R. A. Sailer and M. D. Soucek, *Macromol. Chem. Phys.*, 2000,

201, 722–732.
259 United States Patent, US5264148A, 1993.
260 United States Patent, US5550191A, 1995.
261 D. K. Chattopadhyay and K. V. S. N. Raju, *Prog. Polym. Sci.*, 2007, 32, 352–418.
262 G. H. Hsiue, W. J. Kuo, Y. P. Huang and R. J. Jeng, *Polymer (Guildf).*, 2000, **41**, 2813–2825.
263 A. Shrivastava, *Introduction to Plastics Engineering*, Elsevier, 2018.
264 T. Kashiwagi, A. B. Morgan, J. M. Antonucci, M. R. VanLandingham, R. H. Harris, W. H. Awad and J. R. Shields, *J. Appl. Polym. Sci.*, 2003, **89**, 2072–2078.
265 F. Uddin, *Metall. Mater. Trans. A Phys. Metall. Mater. Sci.*, 2008, **39**, 2804–2814.
266 S. Pavlidou and C. D. Papaspyrides, *Prog. Polym. Sci.*, 2008, **33**, 1119–1198.
267 E. P. Giannelis, *Adv. Mater.*, 1996, **8**, 29–35.
268 M. Jisheng, S. Zhang and Z. Qi, *J. Appl. Polym. Sci.*, 2001, **82**, 1444–1448.
269 A. J. De Vries, J. P. M. Van Vliet and G. Blasse, *Adv. Mater.*, 1999, **11**, 49–52.
270 J. W. Gilman, *Appl. Clay Sci.*, 1999, **15**, 31–49.
271 S. Solarski, S. Benali, M. Rochery, E. Devaux, M. Alexandre, F. Monteverde and P. Dubois, *J. Appl. Polym. Sci.*, 2005, **95**, 238–244.
272 J. Zhu, A. B. Morgan, F. J. Lamelas and C. A. Wilkie, *Chem. Mater.*, 2001, **13**, 3774–3780.
273 J. M. Yeh, S. J. Liou, M. C. Lai, Y. W. Chang, C. Y. Huang, C. P. Chen, J. H. Jaw, T. Y. Tsai and Y. H. Yu, *J. Appl. Polym. Sci.*, 2004, **94**, 1936–1946.
274 T. Takeichi and Y. Guo, *J. Appl. Polym. Sci.*, 2003, **90**, 4075–4083.
275 S. Sinha Ray and M. Okamoto, *Prog. Polym. Sci.*, 2003, **28**, 1539–1641.
276 J. Yu, J. C. Buffet and D. O'Hare, *ACS Appl. Mater. Interfaces*, 2020, **12**, 10973–10982.
277 J. Yu, C. Chen, J. B. Gilchrist, J. C. Buffet, Z. Wu, G. Mo, F. Xie and D. O'Hare, *Mater. Horizons*, 2021, **8**, 2823–2833.
278 K. Tanabe and W. F. Hölderich, *Appl. Catal. A Gen.*, 1999, **181**, 399–434.
279 J. C. Vedrine, J. M. M. Millet and J. C. Volta, *Catal. Today*, 1996, **32**, 115–123.
280 S. Li, Y. Shi, Y. Yang, Y. Zheng and N. Cai, *Energy & Fuels*, 2013, **27**, 5352–5358.
281 J. N. Brönsted, *Recl. des Trav. Chim. des Pays-Bas*, 1923, **42**, 718–728.
282 G. N. Lewis, *Valence and the structure of atoms and molecules*, Wiley, New York, 1924, vol. 43.
283 H. A. Benesi, *J. Am. Chem. Soc.*, 1956, **78**, 5490–5494.
284 C. Walling, *J. Am. Chem. Soc.*, 1950, **72**, 1164–1168.
285 J. C. Védrine, *Res. Chem. Intermed.*, 2015, **41**, 9387–9423.
286 A. Navajas, I. Campo, G. Arzamendi, W. Y. Hernández, L. F. Bobadilla, M. A. Centeno, J. A. Odriozola and L. M. Gandía, *Appl. Catal. B Environ.*, 2010, **100**, 299–309.
287 R. J. Cvetanovic̆ and Y. Amenomiya, *Catal. Rev.*, 1972, **6**, 21–48.
288 M. Niwa and N. Katada, *Chem. Rec.*, 2013, 13, 432–455.
289 R. J. Cvetanović and Y. Amenomiya, *Adv. Catal.*, 1967, **17**, 103–149.
290 O. Klepel and B. Hunger, *J. Therm. Anal. Calorim.*, 2005, **80**, 201–206.
291 Y. Yanagisawa, K. Takaoka, S. Yamabe and T. Ito, *J. Phys. Chem.*, 1995, **99**, 3704–3710.
292 L. Rodríguez-González and U. Simon, *Meas. Sci. Technol.*, 2010, **21**, 027003.
293 S. L. M. Schroeder and M. Gottfried, Temperature-Programmed Desorption (TPD) Thermal Desorption Spectroscopy (TDS).

294 M. Niwa, K. Suzuki, N. Morishita, G. Sastre, K. Okumura and N. Katada, *Catal. Sci. Technol.*, 2013, **3**, 1919–1927.
295 P. Kenyon, D. W. J. Leung, M. Lyu, C. Chen, Z. R. Turner, J. C. Buffet and D. O'Hare, *J. Catal.*, 2021, **402**, 94–100.
296 R. W. Stevens, R. V. Siriwardane and J. Logan, *Energy & Fuels*, 2008, **22**, 3070–3079.
297 F. Prinetto, G. Ghiotti, R. Durand and D. Tichit, *J. Phys. Chem. B*, 2000, 11117–11126.
298 H. Du, C. T. Williams, A. D. Ebner and J. A. Ritter, *Chem. Mater.*, 2010, **22**, 3519–3526.
299 A. A. Tsyganenko, N. V. Zakharov and P. D. Murzin, *Catal. Today*, 2014, **226**, 73–80.
300 E.-M. Köck, M. Kogler, T. Bielz, B. Klötzer and S. Penner, *J. Phys. Chem. C*, 2013, **117**, 17666–17673.
301 J. I. Di Cosimo, V. K. Díez, M. Xu, E. Iglesia and C. R. Apesteguía, *J. Catal.*, 1998, **178**, 499–510.
302 J. R. Anderson and K. C. Pratt, *Introduction to Characterization and Testing of Catalysts*, Acadamic Press, New York, 1985.
303 K. I. Hadjiivanov and G. N. Vayssilov, *Adv. Catal.*, 2002, **47**, 307–511.
304 A. Zheng, S. J. Huang, S. Bin Liu and F. Deng, *Phys. Chem. Chem. Phys.*, 2011, **13**, 14889–14901.
305 J. Huang, Y. Jiang, V. R. Reddy Marthala, W. Wang, B. Sulikowski and M. Hunger, *Microporous Mesoporous Mater.*, 2007, **99**, 86–90.
306 V. Bosacek, *J. Phys. Chem.*, 1993, **97**, 10732–10737.
307 V. Bosáek, H. Ernst, D. Freude and T. Mildner, *Zeolites*, 1997, **18**, 196–199.
308 V. Bosáček, R. Klik, F. Genoni, G. Spano, F. Rivetti and F. Figueras, *Magn. Reson. Chem.*, 1999, **37**, S135–S141.
309 Q. Zhao, W.-H. Chen, S.-J. Huang, Y.-C. Wu, H.-K. Lee and S.-B. Liu, *J. Phys. Chem. B*, 2002, **106**, 4462–4469.
310 A. Zheng, S.-J. Huang, S.-B. Liu and F. Deng, *Phys. Chem. Chem. Phys.*, 2011, **13**, 14889.
311 B. Guo, L. Ye, G. Tang, L. Zhang, B. Yue, S. C. E. Tsang and H. He, *Chinese J. Chem.*, 2017, **35**, 1529–1539.
312 Y.-K. Peng, Y. Hu, H.-L. Chou, Y. Fu, I. F. Teixeira, L. Zhang, H. He and S. C. E. Tsang, *Nat. Commun.*, 2017, **8**, 1–13.
313 Y.-K. Peng, L. Ye, J. Qu, L. Zhang, Y. Fu, I. F. Teixeira, I. J. McPherson, H. He and S. C. E. Tsang, *J. Am. Chem. Soc.*, 2016, **138**, 2225–2234.
314 G. E. Hickman, MChem Thesis, University of Oxford, 2018.
315 Y. Gao, Z. Zhang, J. Wu, X. Yi, A. Zheng, A. Umar, D. O'Hare and Q. Wang, *J. Mater. Chem. A*, 2013, **1**, 12782.

Chapter Two - Experimental details

2.1 Analytical methods

2.1.1 CO_2 capture values

CO_2 capture readings were carried out on a Micromeritics 3Flex with a chemisorption attachment or a Perkin Elmer TGA 8000. The atmosphere for the Micromeritics 3Flex measurements was 100% CO_2, with a pressure of 100 kPa at 40 °C. The measurements run on PerkinElmer TGA 8000 were carried out under 33% CO_2 67% N_2 at 30 °C. Specific conditions for pre-treatment of samples in each chapter are described in detail in the respective chapters.

2.1.2 Elemental analysis

Elemental C, H, N analysis was performed by Mr Stephen Boyer at London Metropolitan University using a quantitative oxidative combustion technique for results in Chapter Two. For other results, analysis was carried out by Dr Nigel Howard at the University of Cambridge using the same method.

2.1.3 Fourier transform infrared (FTIR) spectroscopy

FTIR spectra were taken on a Bruker VERTEX 80 FTIR spectrometer. Scans were taken with 4 cm^{-1} resolution. Prior to sample scans, 128 scans were taken as background scans. 64 scans were used for samples scans between the range of 600–4000 cm^{-1}.

2.1.4 Inductively coupled plasma mass spectrometry (ICP-MS)

ICP-MS analysis was carried out by Dr Alaa Abdul-Sada at the University of Sussex for Chapter Two, and Dr Nigel Howard for the other chapters, to determine the metal content of LDHs. Measurements were carried out on an Agilent 7500 Series ICP-MS in helium

collision mode. ~20 mg of sample was digested in 10 mL of 10% nitric acid. The solutions were further diluted by a factor of 100 prior to testing with diluted nitric acid. Results were run in triplicate and averaged.

2.1.5 Polyurethane mixing

The mixing of Desmoseal M280 was carried out in an Intertronics THINKY Planetary Vacuum Mixer. 0.5 g of Desmoseal M280 was added to the mixing pot along with other components to be specified in a later section.

2.1.6 Powdered X-ray diffraction (XRD)

XRD measurements were carried out on a PANAnalytical X'Pert Pro Diffractometer in scanning mode using Cu Kα radiation (λ= 1.542 Å). Reconstructed samples were dried on a silicon wafer and placed into steel sample holders. All other samples were simply placed into the steel sample holders. The samples were analysed from 2 to 70°, with a step size 0.0334° and scan speed 0.0354° s^{-1}.

$$\mathrm{CDL} = \frac{\mathrm{B}\lambda}{\beta \cos\theta}$$

For the Scherrer equation, B is the Scherrer constant (0.89), λ is the wavelength of the radiation used (Cu Kα, λ = 1.54 Å), θ is the angle of the (003) Bragg reflection and β is the corresponding full width at half maximum (FWHM) in radians. The Scherrer equation only provides an estimation of average LDH platelet thickness due to it requiring an uninterrupted, uniform particle.

2.1.7 Scanning electron microscopy (SEM)

SEM imaging and energy dispersive x-ray spectroscopy (EDS) mapping were carried out by Ms Meng Lyu (University of Oxford) at the David Cockayne Centre for Electron Microscopy, Department of Materials, University of Oxford, using a Zeis Merlin-EBSD microscope with an operating voltage of 5 kV. Samples were prepared by sonicating and

diluting in DI water. A few droplets of each solution were then left to dry on a silicon wafer, adhered on to an aluminium stub. Poly(urethane) samples were carried out by Mr Samuel Roberts (University of Oxford) on a JEOL JSM-60110LV scanning electron microscope. All samples were coated with 4 nm platinum using a Quorum Q150T ES.

2.1.8 Solid state NMR spectroscopy

The ^{1}H, ^{27}Al and ^{13}C solid state NMR spectroscopy were performed by Dr. Nicholas H. Rees (University of Oxford) on a Bruker Advance III HD spectrometer equipped with a 9.4 T magnet using 4.0 mm O.D zirconia rotors and a MAS rate of 10 kHz at 399.9, 104.2, and 100.6 MHz, respectively.

2.1.9 Surface area and pore size distribution

Surface area and pore size distribution analysis was carried out using the Brunauer-Emmett-Teller (BET) method. The N_2 adsorption and desorption isotherms were measured using a Micromeritics TriStar II 3030 instrument at 77 K and the specific surface area was determined using the BET method. 0.1 g of each sample was weighed out and degassed at 110 °C overnight before analysis.

2.1.10 Tap density

~0.5 g of finely ground powder, of which the precise mass of was measured (m), was placed into a volumetric cylinder. The initial volume (v_i) and the volume after 1000 taps (v_f) were measured for each sample. The bulk density is given by m/v_i, while the tap density is given by m/v_f.

2.1.11 Temperature programmed desorption (TPD)

TPD traces were recorded on a Micromeritics AutoChem II 2920 Chemisorption Analyser equipped with a thermal conductivity detector (TCD). Specific programs run in each chapter are described in detail in the following sections.

2.1.12 Transmission electron microscopy (TEM)

TEM imaging was carried out by Ms Meng Lyu (University of Oxford) at the David Cockayne Centre for Electron Microscopy, Department of Materials, University of Oxford. The images were obtained from a JEOL JEM-2100 electron microscope with an accelerating voltage of 200 kV using a single tilt specimen. Samples were prepared by sonicating and diluting in DI water. A few droplets of each solution were then left to dry on a copper mesh covered with a carbon grid.

2.1.13 Thermogravimetric analysis (TGA)

TGA were run using a Perkin Elmer TGA 8000. 10 mg of sample was placed in a ceramic crucible on the auto-sampler. After being loaded into the chamber, the sample was heated from 30–800 °C at a ramp rate of 5 °C min^{-1} under a gas flow of 30 mL min^{-1} dry N_2 sample purge gas and 40 mL min^{-1} dry N_2 balance gas.

2.1.14 Zeta potential

Zeta Potential measurements were carried out by Ms Meng Lyu (University of Oxford) at Begbroke Science Park, Department of Materials, University of Oxford using a Malvern Zetasizer Nano ZS. Samples were sonicated in DI water for 15 min prior to usage. The solution was used to fill a folded capillary cell and placed into the machine for measurement.

2.2 Starting materials and chemicals

$Mg(NO_3)_2.6H_2O$, $Al(NO_3)_3.9H_2O$, Na_2CO_3, KNO_3, KBr, methanol, ethanol, 2-propanol, acetone, ethyl acetate, 1-hexanol, toluene, hexane, octane, benzoic acid, bromothymol blue, phenolphthalein, clayton yellow and Activated Carbon were all obtained from Sigma-Aldrich and used as received. NaOH solutions were made from pellets from Fisher Scientific. Desmoseal M280, Cabot Norit 8033-7, Nerox 600, Printex 3 and SCG LDH were

used as received from SCG Chemicals Co., Ltd. VXCMAX22 and TPK1099R were used as received from Cabot Corporation.

2.3 Experimental details for Chapter Six

2.3.1 Mixing of Desmoseal M280

The content of each mixture, outlined in Table 2.1, were added to a plastic mixing container. Holes were created in the lid of the container to allow for a vacuum to form inside. The container was then mounted into an Intertronics THINKY Planetary Vacuum Mixer and spun at 500 rpm for 1 min, then 1000 rpm for 1 min and finally 2000 rpm for 2 min. Pressure was at 100 kPa, 30 kPa and 5 kPa respectively unless specified otherwise. The resulting mixture was placed in a fumehood or 99% humidity box for the amount of time specified in the table below.

The 99% humidity box was created by placing a saturated solution of KNO_3 in an air tight container and the humidity was monitored by a digital hydrometer.

Table 2.1 - Details for the different conditions of PU curing tested.

	PU (mL)	Solid wt%	Water (mL)	Carbon (g)	LDH (g)	Core shell (g)	Carbon : LDH	Curing	Curing time (h)	Pre-treatment	Vacuum
1	5	\	0					Fume hood	96	\	Vac
2	5	\	0					Humidity box	72	\	Vac
3	5	\	1					Humidity box	24	\	Vac
4	5	\	0.5					Humidity box	24	\	Vac
5	5	2	1	Cabot (0.1)				Humidity box	2	\	Vac
6	5	2	1	Nerox (0.1)				Humidity box	2	\	Vac
7	5	2	1	Printex (0.1)				Humidity box	2	\	Vac
8	5	2	1		Mg_2Al W (0.1)			Humidity box	2	\	Vac
9	5	2	0	Cabot (0.1)				Humidity box	72	\	Vac
10	5	2	0	Nerox (0.1)				Humidity box	72	\	Vac
11	5	2	0	Printex (0.1)				Humidity box	72	\	Vac
12	5	2	0		Mg_2Al W (0.1)			Humidity box	72	\	Vac
13	5	2	1			Cabot@LDH (0.1)	1:7	Humidity box	2	\	Vac
14	5	2	1			Nerox@LDH (0.1)	1:7	Humidity box	2	\	Vac
15	5	2	1			Printex@LDH (0.1)	1:7	Humidity box	2	\	Vac

16	5	2	1	Cabot@LDH (0.1)	1:5	Humidity box	2	\	Vac
17	5	2	1	Nerox@LDH (0.1)	1:5	Humidity box	2	\	Vac
18	5	2	1	Printex@LDH (0.1)	1:5	Humidity box	2	\	Vac
19	5	2	1	Cabot@LDH (0.1)	1:3	Humidity box	2	\	Vac
20	5	2	1	Nerox@LDH (0.1)	1:3	Humidity box	2	\	Vac
21	5	2	1	Printex@LDH (0.1)	1:3	Humidity box	2	\	Vac
22	5	2	0	Mg_2Al E (0.1)		Humidity box	72	\	Vac
23	5	2	1	Mg_2Al E (0.1)		Humidity box	2	\	Vac
24	5	2	1	Mg_2Al W (0.1)		Humidity box	2	400, 2h, 100	Vac
25	5	2	1	Mg_2Al E (0.1)		Humidity box	2	400, 2h, 100	Vac
26	5	2	0	Mg_3Al W (0.1)		Humidity box	72	\	Vac
27	5	2	0	Mg_3Al E (0.1)		Humidity box	72	\	Vac
28	5	2	0	Mg_3Al A (0.1)		Humidity box	72	\	Vac
29	5	2	0	Mg_3Al IPA (0.1)		Humidity box	72	\	Vac
30	5	2	0	Mg_3Al EA (0.1)		Humidity box	72	\	Vac
31	5	2	0	Mg_3Al 1-H (0.1)		Humidity box	72	\	Vac

32	5	2	1	Mg_3Al W (0.1)		Humidity box	3	\	Vac
33	5	2	1	Mg_3Al E (0.1)		Humidity box	3	\	Vac
34	5	2	1	Mg_3Al A (0.1)		Humidity box	3	\	Vac
35	5	2	1	Mg_3Al IPA (0.1)		Humidity box	3	\	Vac
36	5	2	1	Mg_3Al EA (0.1)		Humidity box	3	\	Vac
37	5	2	1	Mg_3Al 1-H (0.1)		Humidity box	3	\	Vac
38	5	2	2	Mg_2Al W (0.1)		Humidity box	45min	400, 2h, 100	Vac
39	5	2	3	Mg_2Al W (0.1)		Humidity box	30min	400, 2h, 100	Vac
40	5	2	4	Mg_2Al W (0.1)		Humidity box	25min	400, 2h, 100	Vac
41	5	2	1	Cabot@LDO (0.1)	1:1	Humidity box	2	400 2h 50	No vac
42	5	2	4	Cabot@LDO (0.1)	1:1	Humidity box	25min	400 2h 50	No vac
43	5	2	1	Cabot@LDO (0.1)	1:1	Humidity box	2	400 2h 50	Vac
44	5	2	4	Cabot@LDO (0.1)	1:1	Humidity box	25min	400 2h 50	Vac
45	5	2	4	Cabot@LDO (0.1)	1:1	Humidity box	4	400 2h 50	Vac
46	5	2	1	Cabot@LDO (0.1)	1:1	Humidity box	72	400 2h 50	Vac
47	5	2	4			Humidity box	25min	\	No vac

48	5	2	4		Mg_2Al W (0.1)	Humidity box	25min	\	No vac
49	5	2	4		Mg_2Al W (0.1)	Humidity box	25min	400 2h 50	No vac
50	5	2	4	Cabot (0.1)		Humidity box	25min	400 2h 50	No vac

Chapter Three - Studies of the acidity and basicity of LDHs

3.1 Introduction

In recent years, O'Hare and co-workers have developed two post synthesis treatment methods for LDHs in order to modify their properties – aqueous miscible organic (AMO) and aqueous immiscible organic (AIM) solvent treatments.[1,2] The solvent treatments have been shown to alter the physical properties of LDHs, such as surface area, pore volume and tap density. These families of novel LDHs have been used as catalysts and supports for ethylene polymerisation and have shown improved activities and other properties compared to conventional LDH supports.[3,4] These studies show that the improvements are not only a result of the enhanced physical properties, but also due to the changes in the chemical properties of the LDHs. While acidity and basicity of LDOs have been briefly studied, no in-depth studies have been carried out, nor have they been related to the subsequent performances.[5]

Different techniques have been utilised to probe the surface acidity and basicity of LDHs and metal oxides. Védrine *et al*. have demonstrated the use of indicators to probe the different strengths of Brønsted acidity and basicity in solids, however, the values obtained from this method are less accurate due to the limitations of the usage of Hammett indicators in a heterogeneous system, such as the dispersibility of the solid in the solvent and that the solvent could be absorbed onto the active sites. For Lewis acidity and basicity, the most widely used technique is temperature programmed desorption (TPD). Combined

with *in situ* Fourier transform infrared (FTIR) spectroscopy studies have been carried out to assign different bonding modes to active sites of different strengths.[6,7]

In this chapter, alongside the conventional water washed sample (**LDH W** and **LDO W**), the five following solvent treated $[Mg_{0.72}Al_{0.28}(OH)_2](CO_3)_{0.14}$ ($Mg_{2.5}Al\ CO_3$) LDHs and LDOs are being investigated, for AMO: ethanol (**LDH E** and **LDO E**), acetone (**LDH A** and **LDO A)** and isopropyl alcohol (**LDH IPA** and **LDO IPA**); for AIM: ethyl acetate (**LDH EA** and **LDO EA**) and 1-hexanol washed (**LDH 1-H** and **LDO 1-H**). Both LDHs and LDOs are tested for their Brønsted basicity using Hammett indicators.[8,9] Their Lewis acidity and basicity are probed using *in situ* FTIR spectroscopy and TPD. To determine the effect of solvent treatment on the surface chemistry of the LDH/LDO nanosheets, solid state nuclear magnetic resonance (ssNMR) spectroscopy is utilised to probe the ^{1}H and ^{27}Al environments. Finally, their use as carbon dioxide (CO_2) sorption materials is tested.

3.2 Experimental details

3.2.1 Synthesis $Mg_{2.5}Al\ CO_3$ W LDH (LDH W)

LDH W was synthesised using the co-precipitation method adapted from a literature procedure.[10] $Mg(NO_3)_2.6H_2O$ (0.075 mol, 19.23 g) and $Al(NO_3)_3.9H_2O$ (0.025 mol, 9.37 g) (targeted Mg^{2+}/Al^{3+} ratio = 3) were dissolved in 100 mL DI water to make solution A. Na_2CO_3 (0.050 mol, 5.30 g) was then dissolved in another 100 mL DI water to make solution B. Solution A was added to solution B dropwise, while mixing at 375 rpm, over 1 h. The mixture was kept at pH 10 for the synthesis with the simultaneous addition of 4 M NaOH solution. When the addition of the solution A was completed and the final pH set to 10, the reaction was stirred for 24 h at room temperature. After the ageing process, the LDH product was washed with DI water until pH 7 and filtered. The product was left to dry overnight in a vacuum oven at room temperature.

3.2.2 Synthesis of solvent treated LDHs

Solvent treated LDHs were synthesised using the AMO and AIM solvent treatment methods adapted from a literature procedure.[2,10–12] $Mg_{2.5}Al\ CO_3$ LDH was prepared as described in the section above. After washing the LDH product with DI water until pH 7, special caution was taking to keep the LDH wet, the solid was then divided into 3 equal portions. Each portion was washed with 200 mL of the chosen solvent and dispersed in another 200 mL of the same solvent and stirred vigorously for 4 h (ethanol for LDH E, acetone for LDH A, 2-propanol for LDH IPA, ethyl acetate for LDH EA and 1-hexanol for LDH 1-H). The slurry was filtered and left to dry overnight in a vacuum oven at room temperature.

3.2.3 Brønsted basicity titrations

For Brønsted basicity titrations, 50 mg of the sample was then dispersed in 30 mL methanol and 0.5 mL of a 0.1% solution chosen indicator (bromothymol blue (pKa = 7.1), phenolphthalein (pKa = 9.3) and clayton yellow (pKa = 12.7)) in methanol was also added. The solution was then titrated against benzoic acid (0.1 M) using a syringe pump with a drop rate of 50 mL h^{-1} and stirred at 375 rpm until a colour change was observed (bromothymol blue: blue to yellow, phenolphthalein: pink to colourless, and Clayton yellow: red to yellow). At the point of colour change, the syringe pump is stopped and a reading is taken from the machine indicating volume titrated. For LDOs, the procedure was performed under N_2 atmosphere using a Schlenk line and samples were dispersed in anhydrous methanol that was further dried over 3 Å molecular sieves. The values obtained from this method are less accurate when compared to TPD due to the limitations of the usage of Hammett indicators in a heterogeneous system.[13] As a result, the number of basic sites obtained in this fashion will be less than the actual value. Hence it can only be taken in a qualitative way and be used to observe relative trends between samples.

3.2.4 *In situ* FTIR for Lewis basicity

In situ FTIR spectra were taken on a Bruker VERTEX 80 on a Specac High Temperature High Pressure cell with an Ar and CO_2 gas supply. The spectrometer was set to record 64 sample scans between 600–4000 cm^{-1} with a resolution of 4 cm^{-1}. 5 mg of sample was ground together with 300 mg KBr and pressed into a pellet. The pellet was then loaded into the cell and heated to the desired pre-treatment temperature, 200 °C for LDHs, for 1 h under Ar flow (0.8 cm^3 min^{-1}). The sample was then cooled to 100 °C and a spectrum was recorded as a background. Then, CO_2 was flown through the cell for 1 h to fully saturate all the basic sites. Ar was then flown through the cell to remove any excess and physisorbed CO_2 for 1 h. Finally, a spectrum was recorded after 1 h of gas flow.

3.2.5 TPD measurements for Lewis acidity and basicity

CO_2 TPD traces were recorded on a Micromeritics AutoChem II 2920 Chemisorption Analyser equipped with a thermal conductivity detector (TCD). The sample (100 mg) was loaded in a quartz U-tube and first purged in a flow of He (50 cm^3 min^{-1}) at room temperature for 10 min to remove impurities. The temperature was then raised to 450 °C at a ramp rate of 10 °C min^{-1} and held at this temperature for 1 h to remove water and any other impurities. The temperature was then reduced to 100 °C. For basicity tests, the gas changed to CO_2 in He (30 cm^3 min^{-1} CO_2, 50 cm^3 min^{-1} He) and flown over the sample for 1 h. For acidity test, a 10% NH_3 in He gas flow was used instead. Physically adsorbed CO_2/NH_3 was then removed by changing the gas flow to He (50 cm^3 min^{-1}) for 1 h. For the desorption step, the sample was heated from 100 to 450 °C under He flow (50 cm^3 min^{-1}) and a sampling rate of 1 measurement per second.

3.2.6 CO_2 capture values

CO_2 capture readings were carried out on a Micromeritics 3Flex with a chemisorption attachment. LDO samples were first calcined *ex situ*. 100 mg of sample was placed in the

machine for a further calcination at 450 °C at a ramp of 5 °C min^{-1} for 1 h. The sample was cooled to 40 °C at a ramp of 30 °C min^{-1} and left to evacuate to a vacuum at 40 °C for 3 h. The CO_2 measurements were then carried out twice at 40 °C. The first value provides the total adsorption value, the second provides physisorption. The difference between the two values provides the chemisorption value.

3.3 Characterisation of LDHs

A conventional $[Mg_{0.72}Al_{0.28}(OH)_2](CO_3)_{0.14}$ ($Mg_{2.5}Al$-CO_3 LDH) (**LDH W**) was synthesised using an adapted literature co-precipitation procedure in water.[10] Solvent treated LDH samples were prepared by re-dispersing an aqueous $Mg_{2.5}Al$ CO_3 LDH wet cake after neutralisation to pH 7 in the chosen dispersion solvent for 4 h. The dispersion solvents used were ethanol, acetone, isopropyl alcohol, ethyl acetate and hexan-1-ol to yield **LDH E**, **LDH A**, **LDH IPA**, **LDH EA** and **LDH 1-H**, respectively. These solvents were chosen as they all contain electron donating groups. The chemical compositions of the LDHs, as determined by inductively coupled plasma mass spectrometry (ICP-MS) and CHN elemental analysis, are shown in Table 3.1.

Table 3.1 - Summary of ICP-MS and CHN elemental analysis data for LDH samples. W = water (H_2O); E = ethanol (C_2H_5OH); A = acetone ($(CH_3)_2CO$); IPA = isopropanol ($(CH_3)_2CHOH$); EA = ethyl acetate ($CH3COOC_2H_6$); 1-H = hexan-1-ol ($C_6H_{13}OH$).

Sample	Mg/Al	Elemental composition (%)				Chemical formula
		Mg	Al	C	H	
LDH W	2.57	22.07	8.58	2.25	1.98	$[Mg_{0.72}Al_{0.28}(OH)_2](CO_3)_{0.14}.H_2O_{0.66}$
LDH E	2.49	18.63	7.46	2.93	1.84	$[Mg_{0.71}Al_{0.29}(OH)_2](CO_3)_{0.15}(H_2O)_{1.08}(E)_{0.038}$
LDH A	2.57	22.07	8.58	2.85	3.00	$[Mg_{0.72}Al_{0.28}(OH)_2](CO_3)_{0.14}(H_2O)_{0.61}(A)_{0.016}$
LDH IPA	2.57	22.07	8.58	2.86	2.91	$[Mg_{0.72}Al_{0.28}(OH)_2](CO_3)_{0.14}(H_2O)_{0.61}(IPA)_{0.016}$
LDH EA	2.57	22.07	8.58	2.68	2.53	$[Mg_{0.72}Al_{0.28}(OH)_2](CO_3)_{0.14}.(H2O)_{0.61}(EA)_{0.009}$
LDH 1-H	2.49	18.63	7.46	16.00	4.82	$[Mg_{0.71}Al_{0.29}(OH)_2](CO_3)_{0.15}.(H_2O)_{0.38}(1\text{-}H)_{0.181}$

The solvent content for most of the solvent treated LDH remains low at < 0.04 mol mol_{LDH}^{-1}, with the exception of **LDH 1-H** at 0.181 mol mol_{LDH}^{-1}. The effects of the incorporated solvent can be seen in the powdered X-ray diffraction (XRD) patterns of the as synthesised LDHs, shown in Figure 3.1. As previously reported, small variations in the lattice constants (Table 3.2) and peak widths of the Bragg reflections for solvent treated LDHs compared to the conventional sample (**LDH W**) are observed.[2,10] All the LDHs exhibit similar XRD patterns with the exception of **LDH 1-H** where there is a small shoulder reflection present near the (006) Bragg reflection (2θ = 19.9°). This was also reported in previous works from the group.[2,4,12] The d-spacing obtained from the position of the (003) Bragg reflection remains similar at ~7.8 Å, as does the lattice parameters *a/b* (3.06 Å), which are obtained from the position of the (110) Bragg reflection.

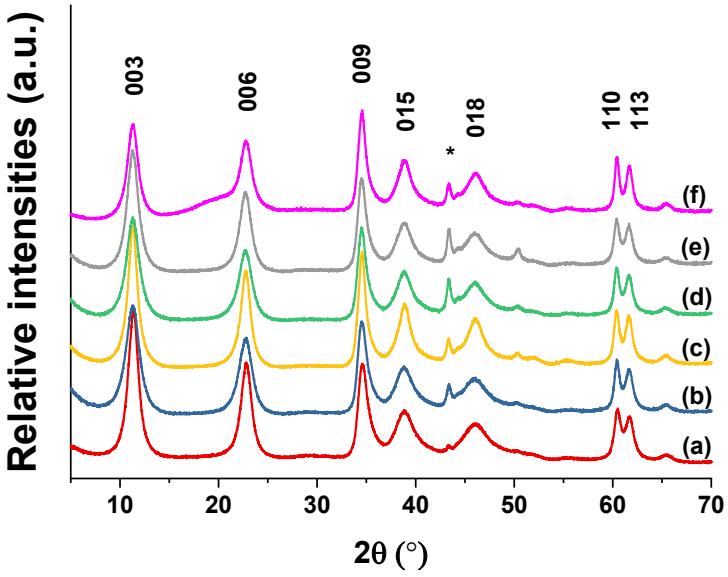


Figure 3.1 - XRD patterns of (a) **LDH W**, (b) **LDH E**, (c) **LDH A**, (d) **LDH IPA**, (e) **LDH EA** and (f) **LDH 1-H**. (*) denotes peak from sample holder.

Table 3.2 - Lattice parameters of various LDH samples calculated from the XRD patterns (Figure 2.1).

Sample	Lattice parameters [a]		
	a/b (Å)	*c* (Å)	Interlayer-spacing (Å)
LDH W	3.06	23.34	7.78
LDH E	3.06	23.43	7.81
LDH A	3.06	23.49	7.83
LDH IPA	3.06	23.49	7.83
LDH EA	3.06	23.64	7.88
LDH 1-H	3.06	23.34	7.78

[a] Indexed using the rhombohedral unit cell ($a = b \neq c$; $\alpha = \beta = 90°$, $\gamma = 120°$)

As shown from the TGA curves (Appendix A), solvent, as well as water, molecules are thermally desorbed for all samples at ~180 °C to form dehydrated LDHs. Therefore to confirm that the shoulder on the (006) Bragg reflection in the XRD spectrum of **LDH 1-H** is a result of residual solvent, the sample was treated at 200 °C for 1 h. However it is not due to its incorporation into the repeating structure as a change in reflection is only observed near the (006) Bragg reflection.

After heating at 200 °C for 1 h, the Bragg reflection at $2\theta = 19.9°$ disappears (Figure 3.2). This reflection can therefore be attributed to the presence of a small amount of an LDH phase containing intercalated 1-hexanol following the post solvent treatment. Its relatively high boiling point of 157 °C required a heating temperature of 200 °C to remove the 1-hexanol molecules from the interlayer galleries. The resulting Bragg reflections experienced a slight broadening when comparing their full width at half maximum (FWHM), indicating a slightly less crystalline material.

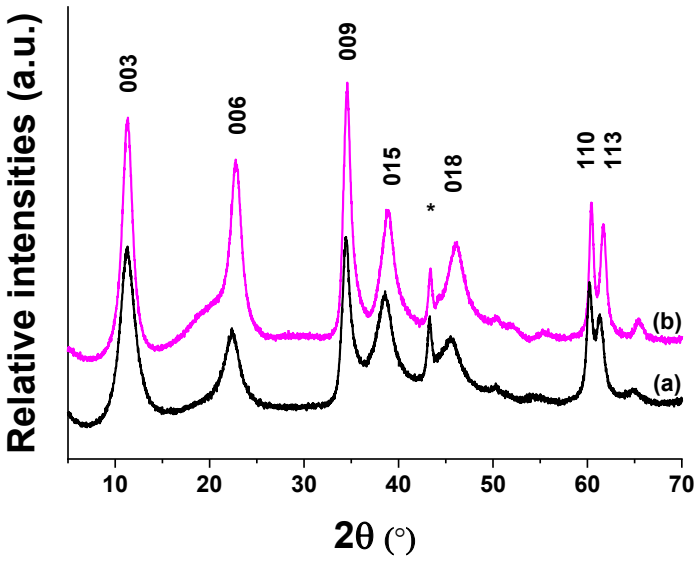


Figure 3.2 - XRD patterns of (a) **LDH 1-H** pre-treated at 200 °C for 1 h and (b) **LDH 1-H**.

3.4 Basicity study of solvent treated LDHs

The Brønsted basicity of these materials was studied by a titration technique adapted from literature,[13] using three Hammett indicators: bromothymol blue ($pK_a = 7.1$), phenolphthalein ($pK_a = 9.3$) and clayton yellow ($pK_a = 12.7$). For the purpose of this study, Brønsted basic sites pH > 12.7, 9.3 ≤ pH ≤ 12.7 and 7.1 ≤ pH ≤ 9.3 are assigned the labels 'strong', 'medium' and 'weak' respectively, and are presented as values in mmol g^{-1}. This system is less accurate compared to other techniques, such as *in situ* FTIR and TPD, performed in this chapter as it is subject to the limitations of Hammett indicators in a heterogeneous system: specifically the ability of the LDHs to disperse in the methanol system will affect the interactions of the indicator and the acid. Methanol was chosen as the solvent due to its miscibility with both water and organic solvents used in the study alike, but due to it being an organic solvent, the solvent treated samples will be more easily dispersed. As a result, the values presented for this technique would be less than the actual number basic sites on the materials. Although this system has its limitations and is not able to fully quantify the basic sites in the samples, the data collected still reflect the number of

sites accessible for chemical reactions using an organic solvent as the LDH dispersing medium.

The titration results indicate that all solvent treated LDHs have enhanced number of basic sites compared to an untreated conventional LDH, **LDH W**, which only exhibited a total basic site number of 0.70 mmol g^{-1} (Figure 3.3 and Table 3.3). **LDH 1-H** exhibited the highest total number of basic site of 0.92 mmol g^{-1}, corresponding to a 31% increase in sites relative to **LDH W**, while **LDH EA** showed the lowest number of basic sites for solvent treated samples (0.85 mmol g^{-1}).

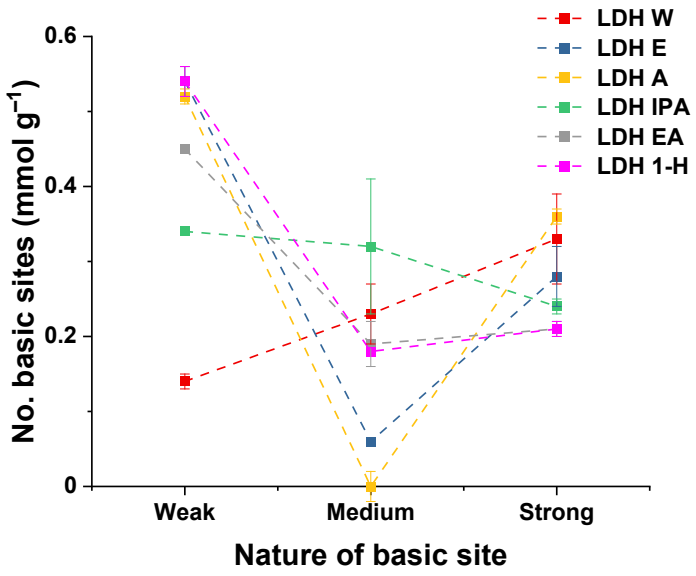


Figure 3.3 - Number of Brønsted basic sites for water washed and solvent treated LDH samples as determined by titration method. Dotted lines are just a guide for the eye. Error bars from repeated measurements.

Table 3.3 - Summary of titration data of LDH samples.

Sample	Basic site distribution (mmol g^{-1})			
	Weak	**Medium**	**Strong**	**Total**
LDH W	0.14 ± 0.01	0.23 ± 0.04	0.33 ± 0.06	0.70 ± 0.01
LDH E	0.54 ± 0.00	0.06 ± 0.02	0.28 ± 0.04	0.88 ± 0.00
LDH A	0.52 ± 0.01	0.00 ± 0.04	0.36 ± 0.01	0.86 ± 0.01
LDH IPA	0.34 ± 0.00	0.32 ± 0.09	0.24 ± 0.01	0.90 ± 0.00
LDH EA	0.45 ± 0.00	0.19 ± 0.03	0.21 ± 0.01	0.85 ± 0.00
LDH 1-H	0.54 ± 0.00	0.18 ± 0.02	0.21 ± 0.01	0.92 ± 0.00

Out of the total number of basic sites, the strong basic sites account for the largest mol fraction for **LDH W** (0.33 mmol g^{-1}), with weak basic sites constituting the least (0.14 mmol g^{-1}). This basic site distribution profile is not followed by any LDHs which have undergone solvent treatment. **LDH IPA** displayed the opposite of this trend with the highest proportion of the basic sites being weak sites (0.34 mmol g^{-1}), and lowest being strong sites (0.24 mmol g^{-1}). All solvent treated samples, except **LDH IPA**, recorded an increase in weak basic sites by at least a factor of 3. **LDH E** and **LDH 1-H** possessed the highest number of weak basic sites of 0.54 mmol g^{-1}. Apart from **LDH A**, all solvent treated LDHs experienced a decrease in medium basic sites. **LDH E** showed a reduced number of medium sites of 0.06 mmol g^{-1} while **LDH A** had a complete elimination of medium sites. **LDH EA** and **LDH 1-H**, samples treated with AIM solvents, experienced less significant decreases in medium sites, only diminishing by 0.04 and 0.05 mmol g^{-1} respectively. Despite showing a complete elimination of medium basic sites, **LDH A** is the only solvent treated LDH to show an increase in strong basic sites relative to **LDH W** (0.36 and 0.33 mmol g^{-1} respectively). AIM solvent treated samples experienced the

largest decrease in strong basic sites: both **LDH EA** and **LDH 1-H** possess 0.21 mmol g^{-1}, corresponding to a 36% decrease from **LDH W**.

Without any pre-treatment of the samples prior to titration, the basic sites showed a small dependence on the pK_a of the dispersing solvent. This is due to the possibility of the solvents interacting with the titrating acid as bases or with the basic sites on the LDH surface. Furthermore, the solvent content in each treated LDH sample is not uniform, as seen in Table 3.1. Lastly, different solvents can affect the pK_a of acids and bases, especially when the solvent used can participate in proton exchange reactions. Therefore, to remove the uncertainty of the solvent interference with the titration data, the TGA data indicated that if the samples were pre-treated at 200 °C for 1 h would be sufficient to remove water and any residual solvent (Appendix A).

3.5 Basicity study of dehydrated solvent treated LDHs

There is a large increase in the available surface area and pore volume of the dehydrated solvent treated LDHs compared to **LDH W** (Table 3.4). **LDH E** showed the highest surface area of 196 m^2 g^{-1} while **LDH EA** had the highest pore volume of 0.83 cm^3 g^{-1}.

Dehydration of the samples changed both the number and distribution of basic sites. Compared to the untreated samples where each one showed a different distribution of basic sites, all samples displayed similar responses of having fewer medium Brønsted basic sites compared to the strong and weak ones after being subjected to a pre-treatment of 200 °C for 1 h (Figure 3.4). Analysis of the total number of Brønsted basic sites (Table 3.4), revealed that all solvent treated LDHs exhibited a higher total number compared to **LDH W** (0.41 mmol g^{-1}), but showed overall a decrease compared to the untreated sample, with the largest reduction seen in **LDH E** (0.31 mmol g^{-1}). **LDH IPA** and **LDH 1-**

H showed the highest total basicity at 0.67 mmol g^{-1}. **LDH IPA** exhibited the highest number of medium basic sites (0.15 mmol g^{-1}), double that of any other solvent treated LDHs, echoing the trend shown in Figure 3.3. However, once the surface area was taken into account, the AMO-LDHs showed lower basic site densities compared to **LDH W** (4.52 µmol m^{-2}). **LDH 1-H** had the highest Brønsted basic site density of all the solvent treated LDHs at 4.04 µmol m^{-2}.

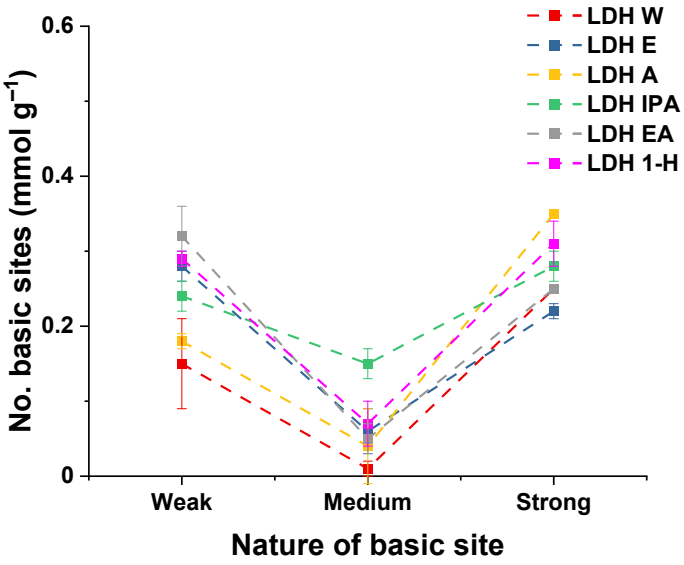


Figure 3.4 - Number of Brønsted basic sites of dehydrated LDH samples as determined by titration method. Dotted lines are just a guide for the eye. Error bars from repeated measurements

Table 3.4 - Summary of titration data of dehydrated LDH samples.

Sample	N_2 BET surface area (m^2 g^{-1})	Pore volume (cm^3 g^{-1})	Total basic sites (mmol g^{-1})	Basic site density (µmol m^{-2})
LDH W	91.6	0.54	0.41 ± 0.06	4.52 ± 0.65
LDH E	196	0.70	0.57 ± 0.02	2.92 ± 0.10
LDH A	173	0.82	0.57 ± 0.01	3.29 ± 0.06
LDH IPA	184	0.81	0.67 ± 0.02	3.62 ± 0.01
LDH EA	175	0.83	0.61 ± 0.04	3.48 ± 0.23
LDH 1-H	166	0.61	0.67 ± 0.01	4.04 ± 0.06

Post-synthesis solvent dispersion affects the LDH surface but had little effect on the structural arrangement of the layers. Although solvent treatment increases the available specific surface area, *a priori*, it would not be expected to change the basic site density of all samples, especially when the samples have been pre-treated at 200 °C, removing all solvent molecules.

Previous studies suggest that thermal treatment of AMO-LDHs at 200 °C only removes surface bound solvent molecules, leaving the LDH structure intact.[1,10,12] However, the decrease in the total basic site density observed in this study for some solvent treated samples suggests that trace amounts of residual solvent may adsorb to, and therefore block, some surface basic sites. This interaction has been observed between alcohols and LDHs, resulting in hydroxyl groups becoming inaccessible.[14]

To investigate the Lewis basicity of the dehydrated LDHs, *in situ* Fourier transform infra-red (FTIR) spectroscopy using CO_2 as the probe molecule was employed. The bonding modes and corresponding vibrational frequencies of CO_2 on LDH and LDO surfaces are summarised in Table 3.5. As shown in Figure 3.5, **LDH W** exhibits a strong absorbance between 1360–1400 cm^{-1} and a less intense absorbance between 1470–1580 cm^{-1}, which are associated with a monodentate carbonate surface coordination, and typically corresponds to a strong Lewis basic site. A weak bidentate carbonate stretching vibration (1580–1670 cm^{-1}) can be assigned to a medium strength basic site in **LDH W**. These findings are consistent with previously reported literature results, which showed that different bonding modes of CO_2 on the surface of LDHs exhibit different frequencies.[7,15] Solvent treatment appears to alter the overall Lewis basicity profile of solvent treated LDHs, exhibiting varying levels of both strong and medium strength Lewis basic sites. In particular, both **LDH E** and **LDH 1-H** exhibited enhanced numbers of medium strength basic

sites, while the medium basic sites are eliminated by treatment with acetone and isopropanol. Measurements were taken at 100 °C to avoid the rehydration of the dehydrated LDH from the moisture in the carrier gas. The absence of absorptions corresponding to weak bicarbonate stretches is consistent with the findings of Di Cosimo *et al*., who studied the bonding modes associated with the CO_2 bound to the surface of LDHs/LDOs. They suggested that the weak bonding mode is removed at 100 °C.[7]

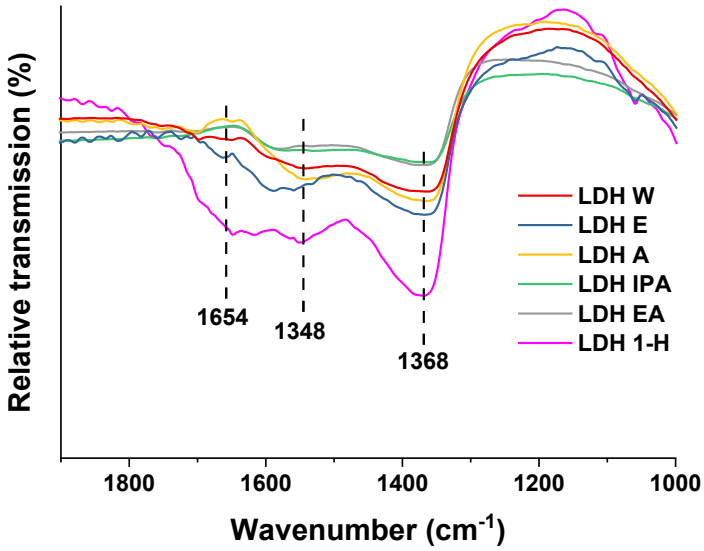
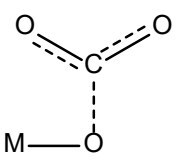
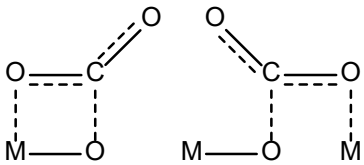
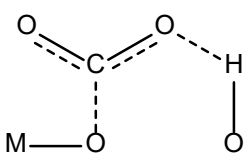


Figure 3.5 - *In situ* FTIR spectra of pre-treated LDH samples with CO_2 as a probe molecule.

Table 3.5 - CO_2 bonding modes and their corresponding IR frequencies when bound to LDH and LDO surfaces.[7,15]

Bonding mode			
	Monodentate	Bidentate and bridging	Bicarbonate
Basic strength	Strong	Medium	Weak
Frequencies (cm^{-1})	1360–1450 1470–1580	1320–1350 1580–1670	1220 1480 1650

3.6 Basicity and acidity studies of solvent treated LDOs

Solvent treated LDOs were prepared by calcining the solvent treated LDH at 450 °C for 12 h with a heating ramp rate of 5 °C min^{-1}. The LDO products were named **LDO W**, **LDO E**, **LDO A**, **LDO IPA**, **LDO EA** and **LDO 1-H** by calcination of the appropriate solvent treated LDH.

As shown in Figure 3.6, the basic site distribution for all samples, as determined by the titration method, changed drastically from that of LDHs and dehydrated LDHs. With the exception of **LDO EA**, the general trend for solvent treated LDO samples is that the number and strength of the Brønsted sites increases compared to the parent LDH. This increase in the number of strong Brønsted basic sites is due to the decomposition of hydroxide groups to unsaturated oxygen atoms and metal-oxygen pairs on the surface of the LDH nanosheets, which have higher basicity.[6] **LDO 1-H** showed the highest number of total Brønsted basic sites at 1.58 mmol g^{-1}. Interestingly, both **LDO E** and **LDO IPA** exhibit a negligible number of weak basic sites and **LDO EA** did not have any medium basic sites. In general, both the total number of basic sites and the basic site density of LDOs increases from that of their parent LDH. This is due to an increase in surface area from LDH to LDO as the LDH nanosheets undergo dehydroxylation, decarbonation and more thorough dehydration from the interlayer region. Furthermore, some aluminium ions migrate from octahedral into tetrahedral sites, leading to the formation of apical oxygen and exposure of more basic sites.[16] All solvent treated LDOs, except **LDO 1-H**, displayed a lower basic site density compared to **LDO W** (4.83 μmol m^{-2}), while **LDO 1-H** has the highest total number of sites and highest basic site density at 1.58 mmol g^{-1} and 5.79 μmol m^{-2} respectively (Table 3.6), which is higher than that of **LDO W**.

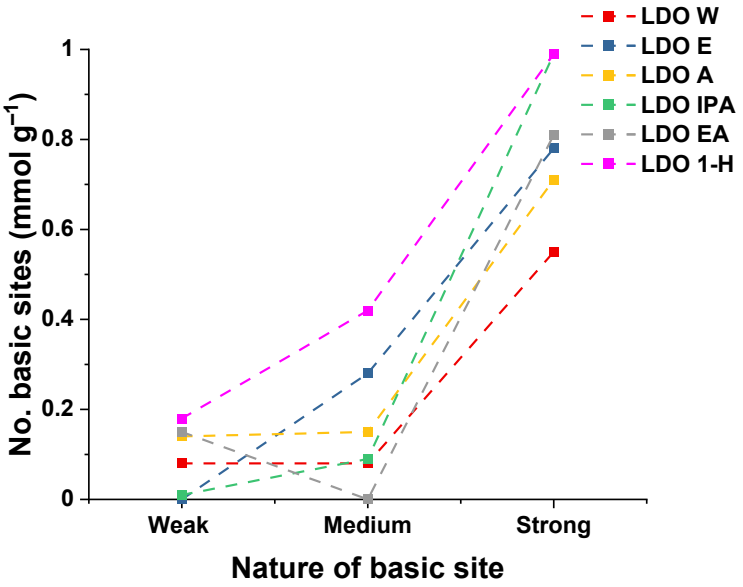


Figure 3.6 - Number of Brønsted basic sites of LDO samples as determined by titration method. Dotted lines are just a guide for the eye. Error bars from repeated measurements

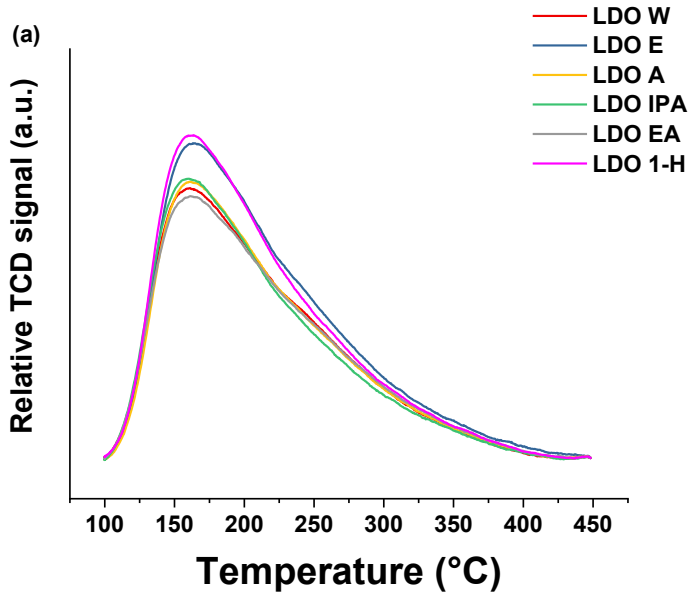
Table 3.6 - Summary of physical properties and basic site titration data of LDO samples.

Sample	N_2 BET surface area ($m^2\ g^{-1}$)	Pore volume ($cm^3\ g^{-1}$)	Total basic sites ($mmol\ g^{-1}$)	Basic site density ($\mu mol\ m^{-2}$)
LDO W	147	0.69	0.71	4.83
LDO E	310	1.33	1.04	3.35
LDO A	251	1.18	1.00	3.99
LDO IPA	286	1.27	1.09	3.81
LDO EA	243	1.12	0.89	3.67
LDO 1-H	273	1.17	1.58	5.79

Temperature programmed desorption (TPD) using both CO_2 and NH_3 have been used to probe the Lewis basicity and acidity of the LDO samples respectively. There are no noticeable differences in the general desorption profiles for the CO_2 TPD (Figure 3.7 (a)), indicating that there is no change in the distribution profile of Lewis basic sites. To gain further insight into the distribution of bonding modes, the CO_2 peaks were deconvoluted

based on the findings of Di Cosimo *et al.*,[7] and the weightings are displayed in Table 3.8 and the fittings are shown in Appendix A. As the adsorption of CO_2 was carried out at 100 °C, the desorption profiles were only deconvoluted into the 2 peaks corresponding to bidentate and monodentate CO_2 bonding modes. The weighting between the 2 peaks remained consistent between all samples (*ca.* 40:60 for bidentate:monodentate). **LDO E** displayed the lowest bidentate fraction of 36% while **LDO IPA** exhibited the highest of 41%, although this could be within error of the fitting program.

The samples treated with acetone, IPA and ethyl acetate all displayed very similar number of basic sites *ca.* 1.96 mmol g^{-1}, which is similar to **LDO W**, while **LDO E** and **LDO 1-H** displayed enhanced numbers of Lewis basic sites, in excess of 2.2 mmol g^{-1}. However, once the surface areas of the LDOs are taken into account, all solvent treated samples present similar Lewis basic site densities in the range of 7.22–8.10 μmol m^{-2} (Table 3.7), which are much lower than that of **LDO W** (13.29 μmol m^{-2}). This is a similar trend to that observed in the Brønsted basic site densities of dehydrated LDHs and LDOs.



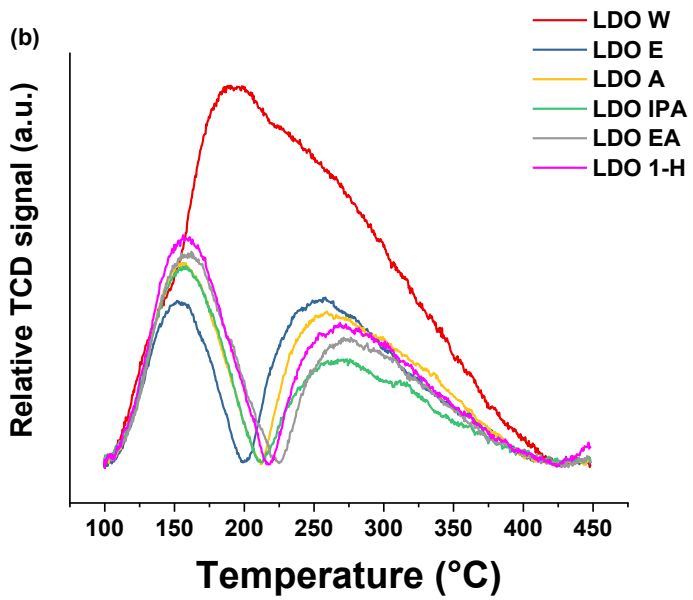


Figure 3.7 - (a) CO_2 and (b) NH_3 TPD curves of LDO samples.

Table 3.7 - Summary of TPD data of LDO samples.

Sample	Total basic sites (mmol g^{-1})	Basic site density (µmol m^{-2})	Total acidic sites (mmol g^{-1})	Acidic site density (µmol m^{-2})	Acid/base ratio
LDO W	1.95	13.29	0.38	2.59	0.19
LDO E	2.24	7.22	0.19	0.61	0.08
LDO A	1.97	7.86	0.21	0.84	0.11
LDO IPA	1.97	6.88	0.16	0.57	0.08
LDO EA	1.95	8.03	0.19	0.77	0.10
LDO 1-H	2.21	8.10	0.21	0.77	0.09

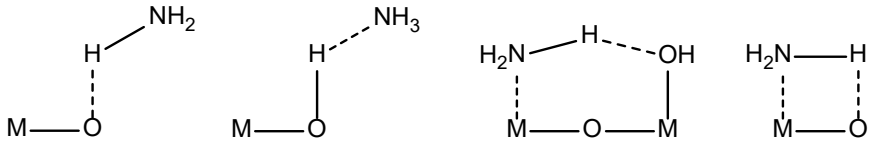
The NH_3 TPD experiments were conducted to probe Lewis acidity (Figure 3.7 (b)). The total acidity of **LDO W** is 0.38 mmol g^{-1} while the solvent treated LDOs had a significantly lower value in the range of 0.16–0.21 mmol g^{-1}, where **LDO IPA** has the lowest acidity value of 0.16 mmol g^{-1} (Table 3.7). Considering the Lewis acidic site density, all solvent treated LDO samples exhibit a Lewis acidic site density 3–5 times

lower than that of **LDO W**. These values are similar to those reported in literature by Bezen *et al*.[5]

LDO W exhibited an intense, broad peak over the range of 100–450 °C. In contrast, solvent treated LDOs exhibited two distinct peaks: one in the low temperature range (100–200 °C), assigned to a weak Lewis acid site, and the other in the high temperature range (200–450 °C), which correspond the strong Lewis acid sites. Prinetto *et al.* have shown that, for LDOs, the peak in the NH_3 TPD at 150 °C is due to the hydrogen bonding between NH_3 and surface oxide / hydroxide groups (OH peak) (Scheme 3.1 (a)).[17] The resulting metal peak is a result from a combination of two different bonding modes involving the bonding between the nitrogen and surface metal, and hydrogen bonding of a hydrogen on ammonia to a neighbouring oxygen site (metal peak) (Scheme 3.1 (b)). These two bonding modes could not be resolved into separate features. The separation of the peaks is due to the suppression of one of the strong Lewis acid sites. This may arise from solvents interacting strongly with acid sites during treatment, via the lone pairs on the oxygen atoms of the solvents and the metal sites of the nanosheets, leading to blocking of some of the acid sites even after calcination. By deconvoluting the peaks (deconvolution shown in Appendix A), **LDO W** is seen to display the lowest relative weighting for the OH peak (28%) (Table 3.8). With the absence of one of the metal-bound peaks in solvent treated LDOs, the relative weighting of the OH peak increases to a maximum of 51%, seen in **LDO IPA**. **LDO E** displayed the most similar peak distribution when compared to **LDO W**. Peak fitting reveals a small residual peak around 200–250 °C, which shows that rather than a complete elimination of either one of the bonding modes characteristic of strong acid sites, there is severe reduction of the first metal peak. However, it is important to note that both modes involve bonding to metal sites and both sites see a complete suppression and reduction in intensity respectively.

Table 3.8 - Weighting of the peaks obtained from TPD data for LDO samples.

Sample	Basic site weighting (%)		Acid site weighting (%)		
	Bidentate	Monodentate	OH peak	Metal peak	
				Peak 1	Peak 2
LDO W	37	63	28	72	
LDO E	36	64	31	25	44
LDO A	39	61	39	16	45
LDO IPA	41	58	51	15	34
LDO EA	38	62	50	14	35
LDO 1-H	40	60	48	14	37



(a) (b)

Scheme 3.1 - The different bonding modes of NH_3 on the surface of an LDO.

It is interesting to find that the Lewis acid/base ratio for LDOs can be easily tuned from 0.08 to 0.19 by using different dispersing solvents. The Lewis acid/base ratio shows a correlation with the surface areas of the LDOs: the higher the surface area, the lower the ratio (Figure 3.8). This is due to both surface area and reduction in acid sites being a reflection of solvent penetration. A high surface area is the result of effective solvent replacement of surface and interlayer water molecules. This results in more solvent molecules being incorporated into the structure which will block more acid sites upon heat treatment.

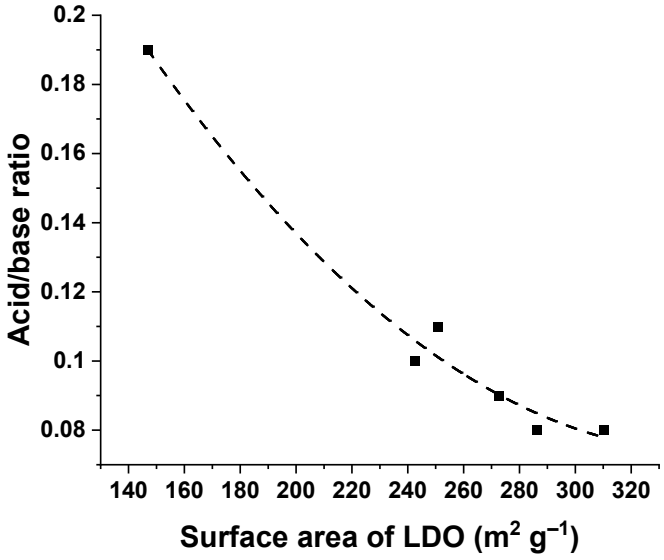


Figure 3.8 - Acid/base ratio of solvent treated LDOs as a function of surface area. Dotted line is just the guide for the eye.

While the NH_3 bonding modes mainly occur through the metal site, the CO_2 bonding modes mainly concern surface oxygen sites. This indicates that the oxygen sites on the surface treated samples seem unaffected.

The change in the NH_3 TPD curves, along with the reduction in basic site densities suggests that blocking of specific surface metal sites occurs upon solvent treatment. To investigate the possibility of solvents remaining in the structure, CHN elemental analysis of the LDOs was carried out and the results are presented in Table 3.9. The assumptions made were 1) the ideal calcined material is a complete conversion to mixed metal oxides with no remaining hydroxides, 2) any deviations from oxides results in hydroxyl groups which are balanced out by carbonates due to incomplete calcination to full LDOs, and 3) all LDO samples display the same level of decomposition as the samples all underwent the same calcination prodecure. **LDO W** was used as a baseline for the composition of all LDOs present. Any excess carbon can therefore be attributed to the presence of solvent or their decomposed derivatives. It is not possible to identify the additional carbon-containing residue (denoted as S in Table 3.9) post calcination.

Table 3.9 - Summary of CHN elemental analysis data for LDO samples. S denotes solvent residue.

Sample	Mg:Al	C (%)	H (%)	Composition
LDO W	2.57	0.90	1.02	$Mg_{0.72}Al_{0.28}O_{1.06}(OH)_{0.08}(CO_3)_{0.04}(H_2O)_{0.21}$
LDO E	2.44	0.89	1.15	$Mg_{0.72}Al_{0.28}O_{1.06}(OH)_{0.08}(CO_3)_{0.04}(H_2O)_{0.21}(S)_0$
LDO A	2.57	0.82	0.99	$Mg_{0.72}Al_{0.28}O_{1.06}(OH)_{0.08}(CO_3)_{0.04}(H_2O)_{0.21}(S)_0$
LDO IPA	2.57	1.16	1.20	$Mg_{0.72}Al_{0.28}O_{1.06}(OH)_{0.08}(CO_3)_{0.04}(H_2O)_{0.21}(S)_{0.024}$
LDO EA	2.57	0.96	0.91	$Mg_{0.72}Al_{0.28}O_{1.06}(OH)_{0.08}(CO_3)_{0.04}(H_2O)_{0.21}(S)_{0.0064}$
LDO 1-H	2.44	0.97	1.10	$Mg_{0.72}Al_{0.28}O_{1.06}(OH)_{0.08}(CO_3)_{0.04}(H_2O)_{0.21}(S)_{0.0024}$

LDO IPA, **LDO EA** and **LDO 1-H** displayed excess carbon whereas **LDO E** and **LDO A** exhibited less carbon than was needed to form the base LDO compound compared to **LDO W**. This would suggest that for these two compounds the decomposition was more thorough and complete. This would allow us to assume this approach provides us with an underestimation of how much solvent residue is present in the materials post calcination.

To further probe how the remaining solvent residue interacts with the surface of the LDOs, ssNMR spectroscopy was performed. The ^{27}Al DPMAS NMR spectra of the LDHs show that all the Al^{3+} centres are in O_h environments (δ = –25–30 ppm), as expected from a normal LDH structure, which consists of edge-sharing $M^{n+}(OH)_6$ octahedra (Appendix A). The ^{1}H NMR spectra also show resonances corresponding to the dispersing solvent, water and different surface hydroxyl environments ($\delta = 0$–4 ppm). Once calcined at 450 °C, the material changes, forming pure MgO domains with some Al^{3+} doped MgO regions. Some Al^{3+} centres also migrate into T_d environments which share oxygens with the bulk MgO, while maintaining some surface hydroxyl groups.[18] For **LDO W**, the relative distribution of Al^{3+} sites are 50:50 between T_d:O_h. All solvent treated LDO samples exhibited a lesser relative population of T_d Al^{3+} sites (δ = 30–100 ppm) (Figure 3.9). **LDO A** displayed the

largest change in T_d centres, possessing only 42% T_d sites. **LDO 1-H** possessed the highest relative T_d population of 47%.

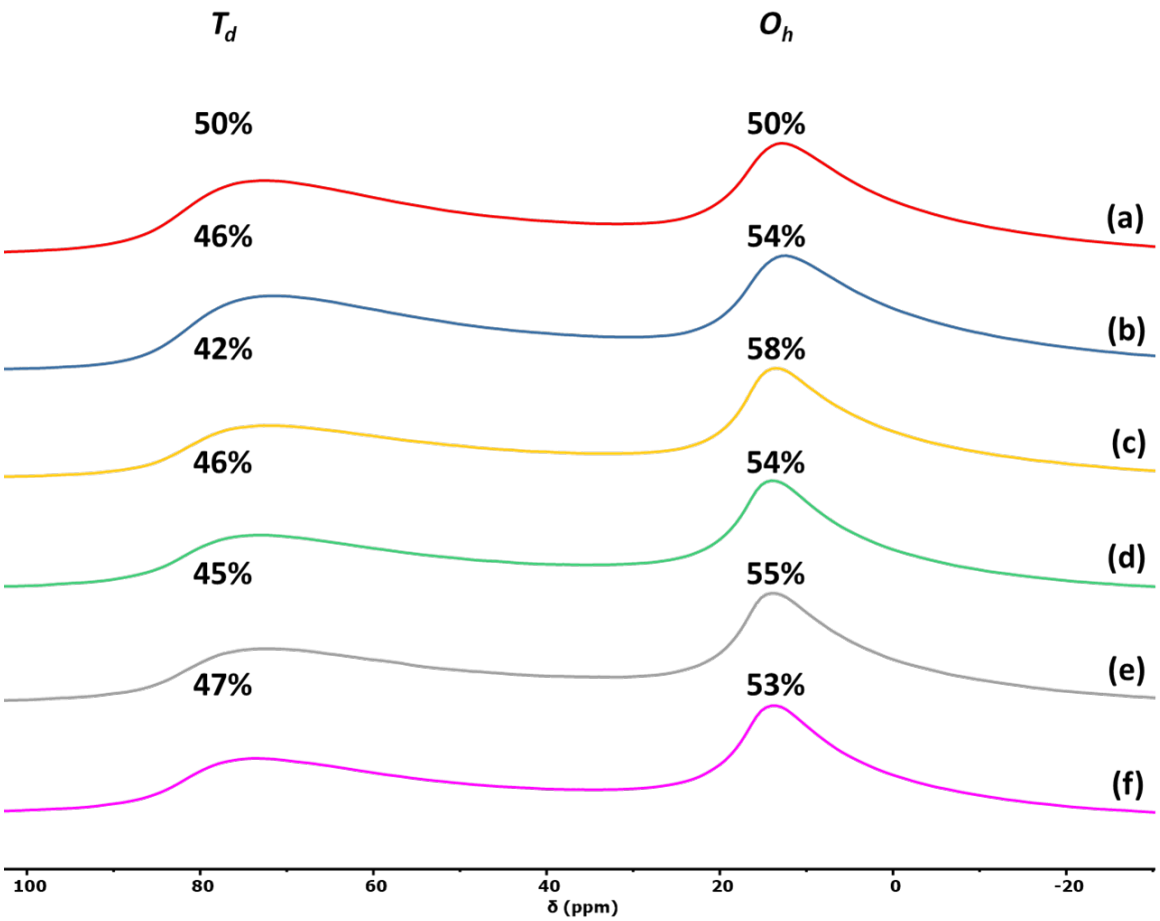


Figure 3.9 - ^{27}Al DPMAS ssNMR of (a) **LDO W**, (b) **LDO E**, (c) **LDO A**, (d) **LDO IPA**, (e) **LDO EA** and (f) **LDO 1-H**. Percentages denote relative population of each coordination. The Al^{3+} resonances at δ = –25–30 ppm has been assigned to O_h centres while the Al^{3+} resonances at δ = 30–100 ppm has been assigned to T_d centres.

The various distinct OH environments can be observed in the solid state ^{1}H NMR spectra of the LDO samples (Figure 3.10). The ^{1}H resonances between δ = –1–3 ppm are assigned to various Mg-OH environments,[19] the different ^{1}H chemical shifts arise from the variations in the number in neighbouring Al^{3+} atoms. A relatively weak ^{1}H resonance at δ = 7.3 ppm can be observed in the ^{1}H MAS NMR spectrum of **LDO W**. This has not been studied in the literature for LDH or LDO materials, but in related Al^{3+}-containing materials (boehmite and bayerite) studied by Piedra *et al.*, this resonance can be attributed to an apical Al-OH moiety.[20] This agrees with the LDO model, as it has been previously shown

that some surface OH groups are still present post calcination,[18,21] and will be further discussed in Chapter Four. The integrated signal intensity is larger in **LDO E**, **LDO IPA** and **LDO 1-H**, while the signal is reduced in the other solvent samples. All solvents used in this study possess oxygen containing functional groups. Furthermore, the solvents which displayed increased integrated signal intensities are all alcohols.

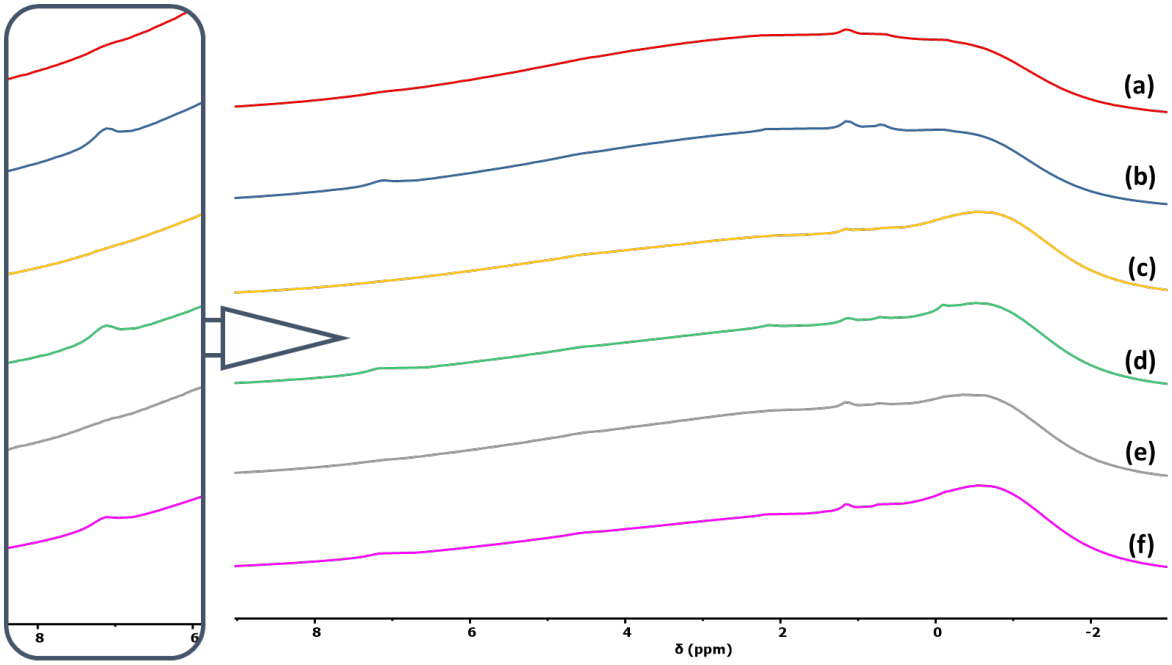
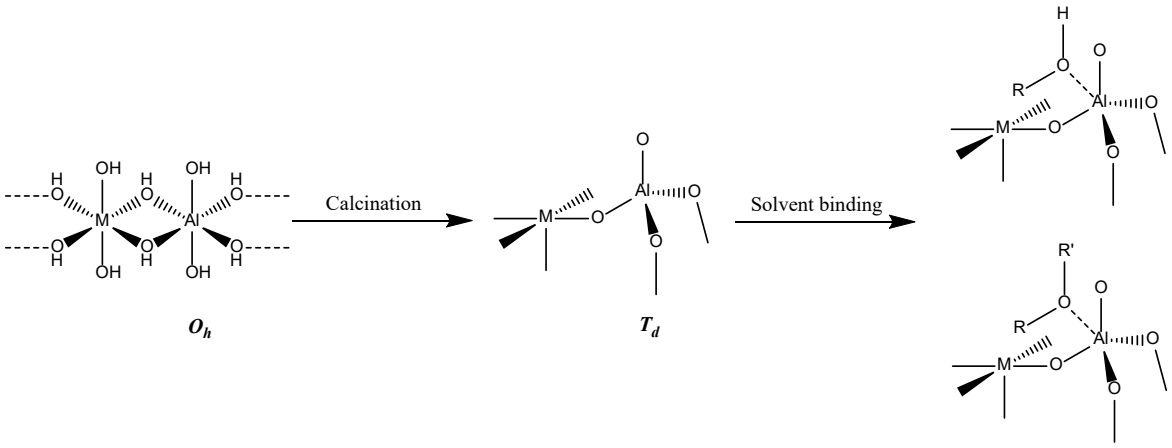


Figure 3.10 - ^{1}H MAS ssNMR of (a) **LDO W**, (b) **LDO E**, (c) **LDO A**, (d) **LDO IPA**, (e) **LDO EA** and (f) **LDO 1-H**.

This leads to the following hypothesis, depicted in Scheme 3.2. Following LDH calcination, a fraction of Al^{3+} cation centres migrate from the bulk O_h coordination to T_d coordinated centres. Then a small amount of solvent present in the structure can now bond onto the less sterically hindered *T_d* coordinated centres using the electron-donating oxygen atoms in either an alcohol or carbonyl group. This causes a small shift in Al^{3+} environment from *T_d* to *O_h* as seen in the ^{27}Al NMR spectrum. When the solvent involved has an alcohol functional group, this provides an addition Al-OH environment compared to **LDO W**, which result in the increase in signal intensity observed at $\delta = 7.3$ ppm in ^{1}H MAS NMR spectra for **LDO E**, **LDO IPA** and **LDO 1-H**.



Scheme 3.2 - Graphic representation of proposed mechanism for solvent interactions on an LDO surface upon calcination from an LDH. R and R' denote carbon containing group.

This theory suggests that the solvent selectively bonds and interacts with the Al^{3+} cations and no interaction with the surface oxygens. This is confirmed by CO_2 TPD, where adsorption occurs primarily through surface oxygens, which displayed no difference between the water washed and solvent treated LDOs. In comparison, the desorption curves in NH_3 TPD, where bonding modes rely on N-M interactions, showed drastic differences between water washed and solvents treated samples. This would also suggest the bonding motif involving interactions with a further oxygen or OH would be the more severely suppressed peak seen in the NH_3 TPD curves. Currently it can only be confirmed that the solvent interacts with the Al^{3+} cations. Any interactions with the surface accessible Mg^{2+} cations were not confirmed as methods to probe interactions with Mg^{2+} are not widely available (e.g. Mg XAS) or sufficiently sensitive, e.g. ^{25}Mg NMR.

To further investigate this hypothesis, solvent treated **LDO T**, **LDO H** and **LDO O** were synthesised by dispersing LDH suspensions in toluene, hexane and octane, respectively. Toluene was chosen due to the possibility of the aromatic ring interacting with the Al^{3+} centre while not possessing an oxygen containing functional group. Hexane and octane were chosen due to their complete lack of polar functional groups. All three solvents possess boiling points that are within the range of the original solvents used

(toluene: 110.6 °C, hexane: 69.0 °C and octane: 125.6 °C), so should provide a fair comparison with the previous set of solvent treated LDOs with regard to solvent residue post calcination.

The CO_2 TPD curves observed in Figure 3.11 (a) showed the same profile as those shown in Figure 3.7 (a). This indicates that the distribution of basic sites in the LDOs is unaffected by the solvents, which is due to the lack of Lewis acidic groups in the solvent molecules that could interact with surface oxygens. The difference, once again, can be observed in the NH_3 TPD profiles (Figure 3.11 (b)): toluene affects the profile of **LDO T** in the same manner as the oxygen containing solvents. There is an elimination of the further reaching metal bonding mode while a reduction in the other bonding mode is also observed. This could possibly be due to the aromatic ring bonding to the lesser coordinated Al^{3+} centres through a π-type bonding motif, similar to those in organometallic compounds.[22,23]

The hydrocarbon solvent treated samples, unlike the other solvents used, displayed a similar NH_3 TPD curve to that of **LDO W**, with no elimination or reduction in peaks. The absence of polar or lone pair containing functional groups in these pure hydrocarbons means they cannot form favourable interactions with the surface metal centres. Therefore, despite having higher boiling points than some of the other solvents used, they do not remain on the surface upon calcination and no site blocking occurs as a result.

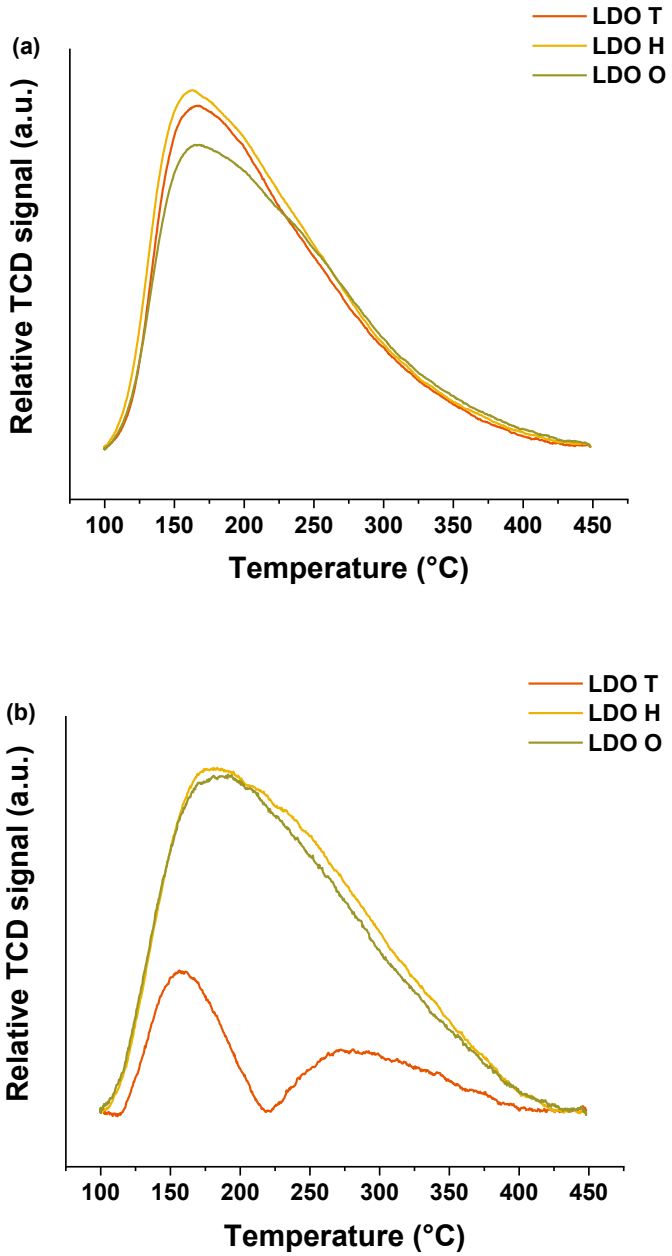


Figure 3.11 - (a) CO_2 and (b) NH_3 TPD curves of **LDO T**, **LDO H** and **LDO O**.

3.7 CO_2 adsorption on LDOs

The CO_2 adsorption capacity of the various solvent treated LDOs at 40 °C is shown in Figure 3.12 and the adsorption profiles are shown in Appendix A. The CO_2 adsorption values have been separated into chemisorption and physisorption. Physisorption is the adsorption due to Van der Waals interactions between CO_2 molecules and the

surface of the LDOs. Chemisorption is defined as the interactions resulting from the formation of chemical bonds to the surface.[24] Multilayer adsorption is possible for physisorption whereas only a monolayer is achievable for chemisorption. As a result, it was observed that CO_2 physisorption is always greater than that of chemisorption. **LDO W** showed a total CO_2 adsorption of 0.64 mmol g^{-1} (0.44 and 0.20 mmol g^{-1} for physisorption and chemisorption respectively). Overall, solvent treated LDOs show a CO_2 adsorption capacity increase of *ca*. 50% in both physisorption and chemisorption.

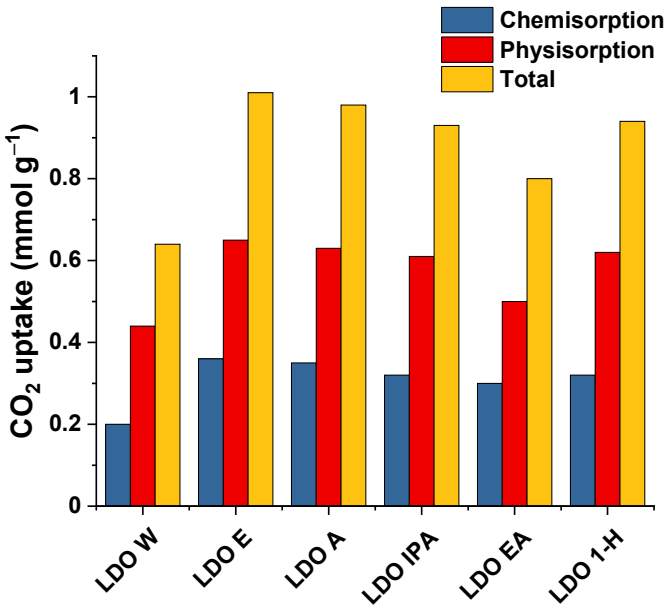
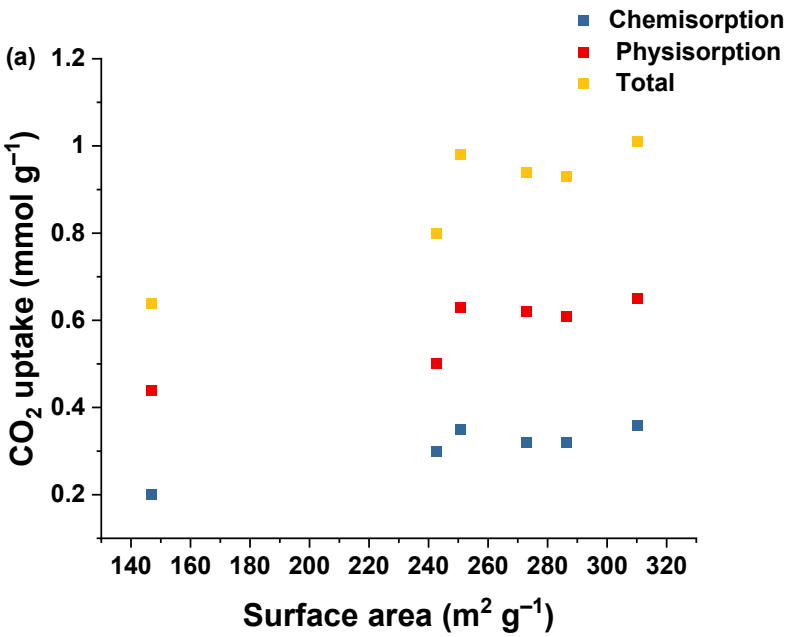


Figure 3.12 - CO_2 adsorption of LDO samples at 40 °C and 100 kPa.

LDO E exhibited the highest total CO_2 uptake of 1.01 mmol g^{-1}, a 58% increase relative to **LDO W**. This is higher than previously reported figures for CO_2 capture using LDOs under similar conditions. Sharma *et al.* have reported a CO_2 capture capacity of 0.38 mmol g^{-1} at 30 °C using a calcination temperature of 350 °C for a conventional water washed LDO while Shang *et al.* reported a CO_2 capture value of 0.83 mmol g^{-1} at 50 °C for an acetone-treated Mg_3Al CO_3 LDH after a pretreatment temperature of 180 °C.[25,26] The adsorption temperature used in this study is higher than

that used by Sharma *et al.*. This leads to a reduction in the physisorption value. **LDO EA** exhibited the lowest CO_2 uptake of 0.80 mmol g^{-1} amongst the solvent treated LDO samples tested. The chemisorption value of 0.30 mmol g^{-1} was comparable with the other solvent treated samples, but the physisorption figure has decreased due to the lower surface area.

The CO_2 adsorption per g correlates with the LDO N_2 BET surface area (Figure 3.13 (a)). The higher the surface area, the more active adsorption sites are exposed, leading to a higher CO_2 adsorption. CO_2 adsorption per g also correlates strongly with the measured pore volume (Figure 3.13 (b)).



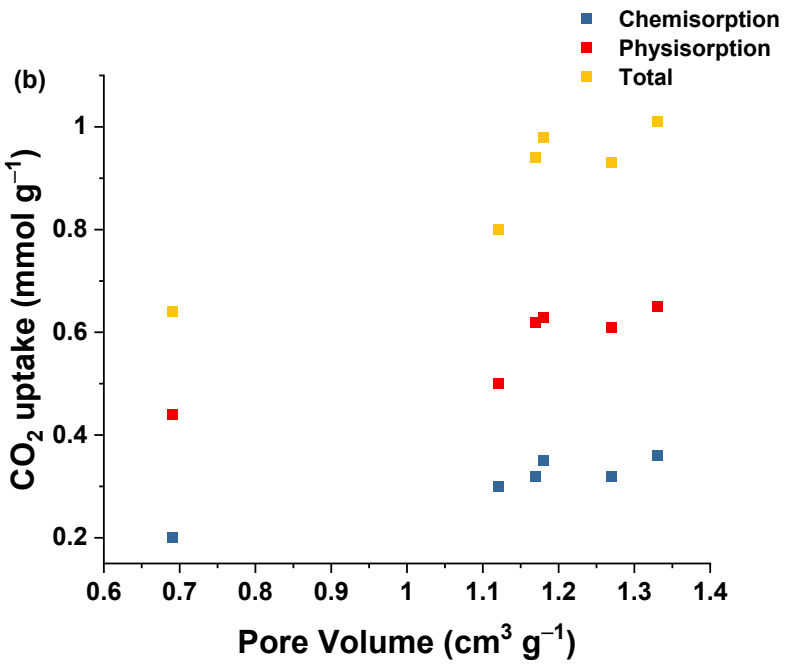


Figure 3.13 - CO_2 adsorption of LDOs as a function of (a) surface area and (b) pore volume.

There is a linear correlation (R = 0.94) relating the CO_2 adsorption per surface area to the ratio of total acidic to basic sites of the LDOs (Figure 3.14). This positive correlation indicates that a higher acid/base ratio is more favourable for CO_2 adsorption per surface area. It is worth noting that the measured acid sites involve the surface hydroxyl groups as shown in Scheme 3.1. These hydroxyl groups can participate in CO_2 adsorption via weak CO_2 bidentate bonding, however this bonding mode is not present in the CO_2 TPD due to the adsorption temperature of 100 °C.[7,17] This also agrees with the theory proposed in the Section 3.6, as the acid/base ratio is an indicator of at extent of solvent remaining on and blocking the surface. With a lower acid/base ratio, the active sites on the surface are blocked by adsorbed solvent molecules and therefore render the surface less active towards CO_2 adsorption.

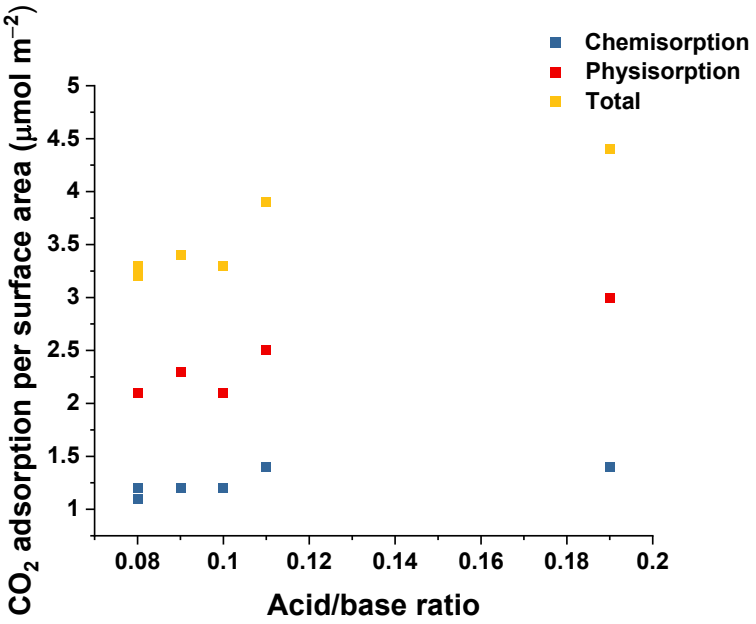


Figure 3.14 - CO_2 adsorption of LDO samples per surface area as a function of acid/base ratio.

3.8 Conclusions

A quantitative and comparative study of the basic and acidic features of conventional water washed and solvent treated LDHs and LDOs has been performed. Titration showed that solvent treatment leads to increases in Brønsted basicity in the LDHs but basic site density decreased as a result of higher surface areas, which would suggest the majority of basic sites are located on the edge of the sheets, as these do not change with exfoliation. In terms of Lewis basicity, all dehydrated LDH samples showed evidence for monodentate carbonate binding while only **LDH E** and **LDH 1-H** exhibited stretching vibrations assigned to bidentate carbonate bonding. These results show that changes in the Lewis basicity of LDHs can be achieved using the solvent treatment methods.

LDOs showed a general increase in total Brønsted basic sites and basic site density compared to the parent LDH. All solvent treated LDOs exhibited lower basic site densities compared to **LDO W**. All solvent treated LDOs showed no change in the distribution of basic strengths compared to **LDO W**. The NH_3 TPD desorption profiles for solvent treated

LDOs showed an elimination of the medium strength peak along with a reduction in intensity of the strong acidic peak, both of which involve NH_3 bonding to the surface metal sites. This evidence, along with the reduction in basic site densities of solvent treated samples, strongly suggests that solvent molecules coordinate to the cationic metal sites upon thermal treatment, which leads to blocking of active sites.

^{1}H and ^{27}Al ssNMR spectroscopy confirms the existence of an apical Al-OH species in the LDOs using OH containing dispersing solvents. LDH samples prepared by dispersion in toluene, hexane and octane, led to the confirmation of the hypothesis of acid site blocking due to the presence of electron donating functional groups in the dispersing solvents.

Solvent treated LDOs displayed an increase in CO_2 uptake capacity compared to conventional LDO (**LDO W**; 0.64 mmol g^{-1}). **LDO E** exhibited the highest total CO_2 uptake of 1.01 mmol g^{-1}, which represents a 58% increase compared with **LDO W** and it is believed to be the highest value for solvent treated LDOs reported in the literature. It was also discovered that CO_2 adsorption per surface area increases with an increasing acid/base ratio. Overall, this study has found that the acid/basic properties of LDH can be fine-tuned by using (AMO or AIM) solvent treatments, which offers promising opportunities in selective catalysis and adsorption.

3.9 Outlook

In the studies of this chapter, the solvents used, with the exception of the hydrocarbons, all contained electron donating groups. This allowed for the solvent molecules to interact with the metal centres on the surface of the layered materials. This was shown to affect the acidity by reducing the ability of the layered materials to interact with basic molecules. In the future, other solvent systems can be investigated, in particular haloalkanes and epoxides. These families of compounds are similar in structure to alcohols, but they more

readily undergo S_n2 reactions. This will, therefore, allow them to interact with the surface oxygens of the LDH, blocking it in the same manner in which the solvents in the current study block off the metal centres. Another method to modify the surface oxygens is through silane modification of LDHs, first developed by Chen *et al*.[27] and currently being further studied in the group. Muramatsu *et al*. have also developed tripodal ligands that bind onto the surface of an LDH through the hydroxyl groups.[14] These methods could potentially drastically change their basicity and as a result could affect their affinity towards basic molecules. This effect could increase the adsorption of molecules such as NH_3 and CO, therefore further improving their versatility. The ability to control the surface acidity/basicity of LDHs could enhance the performance of LDH catalyst supports in polymerisation reactions where it has been shown that acidic supports improve polymerisation productivity.[4]

3.10 References

1 M. Yang, O. McDermott, J.-C. Buffet and D. O'Hare, *RSC Adv.*, 2014, **4**, 51676–51682.
2 K. Ruengkajorn, V. Erastova, J.-C. Buffet, H. C. Greenwell and D. O'Hare, *Chem. Commun.*, 2018, **54**, 4394–4397.
3 J.-C. Buffet, Z. R. Turner, R. T. Cooper and D. O'Hare, *Polym. Chem.*, 2015, **6**, 2493–2503.
4 G. E. Hickman, C. M. R. Wright, A. F. R. Kilpatrick, Z. R. Turner, J.-C. Buffet and D. O'Hare, *Mol. Catal.*, 2019, **468**, 139–147.
5 M. C. I. Bezen, C. Breitkopf and J. A. Lercher, *Appl. Catal. A Gen.*, 2011, **399**, 93–99.
6 Federica Prinetto, G. Ghiotti, R. D. and and D. Tichit*, , DOI:10.1021/JP002715U.
7 J. I. Di Cosimo, V. K. Díez, M. Xu, E. Iglesia and C. R. Apesteguía, *J. Catal.*, 1998, **178**, 499–510.
8 H. A. Benesi, *J. Am. Chem. Soc.*, 1956, **78**, 5490–5494.
9 C. Walling, *J. Am. Chem. Soc.*, 1950, **72**, 1164–1168.
10 C. Chen, M. Yang, Q. Wang, J.-C. Buffet and D. O'Hare, *J. Mater. Chem. A*, 2014, **2**, 15102–15110.
11 Q. Wang and D. O'Hare, *Chem. Rev.*, 2012, **112**, 4124–4155.
12 K. Ruengkajorn, C. M. R. Wright, N. H. Rees, J.-C. Buffet and D. O'Hare, *Mater. Chem. Front.*, 2018, **2**, 2277–2285.
13 A. Navajas, I. Campo, G. Arzamendi, W. Y. Hernández, L. F. Bobadilla, M. A.

Centeno, J. A. Odriozola and L. M. Gandía, *Appl. Catal. B Environ.*, 2010, **100**, 299–309.
14 K. Muramatsu, Y. Kuroda, H. Wada, A. Shimojima and K. Kuroda, *Dalton Trans.*, 2018, **47**, 3074–3083.
15 R. W. Stevens, R. V. Siriwardane and J. Logan, *Energy & Fuels*, 2008, **22**, 3070–3079.
16 M. J. Hudson, S. Carlino and D. C. Apperley, *J. Mater. Chem.*, 1995, **5**, 323.
17 F. Prinetto, G. Ghiotti, R. Durand and D. Tichit, *J. Phys. Chem. B*, 2000, 11117–11126.
18 M. Bellotto, B. Rebours, O. Clause, J. Lynch, D. Bazin and E. Elkaïm, *J. Phys. Chem.*, 1996, **100**, 8535–8542.
19 J. M. Rimsza, E. G. Sorte and T. M. Alam, *ACS Omega*, 2019, **4**, 1033–1044.
20 G. Piedra, J. J. Fitzgerald, N. Dando, S. F. Dec and G. E. Maciel, *Inorg. Chem.*, 1996, **35**, 3474–3478.
21 C. M. R. Wright, K. Ruengkajorn, A. F. R. Kilpatrick, J.-C. Buffet and D. O'Hare, *Inorg. Chem.*, 2017, **56**, 7842–7850.
22 D. S. Breslow and N. R. Newburg, *J. Am. Chem. Soc.*, 1959, **81**, 81–86.
23 J. C. W. Chien, *J. Am. Chem. Soc.*, 1959, **81**, 86–92.
24 M. Kralik, *Chem. Pap.*, 2014, 1625–1638.
25 S. Shang, A. Hanif, M. Sun, Y. Tian, Y. S. Ok, I. K. M. Yu, D. C. W. Tsang, Q. Gu and J. Shang, *J. Hazard. Mater.*, 2019, **373**, 285–293.
26 U. Sharma, B. Tyagi and R. V. Jasra, *Ind. Eng. Chem. Res.*, 2008, **47**, 9588–9595.
27 C. Chen, J. C. Buffet and D. O'Hare, *Dalton Trans.*, 2020, **49**, 8498–8503.

Chapter Four- A study of the CO_2 capture performance of Mg_xAl LDHs and LDOs

4.1 Introduction

Due to their highly tuneable and customisable nature, LDHs and their derivatives have been used in a multitude of applications, from catalysts and flame retardant materials to drug carrier agents.[1–5] More recently, LDOs have been used as heterogeneous CO_2 sorption materials due to their inherent basicity.[6–8] Studies on effects of calcination temperature[9–11] and K-doping[12,13] on improving CO_2 capture performance have been previously published (Section 1.3.4), but not many have discussed how these effects have altered the surface chemistry of the material. Furthermore, the more subtle parameters such as calcination time and ramp rate have not yet been explored fully and in some cases, not reported in studies. Being able to optimise the calcination parameters for the base LDH material and understanding the change in surface chemistry with these changes should allow for the maximisation of their utility as CO_2 sorption materials.

In this chapter, the CO_2 capture performances of $[Mg_{0.66}Al_{0.34}(OH)_2](CO_3)_{0.17}$ LDH ($Mg_{1.9}Al$ W) calcined under different conditions by varying calcination temperature, calcination time and ramp rate, are investigated and optimised. The surface chemistry of the different samples is probed and characterised extensively using hydroxyl titration, solid state nuclear magnetic resonance (ssNMR) and temperature programmed desorption (TPD). The metal ratio is varied to observe its effect on the layered structure ($Mg_{2.5}Al$ W:

$[Mg_{0.72}Al_{0.28}(OH)_2](CO_3)_{0.14}$, $Mg_{3.2}Al$ W: $[Mg_{0.76}Al_{0.24}(OH)_2](CO_3)_{0.12}$, $Mg_{3.4}Al$ W: $[Mg_{0.77}Al_{0.23}(OH)_2](CO_3)_{0.115}$ and $Mg_{4.7}Al$ W: $[Mg_{0.79}Al_{0.21}(OH)_2](CO_3)_{0.105}$), surface chemistry and CO_2 capture performance. Finally, by combining the conditions for the best CO_2 capture results, an optimised Mg_xAl LDO system for CO_2 capture is described.

The nomenclature in this chapter is as follows: **Mg_xAl** (*x* denotes the Mg^{2+}/Al^{3+} ratio measured by ICP-MS) **W/E** (water washed or ethanol treated) **calcination temperature** (°C) - **calcination time** (h) - **ramp rate** (°C min^{-1})). For example, $Mg_{1.9}Al$ W 400-2h-5 stands for a $Mg_{1.9}Al$ water washed sample calcined at 400 °C for 2 h with a ramp rate of 5 °C min^{-1} (Figure 4.1).

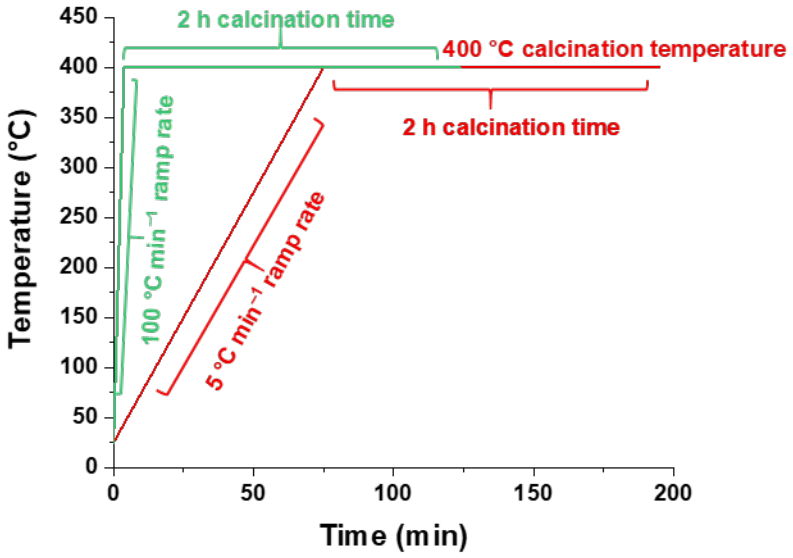


Figure 4.1 - Graphical illustration of calcination parameters of 400-2h-5 (red) and 400-2h-100 (green).

4.2 Experimental details

4.2.1 Synthesis of Mg_xAl W LDHs

Mg_xAl CO_3 W LDH was synthesised using the co-precipitation method adapted from a literature procedure.[14] $Mg(NO_3)_2.6H_2O$ and $Al(NO_3)_3.9H_2O$ were dissolved in 100 mL DI

water to make solution A, exact amounts, targeted and measured ratios are shown in Table 4.1. Na_2CO_3 (0.050 mol, 5.30 g) was then dissolved in another 100 mL DI water to make solution B. Solution A was added to solution B dropwise, while mixing at 375 rpm, over 1 h. The mixture was kept at pH 10 for the synthesis with the simultaneous addition of 4 M NaOH solution. When the addition of the solution A was completed and the final pH set to 10, the reaction was stirred for 24 h at room temperature. After the ageing process, the LDH product was washed with DI water until pH 7 and filtered. The product was left to dry overnight in a vacuum oven at room temperature.

Table 4.1 - Summary of amounts of metal nitrates added in Mg_xAl W LDH synthesis.

Sample	Targeted Mg^{2+}/Al^{3+} ratio	Measured Mg^{2+}/Al^{3+} ratio	$Mg(NO_3)_2$ added (g)	$Al(NO_3)_3$ added (g)
$Mg_{1.9}Al$ W	2	1.9	17.09	12.50
$Mg_{2.5}Al$ W	3	2.5	19.23	9.37
$Mg_{3.2}Al$ W	3.5	3.2	19.95	8.37
$Mg_{3.4}Al$ W	4	3.4	20.51	7.50
$Mg_{4.7}Al$ W	5	4.7	21.36	6.25

4.2.2 Synthesis of ethanol treated LDHs

Ethanol treated LDHs were synthesised using the AMO solvent treatment method adapted from a literature procedure.[14–17] $Mg_{1.9}Al$ CO_3, $Mg_{2.5}Al$ CO_3 and $Mg_{3.4}Al$ CO_3 LDH were prepared as described in the section above. After washing the LDH products with DI water until pH 7, special caution was taking to keep the LDH wet, and washed with 400 mL of ethanol and dispersed in another 400 mL of the same solvent and stirred vigorously for 4 h. The slurry was filtered and left to dry overnight in a vacuum oven at room temperature.

4.2.3 Surface OH number titration

The OH titrations were carried out by Dr Philip Kenyon and Ms Katherine Laney (University of Oxford) using a procedure adapted from literature.[18] 5 mg LDH and 10 mg $Mg(CH_2Ph)_2(THF)_2$ were mixed in 500 μL d_6-benzene containing $Si(SiMe_3)_4$ as an internal standard (c = 6.23 mmol dm^{-3}) in a Young's tap NMR tube. Production of toluene resulting from protonation of the benzyl by the surface hydroxyl groups was monitored by ^1H NMR spectroscopy and the toluene methyl resonance integrated against that of $Si(SiMe_3)_4$ to obtain the hydroxyl number.

4.2.4 CO_2 measurements

CO_2 capture readings were carried out on a Micromeritics 3Flex with a chemisorption attachment or a Perkin Elmer TGA 8000. All samples used in CO_2 adsorption were calcined *in situ* under N_2 atmosphere at the conditions described. For samples run using the Micromeritics 3Flex, 100 mg of sample was placed in the machine for the specified calcination. The sample was cooled to 40 °C at a ramp of 30 °C min^{-1} and left to evacuate to a vacuum at 40 °C for 3 h. The CO_2 measurements were then carried out twice at 40 °C under 100% CO_2 atmosphere. The first value provides the total adsorption value, the second physisorption. The difference between the two values provides the chemisorption value.

4.3 Varying calcination temperature

The calcination temperature was varied between 100–600 °C and tested for CO_2 adsorption. The XRD patterns of all the samples can be seen in Figure 4.2. $Mg_{1.9}Al$ W 100-2h-100 exhibits the typical LDH structure, with a d_{003}-spacing of 7.84 Å (2θ = 11.3°). As the calcination temperature increases, the LDH becomes dehydrated, leading to a decrease in the interlayer spacing observed in $Mg_{1.9}Al$ W 300-2h-100 to 6.77 Å (2θ = 13.1°) while the

(003) Bragg reflection experiences a slight peak broadening, suggesting a reduction in crystallinity. This is due to the removal of surface and interlayer water molecules leading to the reduction of the hydrogen bonding between water molecules and hydroxyl groups on the layered sheets.[19,20] This removal of water molecules has also been shown to reduce the bonding of the metal hydroxides, which is balanced the formation of bonds to the interlayer carbonates.[21] $Mg_{1.9}Al$ W 200-2h-100 exhibited an intermediate pattern with both phases of LDHs due to being partially dehydrated. $Mg_{1.9}Al$ W 300-2h-100 also exhibited broad Bragg reflections at $2\theta = 43.5°$ and 62.3°, corresponding to the (200) and (220) Bragg reflections in an MgO structure. As the temperature is increased further from 300 °C, the samples all clearly displayed typical Mg_xAl LDO patterns exhibiting the characteristic (111), (200) and (220) Bragg reflections observed in MgO structures with the slight preferred growth orientation of (200).[22] Figure 4.3 shows the N_2 BET surface area and pore volume of the materials. $Mg_{1.9}Al$ W 500-2h-100 displayed the highest surface area and pore volume, at 294 $m^2\ g^{-1}$ and 1.21 $cm^3\ g^{-1}$ respectively. A significant increase in surface area and pore volume can be observed between $Mg_{1.9}Al$ W 300-2h-100 and 400-2h-100, which corresponds to the transition from the LDH structure to LDO, as shown in their XRD patterns (Figure 4.2). A similar trend in can be observed in the surface areas reported by Bellotto *et al.* for a Mg_2Al LDH calcined between 150 and 500 °C with a ramp rate of 10 °C min^{-1}.[23]

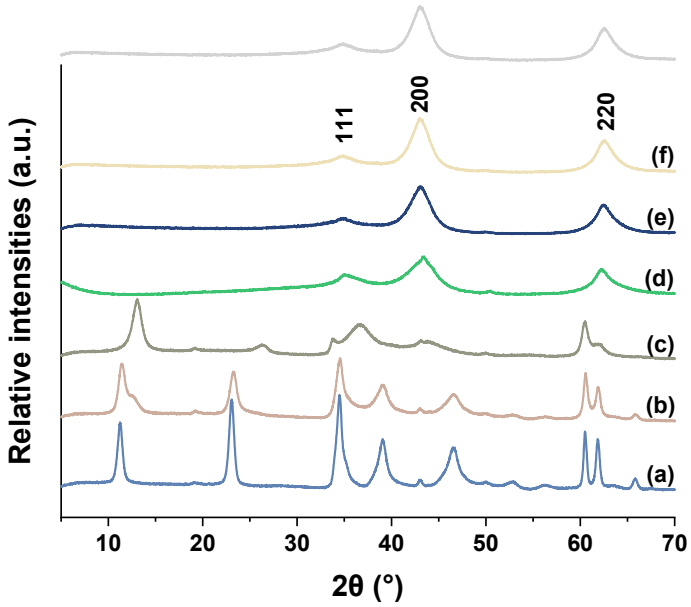


Figure 4.2 - XRD patterns of $Mg_{1.9}Al$ W (a) 100-2h-100, (b) 200-2h-100, (c) 300-2h-100, (d) 400-2h-100, (e) 500-2h-100 and (f) 600-2h-100.

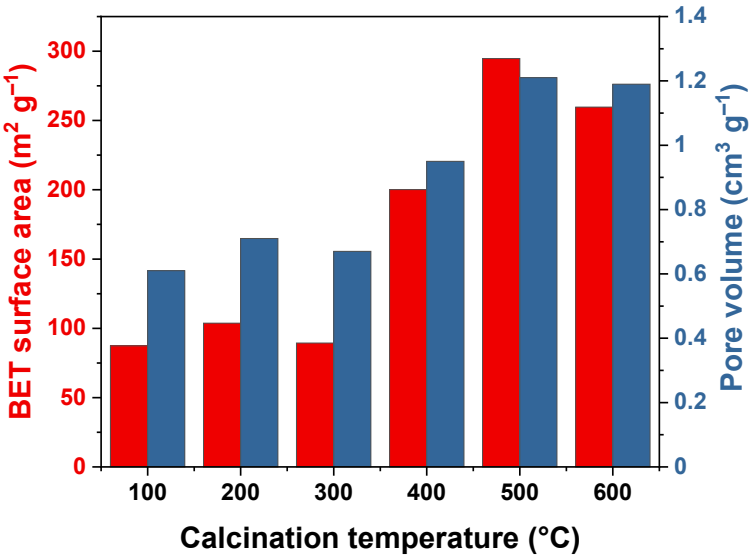


Figure 4.3 - N_2 BET surface area and pore volume of $Mg_{1.9}Al$ W X-2h-100 samples.

As temperature studies for total CO_2 uptake have previously been investigated extensively,[24–27] the CO_2 uptake has been separated into physisorption and chemisorption (Figure 4.4), which will allow for a much more in-depth investigation into the different factors contributing towards CO_2 adsorption for $Mg_{1.9}Al$ layered materials. The separation

of adsorption type was achieved by carrying out two consecutive CO_2 measurements. The first measurement provides the total adsorption value and the second the physisorption value. The difference between the values provides the chemisorption value.

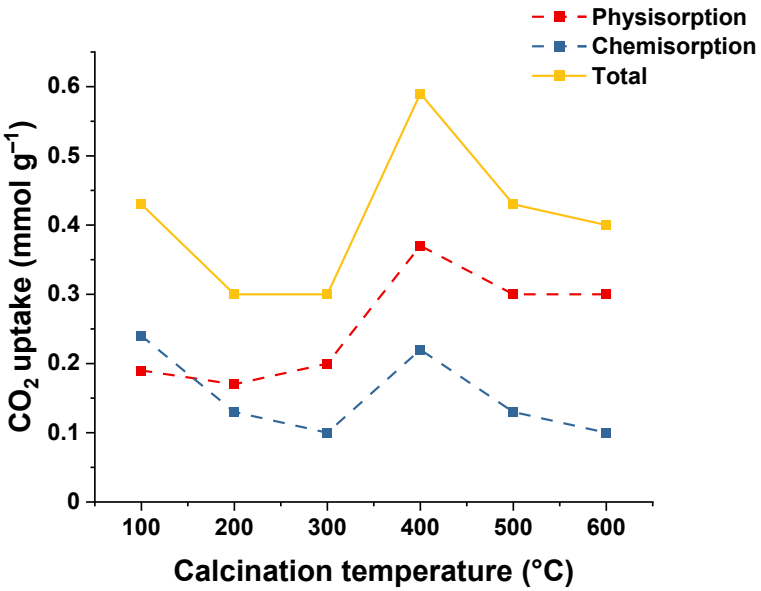


Figure 4.4 - CO_2 adsorption for $Mg_{1.9}Al$ W X-2h-100 samples at 40 °C and 100 kPa.

The total CO_2 capture value decreases as the calcination temperature was increased between 100–300 °C when the LDH becomes more dehydrated. It has been shown in literature that the addition of water improves CO_2 uptake due to the ability to dissolve CO_2.[10,28] The optimal calcination for CO_2 uptake is 400 °C, with a total adsorption of 0.59 mmol g^{-1} which corresponds to other findings in the literature for Mg_xAl LDHs.[26] Upon further breakdown into the different adsorption components, $Mg_{1.9}Al$ W 400-2h-100 also showed the highest physisorption of 0.37 mmol g^{-1}. $Mg_{1.9}Al$ W 100-2h-100 exhibited the highest chemisorption value of 0.24 mmol g^{-1}, exceeding even that of $Mg_{1.9}Al$ W 400-2h-100 (0.22 mmol g^{-1}). By comparing the samples calcined at 100, 200 and 300 °C, a trend of decreasing chemisorption can be observed. This could be related to the level of dehydration in these LDH samples as observed in the XRD patterns as it has been shown that the addition of H_2O improved the

CO_2 capture of LDOs.[10,27,29] However, due to their structure remaining as LDHs, the adsorption mechanism could differ slightly from that of an LDO. It could also arise from the dissolution of CO_2 in interlayer water. Wang *et al*. reported for LDHs and LDOs, physisorption is captured on an amorphous surface, while the more crystalline regions are responsible for chemisorption.[30] The slight broadening of the (003) Bragg reflection as calcination temperature increases between 100–300 °C indicates a loss of crystallinity of the LDH structure, which would result in a decrease in chemisorption. The physisorption fraction also increases slightly between $Mg_{1.9}Al$ W 200-2h-100 and $Mg_{1.9}Al$ W 300-2h-100. This is due to the presence of the more amorphous MgO structure in $Mg_{1.9}Al$ W 300-2h-100 as observed in the XRD pattern.

Further analysis of the relationship between adsorption and surface area of the different calcination conditions shows a different trend (Figure 4.5). The highest value for chemisorption per surface area exhibited was 2.7×10^{-3} mmol m^{-2} for $Mg_{1.9}Al$ W 100-2h-100, more than double that of the next highest value (1.3×10^{-3} mmol m^{-2} for $Mg_{1.9}Al$ W 200-2h-100), again clearly demonstrating the improvement that H_2O has on the CO_2 capture performance of LDHs/LDOs. Both chemisorption and physisorption per surface area for samples calcined at 500 and 600 °C displayed the lowest values. This can be explained through the balance between surface hydroxyl numbers and surface area. Although $Mg_{1.9}Al$ W 500-2h-100 and $Mg_{1.9}Al$ W 600-2h-100 possess the highest surface areas (294.7 and 259.7 m^2 g^{-1} respectively), they also showed the lowest residual wt% post calcination (51.9% and 50.5% respectively). This reduction in residual weight% can be attributed to the loss of carbonate anions as well as hydroxyl groups, as higher calcination temperature would lead to a more complete dehydroxylation process, which was demonstrated by Wright *et al*. using the hydroxyl titration method.[18] It has been shown that

hydroxyl groups are responsible for a bonding mode in CO_2 adsorption (Scheme 4.4).[31,32] Therefore 400 °C was used as the temperature for further optimisation of calcination conditions.

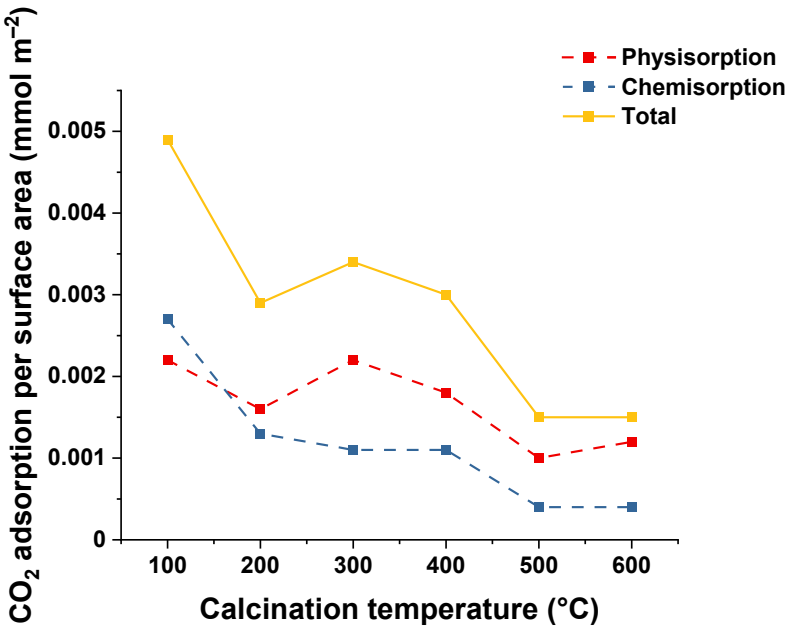


Figure 4.5 - CO_2 adsorption per surface area for $Mg_{1.9}Al$ W X-2h-100 samples at 40 °C and 100 kPa.

4.4 Varying the heating ramp rate

The heating ramp rate was varied between 5 and 100 °C min^{-1} up to 400 °C to observe the effects on in physical, chemical properties and CO_2 capture performance of the LDO. As shown in Figure 4.6, all calcined samples displayed the typical XRD pattern of LDOs obtained from the heat treatment of Mg_xAl LDHs, indicating similar bulk structures of crystalline periclase (MgO) and an amorphous background due to an alumina phase.

The increase in heating ramp rate, however, altered some of the other physical and chemical properties of the LDOs. The N_2 BET surface area increases steadily from 147.2 m^2 g^{-1} for

$Mg_{1.9}Al$ W 400-2h-5 to 200.1 m^2 g^{-1} for $Mg_{1.9}Al$ W 400-2h-100 (Figure 4.7). This is a result of the breaking of LDO platelets as measured from SEM images (Figure 4.8).

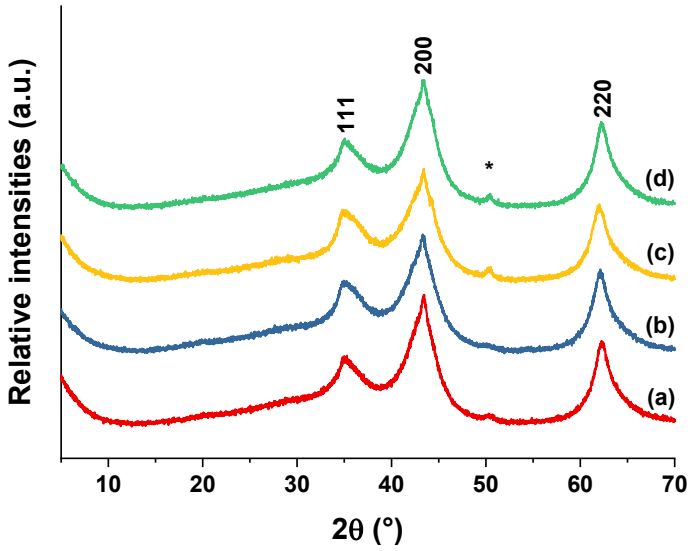


Figure 4.6 - XRD patterns of $Mg_{1.9}Al$ W (a) 400-2h-5, (b) 400-2h-20, (c) 400-2h-50 and (d) 400-2h-100. (*) denotes peak from sample holder.

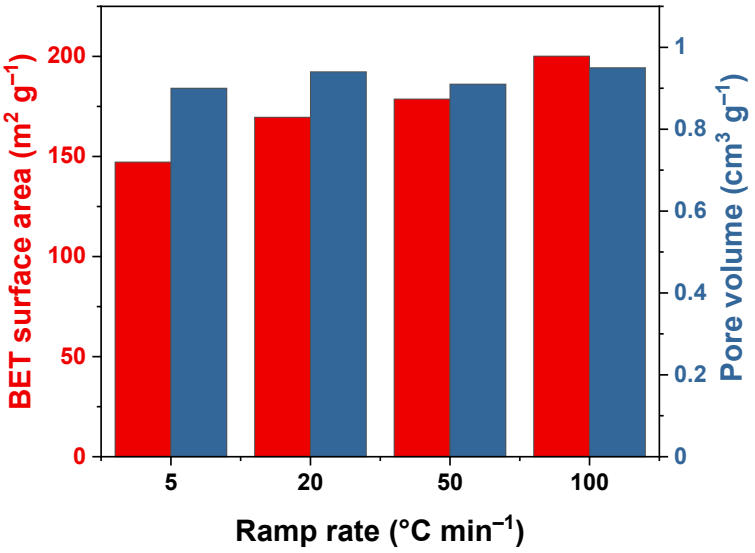


Figure 4.7 - N_2 BET surface area and pore volume of $Mg_{1.9}Al$ W 400-2h-X samples.

Particle measurements were carried out over 10 unobscured platelets imaged using SEM and averaged. For $Mg_{1.9}Al$ W 400-2h-5, the sample has an approximate average size and platelet

thickness of 144±15 and 27±3 nm respectively. As the ramp rate increases, the particle size decreases to 101±12 and 85±4 nm for a ramp of 50 and 100 °C min^{-1} respectively, this is accompanied by a decrease in thickness (24±2 and 18±2 nm respectively). This could be a result of the faster ramp causing a more violent breakdown of the cluster due to the more rapid transitions through the different stages of thermal decomposition.[23] The change in pore volume is less drastic and remains relatively unchanged at *ca* 0.9 cm^3 g^{-1}, exhibiting no clear trend with ramp rate.

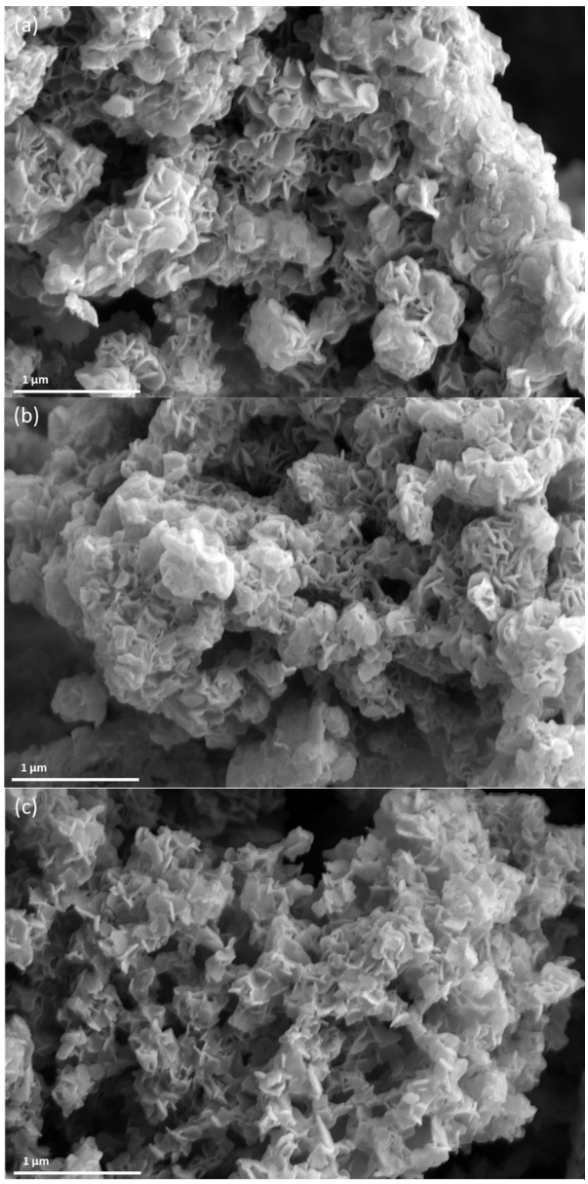


Figure 4.8 - SEM images of $Mg_{1.9}Al$ W (a) 400-2h-5, (b) 400-2h-50 and (c) 400-2h-100.

As shown in Figure 4.9, CO_2 adsorption increases steadily from 0.35 mmol g^{-1} for 5 °C min^{-1}, the lowest value for any sample calcined at 400 °C, to 0.59 mmol g^{-1} for 100 °C min^{-1}, displaying a 69% increase in uptake with samples calcined at the same temperature. The increase in CO_2 capture is not solely due to an increase in surface area, as there is still an increase in capacity when normalised to surface area (Figure 4.10). The more rapid decomposition is shown to result in a less complete dehydroxylation (Figure 4.11). This was probed using a hydroxyl titration adapted from Wright *et al.* (reaction schematic shown in Scheme 4.1),[18] originally performed by Fripiat *et al.* to determine the hydroxyl content in silica gel.[33] The hydroxyl number is shown to double from $Mg_{1.9}Al$ W 400-2h-5 to $Mg_{1.9}Al$ W 400-2h-100 (0.60 and 1.26 mmol g^{-1} respectively). The increase persists even when normalised to surface area. This is expected as a slower ramp rate would allow for a more gradual change in calcination environment which makes sure the decomposition goes through each stage of the process.

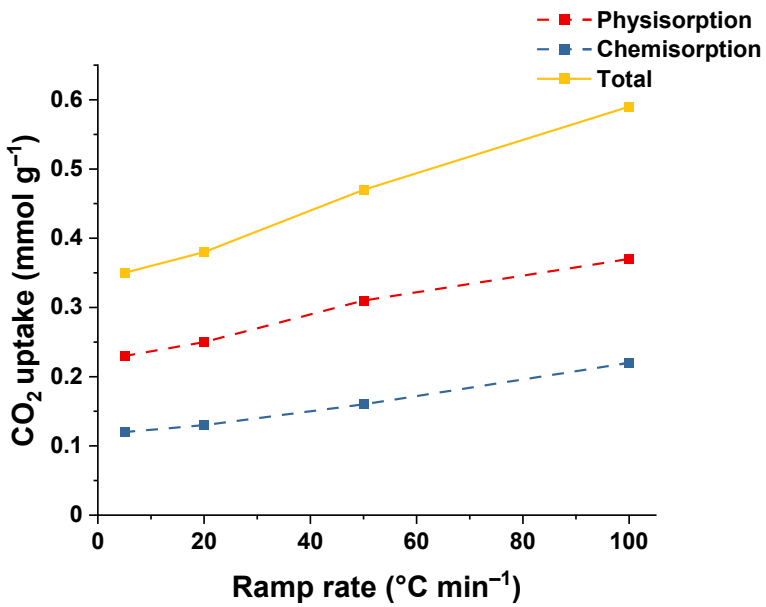


Figure 4.9 - CO_2 adsorption for $Mg_{1.9}Al$ W 400-2h-X samples at 40 °C and 100 kPa.

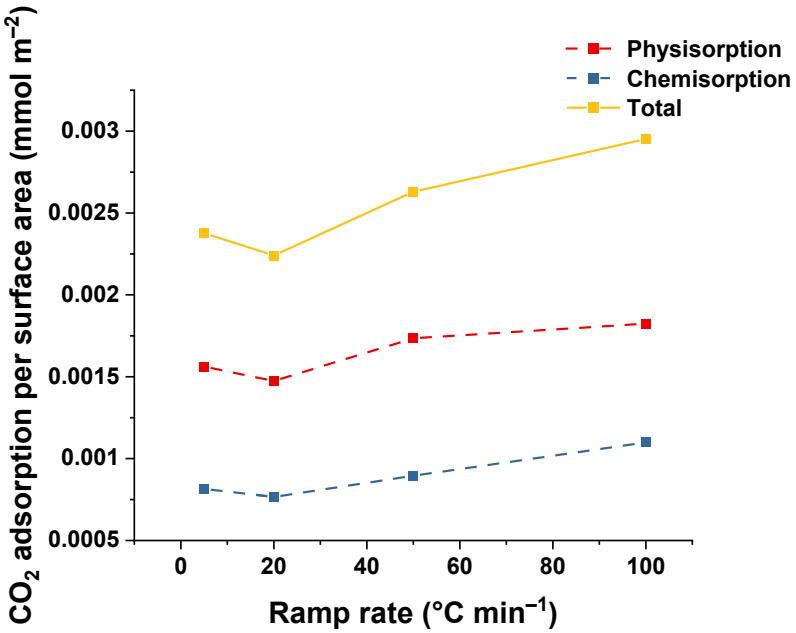


Figure 4.10 - CO_2 adsorption per surface area for $Mg_{1.9}Al$ W 400-2h-X samples at 40 °C and 100 kPa.

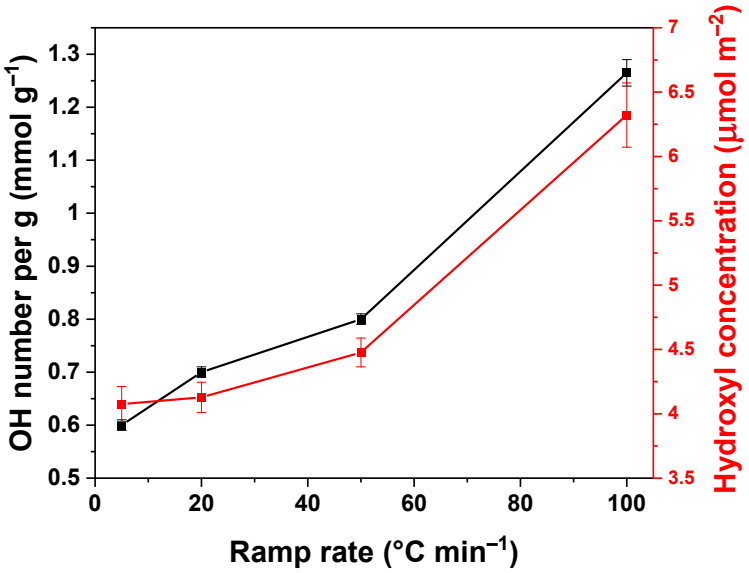
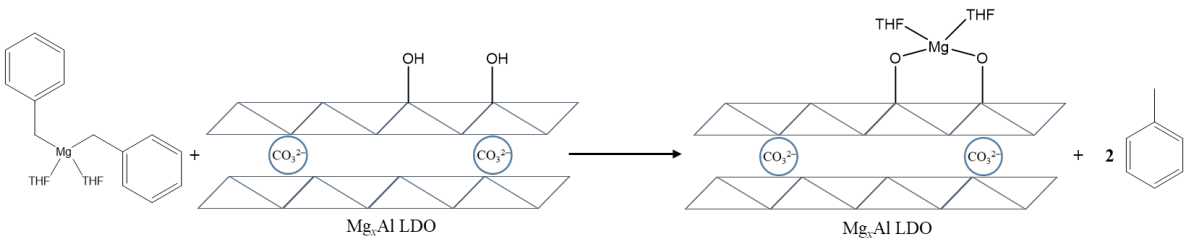


Figure 4.11 - Hydroxyl numbers for $Mg_{1.9}Al$ W 400-2h-X samples. Error bars obtained from repeating measurement.

Figure 4.12 shows the ^{1}H MAS NMR of the samples, compared to that of a conventional crystalline LDH ($Mg_{1.9}Al$ W LDH). The LDH sample (Figure 4.12 (a)) displays the characteristic resonances seen in literature: the surface OH resonance, neighbouring two

Mg^{2+} and one Al^{3+} centres at δ = 1.2 ppm and the resonance at δ = 4.8 ppm arises from the surface and interlayer water molecules.[34] When calcined, several resonances arise between δ = 0–3 ppm, which corresponds to the OH resonances in the bulk MgO structure with differing neighbouring metals, as reported by Rimsza *et al*. in a partially hydroxylated MgO structure.[34,35] As the ramp rate increases, a resonance at δ = 7.3 ppm becomes more prominent. This resonance is not accounted for by any Mg-OH signals as those have been shown to have lower chemical shifts in MgO structures and has not been previously reported in LDH-related structures.[35] Proton signals from related Al-OH materials, such as gibbsite and bayerite (different forms of $Al(OH)_3$), have chemical shifts of *ca* 5 ppm, while boehmite (γ-AlO(OH)) displays a signal at δ = 8.2 ppm.[36] While none of the values from literature correspond directly to the resonance observed in our samples, this resonance is currently speculated to be related to an Al-OH species. The Al-OH species can help provide an extra bonding motif for CO_2 molecules via the weak bicarbonate bonding mode,[37] partially explaining the increase in CO_2 capture ability even when normalising to surface area.



Scheme 4.1 - Schematic representation of the reaction between $Mg(CH_2Ph)_2(THF)_2$ and Mg_xAl LDO to obtain the hydroxyl number.

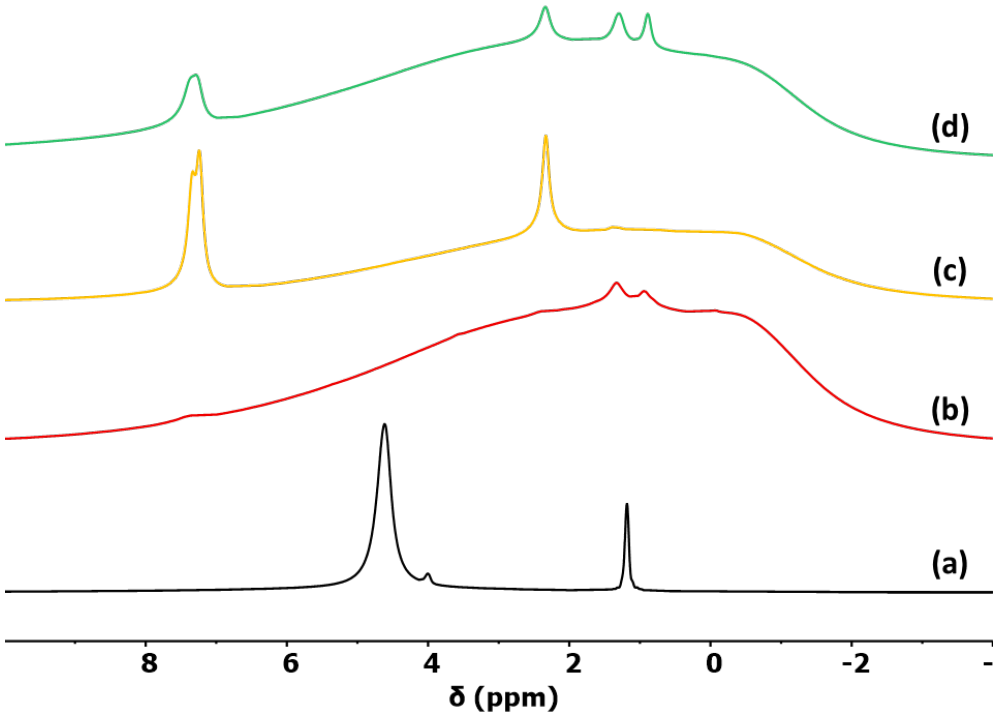
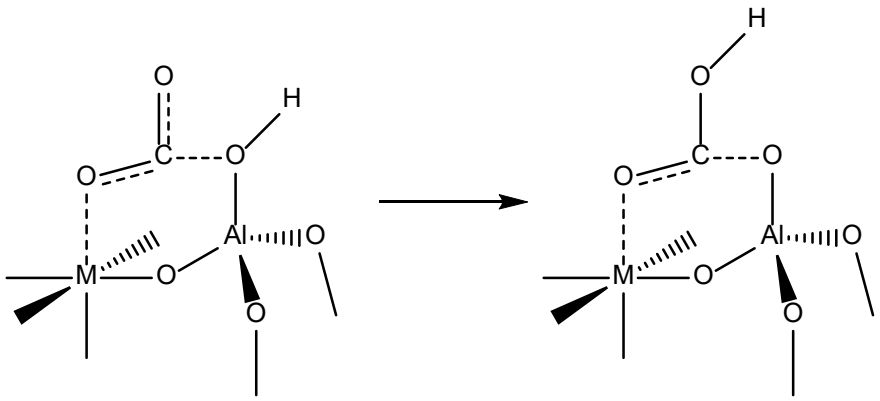


Figure 4.12 - ^{1}H MAS NMR of $Mg_{1.9}Al$ W (a) LDH, (b) 400-2h-5, (c) 400-2h-50 and (d) 400-2h-100.

Pan *et al.* have used DFT calculations to prove that a partially hydroxylated surface of γ-Al_2O_3 results in an increase in CO_2 capture ability compared to their dried analogue.[38] In this study, it was discovered for a dry γ-Al_2O_3, the CO_2 molecule binds favourably on the surface in a bidentate manner and preferentially bonds to Al^{3+} centres of lower coordination due to the lesser steric hindrance. On a partially hydroxylated surface, it was shown that when bound in close proximity to a proton, the bound CO_2 molecule undergoes proton transfer to form a bound bicarbonate moiety. The overall reaction energy for proton transfer was very favourable (–0.97 eV), while the transition state was calculated to be slightly endothermic (0.42 eV). This demonstrates that the conversion of surface bound CO_2 molecules can easily and favourably form bicarbonates in the presence of hydroxides or excess water on the surface of a partially hydrated alumina. This was also shown to be observed in other sorbent materials such as zeolites.[39] Due to the similar environment of an apical hydroxyl group bonded to an Al^{3+} centre, the following hypothesis is proposed: the presence of an Al-OH in

LDOs with higher ramp rates leads to the promotion of a proton transfer reaction with favourable thermodynamics (Scheme 4.2). This in turns leads to an increase in the overall CO_2 capture ability of the material.



Scheme 4.2 - Proposed mechanism for proton transfer process of CO_2 molecule bound to the surface tetrahedral Al^{3+} centre of an LDO in close proximity to a hydroxyl group.

There is also a slight change in C environment for the remaining interlayer carbonate anions as seen in the ^{13}C NMR spectrum (Figure 4.13). Compared to the resonance at δ = 171 ppm observed in the parent $Mg_{1.9}Al$ W LDH corresponding to the CO_3^{2-} anions, there is a small shift to lower frequency when the sample is calcined at ramp rate of 50 °C min^{-1} to δ = 167 ppm. This could be due to the difference in the environment of the CO_3^{2-} by the dehydration and dehydroxylation process.

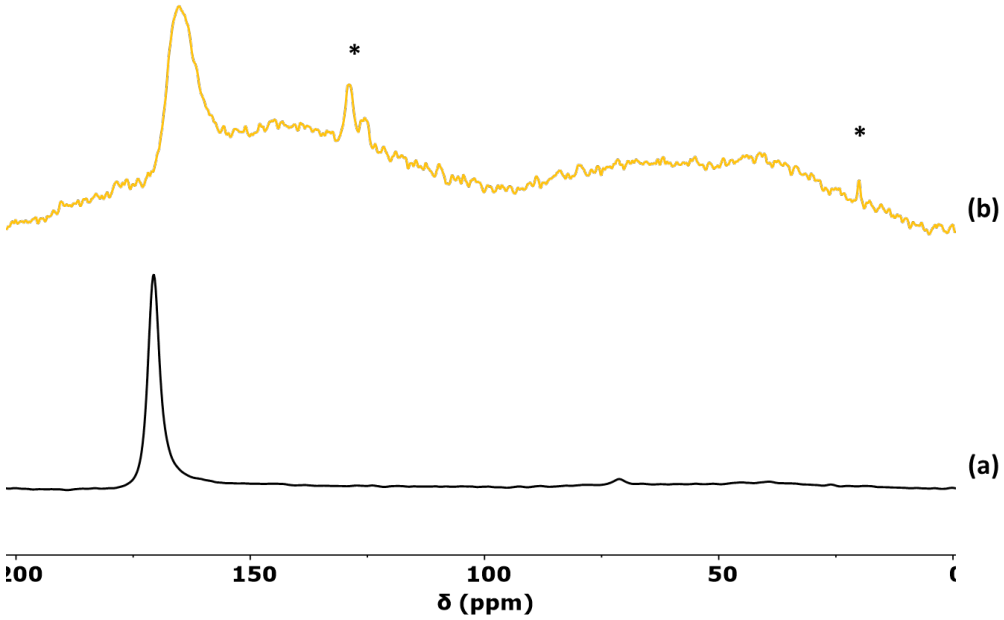


Figure 4.13 - ^{13}C CPMAS NMR of $Mg_{1.9}Al$ W (a) LDH and (b) 400-2h-50. (*) denotes impurities.

The ^{27}Al DPMAS shows there is a small change in Al^{3+} environments that results from the increase in ramp rates (Figure 4.15). Upon calcination of an LDH, loss of hydroxyl groups leads to a change in some Al^{3+} centres from an edge sharing octahedral brucite structure (δ = –25–30 ppm) to a tetrahedral coordination environment (δ = 30–100 ppm) (Figure 4.14). This change in coordination number is a result of the expulsion of Al^{3+} from the bulk MgO structure upon calcination, which has an O_h coordination around each metal centre. The expelled Al^{3+} ions form tetrahedrally coordinated aluminium oxide environments, which share 3 oxygen atoms with the surface of the bulk oxide structure (Figure 4.14).[23]

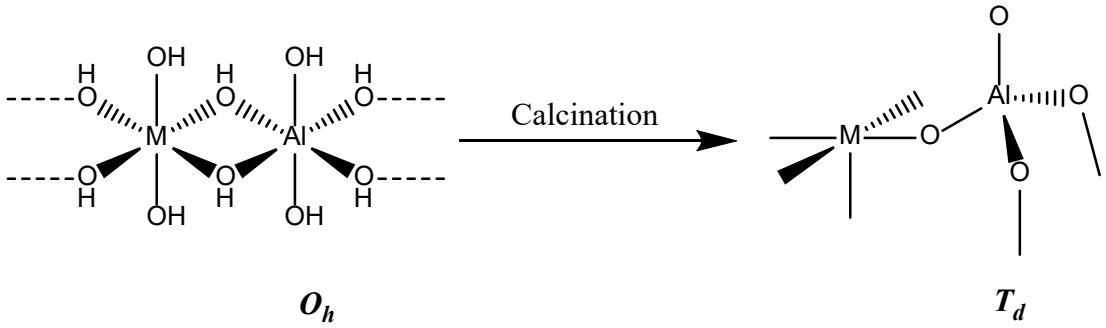


Figure 4.14 - Graphic representation of the change in Al^{3+} centres from octahedrally coordinated to tetrahedrally coordinated upon calcination from LDH to LDO.

It can be observed that in the LDH form, 100% of the Al^{3+} centres are in an octahedral environment in the edge-sharing octahedral layers. When calcined using a ramp rate of 5 °C min^{-1}, the T_d% is 62% which is the highest of the tested ramp rates. When calcined at higher ramp rates of 50 and 100 °C min^{-1}, the T_d population drops slightly to 58%. This could be due to a kinetic effect, however could be within error margins. The higher temperature ramp rates may not allow for a complete migration of Al^{3+} cations and so thermal equilibrium is not reached. Comparing heating ramp rates of 5 and 100 °C min^{-1}, the slower heating ramp sample results in an extra 30 minutes of calcination time above 200 °C (Figure 4.1), which is the temperature at which migration starts to occur.[6,20,23]

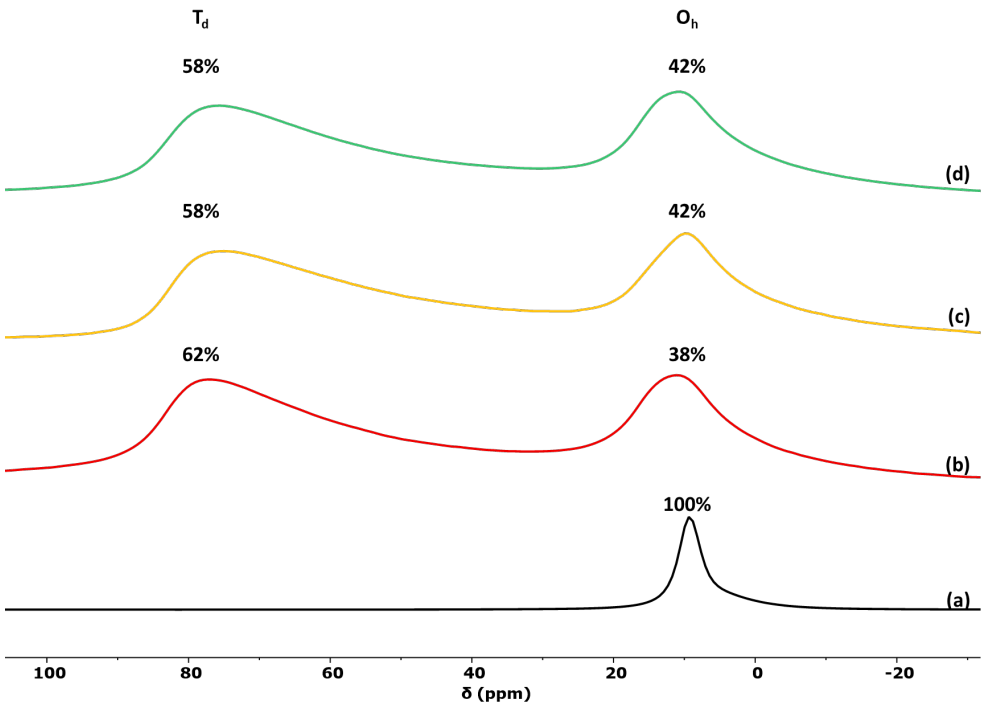
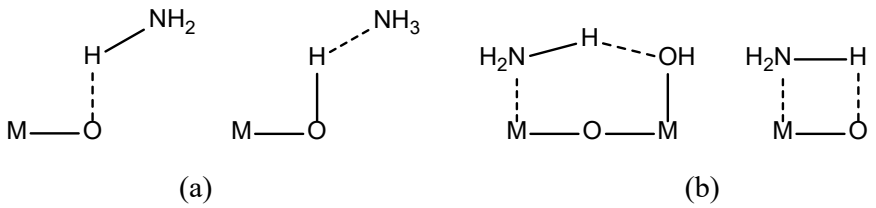
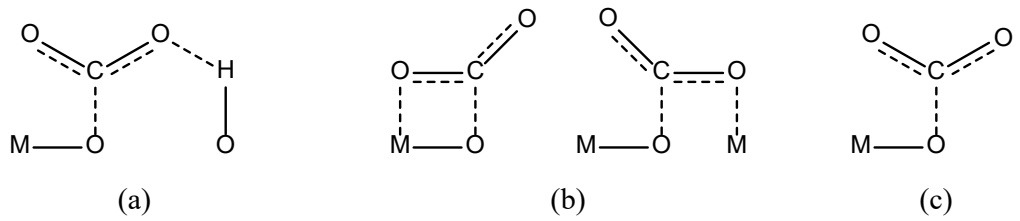


Figure 4.15 - ^{27}Al DPMAS NMR of $Mg_{1.9}Al$ W (a) LDH, (b) 400-2h-5, (c) 400-2h-50 and (d) 400-2h-100. δ = –25–30 ppm has been assigned to O_h centres while δ = 30–100 ppm has been assigned to T_d centres.

Further physicochemical changes as a result of increasing the calcination ramp rate can be observed in the acidity and basicity of the LDOs, as probed by TPD. CO_2 was used as the probe molecule for Lewis basicity while NH_3 was used for acidity. The resulting desorption profiles for CO_2 and NH_3 (Figure 4.16 (a) and (b)) have been broken down and deconvoluted into separate peaks, according to analysis carried out by Di Cosimo *et al.* and Prinetto *et al.* respectively via *in situ* FTIR,[32,40] and displayed in Table 4.2. The different bonding modes are depicted in Scheme 4.3 and Scheme 4.4.



Scheme 4.3 - NH_3 bonding modes on the surface of an LDO. Bond angles do not reflect actual bond angles in the structure.



Scheme 4.4 - CO_2 bonding modes on the surface of an LDO. Bond angles do not reflect actual bond angles in the structure.

It was discovered that for NH_3 TPDs, the signal can be deconvoluted into two features (deconvolution of TPD signal can be seen in Appendix B). The first peak, which is centred at 150 °C, is the result of hydrogen bonding to surface hydroxyl groups and also between surface oxygens and N-H's. Bonding motifs between N and surface metals result in a signal which only desorbs at higher temperature. A change can be observed in the NH_3 profiles. As TPD is measured through the desorption of molecules over a range of temperatures, the technique is only comparable between samples calcined and prepared at the same temperature. Therefore, the samples calcined at different temperatures could not be measured and compared in the same acid/base discussion. Both total acid sites and acid site densities increase with increasing ramp rate, with the highest of 1.34 mmol g^{-1} observed for 100 °C min^{-1}, over a sevenfold increase compared to the sample prepared at 5 °C min^{-1} (Table 4.2). The peak corresponding to the hydrogen bonding mode (centred at 150 °C) increases with increasing ramp rates, which correlates well with hydroxyl numbers obtained from the titration method, but with lower values (0.38 mmol g^{-1} and 0.60 mmol g^{-1} respectively for $Mg_{1.9}Al$ W 400-2h-5). This could be due to the elevated adsorption temperature leading to less thorough saturation. For $Mg_{1.9}Al$ W 400-2h-5, the vast majority of the acidic sites belong to the metal bonding motif, only 15% of the total acidic sites are attributed to the weaker OH bonding mode (Table 4.3). The weak acidic peak increases in population when the ramp rate increases to 20 °C min^{-1} to 40% and stabilises when the ramp rate further increases to 50 and 100 °C min^{-1} (44%).

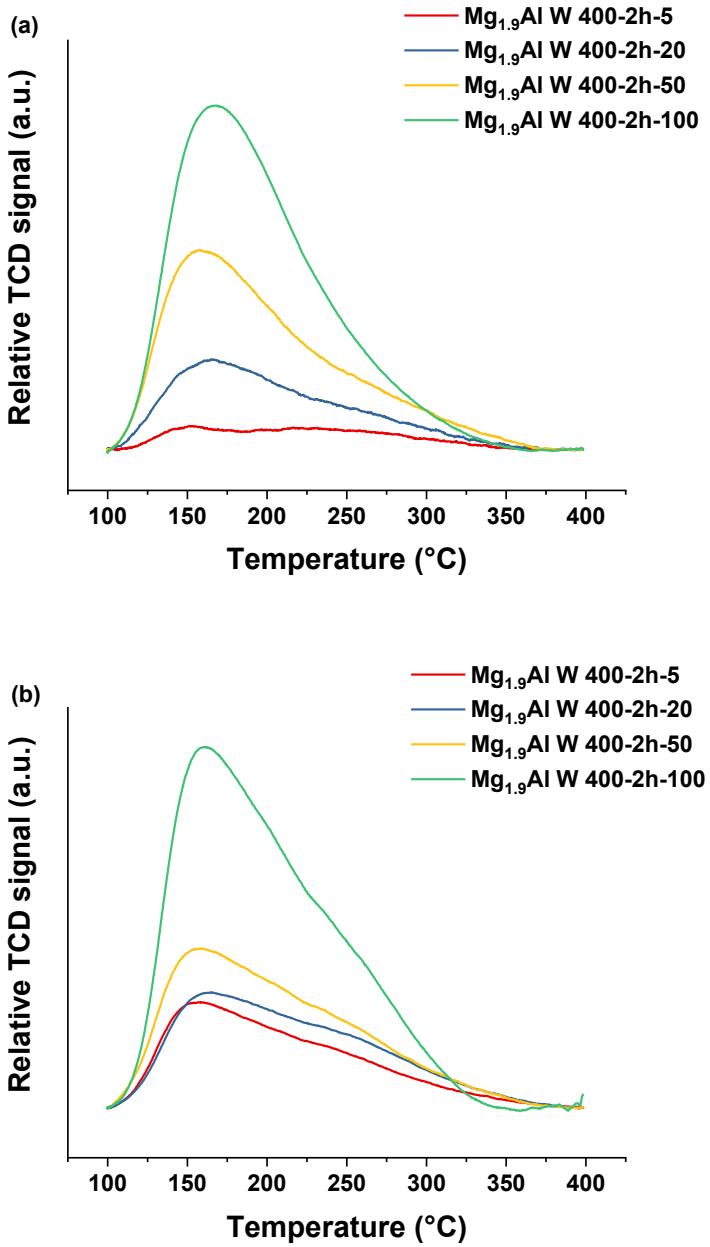


Figure 4.16 - (a) NH_3 and (b) CO_2 TPD of $Mg_{1.9}Al$ W 400-2h-X samples.

Table 4.2 - Summary of TPD data of $Mg_{1.9}Al$ W 400-2h-X samples.

Sample	Total basic sites (mmol g^{-1})	Basic site density (µmol m^{-2})	Total acidic sites (mmol g^{-1})	Acidic site density (µmol m^{-2})	Acid/base ratio
400-2h-5	1.21	8.22	0.17	1.15	0.14
400-2h-20	1.46	8.61	0.40	2.36	0.27
400-2h-50	1.89	10.58	0.84	4.70	0.44
400-2h-100	3.65	18.24	1.34	6.70	0.37

Table 4.3 - Deconvolution of TPD data of $Mg_{1.9}Al$ W 400-2h-X samples.

Sample	Basic site weighting (%)		Acid site weighting (%)	
	Bidentate	Monodentate	OH peak	Metal peak
400-2h-5	15	85	33	67
400-2h-20	41	59	30	70
400-2h-50	44	56	32	68
400-2h-100	44	56	35	65

For the CO_2 TPD, the desorption curves can be deconvoluted into bicarbonate, bidentate and monodentate peaks.[32] Due to the high adsorption temperature of 100 °C, the bicarbonate bonding mode is not present as it was shown to be removed at this temperature using *in situ* FTIR.[32] Both total basic sites and basic site densities displayed an increase with increasing ramp rate. $Mg_{1.9}Al$ W 400-2h-100 displayed three times the number of basic sites of $Mg_{1.9}Al$ W 400-2h-5 (3.65 and 1.21 mmol g^{-1} respectively). The desorption of monodentate basic peak shifts to a lower temperature for $Mg_{1.9}Al$ W 400-2h-100 compared to the lower ramps. All probe molecules were completely desorbed at 350 °C for $Mg_{1.9}Al$ W 400-2h-100 whereas desorption was still occurring up until 400 °C for the samples calcined at slower

ramp rates. This corresponds to a weakening of the monodentate basic site. The distribution between the 2 peaks also undergoes slight changes. With the slower ramps, the strong basic site peak accounts for *ca* 70% of the total measured basic sites. However, when calcined with 100 °C min^{-1} ramp rate, this population decreases to 65%. This suggests that even though there is a drastic increase in total basic sites, the sites exposed at higher ramp rates are those of a weaker bidentate nature.

In conclusion, a ramp rate of 100 °C min^{-1} to 400 °C led to the formation of a smaller LDO particles with increased surface area. As a result of the higher ramp rate, more hydroxyl groups remain on the surface of the LDO, leading to the observation of a novel ^{1}H NMR resonance (δ = 7.3 ppm). This is hypothesised to correspond to an apical OH group on a tetrahedral Al^{3+}, which results in a more favourable adsorption thermodynamics of CO_2, leading to increased CO_2 capture.

4.5 Varying calcination time

With the calcination temperature of 400 °C, calcination time was varied between 1 h, 2 h, 3 h and 6 h. Firstly, there is a drastic difference in structure between the sample calcined for 1 h and the others. By examining the XRD patterns, it can be observed that $Mg_{1.9}Al$ W 400-1h-100 still maintained some of its LDH structure, as shown by the presence of weak (003), (006) and (009) Bragg reflections at 2θ = 12.5°, 26.9° and 36.3° respectively (Figure 4.17). The d_{003} spacing of $Mg_{1.9}Al$ W 400-1h-100 is 7.30 Å, a slight decrease from the 7.59 Å observed for the as-prepared $Mg_{1.9}Al$ W LDH. This is due to the removal of water from the interlayer region. The (110) Bragg reflection at 2θ = 61.0°, gives a = 3.04 Å, that is maintained compared to the as-prepared $Mg_{1.9}Al$ W LDH, which further suggests the phase change from a brucite structure to an MgO structure has not occurred. The other samples

with longer calcination times displayed the characteristic Bragg reflections of (111), (200) and (220) of an MgO structure. The reflection intensities suggest a preference of crystal growth in the *ab* plane.[22]

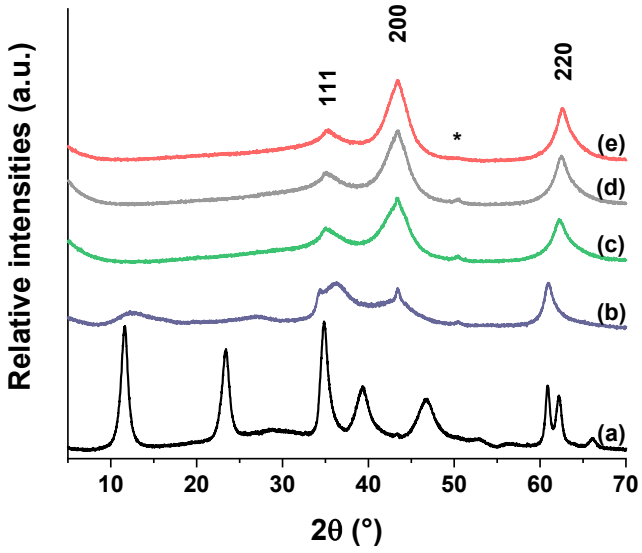


Figure 4.17 - XRD patterns of $Mg_{1.9}Al$ W (a) LDH, (b) 400-1h-100, (c) 400-2h-100, (d) 400-3h-100 and (e) 400-6h-100. (*) denotes peak from sample holder.

As the calcination time increases, the N_2 BET surface area increases, at first rather dramatically from 124 $m^2\ g^{-1}$ after 1 h to 200 $m^2\ g^{-1}$ after heating for 2 h, then steadily to 240 $m^2\ g^{-1}$ after 6 h. The increase after 3 h of calcination could be due to the more thorough removal of carbonate ions leading to more extensive delamination. The pore volume remained relatively unaffected by the calcination time with all samples maintaining a value of *ca* 0.9 $cm^3\ g^{-1}$ (Figure 4.18). The surface hydroxyl number can be seen to increase from 1.15 mmol g^{-1} for 1 h to 1.62 mmol g^{-1} for 6 h (Figure 4.19), mimicking the trend displayed in the surface areas of the sample. This is due to the higher surface area exposing more hydroxyl groups for the organomagnesium reagent to react with during the OH titrations. Converting the results to OH number per m^2 provides a more revealing general trend: the highest hydroxyl concentration belongs to $Mg_{1.9}Al$ W 400-1h-100 with 8.80 μmol m^{-2}. This

is due to the sample maintaining a partial LDH structure post-calcination as demonstrated in its XRD pattern. Then as calcination time increases, the values become comparable after 2h (*ca* 6.5 μmol m^{-2}). This is as expected as a prolonged calcination time would lead to a more complete decomposition of the LDO.

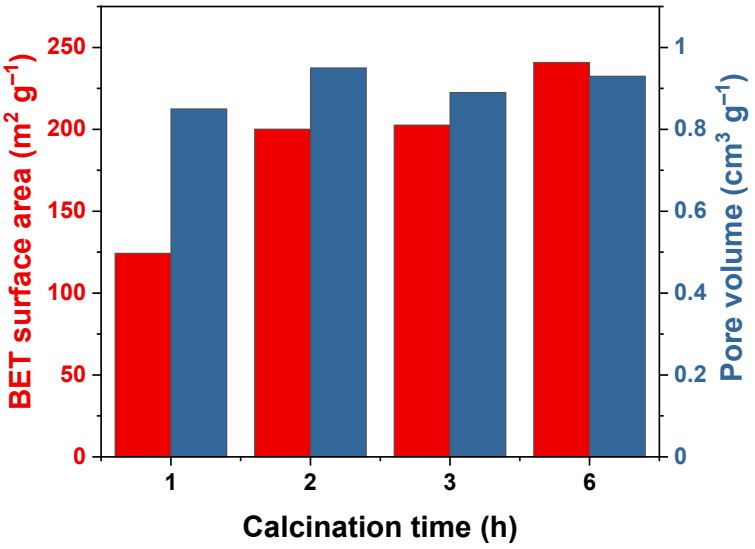


Figure 4.18 - N_2 BET surface area and pore volume of $Mg_{1.9}Al$ W 400-X-100 samples.

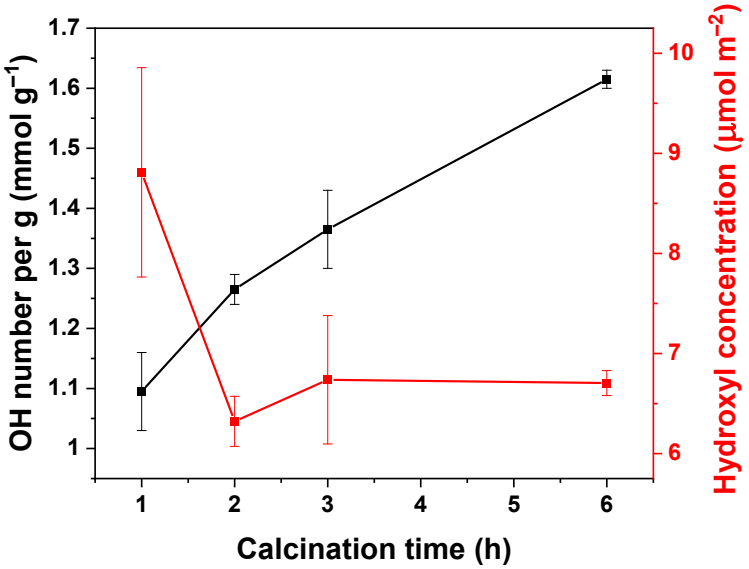


Figure 4.19 - Hydroxyl numbers for $Mg_{1.9}Al$ W 400-X-100 samples.

For CO_2 capture, it was found that the value increases between heating for 1 and 2 h. The CO_2 capture performance then decreases at the longer calcination times of 3 h and 6 h (Figure 4.20). 1 h, 3 h and 6 h displayed similar capture values at *ca* 0.4 mmol g^{-1}. The sample calcined for 2 h ($Mg_{1.9}Al$ W 400-2h-100), in contrast, displayed a CO_2 capture value of 0.59 mmol g^{-1}, almost a 50% increase from the other samples. This agrees with other literature reports of shorter calcination periods leading to improved CO_2 capture: Gao *et al.* demonstrated an optimal calcination time of 2 h for Mg_2Al LDOs.[26] $Mg_{1.9}Al$ W 400-1h-100 displayed lowered CO_2 capture value compared to $Mg_{1.9}Al$ W 400-2h-100 due to part of the material maintaining a dehydrated LDH structure, which as shown in $Mg_{1.9}Al$ W 200-2h-100 and $Mg_{1.9}Al$ W 300-2h-100, is less active as a CO_2 capture material compared to LDOs. The CO_2 adsorption per surface area is shown to decrease with increasing calcination time (Figure 4.21). Exact comparisons with literature is challenging due to the variation in pre-treatment and testing conditions. CO_2 capture values of 0.33 mmol g^{-1} (400 °C, 2 h). 0.25 mmol g^{-1} (450 °C, 5 h) have been reported by Manohara *et al.* and Zhu *et al.* respectively for MgAl LDHs, however in each case the ramp rate was not specified.[41,42]

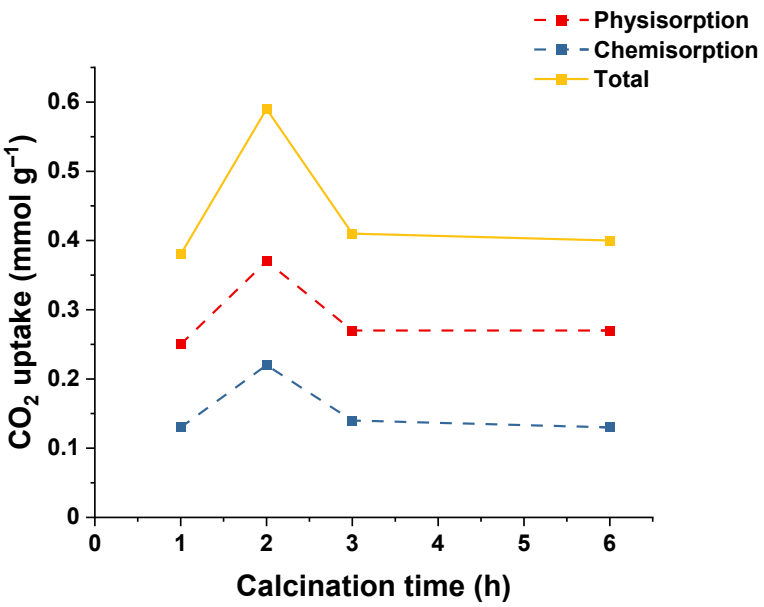


Figure 4.20 - CO_2 adsorption for $Mg_{1.9}Al$ W 400-X-100 samples at 40 °C and 100 kPa.

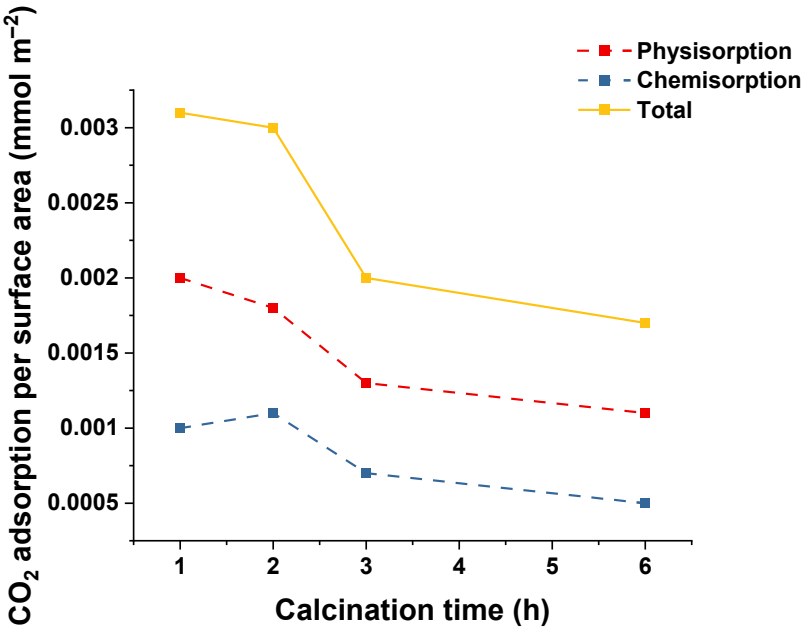


Figure 4.21 - CO_2 adsorption per surface area for $Mg_{1.9}Al$ W 400-X-100 samples at 40 °C and 100 kPa.

Varying calcination time also led to changes in their acidity and basicity (Figure 4.22). The sample calcined for 2 h possessed the highest total acidic site at 1.34 mmol g^{-1} (Table 4.4). 1 h calcination led to the lowest acidity of 1.10 mmol g^{-1}. The acid site density decreases

with increasing calcination time, from 8.85 μmol m^{-2} for 1 h to 5.44 μmol m^{-2} for 6 h (Table 4.5).

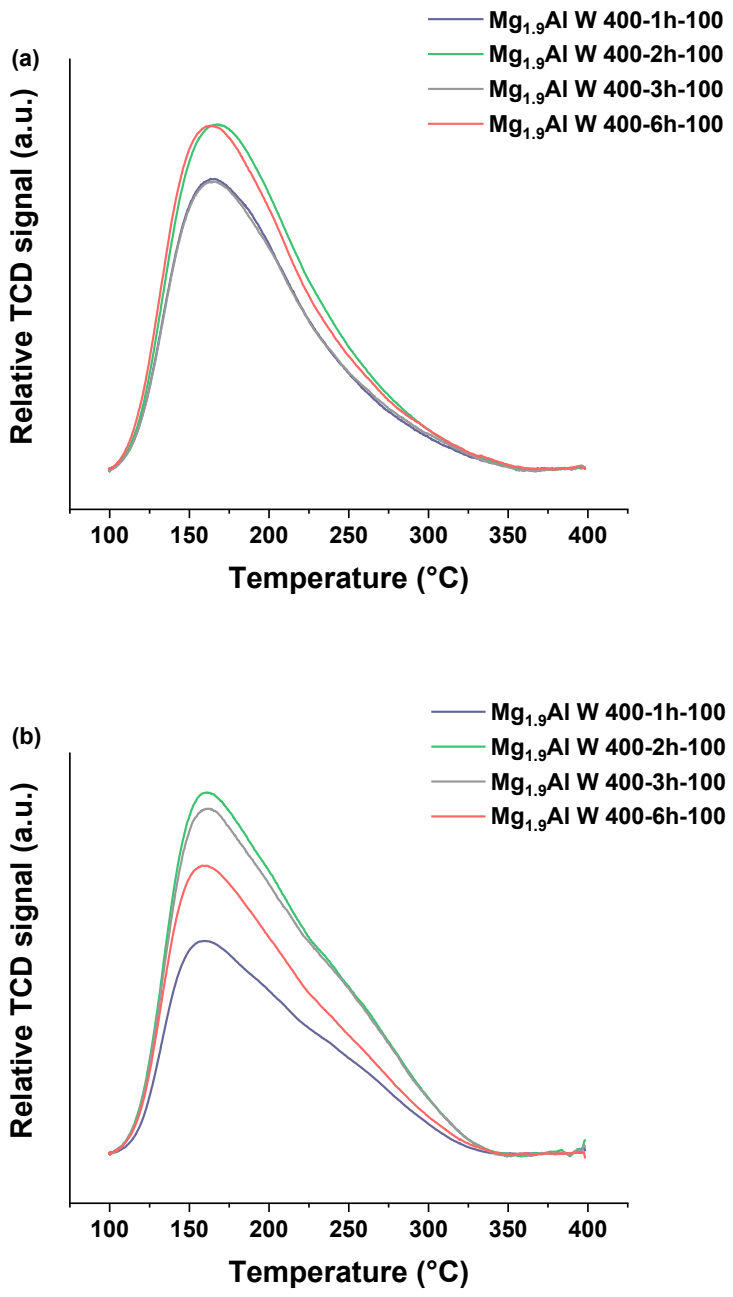


Figure 4.22 - (a) NH_3 and (b) CO_2 TPD of $Mg_{1.9}Al$ W 400-X-100 samples.

Table 4.4 - Summary of TPD data of $Mg_{1.9}Al$ W 400-X-100 samples.

Sample	Total basic sites (mmol g^{-1})	Basic site density (µmol m^{-2})	Total acidic sites (mmol g^{-1})	Acidic site density (µmol m^{-2})	Acid/base ratio
400-1h-100	2.14	17.22	1.10	8.85	0.51
400-2h-100	3.65	18.24	1.34	6.70	0.37
400-3h-100	3.56	17.57	1.11	5.48	0.31
400-6h-100	2.86	11.87	1.31	5.44	0.46

Table 4.5 - Deconvolution of TPD data of $Mg_{1.9}Al$ W 400-X-100 samples.

Sample	Basic site weighting (%)		Acid site weighting (%)	
	Bidentate	Monodentate	OH peak	Metal peak
400-1h-100	35	65	45	55
400-2h-100	35	65	44	56
400-3h-100	35	65	46	54
400-6h-100	37	63	44	56

$Mg_{1.9}Al$ W 400-2h-100 displayed the highest number of basic sites as determined by CO_2 TPD (3.65 mmol g^{-1}). The basicity increases sharply between calcination times of 1 and 2 h, then steadily decreases with prolonged calcination. This reflects the trend observed in their chemisorption CO_2 capture performance. Basic site densities of these samples also reflect a similar trend, but displayed a more sudden decrease with the sample calcined for 6 h. Compared to other samples, $Mg_{1.9}Al$ W 400-6h-100 displayed a slight reduction in the monodentate peak, centred at 220 °C. This peak reflects the strong basic sites on the surface and has a monodentate bonding motif. This is in contrast to the bidentate bonding mode seen in the weaker basic site, which gives rise to the peaked centred at 160 °C. Chizallet *et al.*,

through the use of DFT calculations, suggested that the difference in the basic strength of surface oxygens on MgO correlated to their coordination environment: a lower oxygen coordination number leads to an increase in basicity due to more increased concentration of the lone pair density.[43] Such lower coordination numbers are brought about by surface defects such as edges and corners (Figure 4.23). The decrease in the CO_2 TPD when calcined for 6 h suggests that prolonged calcination time could lead to more ordering on the surface of the LDO, allowing for more oxygens to migrate to more coordinatively saturated environments.

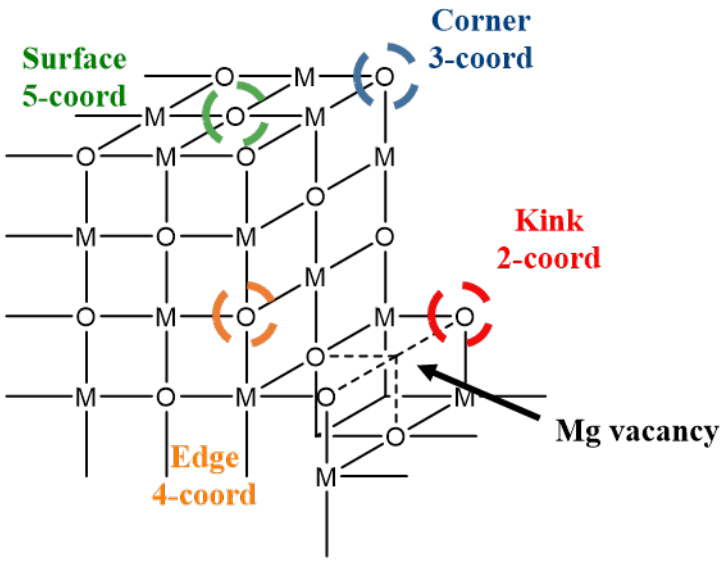


Figure 4.23 - Schematic representation of corner oxygen (blue), edge oxygen (orange) and kink oxygen (red) defects compared to surface oxygen (green) in an MgO structure.

A trend can be extrapolated when comparing the acid/base ratio of all $Mg_{1.9}Al$ W samples calcined at 400 °C (Figure 4.24). It was previously reported in Chapter Two that a positive correlation between CO_2 capture and acid/base ratio was observed.[31] This was observed for acid/base ratio < 0.2. With a wider range of values now collected, a more complete relationship can be observed. When the acid/base ratio is low, the corresponding CO_2 capture value is also low. This is due to the reduced OH bonding mode for NH_3 which also

contributes to the overall CO_2 uptake through the bicarbonate bonding motif (not captured by CO_2 TPD due to the high adsorption temperature (100 °C) used to avoid reconstruction of LDOs through the potential moisture in the carrier gas). At a high acid/base ratio (> 0.4), the CO_2 capture performance is again reduced. This is because CO_2 is fundamentally an acidic molecule, therefore too high an acidic site concentration would present a less favourable surface for the CO_2 molecule to interact with. This could also be due to the formation of coordinatively unsaturated acidic metal sites leading to surface defects, which could cause the reduced ability of the adjacent basic oxygens to interact with the linear CO_2 molecule. When the ratio is between 0.2 and 0.4, there is an increase in CO_2 capture performance, with the optimum ratio at 0.37 for $Mg_{1.9}Al$ W 400-2h-100. This medium ratio allows for a balance between the number of acidic and basic sites which allows for the adequate hydroxyl participation in the bicarbonate bonding mode without oversaturating the surface with the less favourable interactions of the CO_2 molecules and acidic sites.

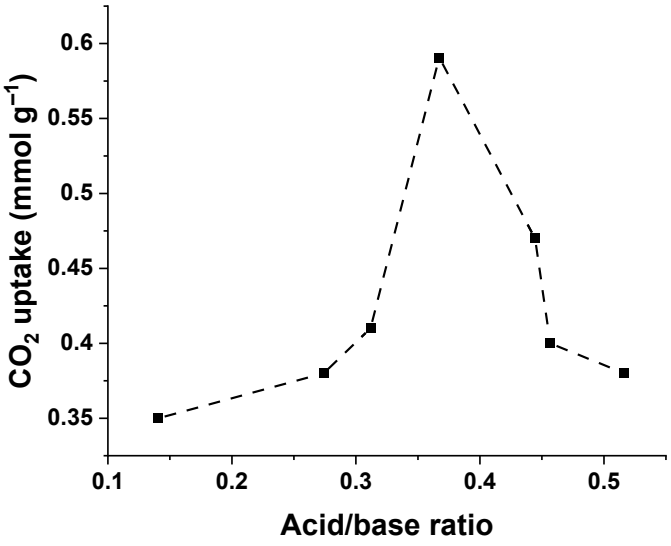


Figure 4.24 - CO_2 uptake (mmol g^{-1}) as a function of acid/base ratio for $Mg_{1.9}Al$ W calcined at 400 °C.

4.6 Varying Mg^{2+}/Al^{3+} ratio

A series of LDHs with Mg^{2+}/Al^{3+} ratio varied between 1.9 and 4.7 were used in the following study, the Mg^{2+}/Al^{3+} ratio for each sample was determined by ICP-MS. The calcination conditions were fixed at 400-2h-100. The XRD patterns of the LDHs and their LDOs are displayed in Figure 4.25 and Figure 4.28 respectively. The lattice parameter *a/b* exhibited a linear correlation with Mg^{2+} content ($R^2 > 0.99$) (Figure 4.26), increasing from 3.04 to 3.08 Å with increasing Mg^{2+} content, obeying Vegard's Law, which states that the lattice parameter is a weighted average of the constituents.[44] The lattice parameter *a/b* is the measurement of the metal-metal distance, therefore as Mg^{2+} possesses a larger ionic radius than that of Al^{3+}, and as XRD is a measurement of the bulk structure, the increase of Mg^{2+} content led to an increase in the average lattice parameter.

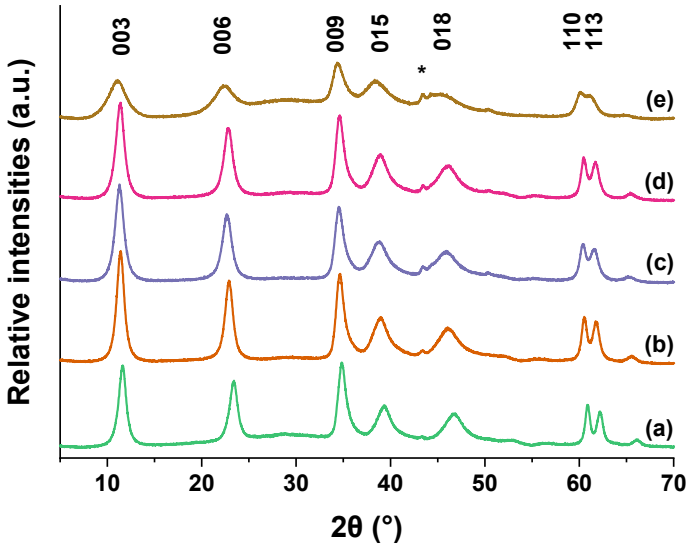


Figure 4.25 - XRD patterns of (a) $Mg_{1.9}Al$, (b) $Mg_{2.5}Al$, (c) $Mg_{3.2}Al$, (d) $Mg_{3.4}Al$ and (e) $Mg_{4.7}Al$ W LDHs. (*) denotes reflection from sample holder.

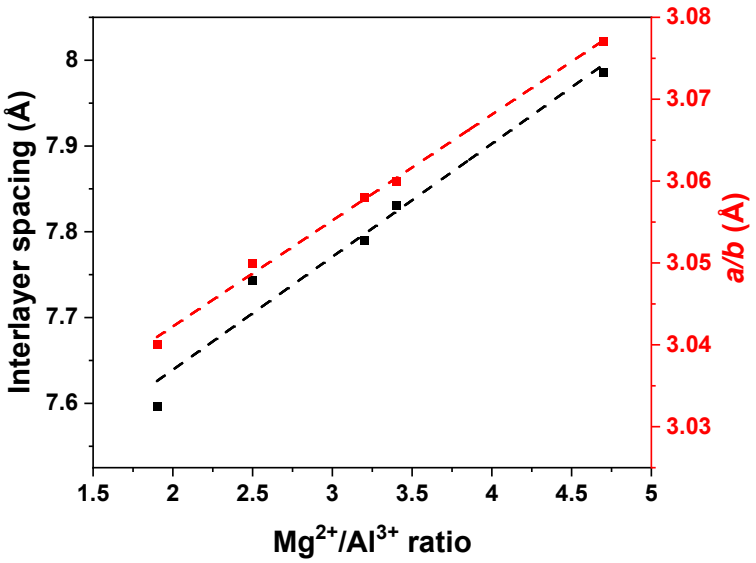


Figure 4.26 - Variation of interlayer spacing and *a/b* lattice parameter of LDHs as a function of Mg^{2+}/Al^{3+} ratio.

An increase in the interlayer spacing can also be observed (7.60 to 7.99 Å). As the Mg^{2+} content increases, less and less CO_3^{2-} ions are needed to balance the excess charge induced by Al^{3+}. This leads to a decrease in electrostatic interactions in the interlayer region, allowing for the cationic layers to separate. There is a slight deviation from linearity which could be due to the variations in solvation content leading to a change in interlayer distances.[45]

The crystallinity of the LDHs was also affected by the metal content. $Mg_{4.7}Al$ W LDH displayed significantly reduced crystallinity compared to other LDHs in the series, as shown by the crystal domain length (CDL) using d_{003} calculated by using the Scherrer equation (Figure 4.27). As the Mg^{2+} increases, there is an initial decrease in CDL between $Mg_{1.9}Al$ and $Mg_{2.5}Al$ (78.5 and 96.7 Å respectively). With further increase of Mg^{2+} content, the CDL decreases to a minimum of 35.6 Å for $Mg_{4.7}Al$ W LDH. $Mg_{2.5}Al$ W possesses the highest CDL value due to it being within the ratio for purest LDH for an Mg_xAl system, therefore resulting in more crystalline particles.

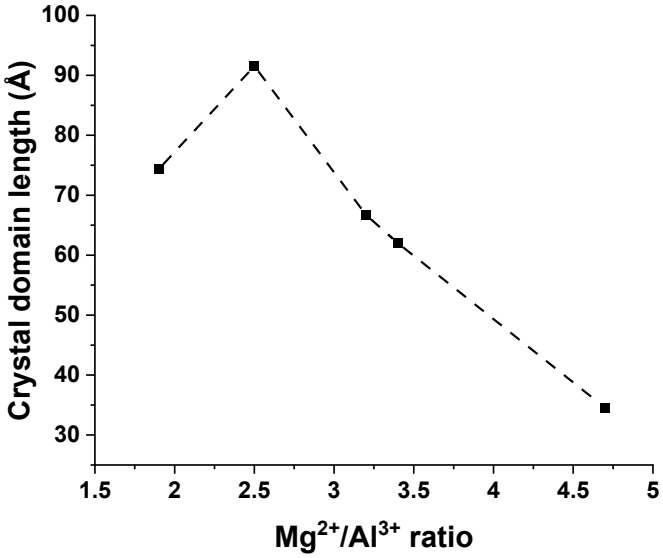


Figure 4.27 - LDH crystal domain length of d_{003} as determined by the Scherrer equation as a function of Mg^{2+}/Al^{3+}.

The XRD patterns of the LDOs calcined at 400 °C exhibit Bragg reflections corresponding to the expected MgO structure (Figure 4.28). $Mg_{1.9}Al$ W 400-2h-100 displayed the highest intensity of (111) Bragg reflection relative to its (200) reflection, with $Mg_{4.7}Al$ W 400-2h-100 exhibiting the lowest. This suggests a reduction in thickness in the (00*l*) plane. The crystallinity of the MgO phases formed also increases with increasing Mg^{2+} content as with less Al^{3+}, a purer MgO can be formed upon calcination.

The surface area and pore volume, as determined by N_2 BET measurements decrease drastically between $Mg_{1.9}Al$ W 400-2h-100 and $Mg_{2.5}Al$ W 400-2h-100 (200 and 153 $m^2\ g^{-1}$, 0.95 and 0.49 $cm^3\ g^{-1}$ respectively). They then increase with increasing Mg^{2+} content. The highest surface area was achieved by $Mg_{4.7}Al$ W 400-2h-100 (336 $m^2\ g^{-1}$).

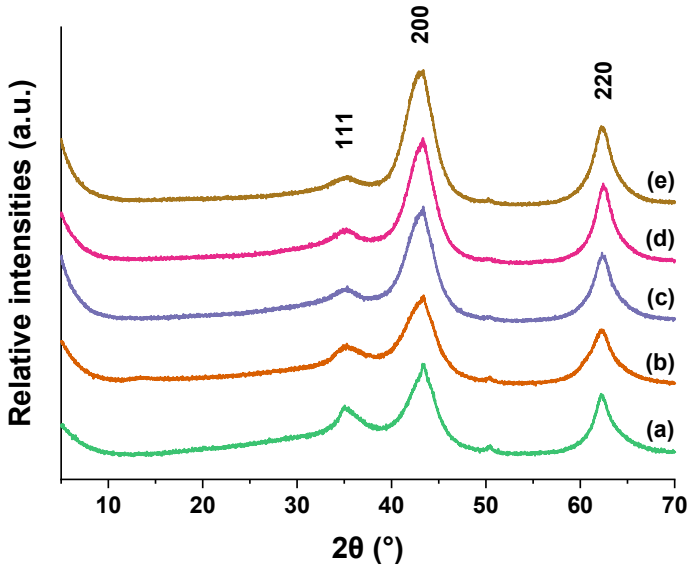


Figure 4.28 - XRD patterns of (a) $Mg_{1.9}Al$, (b) $Mg_{2.5}Al$, (c) $Mg_{3.2}Al$, (d) $Mg_{3.4}Al$ and (e) $Mg_{4.7}Al$ W 400-2h-100 LDOs.

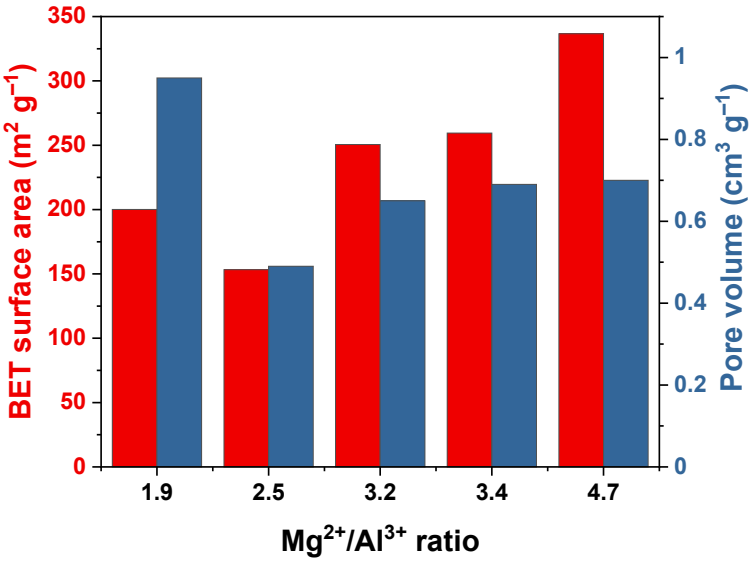


Figure 4.29 - N_2 BET surface area and pore volume of Mg_xAl W 400-2h-100 LDOs.

The change in ratio also led to a change in hydroxyl numbers (Figure 4.30). The hydroxyl number decreases generally with increasing Mg^{2+} content, reaching a minimum with $Mg_{3.5}Al$ W 400-2h-100 of 0.47 mmol g^{-1}. A small increase can be observed between $Mg_{2.5}Al$ W 400-2h-100 and $Mg_{3.2}Al$ W 400-2h-100, from 0.79 to 0.85 mmol g^{-1}, the value

then increases between $Mg_{3.5}Al$ W and $Mg_{4.7}Al$ W. Once normalised to surface area, the hydroxyl concentration displayed a smoother relationship between Mg^{2+}/Al^{3+} ratio and OH number. There is a steady decrease between $Mg_{1.9}Al$ W 400-2h-100 and $Mg_{3.4}Al$ W 400-2h-100, from 6.32 to 1.80 µmol m^{-2}.The value then increases for $Mg_{4.7}Al$ W 400-2h-100 to 3.17 µmol m^{-2}.

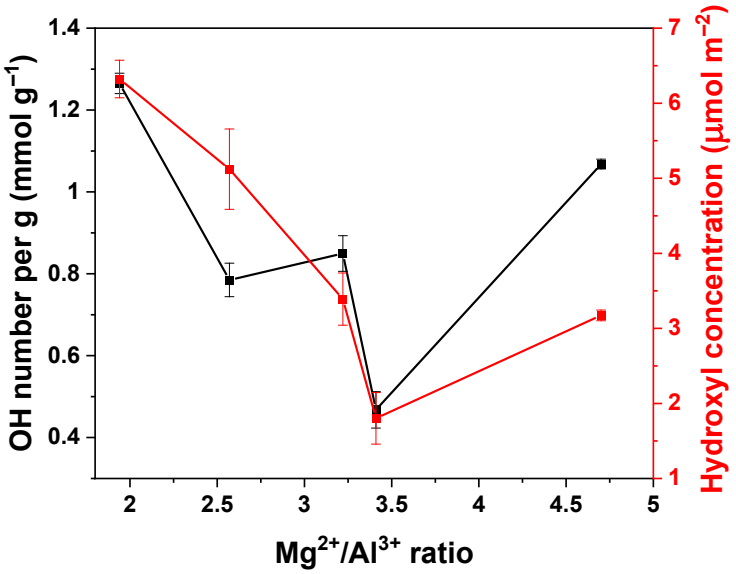


Figure 4.30 - Hydroxyl numbers of Mg_xAl W 400-2h-100 LDOs.

Figure 4.31 displays the CO_2 capture values of the LDO samples. $Mg_{3.4}Al$ W 400-2h-100 exhibited the highest CO_2 capacity of 1.01 mmol g^{-1} while $Mg_{1.9}Al$ W 400-2h-100 showed the lowest at 0.59 mmol g^{-1}. There is a general increase between ratios of 1.9 and 3.4, then a slight decrease to Mg^{2+}/Al^{3+} ratio of 4.7. $Mg_{3.2}Al$ W 400-2h-100 is observed to be an outlier of the general trend. Upon closer inspection of the separate adsorption types, it is shown that the chemisorption of $Mg_{3.2}Al$ W 400-2h-100 is comparable to that of $Mg_{2.5}Al$ W 400-2h-100 (0.27 and 0.26 mmol g^{-1} respectively). The large difference arises from their physisorption value. $Mg_{3.2}Al$ W 400-2h-100 possesses the lowest physisorption of different Mg^{2+}/Al^{3+} samples at 0.36 mmol g^{-1}.

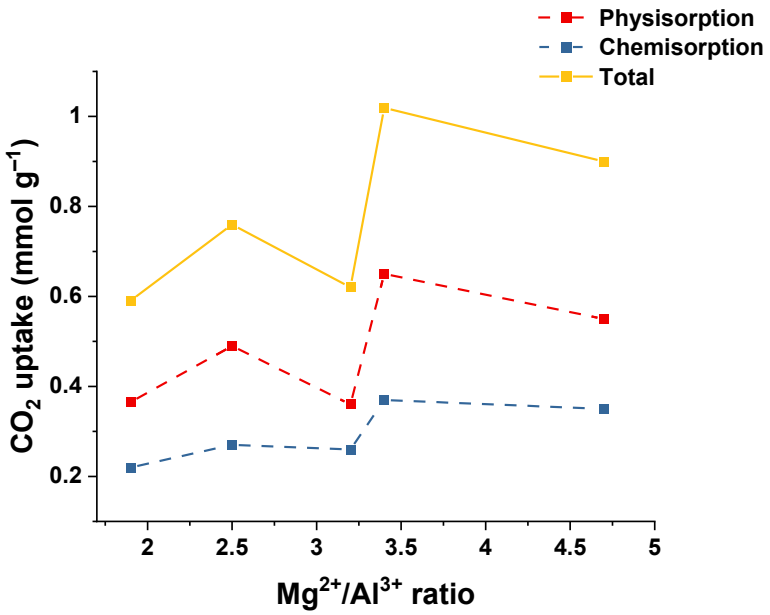


Figure 4.31 - CO_2 adsorption for Mg_xAl W 400-2h-100 LDOs at 40 °C and 100 kPa.

The adsorption per surface area shows a maximum with Mg^{2+}/Al^{3+} = 2.5 (0.0050 mmol m^{-2}), while $Mg_{3.4}Al$ W 400-2h-100 displayed the second highest adsorption per surface area (Figure 4.32). $Mg_{3.2}Al$ W 400-2h-100 shows a decrease in adsorption in both physisorption and chemisorption, displaying the lowest value for both among this series, 0.0014 and 0.0010 mmol m^{-2} respectively. Despite exhibiting the second highest CO_2 capture value of 0.90 mmol g^{-1}, $Mg_{4.7}Al$ W 400-2h-100 displayed one of the lowest adsorption per surface area at 0.0027 mmol m^{-2}. This would suggest despite having a high surface area and CO_2 capacity, the surface of $Mg_{4.7}Al$ W 400-2h-100 is not very active. This agrees with the trend observed by Cheah *et al*., who reported an increase in CO_2 capture values with increasing Mg^{2+}/Al^{3+} ratio, leading to an optimal value with Mg^{2+}/Al^{3+} = 4 and decreases with further increase of the ratio.[46] Their highest obtained CO_2 capture value was 0.82 mmol g^{-1} (calcined at 400 °C, CO_2 adsorption at 200 °C).

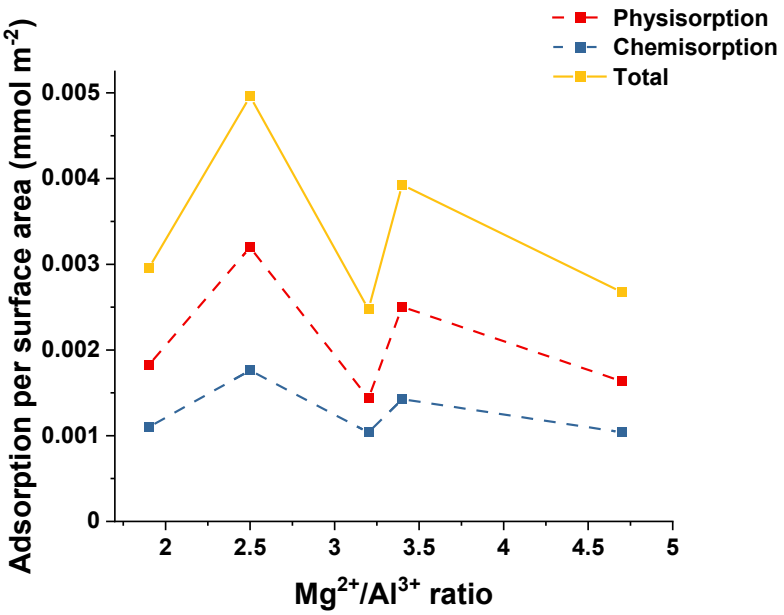


Figure 4.32 - CO_2 adsorption per surface area for Mg_xAl W 400-2h-100 LDOs at 40 °C and 100 kPa.

A closer inspection on the pore size distribution of the samples provides an explanation. Despite possessing the lowest pore volume, $Mg_{2.5}Al$ W 400-2h-100 has the highest concentration of larger pore size (> 300 Å) (Figure 4.33 (b)), whereas $Mg_{3.2}Al$ and $Mg_{4.7}Al$ W 400-2h-100 have a large amount of smaller pores between 40–50 Å (Figure 4.33 (a)). The smaller pores could be more easily blocked by the adsorption of CO_2 and therefore making the inner pores less accessible, which would lead to the appearance of a less active surface for adsorption.

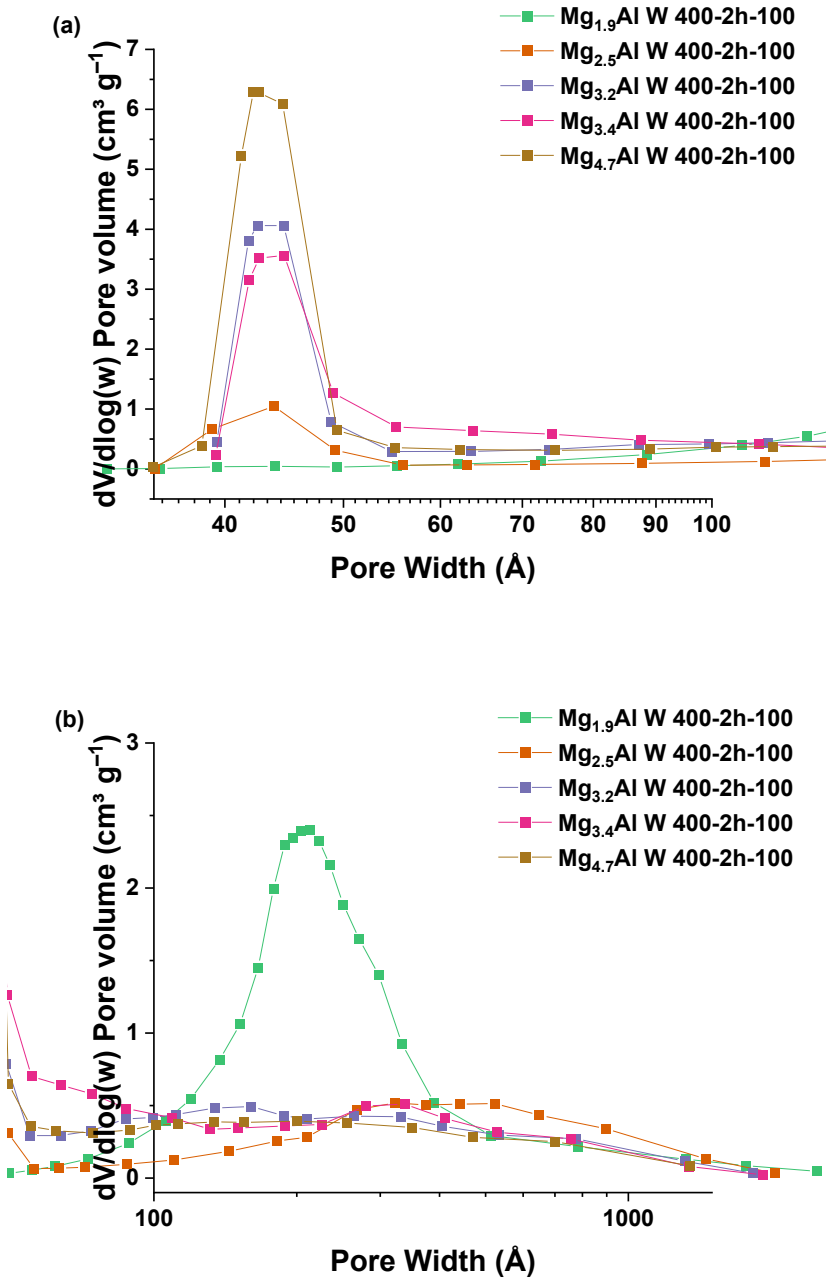


Figure 4.33 - Pore size distribution of Mg_xAl W 400-2h-100 LDOs between (a) 40–100 Å and (b) 100–1500 Å as determined by N_2 BET measurements.

The ^{27}Al DPMAS spectra showed a decrease in T_d population with increasing Mg^{2+} content, reaching a minimum of 37% with a Mg^{2+}/Al^{3+} ratio of 4.7 (Figure 4.34). By normalising the percentage of T_d centres to the amount per mol_{LDH}^{-1}, a more drastic difference can be observed. As observed in Figure 4.35, the total T_d Al^{3+} centres in $Mg_{4.7}Al$ is 0.06 mol mol_{LDH}^{-1}, only 30% of the value obtained from $Mg_{1.9}Al$ W 400-2h-100

(0.20 mol mol_{LDH}^{-1}). This could be due to the lower Al^{3+} content leading to a more facile incorporation of Al^{3+} into the bulk MgO structure, rather than migrating to the surface, therefore possessing an O_h coordination. There is also a slight shift towards a higher chemical shift value for the O_h resonance with increasing Mg^{2+} content from δ = 9.2–14.9 ppm. This is due to the change in the structure to that of a more crystalline MgO, as indicated in the more intense (200) Bragg reflection with increasing Mg^{2+} content. The decrease in T_d centres for $Mg_{4.7}Al$ W 400-2h-100 explains the relatively less active surface for CO_2 capture as it was previously mentioned CO_2 more favourably binds to less saturated centres.[38]

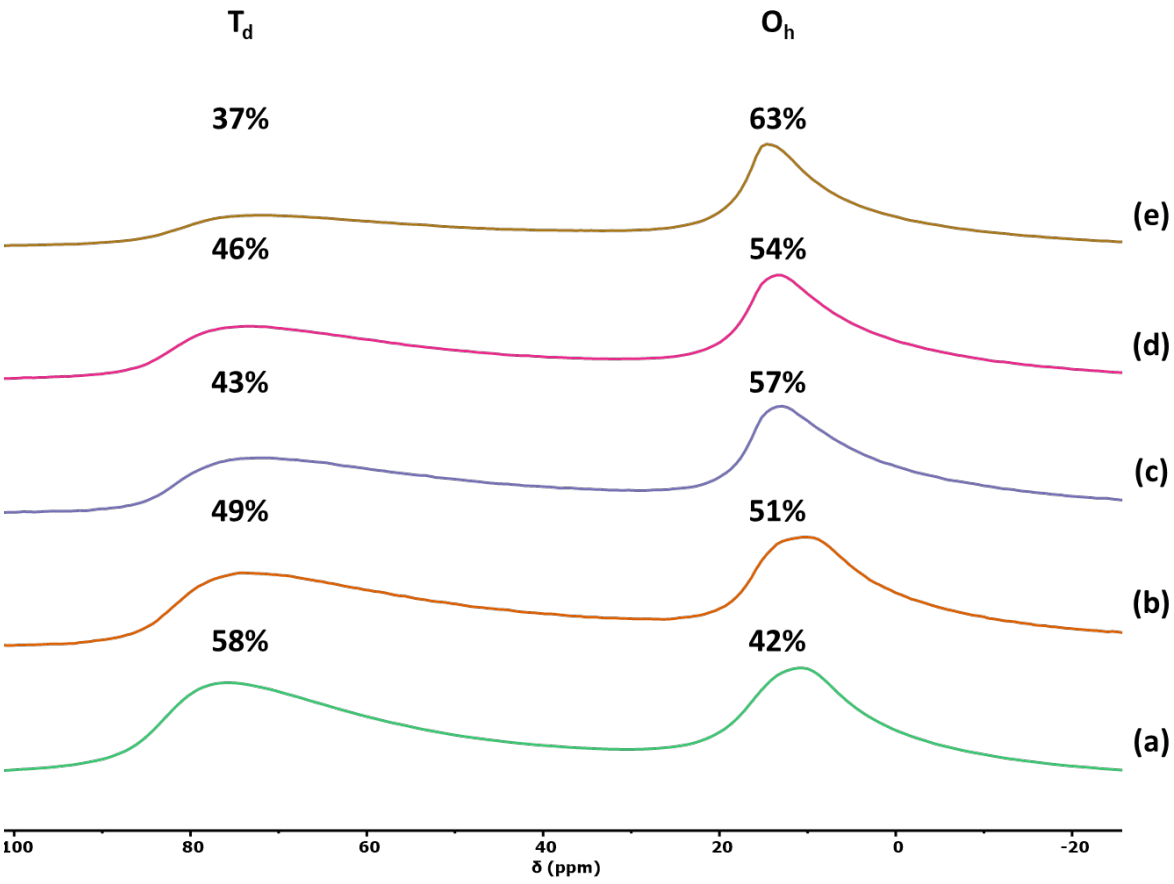


Figure 4.34 - ^{27}Al DPMAS NMR of (a) $Mg_{1.9}Al$, (b) $Mg_{2.5}Al$, (c) $Mg_{3.2}Al$, (d) $Mg_{3.4}Al$ and (e) $Mg_{4.7}Al$ W 400-2h-100 LDOs. δ = –25–30 ppm has been assigned to O_h centres while δ = 30–100 ppm has been assigned to T_d centres.

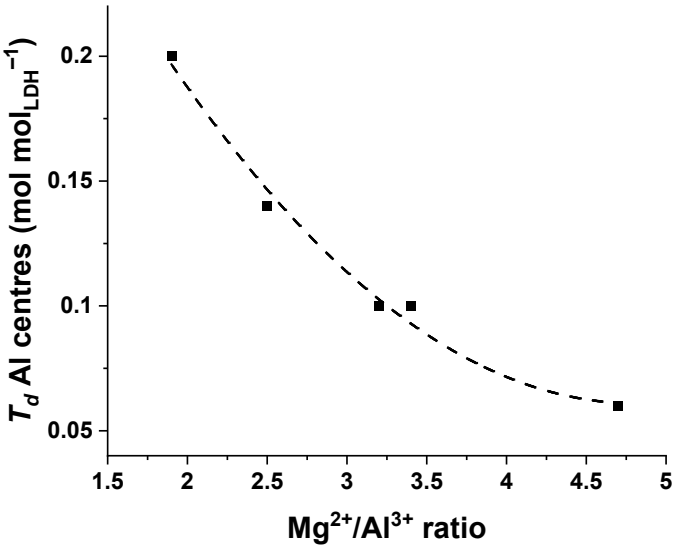


Figure 4.35 - T_d Al^{3+} centres in Mg_xAl W 400-2h-100. Dotted line is just a guide for the eye.

In the ^1H MAS NMR spectra, the resonance at δ = 7.3 ppm can be observed throughout the series in Figure 4.36, although the intensity from $Mg_{2.5}Al$, $Mg_{3.2}Al$ and $Mg_{3.4}Al$ W 400-2h-100 is shown to have been reduced. This corresponds to the reduced hydroxyl number observed in Figure 4.30 and the decreasing T_d Al^{3+} centres with increasing Mg^{2+} content. The increase in intensity observed in $Mg_{4.7}Al$ W 400-2h-100, despite the reduced population of T_d Al^{3+} centres, is due to the increase in hydroxyl concentration. The resonances of the different Mg-OH environments can also be observed. In a partially hydrated MgO structure, it was observed that higher levels of hydration displayed slightly higher chemical shifts.[35] Therefore only $Mg_{1.9}Al$ and $Mg_{4.7}Al$ W 400-2h-100 displayed a resonance at δ = 2.2 ppm due to their high OH number compared to the samples in the series.

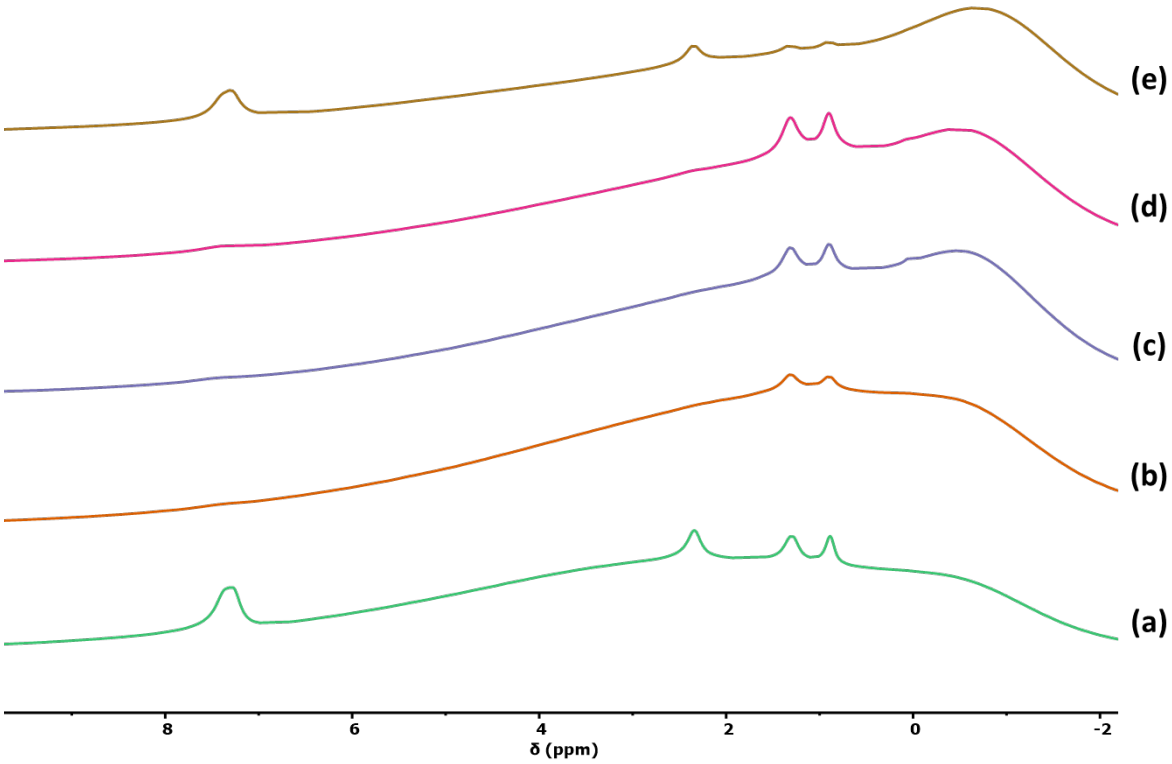


Figure 4.36 - ^{1}H MAS NMR of (a) $Mg_{1.9}Al$, (b) $Mg_{2.5}Al$, (c) $Mg_{3.2}Al$, (d) $Mg_{3.4}Al$ and (e) $Mg_{4.7}Al$ W 400-2h-100 LDOs.

The changes observed in their acid and base properties, as probed by TPD, can be seen to have altered significantly (Figure 4.37). The total acid sites increase between ratios 1.9 to 2.5 (1.34 and 1.74 mmol g^{-1} respectively), then decreases with further increase in Mg^{2+} content to display the lowest number of acid sites in $Mg_{4.7}Al$ W 400-2h-100 of 0.15 mmol g^{-1} (Table 4.6). This is a value similar to those exhibited by the solvent treated LDOs in Chapter Two. This could suggest Al^{3+} contribute more towards the acidity of the LDOs. Moreover, the overall desorption profile also bears resemblance to the desorption profiles of the samples with suppressed acidity due to site blocking by solvents. The difference between $Mg_{4.7}Al$ W 400-2h-100 and the solvent treated samples can be seen in the shape of the second peak, where the solvent treated samples presented with a skewed peak, $Mg_{4.7}Al$ W 400-2h-100 possesses a non-skewed peak (Figure 4.38). This could suggest the reduced Al^{3+} content in the structure leads to the natural elimination, and not a partial

suppression, of one of the metal bonding modes. The reduced T_d population in $Mg_{4.7}Al$ W 400-2h-100, as observed from the ^{27}Al DPMAS spectra, would lead to the lessening of its ability to form N-M bonding modes. This would result in a similar effect as the solvent blocking observed previously. The acid site density reaches a maximum with $Mg_{2.5}Al$ W 400-2h-100 (11.35 μmol m^{-2}) and steadily decreases with increasing Mg^{2+} content. $Mg_{2.5}Al$ W 400-2h-100 displayed the highest number of total acid sites and acid site densities in all the samples tested in this study, displaying almost double the acid site density of all other samples, apart from $Mg_{1.9}Al$ W 400-1h-100.

The CO_2 desorption profile also displayed changes with varying Mg^{2+}/Al^{3+} ratios. The total basic site decreases from Mg^{2+}/Al^{3+} ratio 1.9 to 2.5, from 3.65 to 2.54 mmol g^{-1} (Table 4.7). The value then follows an increasing general trend with increasing Mg^{2+} content. The trend mirrors the opposite observed in the acidity of the samples. The major difference between samples of varying ratios is the distribution of peaks. With increasing Mg^{2+} content, the weighting of the monodentate binding mode increases, to a maximum of 72% for $Mg_{4.7}Al$ W 400-2h-100. This is due to the higher Mg^{2+} concentration leading to the formation a more MgO-like structure. This is also reflected in the increased population of O_h coordinated Al^{3+} centres which could signify the increasing ease of incorporating Al^{3+} into the bulk MgO phase of the LDO.

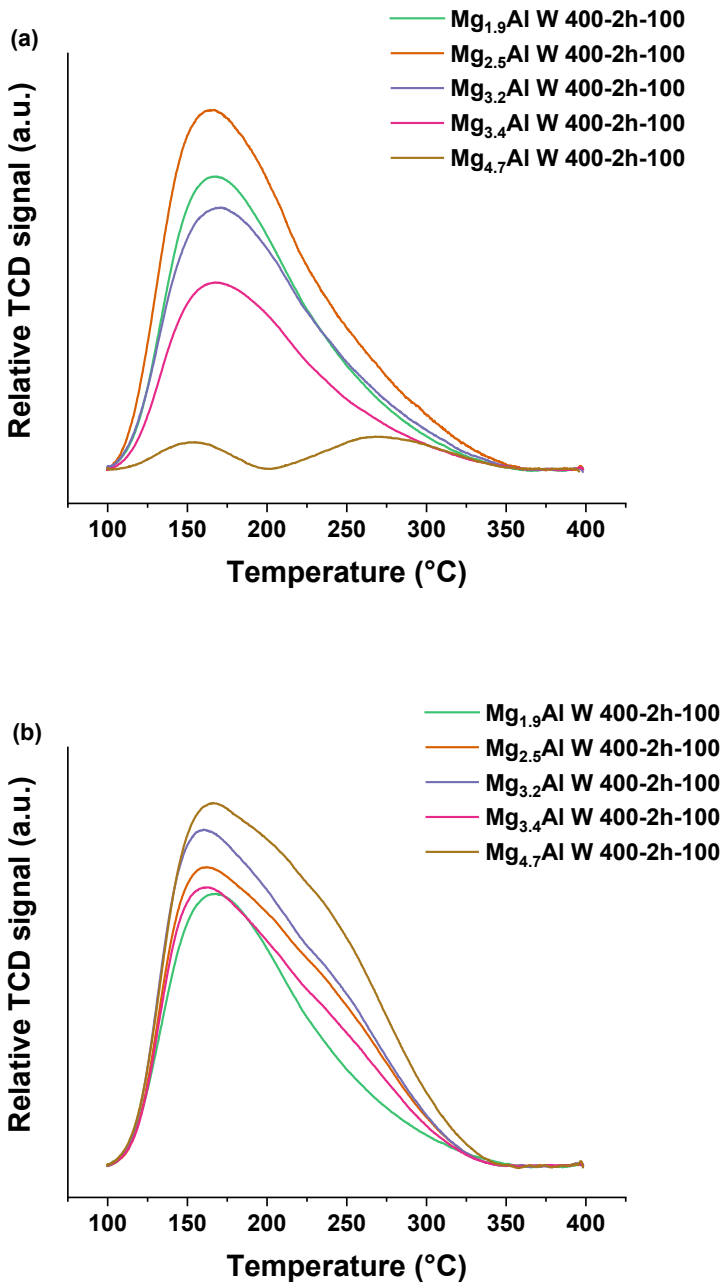


Figure 4.37 - (a) NH_3 and (b) CO_2 TPD curves of Mg_xAl W 400-2h-100 LDOs.

Table 4.6 - Summary of TPD data Mg_xAl W 400-2h-100.

Sample	Total basic sites (mmol g^{-1})	Basic site density (µmol m^{-2})	Total acidic sites (mmol g^{-1})	Acidic site density (µmol m^{-2})	Acid/base ratio
$Mg_{1.9}Al$ W	3.65	18.24	1.34	6.70	0.37
$Mg_{2.5}Al$ W	2.54	16.57	1.74	11.35	0.69
$Mg_{3.2}Al$ W	2.79	11.14	1.26	5.03	0.45
$Mg_{3.4}Al$ W	2.25	8.67	0.88	3.39	0.39
$Mg_{4.7}Al$ W	3.28	9.74	0.15	0.46	0.05

Table 4.7 - Deconvolution of TPD data of Mg_xAl W 400-2h-100.

Sample	Basic site weighting (%)		Acid site weighting (%)	
	Bidentate	Monodentate	OH peak	Metal peak
$Mg_{1.9}Al$ W	44	56	35	65
$Mg_{2.5}Al$ W	31	69	43	57
$Mg_{3.2}Al$ W	33	67	43	57
$Mg_{3.5}Al$ W	34	66	43	57
$Mg_{4.7}Al$ W	28	72	33	67

The maximum acid/base ratio was reached with a Mg^{2+}/Al^{3+} ratio of 2.5 (0.69). With a further increase in Mg^{2+} content, the acid/base ratio decreases (Figure 4.39). This is due to the to the increasing Mg^{2+} content leading to the formation of more MgO while decreasing the overall Al^{3+} content in the material. The initial decrease in acid/base ratio of

$Mg_{1.9}Al$ W 400-2h-100 (0.37) could be due to the more abundant T_d Al^{3+} environment (58%) with apical oxygens leading to more accessible sites with relatively high basicity.

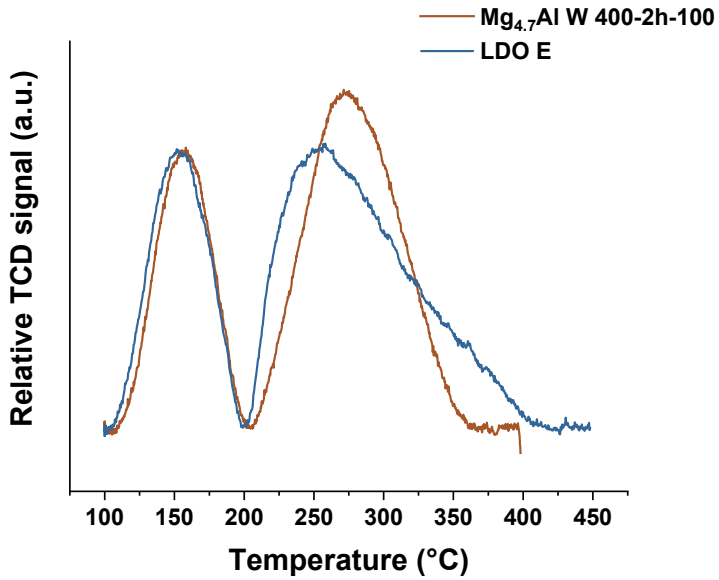


Figure 4.38 - NH_3 TPD curves of $Mg_{4.7}Al$ W 400-2h-100 and **LDO E** from Chapter Two.

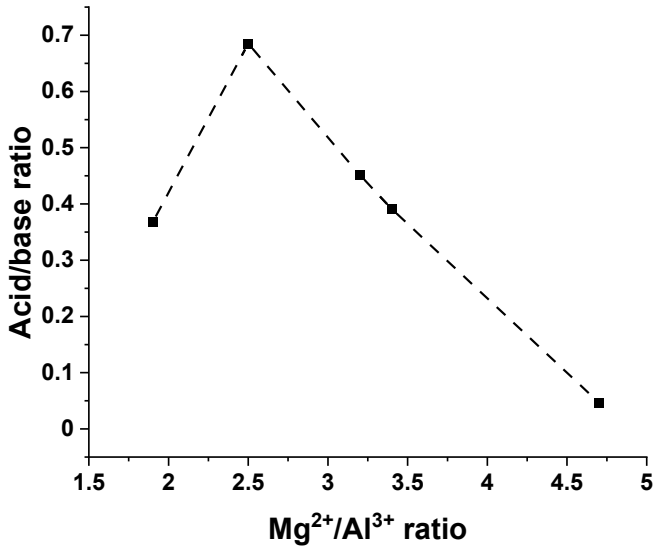


Figure 4.39 - Acid/base ratio of Mg_xAl W 400-2h-100 samples.

There is no observable correlation between the acid/base ratio and CO_2 uptake (Figure 4.40). By comparing acidity and basicity across different Mg^{2+}/Al^{3+} ratios, the composition and

therefore the surface environment differs greatly. There is also a change in distribution of acidic and basic sites. These factors could lead to multiple variables determining the resulting surface chemistry which would require more in-depth investigation, potentially with DFT modelling and calculations.

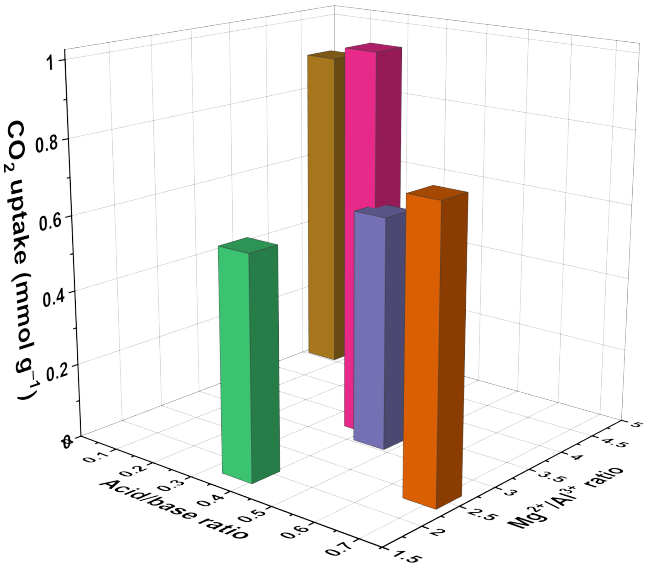


Figure 4.40 - CO_2 uptake (mmol g^{-1}) as a function of acid/base ratio and Mg^{2+}/Al^{3+} ratio of Mg_xAl W 400-2h-100.

4.7 Optimised Mg_xAl LDO for CO_2 capture

Gathering all the results from Chapter Two and this chapter, an optimised Mg_xAl system for CO_2 capture was considered. A series of ethanol treated LDH samples with varying Mg^{2+}/Al^{3+} ratio, between 1.9 and 3.4, were synthesised and tested for their CO_2 capture abilities.

The N_2 BET surface area of the ethanol treated series, shown in Figure 4.41, reflects the trend observed in their conventional water washed counterparts, while displaying enhanced values, similar to those exhibited in various studies and Chapter Two.[14,47] $Mg_{3.4}Al$ E 400-

2h-100 displayed the highest surface area of 401 $m^2\ g^{-1}$. The pore volume also reveals a similar trend, reaching a maximum at Mg^{2+}/Al^{3+} = 3.4 (1.36 $cm^3\ g^{-1}$).

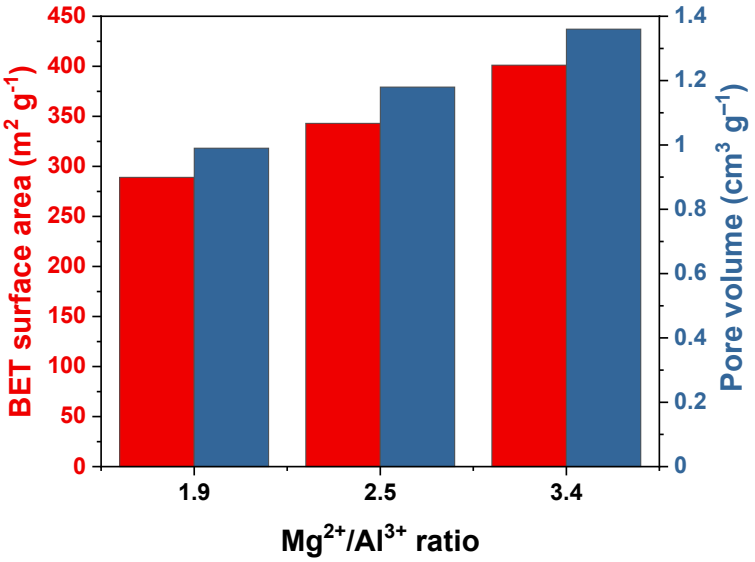


Figure 4.41 - N_2 BET surface area and pore volume of Mg_xAl E 400-2h-100.

The CO_2 capture abilities of the ethanol treated samples were tested using the optimised calcination condition and is displayed in Figure 4.42. The CO_2 uptake of all the ethanol treated samples displayed a marked increase compared to their water washed counterparts: $Mg_{1.9}Al$ E 400-2h-100 exhibiting the largest increase of 127%, from 0.59 to 1.34 mmol g^{-1}. The highest capture value was achieved by $Mg_{3.4}Al$ E 400-2h-100, exhibiting a value of 2.04 mmol g^{-1}. This is an increase of 100% compared to the equivalent conventional counterpart, and is the highest value for a solvent treated LDO reported in literature.[31,48] It is also amongst the highest CO_2 capture performance of any reported Mg_xAl LDH derivative sorbents. One of the highest CO_2 capture Mg_xAl materials in literature was reported by Veerabhadrappa *et al.* to be 2.17 mmol g^{-1} at 30 °C.[49] It was shown that increasing the adsorption temperature decreases the CO_2 capture performance due to the decreased contribution from physisorption.[30] Therefore, it is expected that this value would decrease if

the product was tested under the same 40 °C adsorption temperature as the samples in this chapter.

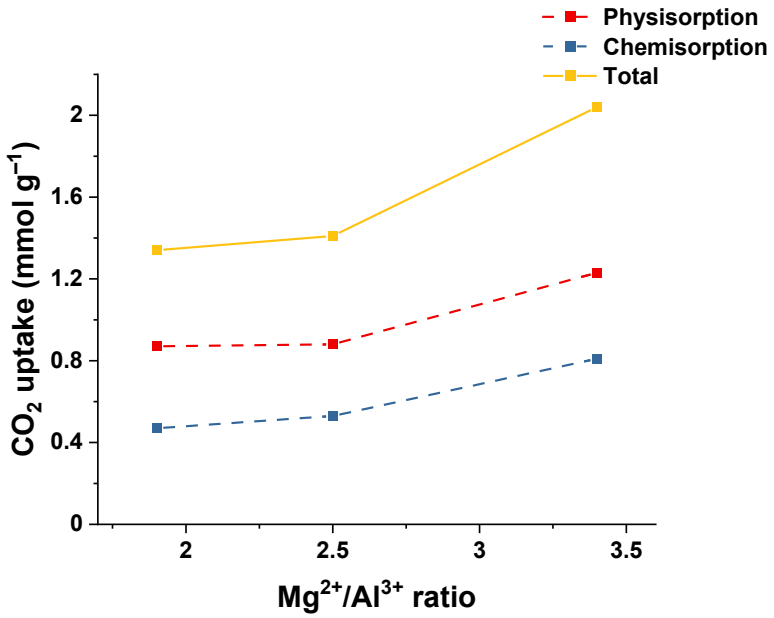


Figure 4.42 - CO_2 adsorption for Mg_xAl E 400-2h-100 at 40 °C and 100 kPa.

Table 4.8 summarises some of the best CO_2 capture performances from literature for LDH materials. The pre-treatment conditions, adsorption temperature and any modifications are also presented. The polymer-intercalated $Mg_{1.75}Al$ LDH reported by Dantas *et al.*, which exhibited a d_{003}-spacing of 28.7 Å and therefore more accessible surface active sites, only displayed a CO_2 capture performance of 1.3 mmol g^{-1}.[50] Despite the expanded gallery height and enhanced basicity due to an aminosilane treated Mg_3Al ($C_{12}H_{25}SO_4$), Wang *et al.* reported a highest CO_2 capture value of 1.75 mmol g^{-1}.[51] However, unlike other LDH-related materials, the CO_2 capture performance increases with increasing adsorption temperature between 25–80 °C. This could be due to the amine functional groups allowing for more chemisorption within the material, therefore resulting in a higher optimal adsorption temperature. At an adsorption temperature of 40 °C, this material only displayed a CO_2 capture performance of *ca* 0.8 mmol g^{-1}.

Table 4.8 - Comparison of CO_2 capture values of LDHs from literature and this chapter.

Sample	Modifications	Pre-treatment condition	Adsorption temperature (°C)	CO_2 uptake (mmol g^{-1})
$Mg_3Al\ CO_3$[52]	K_2CO_3 as anion source	700-7h-5	50	1.15
$Mg_3Fe\ CO_3$[30]	N/A	300-5h- /	200	0.46
$Ca_{1.5}Co_{1.5}Al\ CO_3$[53]	N/A	550-4h- /	350	1.39
$Mg_{1.75}Al$[51]	Polymer intercalated	550- / - /	30	1.3
Mg_4Al acetate[49]	Freeze dried	400-4h-10	30	2.17
$Mg_3Al\ C_{12}H_{25}SO_4$[50]	Aminosilane modified	105-30min-20	80	1.75
$Mg_3Al\ CO_3$[54]	Struvite raw material	400-2h-100	40	0.90
$Mg_{3.4}Al\ CO_3$*	Ethanol treated	400-2h-100	40	2.04

* Work from this chapter.

4.8 Conclusions

An extensive study of the surface acidic and basic properties of LDOs calcined under different conditions has been carried out. The optimum Mg_YAl LDH calcination temperature for CO_2 capture was shown to be 400 °C, although chemisorption was best using a pre-treatment temperature of 100 °C due to the presence of hydrated LDH layers. Overall, the full calcination conditions for optimised CO_2 capture for $Mg_{1.9}Al$ W LDH is a calcination temperature of 400 °C for 2 h with a ramp rate of 100 °C min^{-1}. This led to CO_2 capture value of 0.59 mmol g^{-1}, which is a 69% increase compared to the lowest value of LDO calcined at the same temperature for 2 h.

Solid state NMR studies showed that increasing heating ramp rate led to a lesser population of a tetrahedrally coordinated Al^{3+} environment. A previously unreported resonance at $\delta = 7.3$ ppm in the ^{1}H MAS NMR was also observed, increasing ramp rate and decreasing calcination time resulted in an increase in hydroxyl numbers (111% increase from a ramp rate of 5 to 100 °C min^{-1}). This suggests the formation of an apical "Al-OH" species which would assist in the adsorption of CO_2 by providing extra bicarbonate bonding modes.

It was found that changes in both the acidic and basic sites lead to an optimised acid/base ratio for CO_2 capture for $Mg_{1.9}Al$ LDH. By varying the calcination time and ramp rate, the acid/base ratio can be altered between 0.14–0.51. For CO_2 capture performance, the best ratio was shown to be 0.37. This is believed to be the balance of increasing hydroxyl groups which proves an extra bonding mode for CO_2 and the less favourable interactions between CO_2 molecules and the stronger acidic sites.

For Mg_xAl LDHs, a Mg^{2+}/Al^{3+} ratio of 3.4 was found to yield the corresponding LDO with the best CO_2 capture performance (1.01 mmol g^{-1}). Combining this with an ethanol treatment led to a CO_2 capture value of 2.04 mmol g^{-1} for $Mg_{3.4}Al$ E 400-2h-100, one of the highest reported in literature for an Mg_xAl LDH-based sorbent system.

4.9 References

1 L. Lv, J. He, M. Wei, D. G. Evans and X. Duan, *Water Res.*, 2006, **40**, 735–743.
2 S. J. Palmer and R. L. Frost, *Ind. Eng. Chem. Res.*, 2010, **49**, 8969–8976.
3 T. Hongo, T. Iemura and A. Yamazaki, *J. Fac. Sci. Tech. Seikei Univ.*, 2009, **46**, 47–51.
4 D. G. Evans, X. Duan, C. Mousty, C. Martelet, N. Jaffrezic-Renault, D. H. Zainol, A. B. Salleh, M. A. Sevilla and H. Kim, *Chem. Commun.*, 2006, **75**, 485–496.
5 L. Shi, D. Li, J. Wang, S. Li, D. G. Evans and X. Duan, *Clays Clay Miner.*, 2005, **53**, 294–300.
6 M. J. Hudson, S. Carlino and D. C. Apperley, *J. Mater. Chem.*, 1995, **5**, 323.
7 Y. Ding and E. Alpay, *Process Saf. Environ. Prot.*, 2001, **79**, 45–51.
8 H. T. J. Reijers, S. E. A. Valster-Schiermeier, P. D. Cobden and R. W. Van Den Brink,

Ind. Eng. Chem. Res., 2006, **45**, 2522–2530.
9 N. N. A. H. Meis, J. H. Bitter and K. P. de Jong, *Ind. Eng. Chem. Res.*, 2010, **49**, 1229–1235.
10 K. Coenen, F. Gallucci, G. Pio, P. Cobden, E. van Dijk, E. Hensen and M. van Sint Annaland, *Chem. Eng. J.*, 2017, **314**, 554–569.
11 Q. Wang, Z. Wu, H. H. Tay, L. Chen, Y. Liu, J. Chang, Z. Zhong, J. Luo and A. Borgna, *Catal. Today*, 2011, **164**, 198–203.
12 H. Du, C. T. Williams, A. D. Ebner and J. A. Ritter, *Chem. Mater.*, 2010, **22**, 3519–3526.
13 L. Huang, J. Wang, Y. Gao, Y. Qiao, Q. Zheng, Z. Guo, Y. Zhao, D. O'hare and Q. Wang, *J. Mater. Chem. A*, 2014, **2**, 18454–18462.
14 C. Chen, M. Yang, Q. Wang, J.-C. Buffet and D. O'Hare, *J. Mater. Chem. A*, 2014, **2**, 15102–15110.
15 Q. Wang and D. O'Hare, *Chem. Rev.*, 2012, **112**, 4124–4155.
16 K. Ruengkajorn, V. Erastova, J.-C. Buffet, H. C. Greenwell and D. O'Hare, *Chem. Commun.*, 2018, **54**, 4394–4397.
17 K. Ruengkajorn, C. M. R. Wright, N. H. Rees, J.-C. Buffet and D. O'Hare, *Mater. Chem. Front.*, 2018, **2**, 2277–2285.
18 C. M. R. Wright, K. Ruengkajorn, A. F. R. Kilpatrick, J.-C. Buffet and D. O'Hare, *Inorg. Chem.*, 2017, **56**, 7842–7850.
19 W. K. and W. J. L. Pesic, S. Salipurovic, V. Markovic, D. Vucelic, *J. Mater. Chem.*, 1992, **2**, 1069–1073.
20 F. Millange, R. I. Walton and D. O'Hare, *J. Mater. Chem.*, 2000, **10**, 1713–1720.
21 E. S. Zhitova, H. C. Greenwell, M. G. Krzhizhanovskaya, D. C. Apperlyy, I. V. Pekov and V. N. Yakpvemchuk, *Minerals*, 2020, 961.
22 H. Liu, H. Lu, L. Zhang and Z. Wang, *Nucl. Instruments Methods Phys. Res. Sect. B Beam Interact. with Mater. Atoms*, 2015, **360**, 60–63.
23 M. Bellotto, B. Rebours, O. Clause, J. Lynch, D. Bazin and E. Elkaïm, *J. Phys. Chem.*, 1996, **100**, 8535–8542.
24 U. Sharma, B. Tyagi and R. V. Jasra, *Ind. Eng. Chem. Res.*, 2008, **47**, 9588–9595.
25 M. K. Ram Reddy, Z. P. Xu, G. Q. (Max) Lu and J. C. Diniz da Costa, *Ind. Eng. Chem. Res.*, 2006, **45**, 7504–7509.
26 Y. Gao, Z. Zhang, J. Wu, X. Yi, A. Zheng, A. Umar, D. O'Hare and Q. Wang, *J. Mater. Chem. A*, 2013, **1**, 12782.
27 M. K. Ram Reddy, Z. P. Xu, G. Q. (Max) Lu and J. C. Diniz da Costa, *Ind. Eng. Chem. Res.*, 2008, **47**, 2630–2635.
28 K. Coenen, F. Gallucci, B. Mezari, E. Hensen and M. van Sint Annaland, *J. CO_2 Util.*, 2018, **24**, 228–239.
29 D. A. Torres-Rodríguez, E. Lima, J. S. Valente and H. Pfeiffer, *J. Phys. Chem. A*, 2011, **115**, 12243–12250.
30 Q. Wang, H. H. Tay, D. J. W. Ng, L. Chen, Y. Liu, J. Chang, Z. Zhong, J. Luo and A. Borgna, *ChemSusChem*, 2010, **3**, 965–973.
31 D. W. J. Leung, C. Chen, J. C. Buffet and D. O'Hare, *Dalton Trans.*, 2020, **49**, 9306–9311.
32 J. I. Di Cosimo, V. K. Díez, M. Xu, E. Iglesia and C. R. Apesteguía, *J. Catal.*, 1998, **178**, 499–510.
33 J. J. Fripiat and J. Uytterhoeven, *J. Phys. Chem.*, 1962, **66**, 800–805.
34 P. J. Sideris, U. G. Nielsen, Z. Gan and C. P. Grey, *Science*, 2008, **321**, 113–7.
35 J. M. Rimsza, E. G. Sorte and T. M. Alam, *ACS Omega*, 2019, **4**, 1033–1044.

36 G. Piedra, J. J. Fitzgerald, N. Dando, S. F. Dec and G. E. Maciel, *Inorg. Chem.*, 1996, **35**, 3474–3478.
37 R. W. Stevens, R. V. Siriwardane and J. Logan, *Energy & Fuels*, 2008, **22**, 3070–3079.
38 Y. Pan, C. J. Liu and Q. Ge, *Langmuir*, 2008, **24**, 12410–12419.
39 S. U. Rege and R. T. Yang, *Chem. Eng. Sci.*, 2001, **56**, 3781–3796.
40 F. Prinetto, G. Ghiotti, R. Durand and D. Tichit, *J. Phys. Chem. B*, 2000, 11117–11126.
41 G. V. Manohara, M. Mercedes Maroto-Valer and S. Garcia, *Chem. Eng. J.*, 2021, **415**, 128881.
42 X. Zhu, T. Ge, F. Yang, M. Lyu, C. Chen, D. O'Hare and R. Wang, *J. Mater. Chem. A*, 2020, **8**, 16421–16428.
43 C. Chizallet, G. Costentin, M. Che, F. Delbecq and P. Sautet, *J. Phys. Chem. B*, 2006, **110**, 15878–15886.
44 F. Cavani, F. Trifirò and A. Vaccari, *Catal. Today*, 1991, **11**, 173–301.
45 K. Rozov, U. Berner, C. Taviot-Gueho, F. Leroux, G. Renaudin, D. Kulik and L. W. Diamond, *Cem. Concr. Res.*, 2010, **40**, 1248–1254.
46 L. A. Cheah, G. V Manohara, M. Mercedes Maroto-Valer and S. Garcia, *ChemistrySelect*, 2020, **5**, 5587–5594.
47 C. Chen, J. C. Buffet and D. O'Hare, *Dalton Trans.*, 2020, **49**, 8498–8503.
48 S. Shang, A. Hanif, M. Sun, Y. Tian, Y. S. Ok, I. K. M. Yu, D. C. W. Tsang, Q. Gu and J. Shang, *J. Hazard. Mater.*, 2019, **373**, 285–293.
49 M. G. Veerabhadrappa, M. M. Maroto-Valer, Y. Chen and S. Garcia, *ACS Appl. Mater. Interfaces*, 2021, **13**, 11805–11813.
50 T. C. M. Dantas, V. J. Fernandes Junior, A. P. B. Dos Santos, F. A. Bezerra, A. S. Araujo and A. P. M. Alves, *Adsorpt. Sci. Technol.*, 2015, **33**, 165–173.
51 J. Wang, L. A. Stevens, T. C. Drage and J. Wood, *Chem. Eng. Sci.*, 2012, **68**, 424–431.
52 M. León, E. Díaz, S. Bennici, A. Vega, S. Ordóñ and A. Auroux, *Ind. Eng. Chem. Res.*, 2010, **49**, 3663–3671.
53 X. P. Wang, J. J. Yu, J. Cheng, Z. P. Hao and Z. P. Xu, *Environ. Sci. Technol.*, 2008, **42**, 614–618.
54 W. L. J. Kwok, H. Suo, C. Chen, D. W. J. Leung, J.-C. Buffet, D. O'Hare, J. Leung, J.-C. Buffet and D. O'Hare, *Green Chem.*, 2021, **23**, 1616–1620.

Chapter Five - Design of Carbon@LDH core@shell materials for CO_2 capture

5.1 Introduction

Core@shell materials have been of increasing interest in recent years. For example, they have the potential of acting as multifunctional catalysts due to being composed of two or more different materials. Furthermore, their highly flexible composition also leads to a phenomenal level of tunability.[1] Potential synergy can be exploited which arises from the favourable orientation of the growth of shell material provided by the morphology of the shell, or the creation and exposure of defect sites at the intersection between the two materials.[1] Han *et al.* reported the creation of an improved conductive pathway in ZIF-8-C@NiAl LDH compared to the individual parent materials,[2] while Kwok *et al*. reported the presence of tetrahedrally coordinated Al^{3+} centres in SiO_2@LDH core@shells.[3]

LDH-based core@shells is a relatively novel yet rapidly developing field of interest due to the highly tuneable nature of LDHs allowing for potential synergy with many core materials. Their positively charged layers with an OH-rich surface allows for favourable interactions with other materials, facilitating the synthesis of hybrid materials.[4] The variable composition and sizes of LDHs allow for them to be ideal materials for both the core and shell layers.[4] The use of carbon-based LDH core@shells have mainly been focused around lithium batters and supercapacitors,[5] with only very few examples of carbon/LDH hybrid materials used as CO_2 capture materials.[6,7] Garcia-Gallastegui *et al.* reported a layered graphene oxide GO@LDH core@shell which showed improved CO_2 capture compared to the parent

materials but suffers from a reduced surface area.[6] Activated carbon has shown excellent carbon capture abilities achieved through physisorption with superb adsorption kinetics, due to their high surface area.[8,9] Therefore by synthesising carbon@LDH core@shells, potential synergy through more preferred alignment of LDH platelets could be exploited for a class of materials with good CO_2 capture properties.

In this chapter, different carbon@LDH core@shell synthesis methods are being explored. A series of core@shell materials with increasing LDH content is synthesised and characterised. The samples are tested for CO_2 adsorption and their kinetic rates of adsorption are analysed following a range of calcination conditions. Finally, post-synthesis modifications are trialled to improve on CO_2 capture performances of carbon@LDH core@shells.

5.2 Nomenclature

Carbon@LDH core@shell materials are being synthesised and studied for their synergistic effect on CO_2 capture improvement. Figure 4.1 explains the nomenclature adopted for describing carbon@LDH core@shell materials using various synthesis parameters. The LDH was fixed as $[Mg_{0.66}Al_{0.33}(OH)_2](CO_3)_{0.175}$ (Mg_2Al).

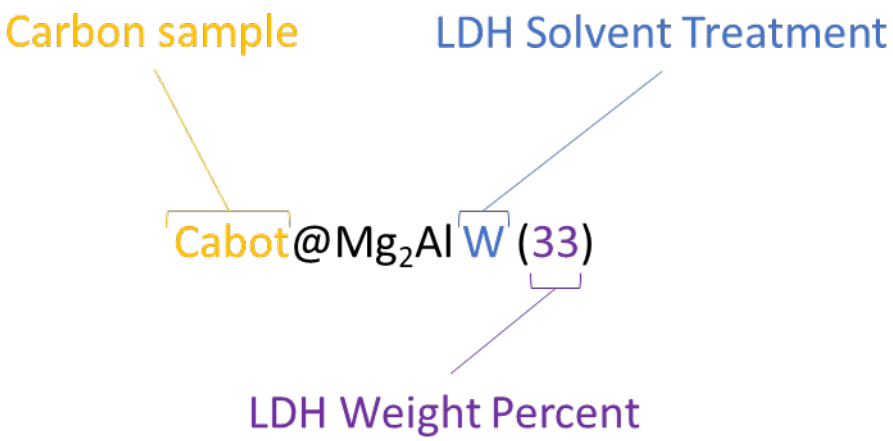


Figure 5.1 - Nomenclature used to describe Cabon@LDH core@shell materials.

5.3 Experimental details

5.3.1 Synthesis of $Mg_2Al\ CO_3$ W

$Mg_2Al\ CO_3$ W LDH was synthesised using the co-precipitation method adapted from a literature procedure.[1] $Mg(NO_3)_2.6H_2O$ (8.38 mmol, 2.14 g) and $Al(NO_3)_3.9H_2O$ (4.13 mmol, 1.56 g) were dissolved in 12.5 mL DI water to make solution A. Na_2CO_3 (6.23 mmol, 0.66 g) was then dissolved in another 100 mL DI water to make solution B. Solution A was added to solution B dropwise, while mixing at 375 rpm, over 1 h. The mixture was kept at pH 10 for the synthesis with the simultaneous addition of 4 M NaOH solution. When the addition of the solution A was completed and the final pH set to 10, the reaction was stirred for 1 h at room temperature. After the ageing process, the LDH product was washed with DI water until pH 7 and filtered. The product was left to dry overnight in a vacuum oven at room temperature.

5.3.2 Synthesis of Cabot@Mg_2Al LDH

Cabot@Mg_2Al LDH was synthesised by adding a predetermined amount of Cabot Norit 8033-7 (described in Table 6.1) to Na_2CO_3 (6.23 mmol, 0.66 g) and allowed to dissolve and mix thoroughly in 100 mL DI water to make solution A. $Mg(NO_3)_2.6H_2O$ (8.38 mmol, 2.14 g) and $Al(NO_3)_3.9H_2O$ (4.13 mmol, 1.56 g) were dissolved in 12.5 mL DI water to make solution B, and was added dropwise over 1 h, while mixing at 375 rpm, to solution A. The mixture was kept at pH 10 for the synthesis with the simultaneous addition of 4 M NaOH solution. When the addition of the solution A was completed and the final pH set to 10, the reaction was stirred for 1 h at room temperature. After the ageing process, the LDH product was washed with DI water until pH 7 and filtered. The product was left to dry overnight in a vacuum oven at room temperature.

Table 5.1 - Amount of Cabot added for each Cabot@Mg_2Al W core-shell material.

Targeted wt%	Obtained wt%	Cabot added (g)
33	36	1.78
43	44	1.17
50	53	0.87
67	68	0.44
75	77	0.29
83	83	0.22
88	88	0.13

5.3.3 Synthesis of solvent treated Cabot@Mg_2Al LDH

Solvent treated LDHs were synthesised using the AMO solvent treatment method adapted from a literature procedure.[7] Cabot@Mg_2Al LDH was prepared as described in the section above. After washing the LDH product with DI water until pH 7, special caution was taking to keep the LDH wet. The wet cake was washed with 100 mL of the chosen solvent and dispersed in another 100 mL of the same solvent and stirred vigorously for 4 h. The slurry was filtered and left to dry overnight in a vacuum oven at room temperature.

5.3.4 Calcination of core@shell material

The calcination of the carbon core-shell materials were carried out in a horizontal tube furnace under N_2 atmosphere. A flow of 100 mL min^{-1} was maintained throughout the calcination procedure.

5.3.5 Synthesis of AC, MAX and TPK core@shell materials

These core-shell materials were synthesised in an identical manner to Cabot@Mg_2Al W (53), with the exception of replacing Cabot Norit 8033-7 with 0.87 g Activated Carbon

(Sigma-Aldrich) for AC@Mg_2Al W (49), 0.87 g VXCMAX22 (Cabot Corp) for MAX@Mg_2Al W (53) and 0.87 g TPK1099R (Cabot Corp) for TPK@Mg_2Al W (56).

5.3.6 Ammonia treatment of carbon@LDH core@shells

150 mg of sample was placed in a quartz U-tube and placed into a Micromeritics AutoChem II 2920 Chemisorption Analyser. It was then first purged in a flow of He (50 cm^3 min^{-1}) at room temperature for 10 min to remove impurities. The temperature was then raised to 400 °C at a ramp rate of 50 °C min^{-1}. The gas was then switch to 30 cm^3 min^{-1} 10% NH_3 in He, 50 cm^3 min^{-1} He and flown over the sample for 1 h while at 400 °C. Excess NH_3 was then removed by changing the gas flow to He (50 cm^3 min^{-1}) for 15 min after the sample was cooled to room temperature.

5.4 Characterisation of carbon materials

Three carbon samples, Cabot (Cabot Norit 8033-7), Nerox (Nerox 600) and Printex (Printex 3), were provided by SCG Chemicals Co. Ltd and their physical properties are shown in Table 5.2.

Table 5.2 - Summary of the different carbon samples and their surface area and pore volume determined by N_2 BET measurements.

Sample	Species	N_2 BET surface area (m^2 g^{-1})	Pore volume (cm^3 g^{-1})
Cabot	Activated carbon	1127	0.87
Nerox	Surface treated carbon black	126	0.70
Printex	Carbon black	81	0.30

Figure 5.2–Figure 5.4 show the morphologies and sizes of the different carbon-based materials. As seen in the scanning election microscopy (SEM) images, the majority of Cabot

particles are large and angular, approximately 2 μm in width, with a well-defined structure. Well-defined large particles provide a good structure as a core material to enable nucleation and growth of the LDH shell. Malak-Polaczyk *et al.* reported a successful synthesis of carbon@CoAl LDH with carbon particles of *ca* 50 μm for supercapacitor applications.[5] The presence of smaller particles on the surface of the larger ones was also observed. This is due to the process used to synthesise activated carbon: raw materials are heated to high temperatures in the absence of oxygen, which does not lend itself to good morphology and size control.[10]

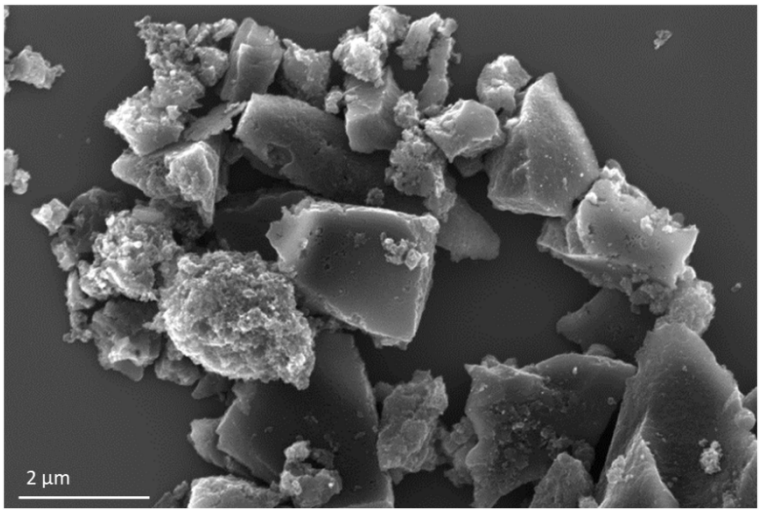


Figure 5.2 - SEM images of Cabot activated carbon (10K magnification).

Nerox presents particle sizes of 20 nm with some large particles/aggregates > 10 μm (Figure 5.3). The wide range of particle size could result in the formation of core@shells with vastly different morphologies. The rough texture of the Nerox particles could be a result of the surface treatment which the base carbon black underwent, however due to this being a commercial sample, the exact process has not been disclosed.

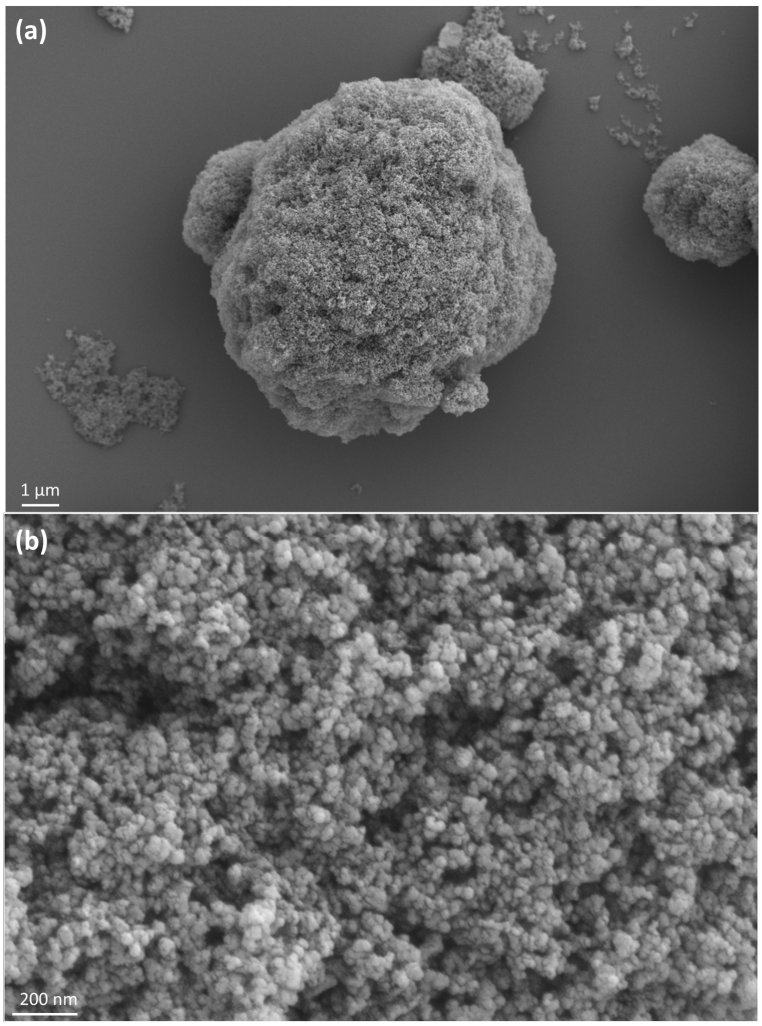


Figure 5.3 - SEM images of Nerox surface treated carbon black with (a) low (5K) and (b) high (50K) magnification.

Printex, shown in Figure 5.4, exhibited approximately the same size as Nerox. With individual carbon particles around 50 nm and largely aggregated, they could provide a similar surface to Nerox for LDH growth, while benefitting from not having previously undergone surface treatment.

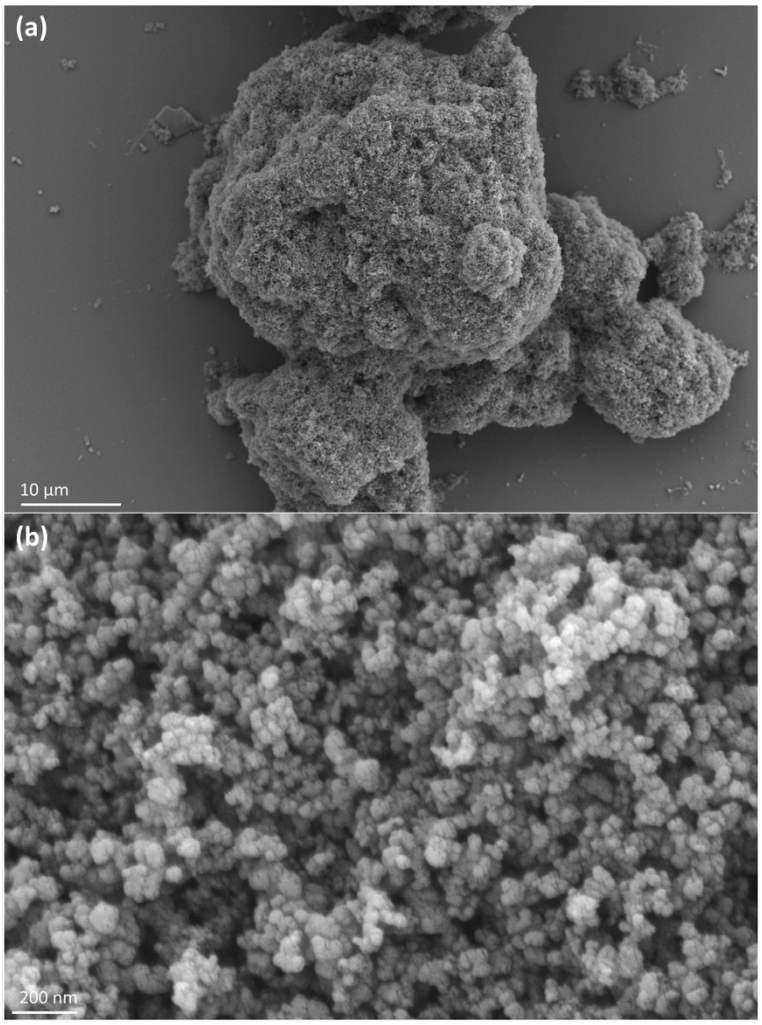


Figure 5.4 - SEM images of Printex carbon black with (a) low (1.5K) and (b) high (50K) magnification.

Preliminary characterisation was carried out on the carbon black/activated carbon samples using X-ray diffraction (XRD), N_2 BET surface area and pore volume (Table 5.2, Figure 5.5 and Figure 5.6). As shown in Figure 5.5 (b) and (c), the Printex and Nerox samples display the same Bragg reflections due to both being carbon black. The broad Bragg reflection at $2\theta = 25.0°$ corresponds to a reduced graphene oxide structure.[7] The Nerox sample possesses a higher pore volume and surface area compared to Printex, as illustrated in Table 5.2. The Cabot sample is a type of activated carbon, which possesses a different physical properties due to the activation process. The XRD pattern (Figure 5.5 (a)) exhibits a slightly different diffraction pattern to the other samples: the sharp Bragg reflections at $2\theta = 26.9°$, 43.4° and

44.8° are due to the presence of graphite, corresponding to (002), (100) and (101) Bragg reflections respectively.[7,11] The pore size distribution showed a shift in pore sizes to less than 60 Å (mesopores). This is accompanied by a significant increase in both pore volume and surface area (1127 m^2 g^{-1}), which is approximately a tenfold increase compared to the other carbon black materials (Table 5.2).

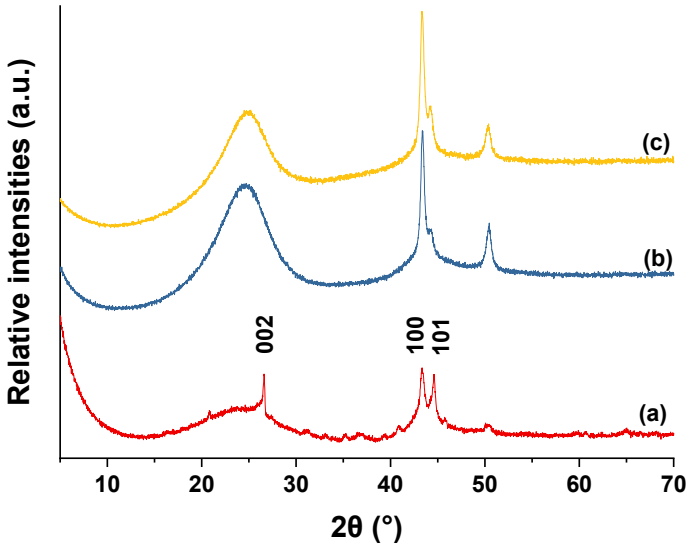


Figure 5.5 - XRD patterns of (a) Cabot, (b) Nerox and (c) Printex.

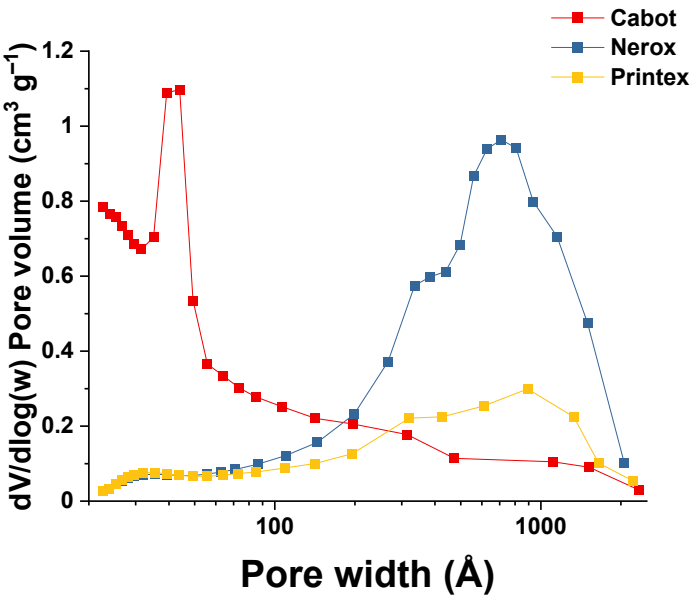


Figure 5.6 - Pore size distributions of different carbon materials determined by N_2 BET measurements.

Zeta potential measurements showed that the surface charge was negative for all three samples (Cabot, Nerox and Printex) when dispersed in deionised (DI) water. This facilitates electrostatic attraction between the carbon particles and the positively charged LDH platelets. It was also observed that the surface charge became increasingly negative upon further dilutions as upon higher dilutions, the mobility of the particles increases. Figure 5.7 shows the dispersibility of the three carbon materials in DI water, and it is clear that Printex, carbon black without any surface modification, is less readily dispersed in DI water compared to the other samples. The Cabot sample forms a more stable dispersion compared to the Nerox sample, which when left to stand, settles less readily compared to Nerox. A better dispersibility would allow for a more thorough mixing with the LDH particles during the co-precipitation synthesis method.

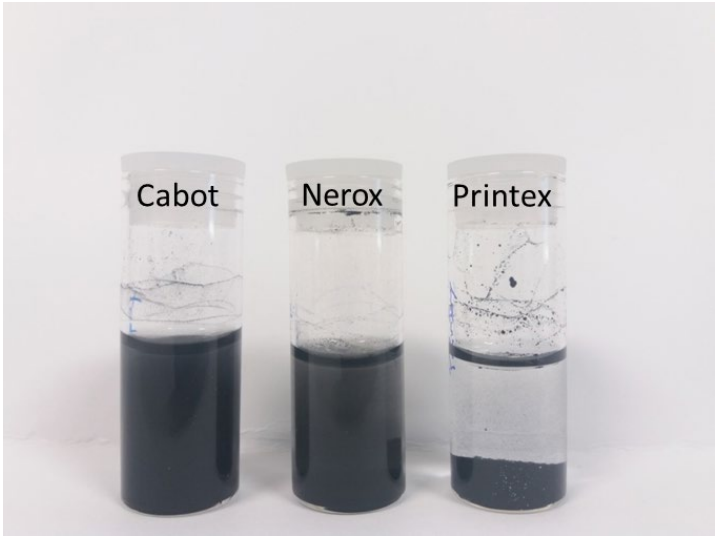


Figure 5.7 - Dispersibility of different carbon materials in DI water.

5.5 Synthesis of carbon@LDH hybrid materials

Transmission electron microscopy (TEM) was used to preliminarily identify successful attempts at synthesising core@shell materials. Figure 4.8 (a) shows a TEM image of a successful synthesis of at Cabot@Mg_2Al W (88). The black areas in the images represent

the Cabot activated carbon and it is clear that LDH particles have successfully adhered to and grown on the surface of the carbon material.

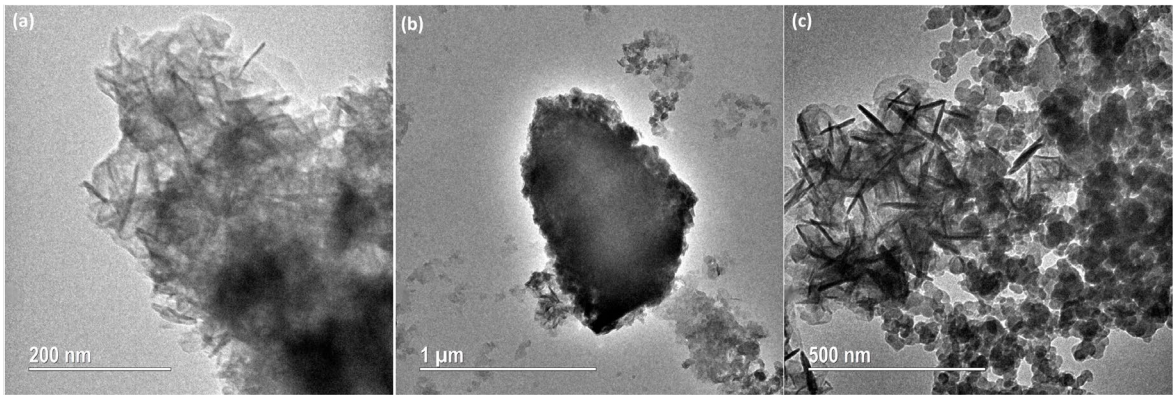


Figure 5.8 - TEM images of (a) Cabot@Mg_2Al W (88), (c) Nerox@Mg_2Al W (88) and (c) Printex@Mg_2Al W (88).

The attempt using Nerox as the core material proved less successful. It also be seen that there are carbon particles without any LDH on the surface even at this high an LDH ratio (Figure 5.8 (b)). Simultaneously, free LDH can also be seen. This shows that the LDH particles does not have as high an affinity for adhering to the surface of the Nerox carbon particle when compared to Cabot.

Printex@Mg_2Al W (88) exhibits considerable adhesion of Printex particles to the LDH structure in Figure 5.8 (c). However, due to the small size of the carbon particles, they do not provide an adequate core for the LDH to grow around. The core carbon aggregate appears to have broken apart into the smaller carbon particles from the synthesis procedure. As a result, the resultant core@shell material exhibits poor coverage of both surfaces and more readily resembles a physical mixture of the two materials.

Reviewing the TEM images, it is clear that Cabot@Mg_2Al W (88) was the most successful core@shell material, with the best LDH coverage of carbon surface whilst also showing little to no evidence of free LDH even at the high LDH content. Furthermore, considering

the high concentration of mesopores, a very high surface area, the larger particle size and better dispersibility in DI water, Cabot activated carbon was chosen as the carbon product to be used in a more extensive study of carbon@LDH synthesis. Both pore size and surface area should contribute to CO_2 capture which will result in an improved physisorption.

5.6 Synthesis and characterisation of Cabot@LDH core@shell materials

To synthesise a complete series, the following ratios for Cabot@Mg_2Al W LDH were targeted: 33, 43, 50, 67, 75, 83 and 88 wt% LDH. The same amount of metal salts was used in each synthesis, the ratio was varied by changing the amount of Cabot added.

A carbon@LDH core@shell has previously been reported in literature by Malak-Polaczyk *et al.*[5] which showed good coverage of the base carbon material. The proposed synthesis method required heating to 95 °C for 48 h. In comparison, the synthesis method developed in this work can be carried out at room temperature and is completed in 2 h, providing a simple, quick and energy efficient method that is optimal for industrial scale-up.

As observed from the TGA of the Cabot sample in Figure 5.9, a dramatic drop in wt% occurs at ~600 °C. Activated carbon can be synthesised through mainly 2 methods: physical and chemical activation. Chemical activation, or wet oxidation method, is a method in which raw materials are exposed to oxidising chemicals, then activated by heating to temperatures between 400–900 °C. In contrast, physical activation is simply carried out by heating the sample in an inert atmosphere to a generally higher temperature of 800–1100 °C. Although the activation method cannot be confirmed as the Cabot material is a commercial product, the TGA (Figure 5.9) shows thermal instability above 600 °C. It can therefore be speculated that the sample was activated using the wet oxidation method and heated to temperatures < 600 °C. Activated carbons have also been shown to undergo further weight loss by

releasing CO_2 even when heated under an inert atmosphere to temperatures > 800 °C due to the presence of oxygen containing surface functional groups, such as carboxylic acids and lactones.[8,12–14]

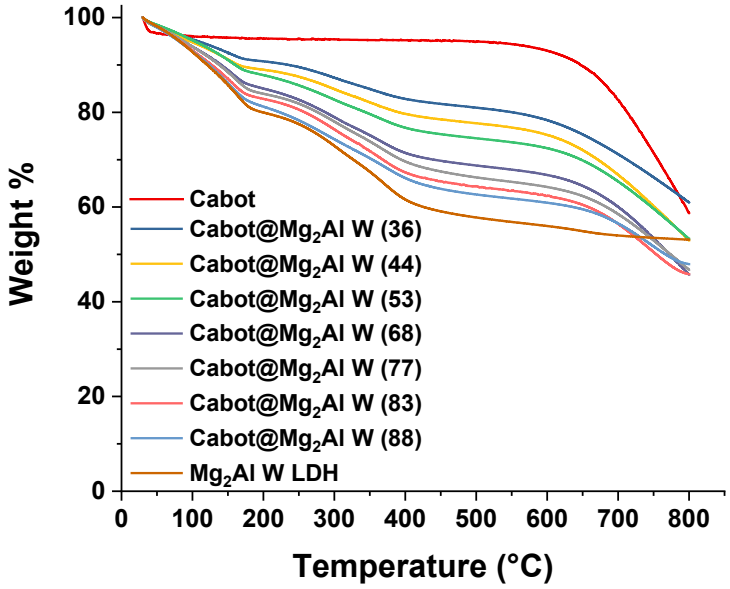


Figure 5.9 - TGA of core@shell materials from 30–800 °C.

The LDH content in the core@shell materials is shown in Table 5.3. They were calculated on the basis of the TGA curves at 400 °C, as this region is thermally stable for both Cabot and LDH materials. Overall, these results agree with the wt% LDH obtained from ICP-MS and elemental analysis of the samples. The instability of the Cabot material at higher temperature, coupled by the further decomposition of LDO into a spinel structure, results in some irregular TGA curves at temperatures > 600 °C. In a normal series of varying wt% in composite materials, it can be assumed that the residual wt% at any point of the TGA curve should not exceed either limit of the parent materials. However, with the exception of Cabot@Mg2Al W (36), all core@shells displayed residual wt% less than that of the pure LDH material at 800 °C. This could potentially be due to the fact that the LDO can act as a catalyst, which could allow for the removal of oxygen-containing groups on the carbon

surface at a lower temperature. It was shown that the LDH can polarise C=O groups with its Lewis acidic centres and catalyse reactions such as the Knoevenagel condensation, which loses H_2O as a by-product.[15]

Table 5.3 - Targeted wt% LDH, compared to obtained wt% LDH at 400 °C from TGA, compared to wt% LDH obtained from CHN elemental analysis.

Targeted wt% LDH	TGA wt% LDH	Elemental wt% LDH
33	37	36
43	46	44
50	55	53
67	71	68
75	76	77
83	83	83
88	87	88

As shown by the XRD patterns (Figure 4.10 (I)), Bragg reflections can be seen from both LDH and Cabot, proving that both materials are present in the products. The interlayer spacing, calculated from the (003) Bragg reflection, remains the unchanged from the pure Mg_2Al W LDH (7.60 Å). An estimate of the mean crystal size crystal domain length (CDL) in the *c*-axis direction can be obtained by using the Scherrer equation and is shown in Figure 5.10 (II).

$$\mathrm{CDL} = \frac{B\lambda}{\beta \cos\theta}$$

B is the Scherrer constant (0.89), λ is the wavelength of the radiation used (Cu Kα, λ = 1.54 Å), θ is the angle of the (003) Bragg reflection and β is the corresponding full width

at half maximum (FWHM) in radians. The Scherrer equation only provides an estimation of average LDH platelet thickness due to it requiring an uninterrupted, uniform particle.[16]

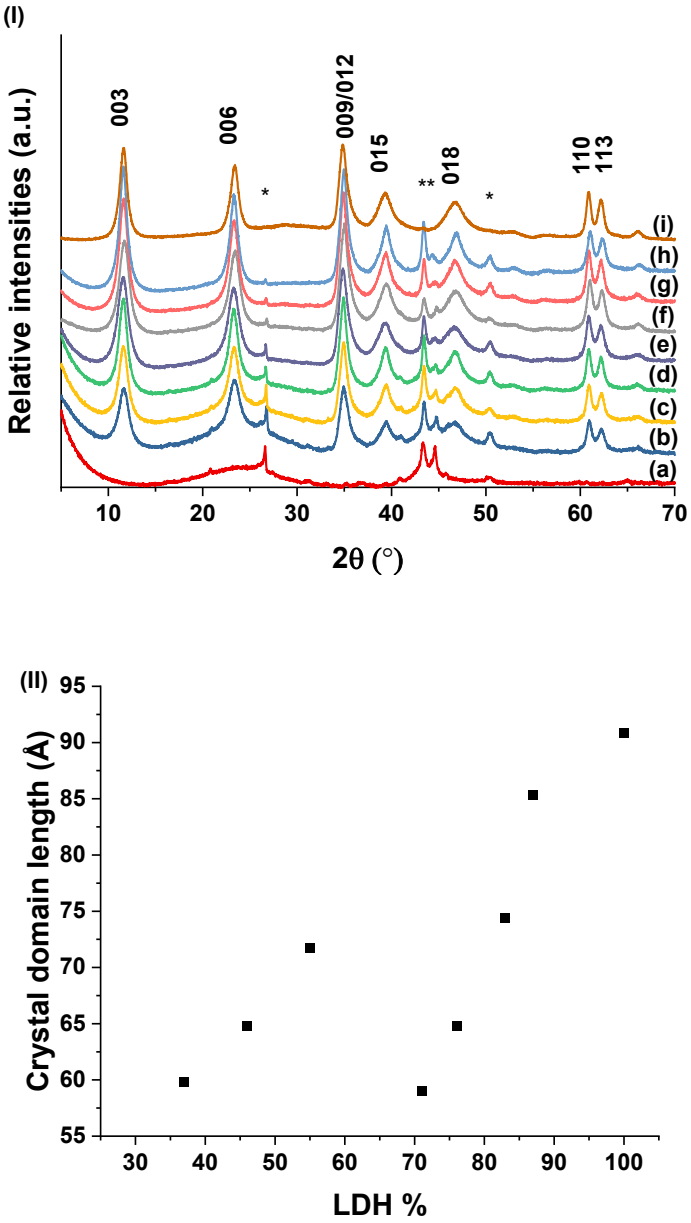


Figure 5.10 - (I) XRD patterns of (a) Cabot, (b) Cabot@Mg_2Al W (36), (c) Cabot@Mg_2Al W (44), (d) Cabot@Mg_2Al W (53), (e) Cabot@Mg_2Al W (68), (f) Cabot@Mg_2Al W (77), (g) Cabot@Mg_2Al W (83), (h) Cabot@Mg_2Al W (88) and (i) Mg_2Al W LDH, and (II) the corresponding crystal domain length of d_{003} as determined by the Scherrer equation. (*) denotes Bragg reflections from Cabot sample.

As shown in Figure 5.10 (II), the trend in CDL along the *c*-direction is composed of two sections: the region from 36 to 53 wt%, and from 68 to 100 wt% LDH. From ratios 36 to 53

wt% LDH, there is an increase in CDL of the LDH particles from 59.8 to 71.8 Å. The value for 68 wt% LDH decreases to smaller than that of 36 wt% LDH (59.0 Å). An increase is then observed from 68 wt% LDH to pure LDH (90.9 Å). No correlation was observed for the lattice parameter *a/b*.

SEM and SEM-Energy Dispersive Spectroscopy (SEM-EDS) were used to probe the morphology and structures of these core@shell materials. Figure 5.11 shows a successful Cabot@LDH core@shell synthesis, confirmed by LDH platelets are growing on the surface of a carbon particle which is illustrated using SEM-EDS. It also shows the different stages of platelet growth on the same activated carbon particle. In Zone I, the particle is an area of exposed carbon. Towards Zone II, few platelets can be seen to grow parallel to the surface. When platelets grow into each other, they then start growing perpendicular and out from the surface of the carbon. This kind of platelet composes the majority of a fully covered surface which can be seen as a hierarchical structure in Zone III.

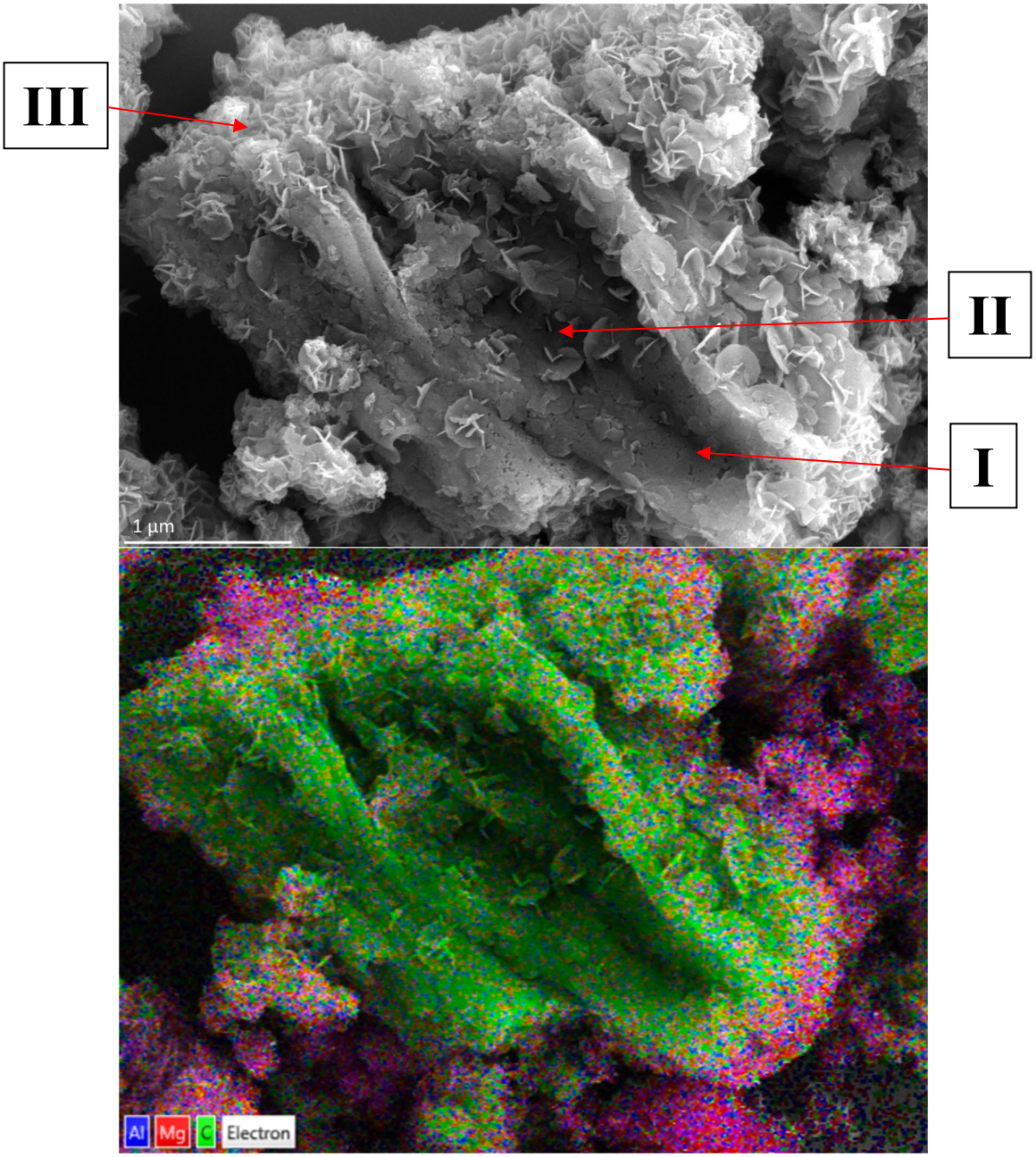


Figure 5.11 - SEM-EDS images of Cabot@Mg_2Al W (44). Colours used for elemental mapping are green (C), blue (Al) and red (Mg).

At the low LDH concentration of Cabot@Mg_2Al W (36), there is only partial coverage of the carbon surface with LDH platelets (Figure 5.12 (a)). The platelets that grow directly on the carbon surface possess a large diameter. Due to the low metal concentration on the surface of the carbon core leading to a less compact distribution of the initial LDH nuclei. This separation allows for the vertical, perpendicular crystal growth to be sacrificed through

Ostwald ripening in favour of the horizontal growth of the LDH platelets which is favoured by the electrostatic interactions between the LDH and core.[4,17] The coverage of the carbon core improves as the wt% LDH increases to 44%. The size of the platelets growing on the carbon particle also increases.

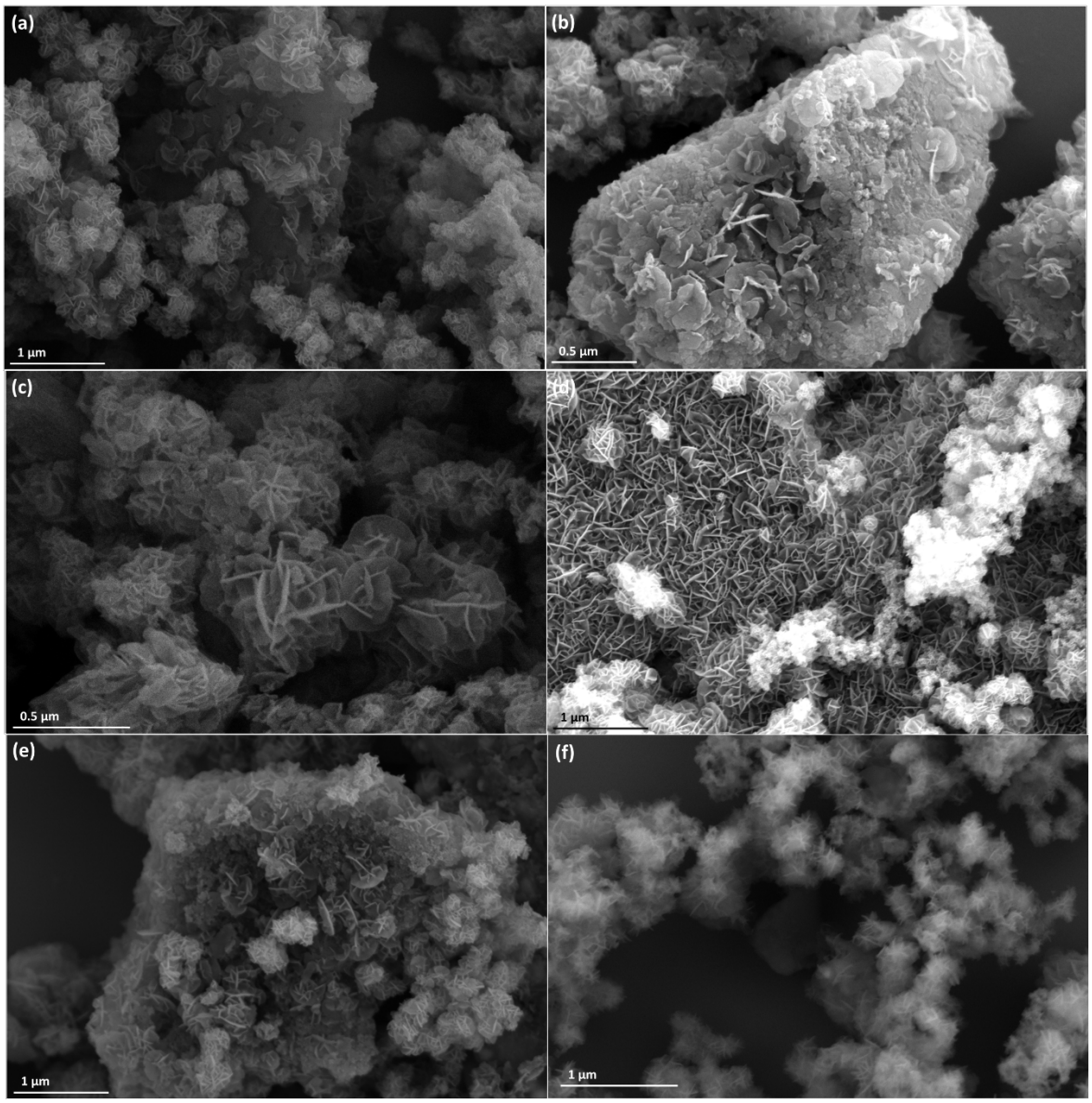


Figure 5.12 - SEM images of (a) Cabot@Mg_2Al W (36), (b) Cabot@Mg_2Al W (44), (c) Cabot@Mg_2Al W (53), (d) Cabot@Mg_2Al W (68), (e) Cabot@Mg_2Al W (77) and (f) Cabot@Mg_2Al W (88).

The coverage is complete when the material reaches 53 wt% LDH in Figure 5.12 (c) and vertical growth of platelets can be seen. This is due to the nucleation sites being closer

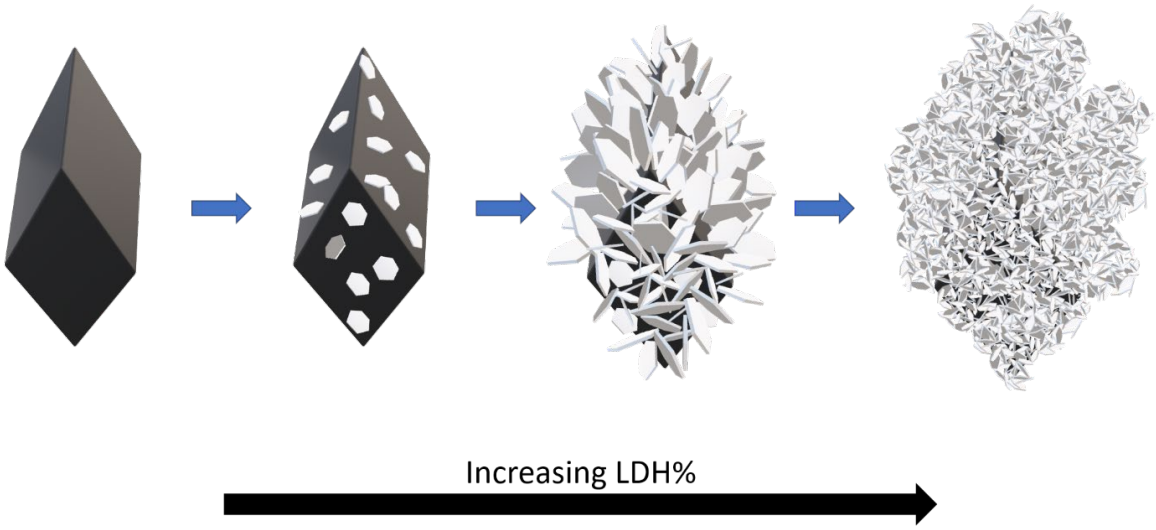
together and therefore vertical growth is favoured. It can be observed that some small rosette aggregates have started to grow as well. The presence of the smaller rosette aggregates further increases as the wt% LDH increases to 68, 77 and 88%. Compared to the larger platelets, which have an average diameter of *ca* 200 nm, the diameter of the smaller aggregates have individual diameters of between 20–50 nm.

The smaller aggregates seem to be growing as a secondary layer on top of the large LDH platelets as seen in Figure 5.12 (d) and (e). The secondary layer of aggregates resembles the morphology of LDHs obtained by the conventional co-precipitation method. At the high wt% LDH of 88% (Figure 5.12 (f)), the core@shell is completely covered by the secondary layer, leading to the appearance of normal, rosette LDH clusters.

This growth of LDH in the core@shell material explains the trend observed in the CDL in Figure 5.10 (II). In the first region between 36 and 53 wt% LDH, the general increase in CDL is due to the growth of the primary layer of large LDH platelets, leading to a local maxima at Cabot@Mg_2Al W (53). However, when the secondary layer of small LDH clusters start to grow at 68 wt% LDH, this decreases the average thickness of LDH, therefore leading to a smaller CDL value of 59.0 Å. The size of the LDH particles in this secondary layer increases with increasing wt% LDH, which therefore results in an overall increase in the CDL in the second section between 68 and 100 wt% LDH.

Scheme 5.1 illustrates the proposed effect of increasing LDH in the Cabot:LDH ratio. At low Cabot:LDH ratios, singular platelets of LDHs grow on the surface of the activated carbon. These platelets grow parallel to the surface until the surface is saturated with LDH platelets due to relatively low LDH concentration compared to the carbon surface area. Then due to the close proximity of the LDH nucleation sites on the horizontal LDH platelets, the horizontal growth is less favoured and vertical platelets are formed instead. The resulting

vertical platelets grow individually and possess large diameters (*ca* 200 nm). As the LDH ratio increases, the vertical platelets grow to cover the entire activated carbon surface. Further increase of wt% LDH at this point will result in the growth of a secondary layer atop the vertical platelets. This layer consists of smaller LDH particles in a rosette structure, with diameters between 20–50 nm, which is more similar to conventional LDH as synthesised using a co-precipitation method. This secondary layer will continue to grow with increasing wt% LDH until it completely covers the original primary layer of large perpendicular platelets, giving the core@shell structure the appearance of a pure LDH material.



Scheme 5.1 - Proposed schematic representation of the different stages of LDH growth on a Cabot particle to give Cabot@Mg_2Al W LDH core@shell.

The N_2 BET surface area shows a strong correlation with the wt% LDH of the sample. The Mg_2Al CO_3 W LDH used possesses a surface area of 165 m^2 g^{-1}, which is an order of magnitude less than Cabot activated carbon (1127 m^2 g^{-1}) (Figure 5.13 (a)). In general, with the increasing amount of LDH present in the sample, the synthesised core@shell materials exhibit slightly lower surface areas than expected when compared to the theoretical value calculated from the parent materials which imitates a mixture of the two materials. This could be due to experimental error. However, a possible reason for the slightly lower surface

area is due to the LDH growing horizontally on the activated carbon particle, leading to the blocking of the porous interior of the Cabot material.

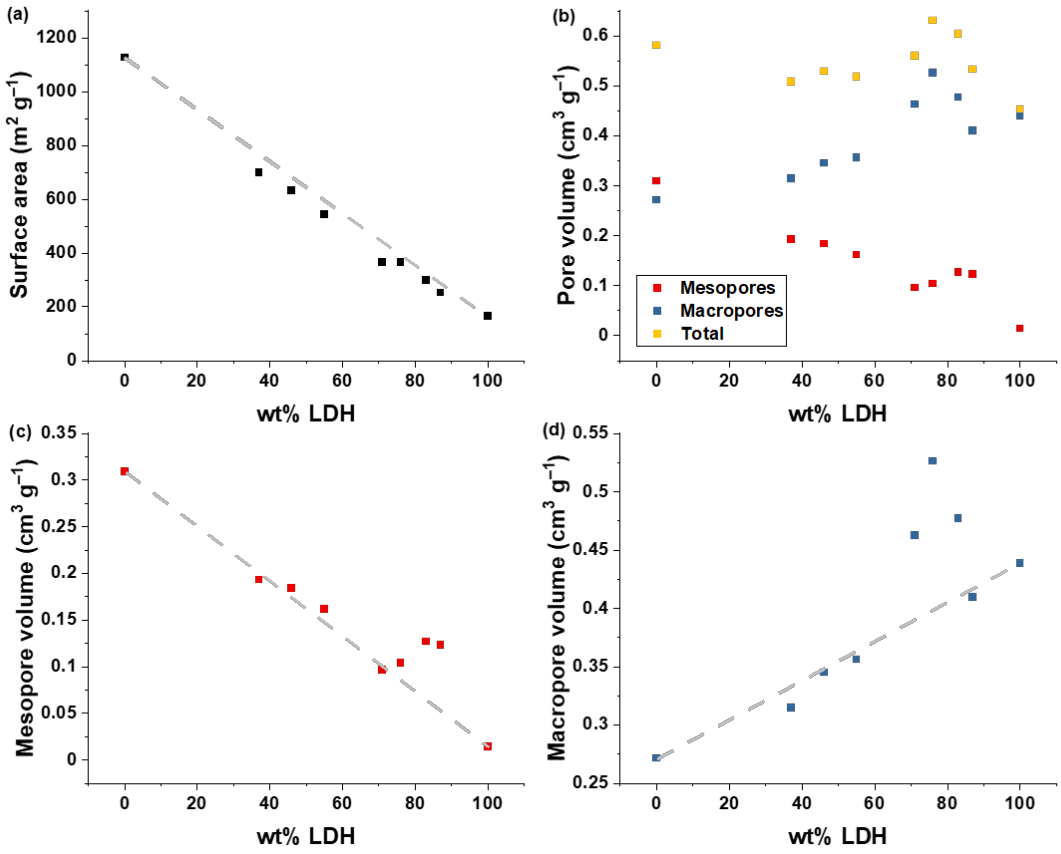


Figure 5.13 - (a) N_2 BET surface area, (b) pore volume, (c) mesopores and (d) macropores of Cabot@LDH core@shell materials in relation to wt% LDH in sample. Dotted line corresponds to expected values of physical mixture.

The mesopores of the core@shell material are shown to decrease with increasing wt% LDH (Figure 5.13 (b)) due to LDH possessing very little mesopores (0.014 cm^3 g^{-1}). Macropores, oppositely, increases with the increase in wt% LDH. Theoretical values for mesopore and macropore values were calculated from the values given by the parent materials and shown in Figure 5.13 (c) and (d). Core@shell materials of 68, 77 and 83 wt% LDH displayed an increase in macropores above the trend of theoretically calculated values for the products. Similarly, core@shell materials of 77, 83 and 88 wt% LDH display higher values for

mesopores when compared to the theoretical value, with Cabot@Mg_2Al W (77) exhibiting the highest value of 0.53 $cm^3\ g^{-1}$. The combination of both trends results in Cabot@Mg_2Al W (68), (77), (83) and (88) exhibiting higher total pore volume when compared to the theoretical values.

Currently, the hypothesis is that the improved macroporosity is the result of the creation of "macropore-like" areas in the space between the primary and secondary layers. Therefore at the higher wt% LDH of 68, 77 and 83, there is access to both the primary layer of large LDH platelets as well as the secondary layer of smaller clusters, leading to an increase in macropores compared to a theoretical value, which does not account for the creation of the additional pore space between the layers. However, when the wt% LDH increases to 88, the primary layer and the area between the layers become inaccessible due to the increased coverage, therefore leading to the pore volume being lowered to the expected value (0.41 $cm^3\ g^{-1}$).

Due to volumetric efficiency, transportation cost and storage, a material with both high surface area and tap density is much more desirable commercially. Tap density is a measurement used in industry to calculate the minimum volume occupied by a given amount of product. Previous methods to increase the surface area of LDHs have mainly led to a decrease in tap density.[18–20] Figure 5.14 displays the tap density of the Cabot@LDH core@shells as a function of their surface area. Cabot possesses the highest tap density, accompanied by the highest surface area (0.34 g mL^{-1} and 1127 $m^2\ g^{-1}$ respectively), whereas Mg_2Al W displayed a tap density amongst the lowest (0.25 g mL^{-1}).

By incorporating the dense and porous Cabot into the composition, there is a general positive correlation between surface area and tap density with decreasing wt% LDH. Cabot@Mg_2Al W (36) displayed only a 0.01 g mL^{-1} decrease in tap density compared to

Cabot. This is due to the low wt% LDH leading to platelet growth which are mainly parallel to the carbon surface (Scheme 5.1) and this allows for more efficient packing of sample. Cabot@Mg_2Al W (83) exhibited a reduced tap density compared to Mg_2Al W (0.24 g mL^{-1}), while Cabot@Mg_2Al W (88) displayed no change in tap density.

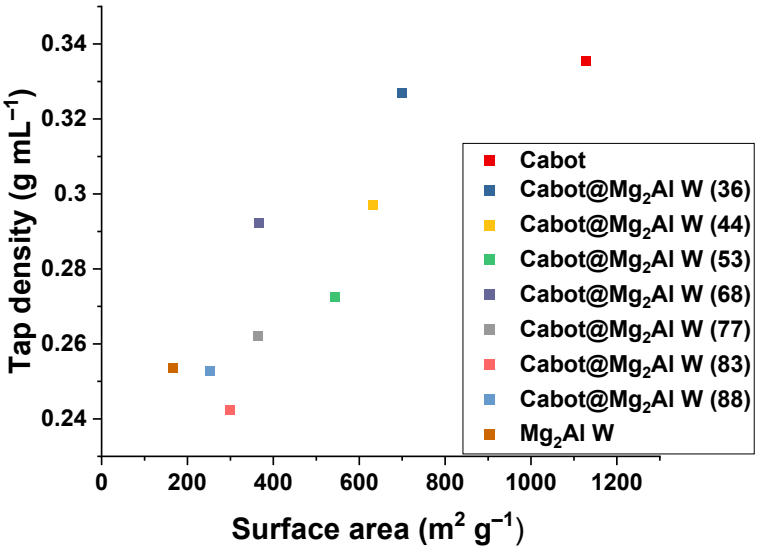


Figure 5.14 - Tap density as a function of N_2 BET surface area for the Cabot@LDH core@shell materials.

5.7 Application of Cabot@Mg_2Al W core@shell materials in CO_2 capture

5.7.1 Cabot@Mg_2Al W LDH for CO_2 capture

In order to access the CO_2 capture abilities of the core@shell series, the samples were tested using a TGA. Sample pre-treatment was carried out at 100 °C for 30 min at 50 °C min^{-1} ramp rate under N_2 atmosphere. Samples were then exposed to an atmosphere with a composition of 33:67 CO_2:N_2. The goal of pre-treatment at 100 °C was to dehydrate the Cabot material while maintaining the LDH composition without transforming it into an LDO. The study of higher pre-treatment temperatures will be explored in Section 4.6.3.

Figure 5.15 shows the CO_2 uptake for the core@shell series, the dotted line indicates the expected value from a physical mixture with the same wt% LDH. Firstly, it is clear that using the set pre-treatment method, the pure Cabot sample does not display any significant CO_2 capture abilities (0.02 mmol g^{-1}). This could be due to incomplete removal of H_2O in the pores which can lead to ineffective CO_2 capture. The dotted line indicates the expected value for a physical mixture, therefore any points above the line can be seen as showing synergy. The series of core@shell materials show a general upward trend in CO_2 capture with increase in wt% LDH. This is due to LDH being the sole active CO_2 capture species using this pre-treatment method. Cabot@Mg_2Al W (44), (53) and (68) all displayed synergistic effects, with Cabot@Mg_2Al W (53) exhibiting the highest CO_2 capture value of 0.82 mmol g^{-1}. Cabot@Mg_2Al W (44) and (68) showed similar values of 0.75 and 0.73 mmol g^{-1} respectively. These samples were shown previously to have a good population of the primary layer of large platelets, with Cabot@Mg_2Al W (53) displaying the best coverage of the carbon surface while showing no evidence for the secondary layer of small LDH clusters.

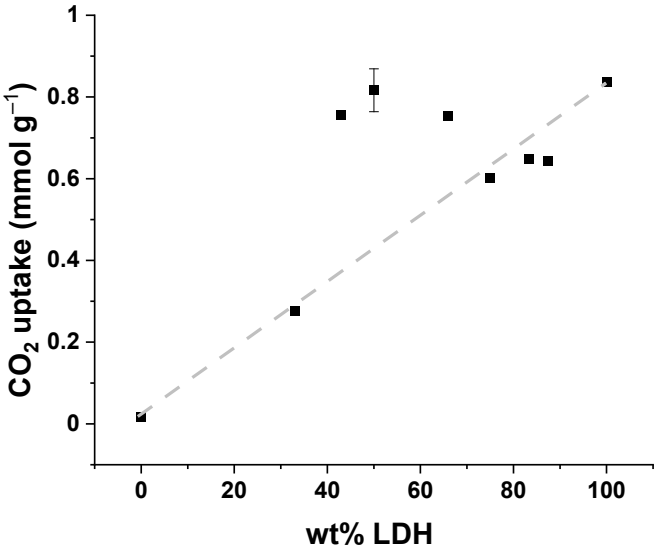


Figure 5.15 - CO_2 adsorption for Cabot@Mg_2Al W core@shell materials. Samples were pre-treated at 100 °C for 30 min at 50 °C min^{-1} ramp rate under N_2 atmosphere. The CO_2 testing atmosphere was 33:67 CO_2:N_2 and the adsorption temperature was 30 °C. Dotted line indicates the value expected from physical mixture.

CO_2 capture values can also be normalised to the amount of LDH in the core@shell as the LDH is the only active species in the material. The value to which the core@shells are compared to is 0.84 mmol g_{LDH}^{-1}, obtained from the CO_2 capture value of pure LDH. As seen in Figure 5.16, Cabot@Mg_2Al W (36) and (77) exhibited values similar to that of pure LDH. Cabot@Mg_2Al W (44) displayed the highest value of 1.76 mmol g_{LDH}^{-1}, more than double that of the pure Mg_2Al W LDH. Cabot@Mg_2Al W (53) and (68) also exhibited high values of 1.63 and 1.14 mmol g_{LDH}^{-1} respectively.

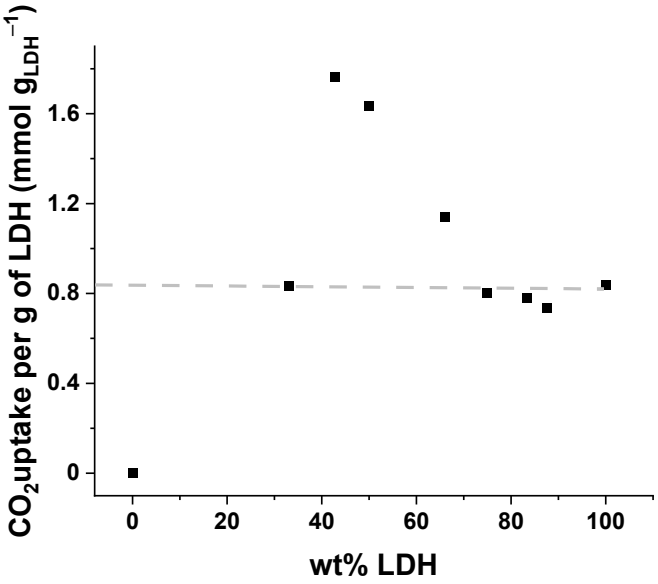


Figure 5.16 - CO_2 adsorption for Cabot@Mg_2Al W core@shell materials normalised for amount of LDH in sample. Samples were pre-treated at 100 °C for 30 min at 50 °C min^{-1} ramp rate under N_2 atmosphere. The CO_2 testing atmosphere was 33:67 CO_2:N_2 and the adsorption temperature was 30 °C. Dotted line indicates expected value from physical mixture.

5.7.2 Ethanol treatment of Cabot@Mg_2Al W core@shells

In Chapter Three and Four, it was shown that ethanol treated LDHs exhibited the largest improvement in CO_2 capture abilities of the solvent treated LDHs. Therefore an ethanol treatment was applied to improve the properties of Cabot@LDH (Cabot@Mg_2Al E (53) and (77)). An increase in surface area in all the ethanol treated samples can be observed. Cabot@Mg_2Al W (77) experienced the largest increase in surface area of 143 m^2 g^{-1} (Table 5.4).

Table 5.4 - N_2 BET surface area of water washed and ethanol treated Cabot@Mg_2Al core@shells.

wt% LDH	N_2 BET surface area (m^2 g^{-1})	
	Water washed	Ethanol treated
53	544	635
77	365	508
100	165	201

Despite an increase in surface area, there was no observable difference between the water washed and solvent treated core@shell of 53 wt% LDH with respect to CO_2 uptake (Figure 5.17). The improvement from solvent treatment is more evident in Cabot@Mg_2Al E (77) with an increase in CO_2 capture value to 1.24 mmol g^{-1}, exhibiting an 82% increase compared to its water washed counterpart. As explored previously, the higher wt% LDH of 77% leads to the growth of the secondary layer of small LDH clusters. This layer is not interacting directly with the core and therefore can be more readily exfoliated, leading to the largest increase in surface area for this core@shell series. This increase in surface area, as a result of exfoliated LDH layers, therefore leads to more CO_2 uptake as the exposed LDH surface is more active towards CO_2 with this pre-treatment method.

When CO_2 adsorption was normalised with respect to LDH, the CO_2 uptake per g of LDH of Cabot@Mg_2Al E (53) is shown to be less active than the water washed core@shell of 44 wt% LDH. Cabot@Mg_2Al E (77) displayed similar capture values to Cabot@Mg_2Al E (53), but still less than that of the highest water washed core@shell (Figure 5.18).

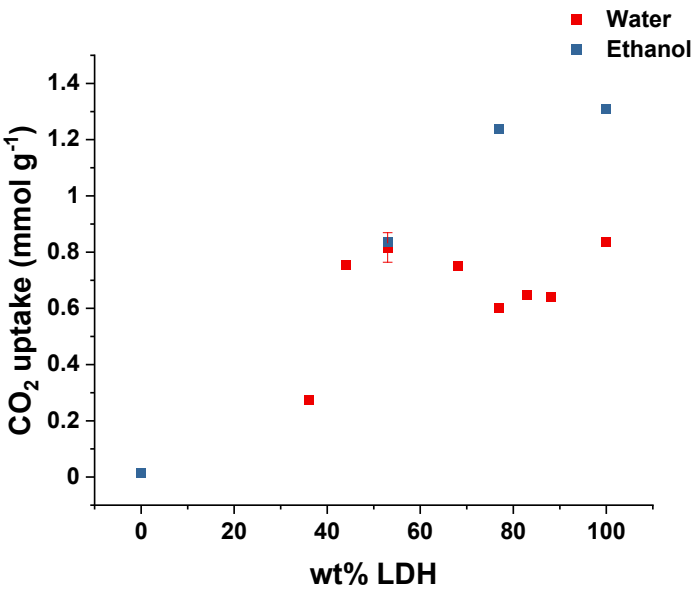


Figure 5.17 - CO_2 adsorption for Cabot@Mg_2Al E core@shell materials compared with Cabot@Mg_2Al W. Samples were pre-treated at 100 °C for 30 min at 50 °C min^{-1} ramp rate under N_2 atmosphere. The CO_2 testing atmosphere was 33:67 CO_2:N_2 and the adsorption temperature was 30 °C.

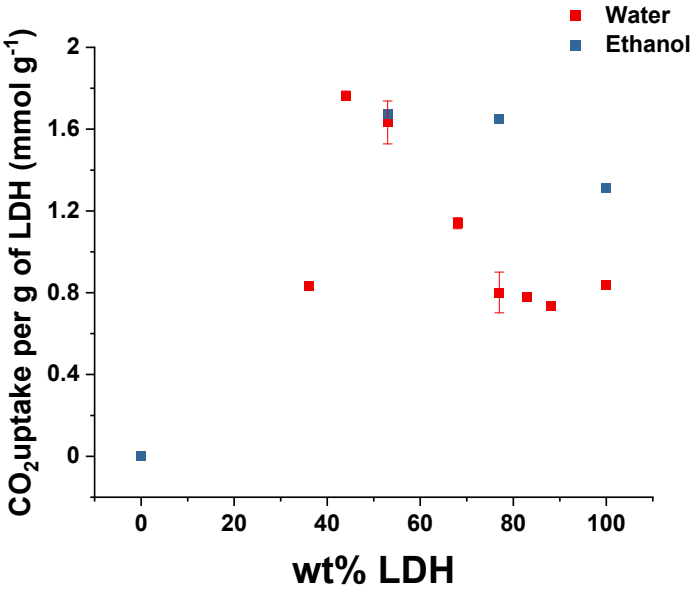


Figure 5.18 - CO_2 adsorption for Cabot@Mg_2Al E core@shell materials normalised for amount of LDH in sample compared with Cabot@Mg_2Al W. Samples were pre-treated at 100 °C for 30 min at 50 °C min^{-1} ramp rate under N_2 atmosphere. The CO_2 testing atmosphere was 33:67 CO_2:N_2 and the adsorption temperature was 30 °C.

5.7.3 Cabot@Mg_2Al W (53) LDO for CO_2 capture

Cabot@Mg_2Al W (53) LDOs will be studied in this section for their use in CO_2 capture as it has been shown in Chapter Three that LDOs exhibit higher CO_2 capture performances compared to their LDH counterparts. Prior to testing any Cabot@LDO samples, different pre-treatment conditions were tested on the Cabot base material to try to optimise conditions. For these tests, the ramp rate was set at 50 °C min^{-1}.

Between 200 and 500 °C, there is no noticeable difference in CO_2 uptake, with values averaging between 0.53–0.55 mmol g^{-1} (Figure 5.19). Compared to the Cabot CO_2 uptake with the 100 °C pre-treatment (0.02 mmol g^{-1}), this is a dramatic increase and would therefore suggest a pre-treatment temperature of 100 °C was not sufficient to completely dehydrate the Cabot material. Between these temperature ranges, TGA showed no change in composition in the Cabot material. Dehydration of the material also occurred nmore thoroughly, therefore leading to the consistency in the readings across this range. From temperatures ≥ 600 °C, a sharp drop-off can be observed. The prolonged calcination at higher temperatures also resulted in lower wt% than previously observed in Figure 5.9. The sample treated at 800 °C retained only 15.6 wt% compared to 58.7 wt% obtained from the TGA curve.

When varying the calcination time between 1 h and 6 h at 400 °C, the CO_2 capacity of the resulting materials remained the same, further proving the thermo-stability of core material at this temperature (Figure 5.20). Due to the consistency of CO_2 capture ability of Cabot with respect to calcination time, 2 h will be chosen moving forwards as it is shown to be the optimal time for $Mg_{1.9}Al$ W LDH from Chapter Three.

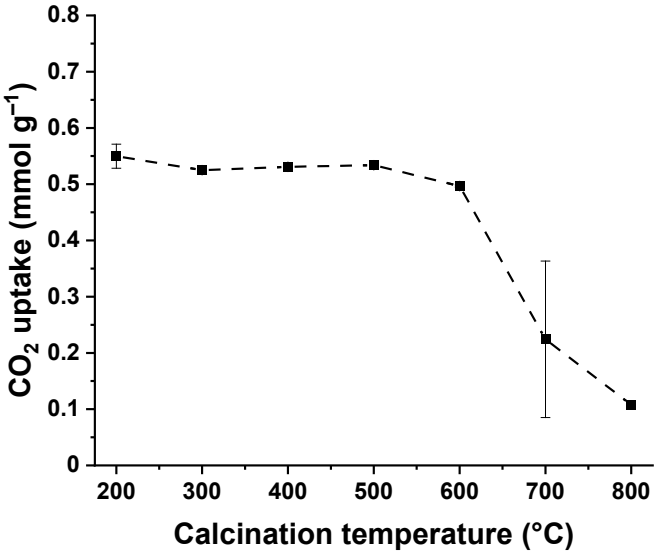


Figure 5.19 - CO_2 adsorption for Cabot calcined at different temperatures for 2 h with 50 °C min^{-1} ramp under N_2 atmosphere. The CO_2 testing atmosphere was 33:67 CO_2:N_2 and the adsorption temperature was 30 °C.

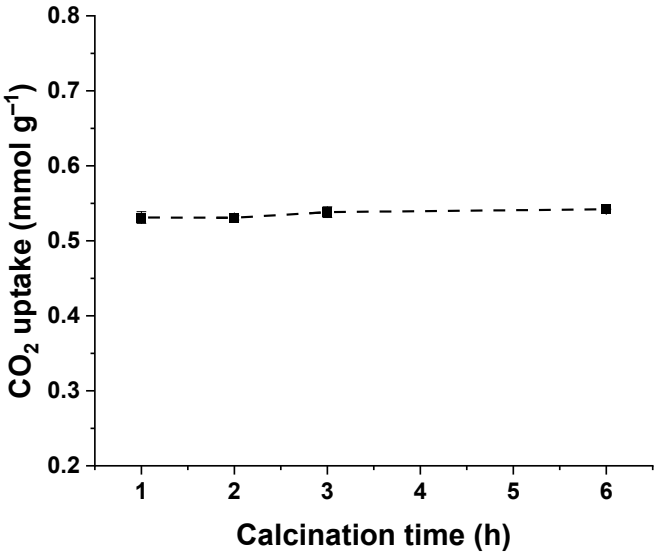


Figure 5.20 - CO_2 adsorption for Cabot calcined at 400 °C with 50 °C min^{-1} ramp for various times under N_2 atmosphere. The CO_2 testing atmosphere was 33:67 CO_2:N_2 and the adsorption temperature was 30 °C.

Table 5.5 compares Cabot with other activated carbon samples reported in literature. The Samchunri sample possesses the most similar physical properties compared to Cabot, but displays a CO_2 capture value of 3.23 mmol g^{-1}, approximately a 6-fold increase compared to Cabot (0.53 mmol g^{-1}).[21] Filtrasorb, with a lower surface area and pore volume, exhibited

a similar capture value of 0.57 mmol g^{-1}, while carried out at a lower adsorption temperature.[22] It has been shown that lower adsorption temperatures lead to higher capture values. The differences between the capture values from literature could be due to different activation methods / temperatures during the production of the activated carbon, or different post-synthesis surface modifications to change the affinity for CO_2. The benefits of Cabot is the relative stability and consistency of CO_2 capture ability between 200 and 600 °C, as well as the insensitivity towards calcination time, which allows for more flexible conditions which are more favourable for the LDH used.

Table 5.5 - Comparison of physical properties and CO_2 capture between Cabot and other commercial activated carbon samples.

	Samchunri[21]	**Filtrasorb**[22]	**Norit**[23]	**Cabot**
Pore volume (cm^3 g^{-1})	0.6-0.8	0.48	-	0.87
Surface area (m^2 g^{-1})	1300	954	-	1127
Pre-treatment temperature (°C)	50	300	200	400
Pre-treatment time (h)	6	1	4	2
CO_2 capture (mmol g^{-1})	3.23	0.57	2.46	0.53
CO_2 capture temperature (°C)	25	25	21	30

Figure 5.21 shows CO_2 capture ability of Cabot@Mg_2Al W (53) after calcining at different temperature for 2 h with a ramp rate of 50 °C min^{-1}, and comparing it with both parent materials. The results are compared with the theoretical value of a physical mixture of the same composition in Figure 5.22.

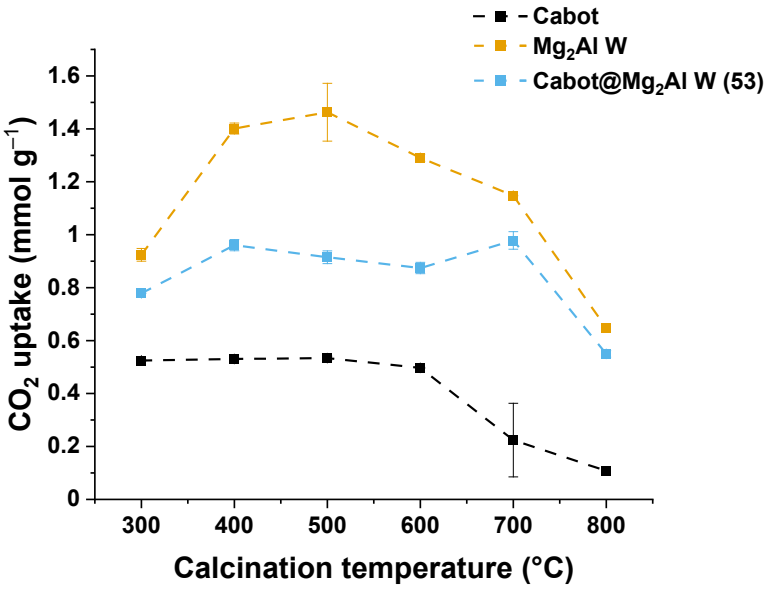


Figure 5.21 - CO_2 capture of Cabot, Mg_2Al W LDH and Cabot@Mg_2Al W (53) with various calcination temperature for 2 h and 50 °C min^{-1}. The CO_2 testing atmosphere was 33:67 CO_2:N_2 and the adsorption temperature was 30 °C.

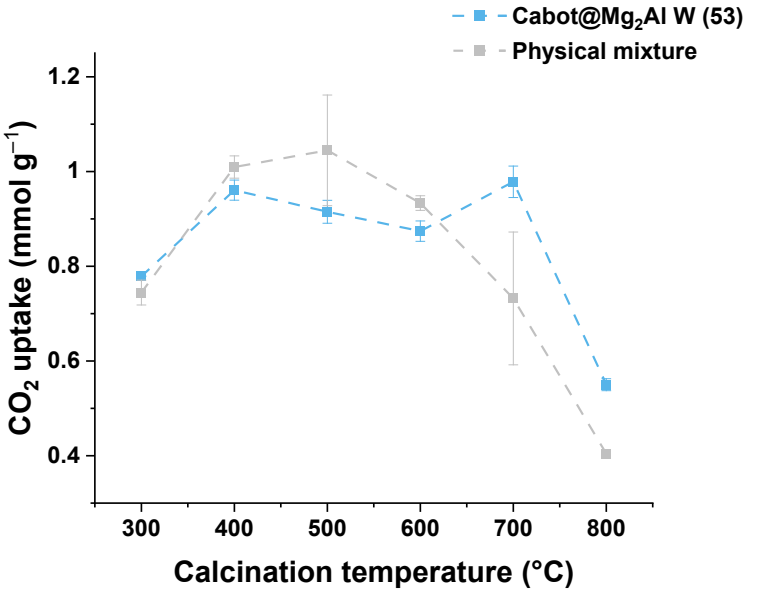


Figure 5.22 - CO_2 capture of Cabot@Mg_2Al W (53) with various calcination temperatures for 2 h and 50 °C min^{-1} ramp under N_2 atmosphere. Grey points represent expected values for a physical mixture. The CO_2 testing atmosphere was 33:67 CO_2:N_2 and the adsorption temperature was 30 °C.

For the CO_2 capture of Mg_2Al W, the results agree with those reported in previous reports in literature[24–26] and those of Chapter Three, with performance reaching a peak at 400 °C,

and decreasing drastically when calcination temperature exceeds 700 °C. The CO_2 capture ability of the core@shell material is shown to be less than the LDO, regardless of calcination temperature. This is as expected as LDO is the main active species in the core@shell, therefore with only 53% of the sample being composed of LDH, a lower capture value can be expected when compared to the LDO. However, unlike both Cabot and LDH which see a drastic decrease when calcined at 700 °C, the core@shell exhibited the highest capture value at 700 °C of 0.98 mmol g^{-1}. Preliminary evidence from residual wt% post calcination from the TGA suggests that when exposed to high temperatures, the LDO in the structure could act as a catalyst that promotes the decomposition of the carbon core, leading to a pseudo-hollow shell material, therefore exposing more of the active LDO surface. The CO_2 capture ability of the core@shell displayed relative stability over the temperature range of 400–700 °C, only varying 0.11 mmol g^{-1} between 0.87 and 0.98 mmol g^{-1}, compared to the 0.31 mmol g^{-1} difference observed in both LDO and Cabot samples over the same range. Furthermore, the CO_2 capture of samples calcined at 400 and 700 °C are very similar, 0.96 and 0.98 mmol g^{-1} respectively. These values are more than double that achieved by the graphene oxide/LDO hybrid material calcined at 400 °C for 1 h and a ramp rate of 10 °C min^{-1} (0.45 mmol g^{-1}), as reported by Garcia-Gallastegui *et al*..[6] The higher performance at 700 °C outperforms the expected value of a physical mixture (Figure 4.22). The appearances of these calcined core@shell materials also support the idea of the formation of a pseudo-hollow shell material (Figure 5.23). When calcined at 600 °C, the material remains black / dark grey, which resembles the original Cabot@Mg_2Al W (53) LDH. Further raising the calcination temperature to 700 °C results in the discolouration of the product to form a lighter grey pale pink material with areas of grey. The grey areas have disappeared, leaving a light pink sample when calcined at 800 °C.

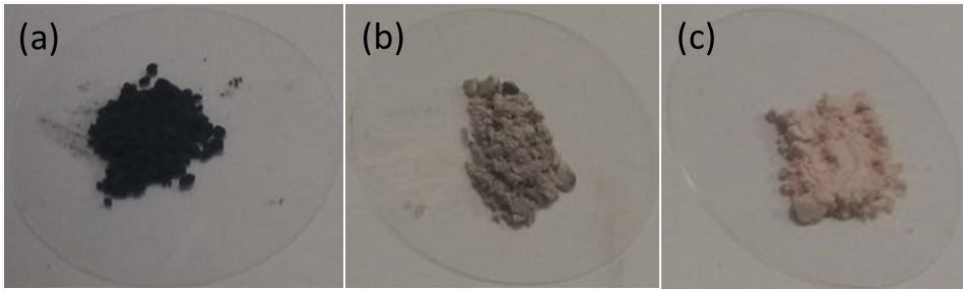


Figure 5.23 - Appearances of Cabot@Mg_2Al W (53) post calcination at (a) 600 °C, (b) 700 °C and (c) 800 °C for 2 h with 50 °C min^{-1} ramp.

Elemental mapping from SEM-EDS images support this hypothesis (Figure 5.24). In Figure 5.24 (a), the concentration of carbon seems the highest, and is reflected in the relative wt% of C/(Mg + Al) = 2.47, as determined by the elemental mapping. The high intensity of C is also accompanied by a slight decrease in concentration in Mg^{2+} and Al^{3+}. When calcined at 600 °C, a small decrease in the elemental ratio (C/(Mg + Al) = 1.65) can be observed. This is due to the slight decrease in carbon content. The drastic change in C content is shown in the mapping of the sample calcined at 700 °C. There is a noticeable difference in the carbon concentration, resulting in a further decrease of the ratio C/(Mg + Al) = 0.31. Despite the loss of carbon content, the material was still able to maintain the core@shell structure (Figure 5.24 (c)).

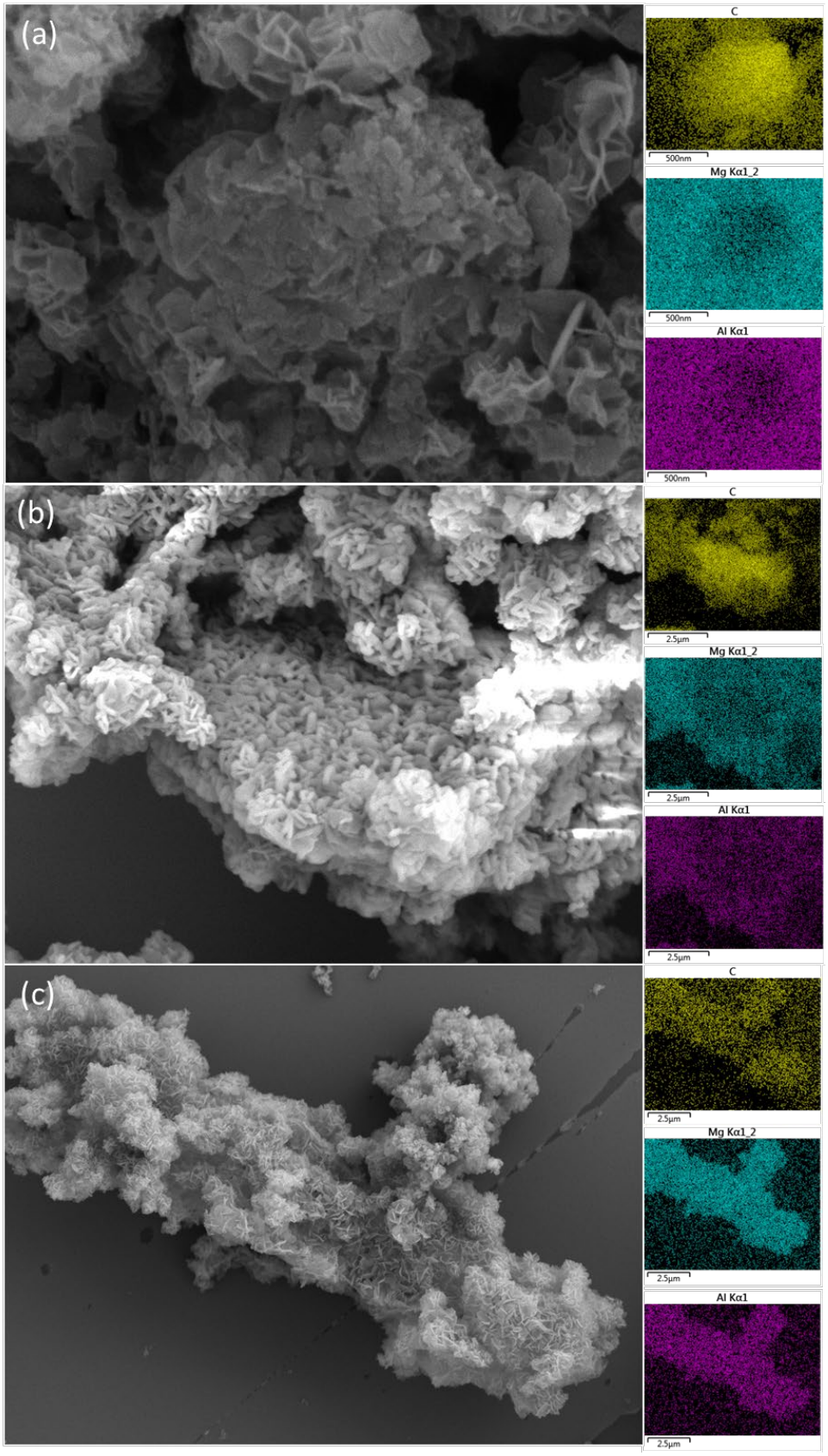


Figure 5.24 - SEM-EDS images of Cabot@Mg_2Al W (53) at (a) room temperature, calcined at (b) 600 °C and (c) 700 °C.

The XRD shows as the calcination temperature increases, the crystalline graphite Bragg reflections at 2θ = 43.3° and 44.6° from Cabot decrease in intensity, especially at 700 and 800 °C (Figure 5.25 (I)). In a pure LDH material, Bragg reflections arising from the formation of the spinel structure are typically observed at those higher temperatures.[27] However, in the core@shell materials, only Bragg reflections that may be indexed to MgO can be seen, no Bragg reflections arising from a spinel phase are observed. There is no currently explanation for this phenomenon in reported in literature and further work should be carried out to understand the mechanism. The surface area experiences an increase with increasing temperature, with the exception of a slight decrease between 500 and 600 °C (Figure 5.25 (II)). In literature, it is shown that higher calcination temperatures above 600 °C leads to a decrease in surface area for LDHs.[28] The increase observed in the Cabot core@shell could be due to the breakdown on the activated carbon, leading to exposure of the internal volume and therefore an increase in surface area.

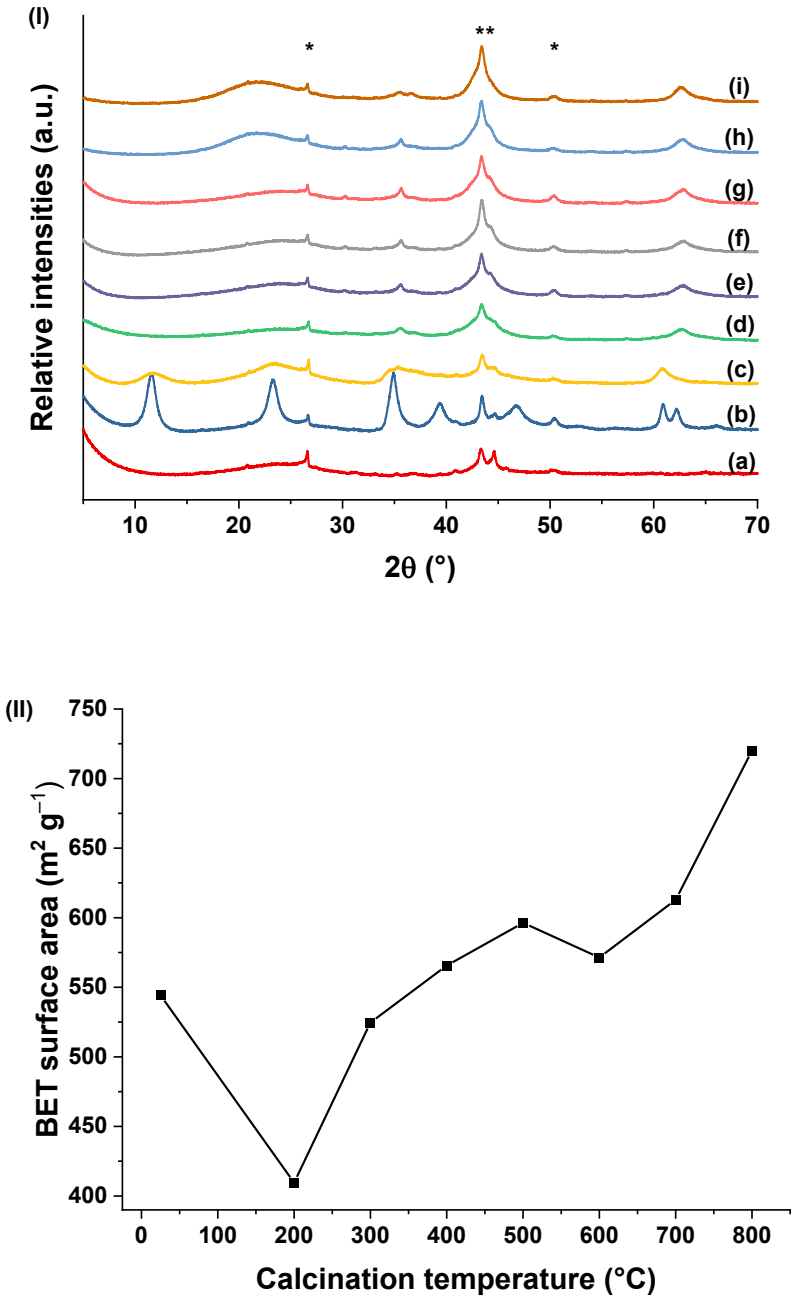


Figure 5.25 - (I) XRD patterns of (a) Cabot, (b) Cabot@Mg_2Al W (53) calcined at (c) 200 °C, (d) 300 °C, (e) 400 °C, (f) 500 °C, (g) 600 °C, (h) 700 °C and (i) 800 °C and (II) the corresponding N_2 BET surface areas. (*) denotes Bragg reflections from Cabot.

5.7.4 Rate of CO_2 adsorption of Cabot@Mg_2Al W core@shells

To be effective CO_2 capture materials, not only do the core@shells need a high gravimetric CO_2 capacity, but they should also display a desirable rate of adsorption to be effective.

To determine the rate of adsorption for these materials, the pseudo-second-order kinetic model has been used. This model is used when the rate-determining step of adsorption involves chemisorption,[29,30] which can be applied to LDO and related materials as the adsorption is combination of physisorption and chemisorption. This model has also been tested along with other adsorption models, such as pseudo-first-order, Thomas, and Yoon and Nelson, on an aluminium based material for CO_2 sorption and shown to have the best correlation with experimental results across different conditions.[31] This model has three assumptions: 1) rate of adsorption is not limited by diffusion, 2) adsorption is not reversible, and 3) concentration of adsorbate remains constant.[32,33] All of these assumptions need to be met for this model to be valid. For the materials mentioned above, they meet the assumptions as 1) rate varies with calcination temperature, not CO_2 (as seen in the CO_2 breakthrough curves shown in Appendix C), 2) desorption has been shown to occur at temperatures higher than current adsorption temperature, usually ~200 °C,[34] and 3) constant CO_2 concentration is maintained using constant flow of gas. Below is the linear form pseudo-second-order kinetic model, proposed by Ho and McKay.[35]

$$\frac{t}{q_t} = \frac{1}{k_2 q_e^2} + \frac{1}{q_e} t$$

t is time in min, q_t is the amount of CO_2 adsorbed at time t (mmol g^{-1}), k_2 is the rate of adsorption in mmol g^{-1} min^{-1} and q_e is the amount of CO_2 adsorbed at equilibrium / final adsorption value (mmol g^{-1}). The rate of adsorption can be deduced from the intercept, while the gradient of the graph of $\frac{t}{q_t}$ v t would provide $\frac{1}{q_e}$, from which the amount of CO_2 adsorbed at equilibrium (max CO_2 capture) can be obtained. Comparing the experimental and theoretical CO_2 capture value, as well as the R^2 values of the fitted graphs, will determine if the pseudo-second-order kinetics model is the best description for these materials.

The comparisons can be seen in Figure 5.26–Figure 5.28. The predicted values for Cabot are identical to those obtained experimentally, whereas the ones predicted for LDO and core@shell materials are slightly higher than those obtained from the TGA, although most are still within experimental error. The explanation for this phenomenon is due to the fact that the adsorption time was limited to 1 h. The slower CO_2 uptake rates of core@shell and LDO didn't allow the material to reach their full CO_2 capacity. The linear fits to the graphs for all samples also possessed very good fits, with most samples possessing $R^2 > 0.99$, shown in Appendix C. Both of these results combine to show that pseudo-second-order kinetic model is indeed a good description of the adsorption curves of all of these materials.

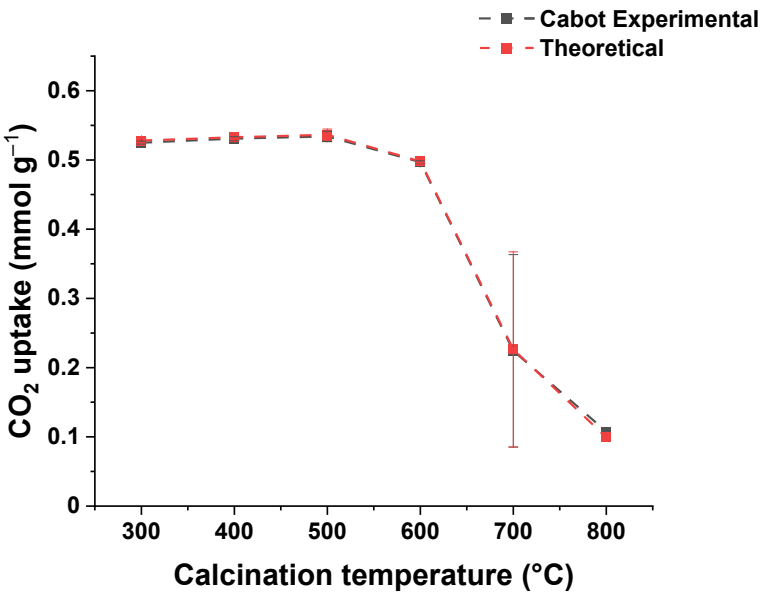


Figure 5.26 - Comparision between experimentally and theoretically determined CO_2 capture values for Cabot calcined at different temperatures.

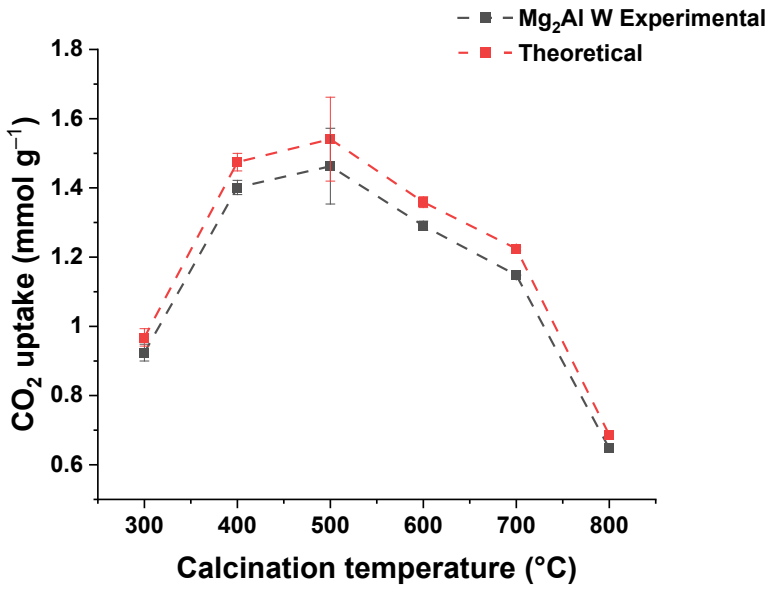


Figure 5.27 - Comparision between experimentally and theoretically determined CO_2 capture values for Mg_2Al W calcined at different temperatures.

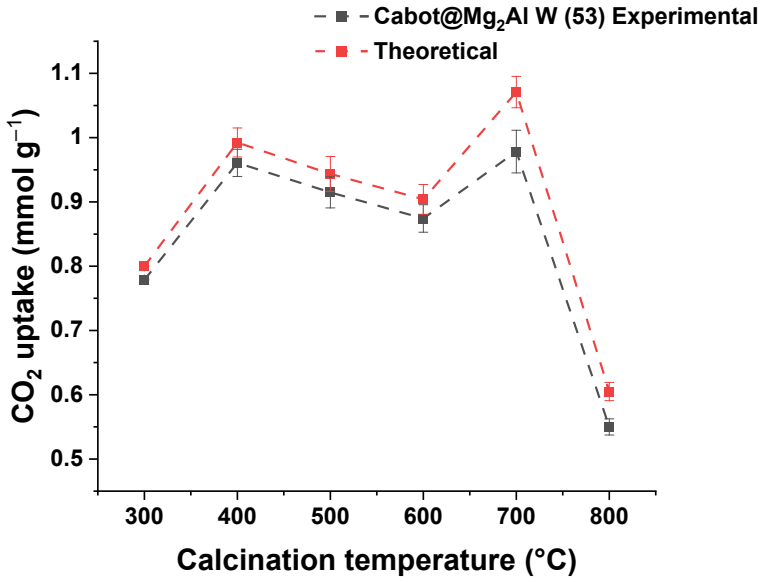


Figure 5.28 - Comparision between experimentally and theoretically determined CO_2 capture values for Cabot@Mg_2Al W (53) calcined at different temperatures.

Rates of CO_2 adsorption of the materials have been calculated and shown in Figure 5.29. Cabot exhibited the highest rate of adsorption at all temperatures, reaching a maximum of 25.33 mmol g^{-1} min^{-1} at a calcination temperature of 400 °C. This is *ca* 50× greater than that of corresponding LDO or core@shell material. This is due to the drastic difference in

surface area between Cabot and LDH, and that activated carbon adsorbs mainly through physisorption which is a faster process than chemisorption, which is more prominent in LDHs/LDOs.[36] Even with the high rate of adsorption, Cabot does not possess a sufficient CO_2 capture capacity due to a less active surface. On the other hand, LDOs, with the highest CO_2 adsorption values at each temperature, displayed the slowest rate of adsorption amongst the 3 materials.

Cabot@Mg_2Al W (53), however, showed a rate of adsorption of roughly double that of LDO between 300–600 °C. The fastest rate of adsorption for the core@shell was 0.63 mmol g^{-1} min^{-1} at 300 °C. 300 °C also resulted in the fastest rate of adsorption for the pure LDO (0.30 mmol g^{-1}). This could be due to the excess hydroxyl groups present after calcination, which might be able to increase the rate of adsorption. At temperatures ≥ 700 °C, the rate of CO_2 adsorption for core@shell drastically decreases and is less than that of the LDOs. This suggests the loss of the contribution from Cabot.

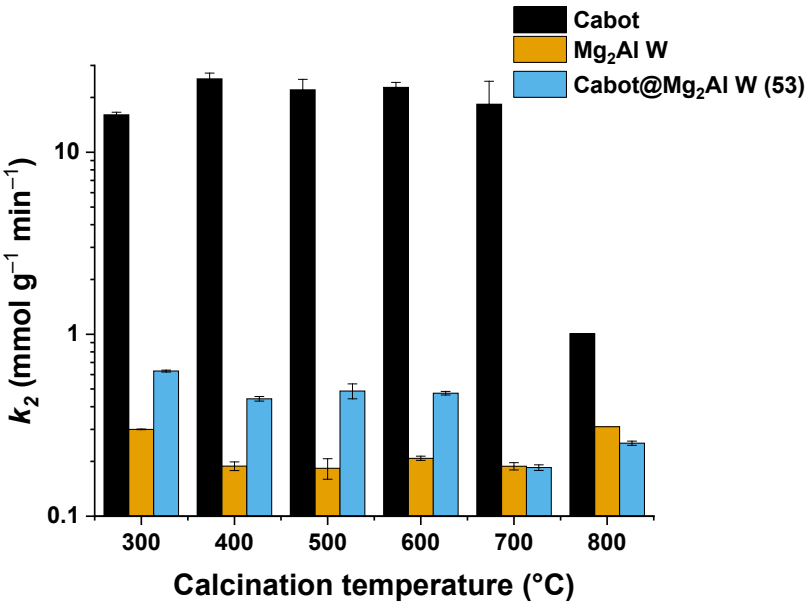


Figure 5.29 - Rate of CO_2 adsorption of Cabot, Mg_2Al W LDO and Cabot@Mg_2Al W (53) core@shell materials calcined at different temperatures as determined by pseudo-second-order kinetics model.

5.8 Carbon core@shells with other carbon materials

5.8.1 Synthesis and characterisation of new carbon@LDH core@shells

Exploring other carbon / activated carbons as core materials could also lead to improvements in CO_2 capture, either through a more active core or better morphology of the core material. This could lead to improved platelet orientation of the LDH on the surface, providing easier access to active sites. To that end, the following materials were selected: MAX (VXCMAX22) and TPK (TPK1099R) are carbon black materials with different morphologies received from Cabot Corporation, while AC (Activated Carbon) is an activated carbon from Sigma Aldrich. Table 5.6 shows the carbon black materials have > 90% carbon content, while AC displayed a surprisingly low carbon content of 66.2%. Even when compared to Cabot, which is also an activated carbon, it showed a much lower carbon content. In addition, the residual weight from TGA at 800 °C is only 21.9%, less than half of that of Cabot (58.7%) (Figure 4.30 (a)).

Table 5.6 - Carbon content and surface area of various carbon materials as determined by CHN elemental analysis and N_2 BET surface area respectively.

Sample	Species	C wt%	N_2 BET surface area (m^2 g^{-1})
MAX	Carbon black	93.5	1362
TPK	Carbon black	99.8	61.7
AC	Activated carbon	66.2	1307
Cabot	Activated carbon	81.7	1127

As shown in the FTIR spectra (Figure 5.30 (b)), despite both Cabot and AC samples being activated carbon, only AC displayed a significant OH stretch (3000–3500 cm^{-1}). Combined with the peak at 1700 cm^{-1}, which corresponds to the C=O stretch, this indicates AC could

possess some carboxylic acid functional group. All carbon species showed peaks belonging to C-H stretches from 2850–3000 cm^{-1}.

AC was chosen as one of the new support materials due to its similar morphology to Cabot (Figure 4.31), while possessing a higher oxygen content, with carboxylic acid functional groups which could lead to a more active surface for CO_2 adsorption. It also has a higher surface area than Cabot. Elemental mapping in SEM-EDS showed an oxygen content of 11.6 wt% MAX was described as a carbon black material with spherical morphology. This would provide a more suitable support structure for more favourable LDH platelet orientation. As shown in literature, with a spherical core material, like SiO_2,[3,37] the platelets grow perpendicularly to the core, therefore exposing more surface area and active sites for CO_2 capture. It was also chosen to compare the difference between activated carbon and carbon black of similar surface area.

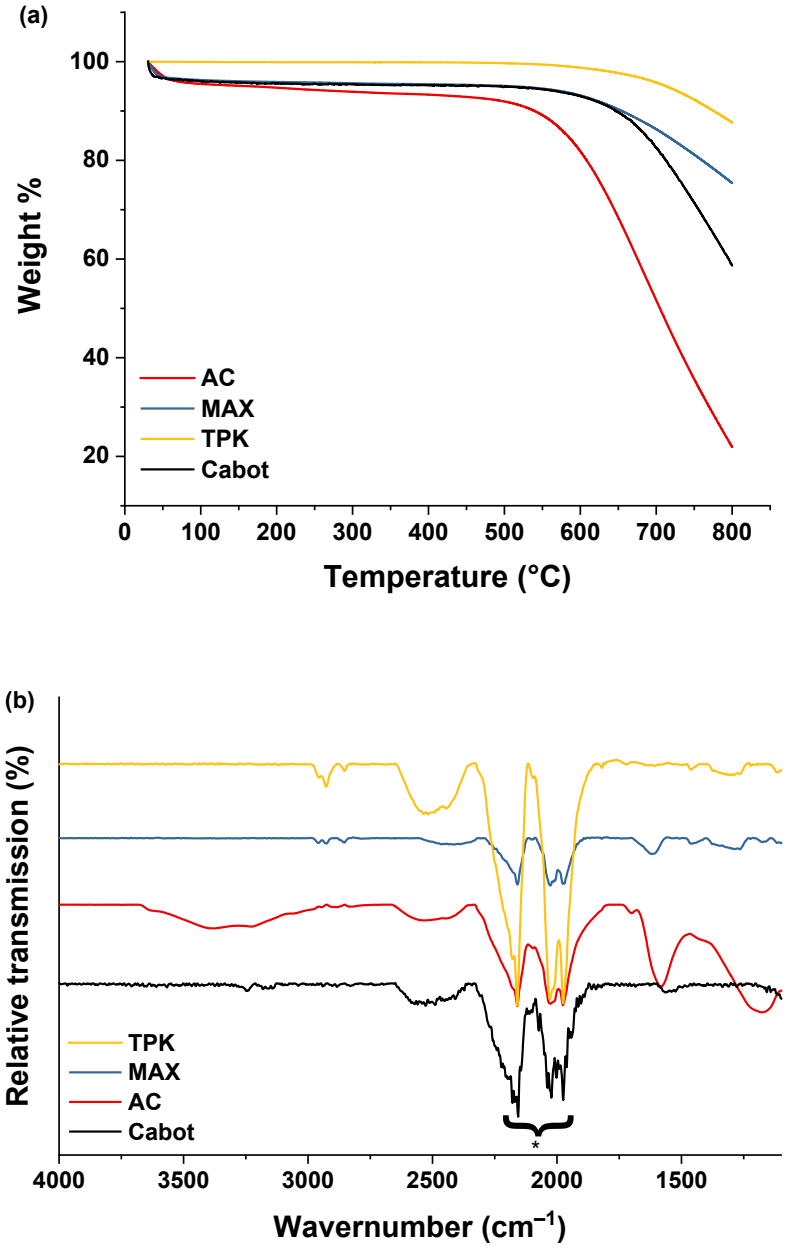


Figure 5.30 - (a) TGA and (b) FTIR spectra of new carbon materials compared to Cabot. (*) denotes signal from sample stage.

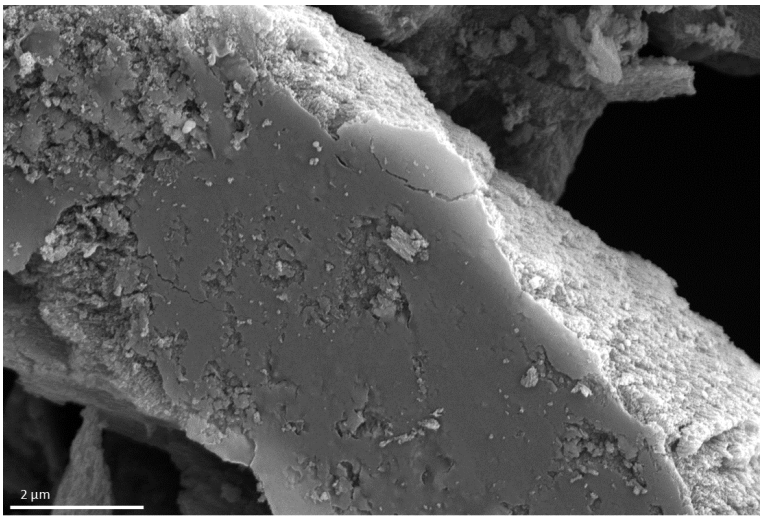


Figure 4.31 - SEM image of AC.

Upon closer inspection of MAX (Figure 5.32 (b)), it is revealed that the spherical morphology was achieved by aggregation of smaller particles. These particles resemble the morphology seen in Printex and Nerox. This could be problematic during the core@shell synthesis process as the stirring of the reaction mixture could cause the core to break apart, hence not providing the desired morphology. As seen in Figure 5.32 (a), the brief sonication period used in the preparation of the sample for SEM led to partial breakdown of the spheres, leading to the thin layer of carbon on the edge of the image.

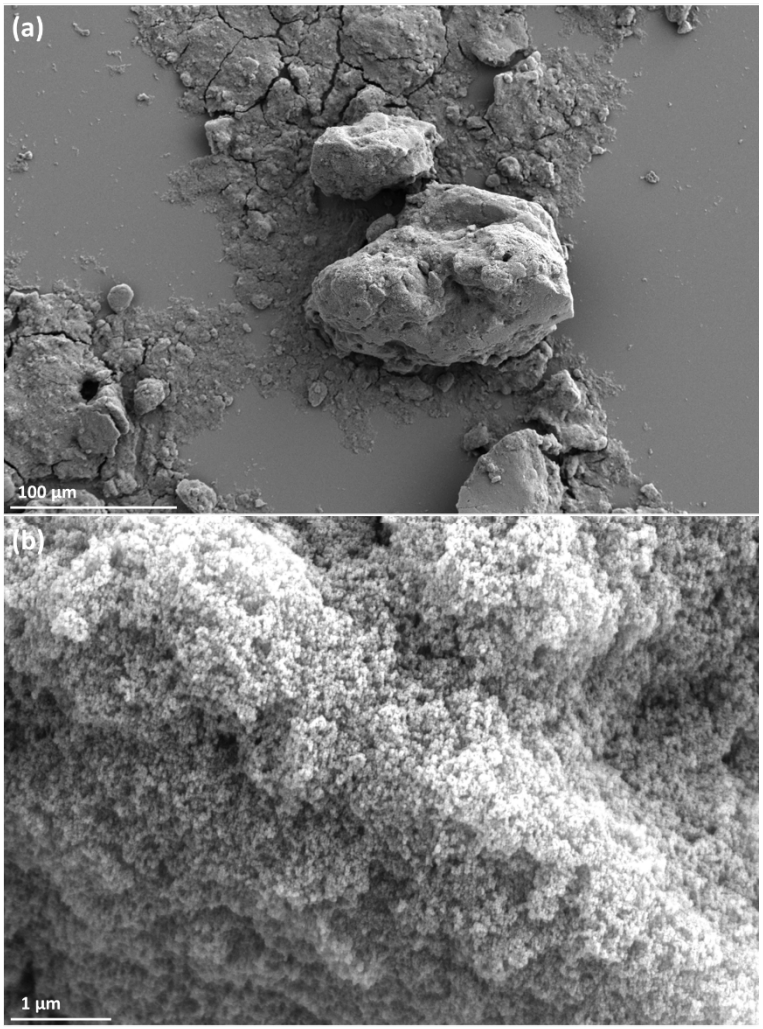


Figure 5.32 - SEM images of MAX with (a) low (250) and (b) high (15K) magnification.

TPK resembles MAX, Printex and Nerox in the large aggregate morphology (Figure 5.33). But upon closer magnification, the individual particles displayed a more regular spherical structure of 50 nm diameter.

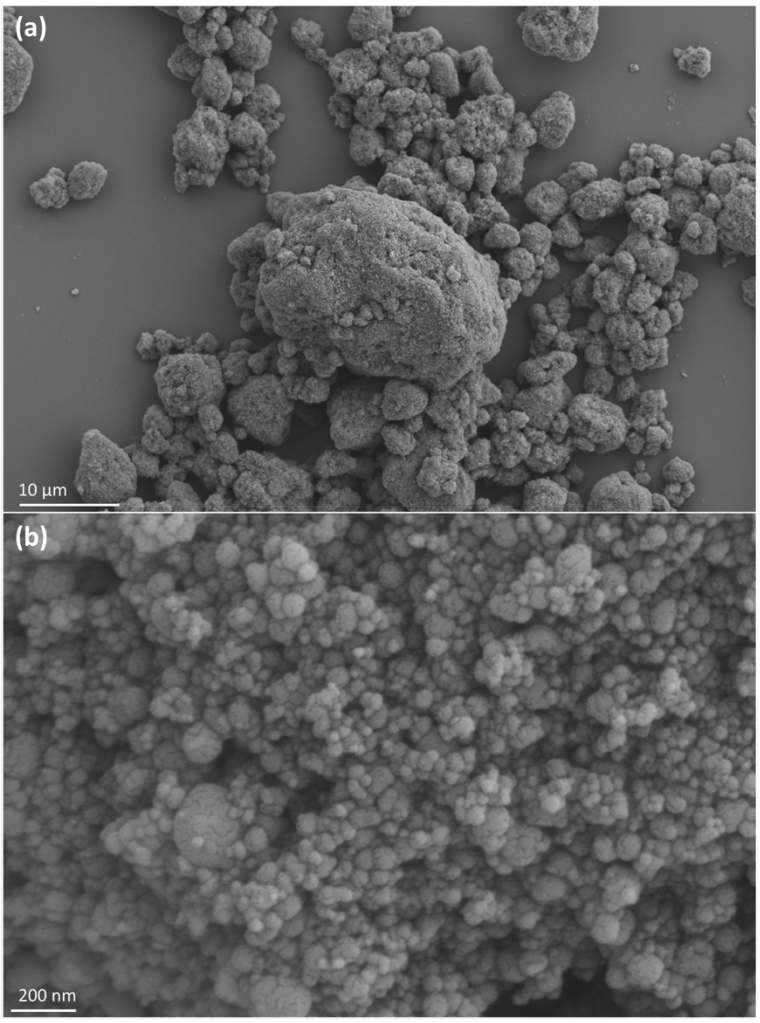


Figure 5.33 - SEM images of TPK with (a) low (1.5K) and (b) high (50K) magnification.

Using the optimised ratio from the previous section, a wt% LDH of 53% was targeted for the synthesis of the core@shell materials with these new carbons. Elemental analysis displayed in Table 5.7 shows the core@shell synthesised with MAX and TPK as the core materials possessed wt% LDH close to those targeted. AC@Mg_2Al W exhibited a wt% LDH of 49%, the lowest of the core@shells with a target wt% of 53%.

Table 5.7 - Carbon content, wt% LDH and surface area of core@shell materials as determined by CHN elemental analysis and N_2 BET surface area respectively.

Sample	C wt%	wt% LDH	N_2 BET surface area ($m^2\ g^{-1}$)
AC@Mg_2Al W (49)	35.5	48.7	744
MAX@Mg_2Al W (53)	45.2	53.4	794
TPK@Mg_2Al W (56)	45.9	55.8	74.3

The morphologies of the new core@shells were investigated using SEM and SEM-EDS. AC@Mg_2Al W (49) displayed the different stages of platelet growth observed in Cabot@Mg_2Al core@shells (Figure 5.34). It is interesting that significantly less LDH platelets can be seen on the smoother surfaces of AC. This incomplete coverage could be due to the slightly reduced LDH content in the material.

MAX@Mg_2Al W (53) displayed less LDH coverage while containing a higher LDH content (Figure 5.35). Moreover, the spherical morphology is absent in the core@shell. It is suspected that the stirring during synthesis broke up the large spherical aggregates into smaller particles. It is suspected that the small particle size of the core material provides a less favourable surface for the LDH to grow on, similar to Nerox and Printex. The final composite material more readily resembles that of a physical mixture. No larger LDH platelets can be seen on the surface of the carbon particle, suggesting that the LDHs grew in a different manner compared to the other core@shells. The LDH morphology is that of a rosette structure, which is the morphology resulting from a conventional co-precipitation method, suggesting there was no favourable interactions between the LDH particles and the carbon surface.

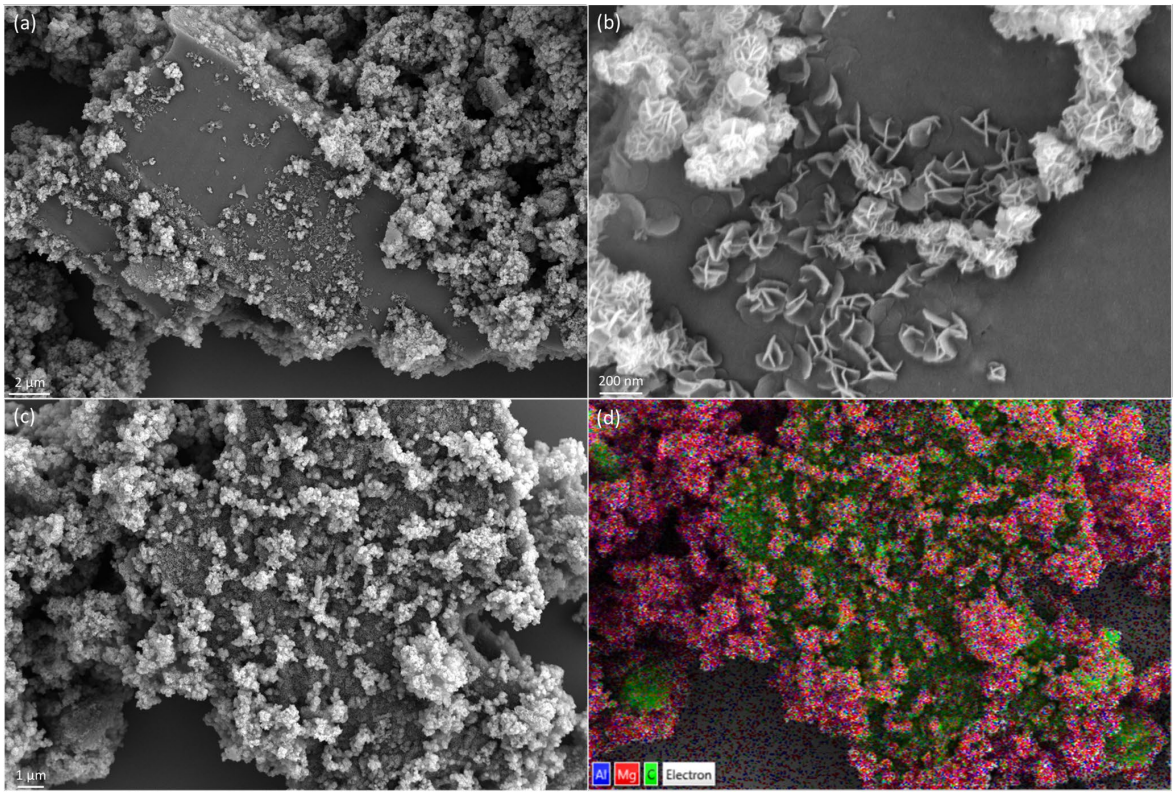


Figure 5.34 - (a)–(c) SEM and (d) SEM-EDS images of AC@Mg_2Al W (49).

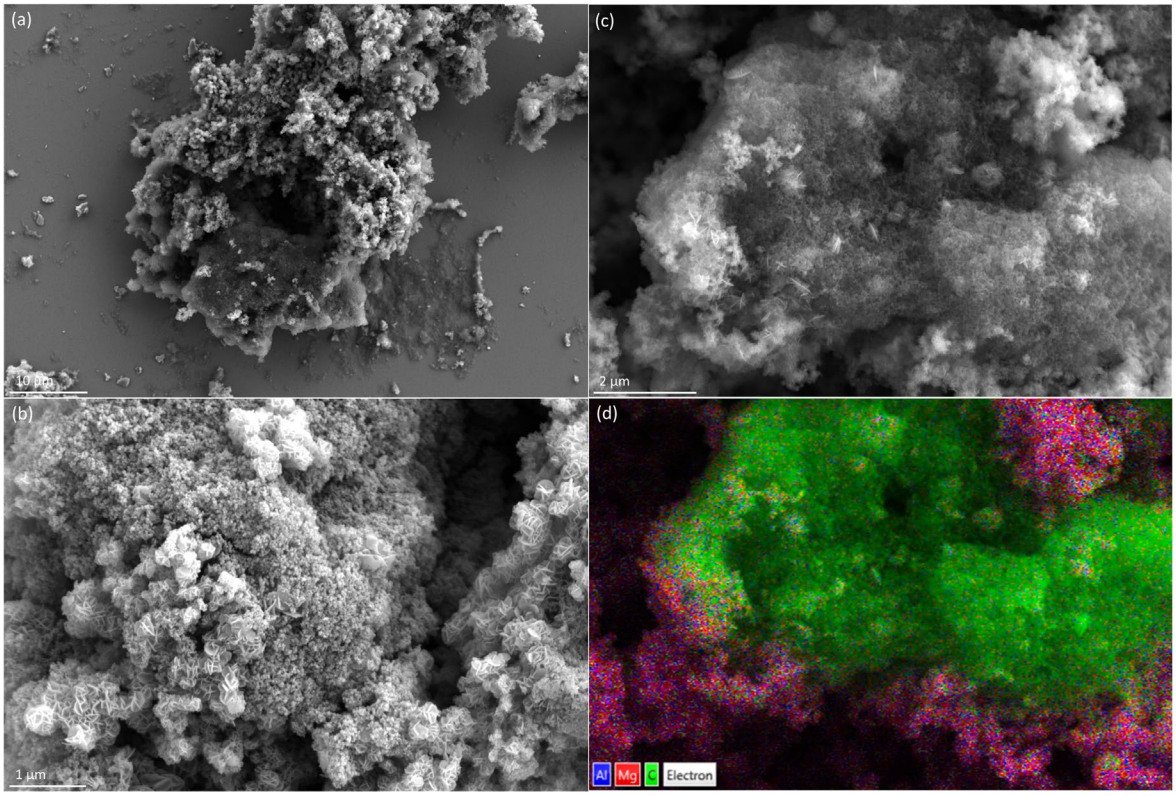


Figure 5.35 - (a)–(c) SEM and (d) SEM-EDS images of MAX@Mg_2Al W (53).

TPK@Mg_2Al W (56), on the other hand, exhibited an LDH morphology resembling the large primary layer seen in Cabot@LDH core@shells (Figure 5.36 (a) and (b)). The LDH platelets displayed diameters of ~200 nm. The carbon core also allowed the LDHs to grow perpendicular to the local carbon materials. However, due to the small nature of the carbon particles, the resulting material presents with regions which resemble an LDH@TPK core@shell (Figure 5.36 (c) and (d)).

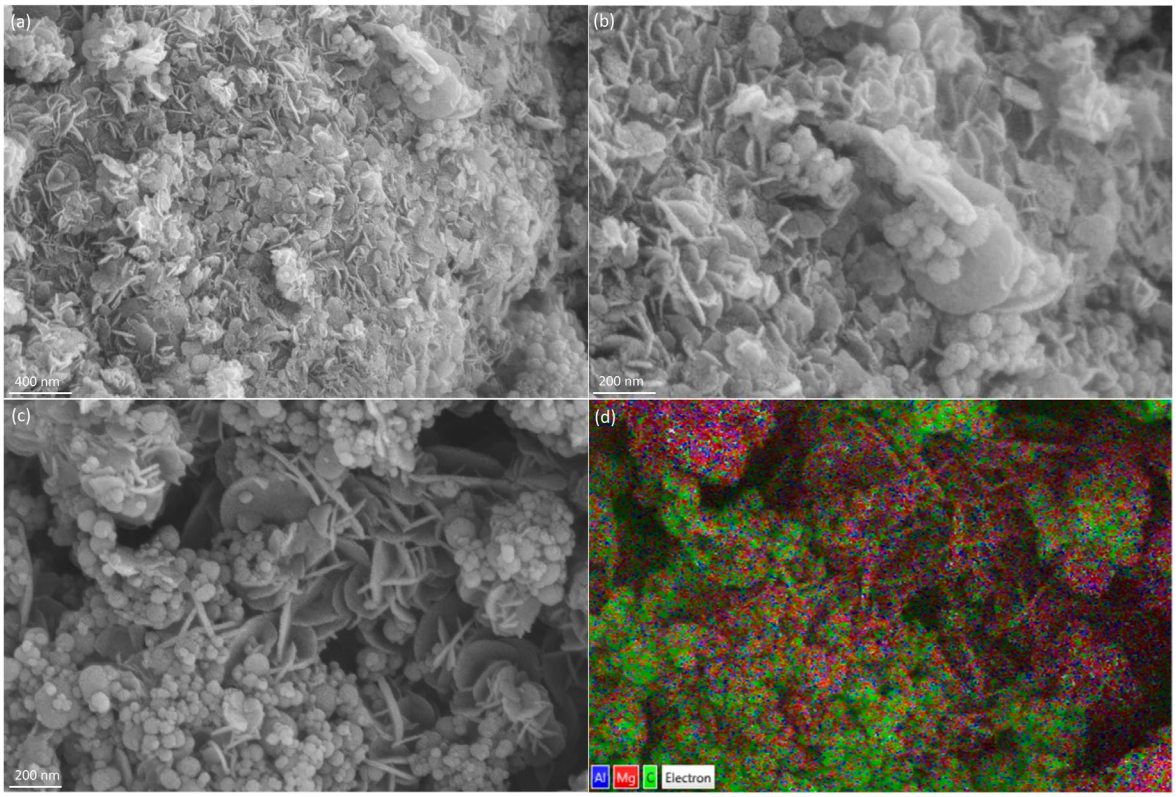


Figure 5.36 - (a)–(c) SEM and (d) SEM-EDS images of TPK@Mg_2Al W (56).

5.8.2 CO_2 adsorption of new carbon@Mg_2Al W LDO core@shell

Utilising the optimised calcination conditions for CO_2 capture from the previous section, the following CO_2 captures were carried out after a pre-treatment of 400 °C for 2 h with a ramp rate of 50 °C min^{-1}.

Comparing the carbon materials, MAX and AC both showed similar CO_2 capture values as Cabot, with 0.52 and 0.57 mmol g^{-1} (Figure 5.37). TPK exhibited no CO_2 capture ability. The slightly higher CO_2 capture performance from AC compared to MAX could be due to more oxygen containing functional groups on the surface of AC, providing an improved adsorption interaction.

Both AC@Mg_2Al W (49) and MAX@Mg_2Al W (53) displayed better CO_2 capture performances than Cabot@Mg_2Al W (53). MAX@Mg_2Al W (53) had a capture value of 1.05 mmol g^{-1}, whereas AC@Mg_2Al W (49) possessed the highest CO_2 uptake of any carbon containing sample (1.24 mmol g^{-1}). This value is comparable to that of Mg_2Al W (1.40 mmol g^{-1}), only exhibiting an 11% decrease in CO_2 capture value while reducing the LDH used by 51%. This is beneficial due to LDH being the more costly material of parent materials.

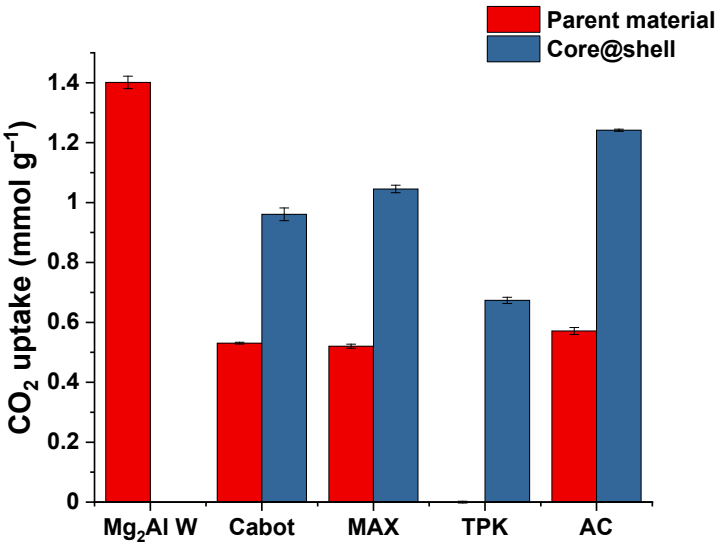


Figure 5.37 - CO_2 capture of various parent materials (red) and core@shell materials (blue) with a calcination temperature of 400 °C for 2 h and 50 °C min^{-1} ramp under N_2 atmosphere. The CO_2 testing atmosphere was 33:67 CO_2:N_2 and the adsorption temperature was 30 °C.

Utilising the pseudo-second-order kinetic model, the rates of adsorption were calculated and displayed in Figure 5.38. Of the carbon materials tested, Cabot still possesses the highest rate of adsorption. AC exhibited a faster rate of adsorption than MAX (6.56 and 3.73 mmol g^{-1} min^{-1}). Similar to Cabot@Mg_2Al W, the rates of adsorption of the core@shell materials decreased significantly compared to the carbon materials, but improved upon Mg_2Al W. The only exception is TPK@Mg_2Al W (56). It was expected that with TPK possessing no CO_2 uptake capacity, there will be no change in the rate of adsorption of the core@shell with respect to Mg_2Al W. Instead, a twofold increase in rate can be observed in TPK@Mg_2Al W (56) (0.36 mmol g^{-1} min^{-1}). This is possibly due to the large LDH platelets present in the core@shell are positioned in a more exposed orientation, allowing for more accessibility to the more active surface of the LDHs.

Despite exhibiting improved CO_2 capture performances, AC@Mg_2Al W (49) and MAX@Mg_2Al W (53) displayed slower rates of adsorption compared to Cabot@Mg_2Al W (53). AC@Mg_2Al W (49) exhibited the lowest rate of capture amongst the core@shells, with a rate of 0.26 mmol g^{-1} min^{-1}. This value is still a 37% increase compared to Mg_2Al W, which combined with their similar CO_2 uptake value, makes the core@shell a better material for CO_2 capture. MAX@Mg_2Al W (53) also shows an improved rate of capture of 0.39 mmol g^{-1} min^{-1}, 105% greater than that of LDH. An increased rate of CO_2 capture from a carbon@LDH core@shell is advantageous due the combination of benefits from both parent materials, a quick adsorption rate from activated carbon and the tolerance of H_2O in flue gas and chemisorption participation from LDH.[36]

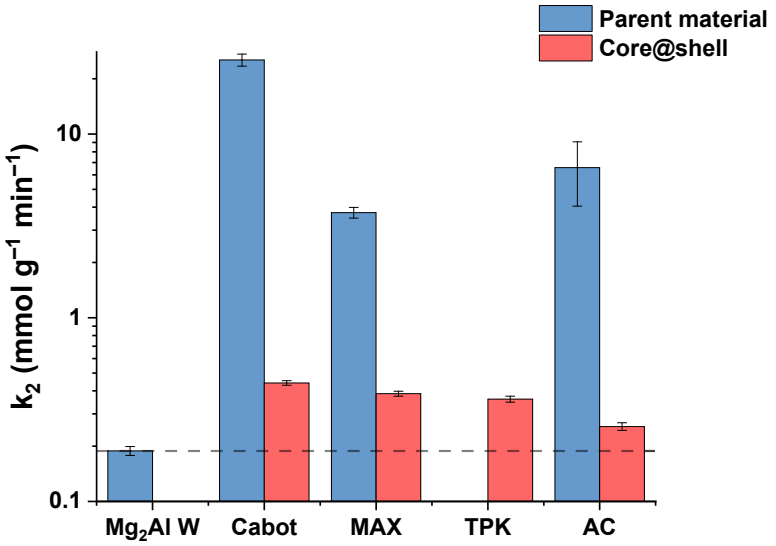


Figure 5.38 - Rate of CO_2 capture of various parent materials (blue) and core@shell materials (pink) as determined by pseudo-second-order kinetics model.

Comparing with literature, AC@Mg2Al W (49) displayed the highest CO_2 capture performance. Bhatta *et al.* reported a K-doped carbon@LDH core@shell with a CO_2 capture performance of 1.10 mmol g^{-1}.[7] However, the adsorption temperature was reported to be 300 °C, this would reduce the physisorption contribution of the base carbon and LDO materials and therefore cannot be compared directly with results obtained from this chapter.

Table 5.8 - Comparison of CO_2 capture values of Carbon/LDH hybrid materials from literature and this chapter.

Sample	Pre-treatment condition	Adsorption temperature (°C)	CO_2 uptake (mmol g^{-1})
K-doped Carbon@$Mg_{1.8}Al\ CO_3$[7]	400-4h- /	300	1.10
GO@$Mg_2Al\ CO_3$ (93)[6]	400-1h-10	300	0.45
Cabot@Mg2Al W (53)*	400-2h-50	30	0.96
AC@Mg2Al W (49)*	400-2h-50	30	1.24

* Work from this chapter.

5.9 NH_3 treatment of carbon@LDH materials

Post synthesis treatments have been made to activated carbons in hopes to improve their CO_2 capture capacities. Przepiórski *et al.* have shown that NH_3 treatment of activated carbons at high temperatures led to increases in CO_2 uptake.[38] The conditions optimised in their studies are compatible with the calcination conditions used here. It is suggested that during the NH_3 treatment, surface oxygen functional groups are replaced with N-containing ones, therefore AC with its high oxygen content is also the most suitable material. The replacement of oxygens with nitrogen will lead to more a basic surface due to the more reactive nature of the nitrogen lone pair.

AC@Mg_2Al W (49) underwent NH_3 treatment to yield AC@Mg_2Al W (49) NH_3. The NH_3 did not yield any improvements in CO_2 capture value or rate of adsorption. A small decrease of 0.09 mmol g^{-1} can be observed for the NH_3 treated sample (Figure 5.39). A similar decrease of 0.02 mmol g^{-1} min^{-1} can be seen in the rate of adsorption. At the treatment temperature of 400 °C, NH_3 would not remain on the surface of the LDO, as seen in the NH_3 TPD curves in previous chapters. The modification would be solely interacting with the surface of AC. This lack of improvement could be due to the inaccessibility of the carbon surface post core@shell synthesis.

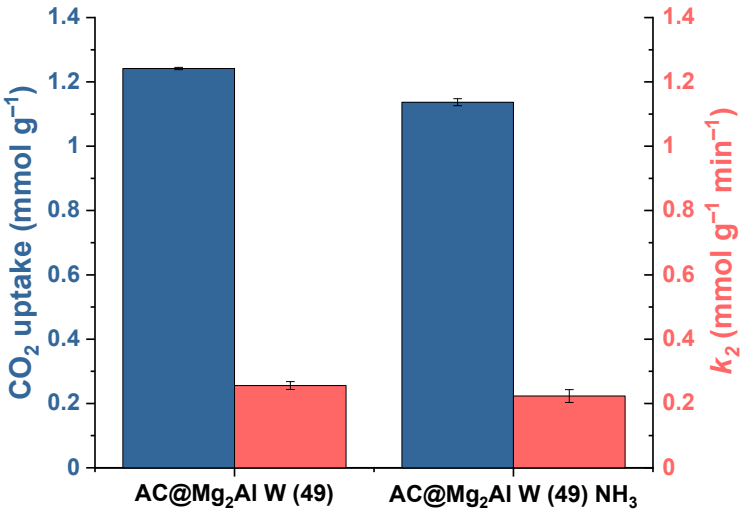


Figure 5.39 - CO_2 capture (blue) and rate of CO_2 capture (pink) of AC@Mg_2Al W (49) and AC@Mg_2Al W (49) NH_3. A calcination temperature of 400 °C for 2 h and 50 °C min^{-1} ramp under N_2 atmosphere was used. The CO_2 testing atmosphere was 33:67 CO_2:N_2 and the adsorption temperature was 30 °C. Rate of adsorption was determined by pseudo-second-order kinetics model.

5.10 Conclusion

A facile synthesis of carbon@LDH core@shells have been developed which dramatically improves the efficiently of the process compared with previous literature methods. The effects of LDH wt% were observed and two types of LDH layers were identified by SEM: a primary layer of large platelets grows directly on the surface of the carbon and a secondary layer of small LDH clusters are observed to grow on the primary layer.

Cabot@LDH materials were used for CO_2 capture studies, the results showed that the optimal performance occurs when the wt% LDH is 53%. There is also evidence of synergy between the two materials for CO_2 capture. The temperature was varied for the calcination of Cabot@Mg2Al W (53) and the best CO_2 capture was achieved with a calcination temperature of 700 °C for 2 h and a ramp rate of 50 °C min^{-1} (0.98 mmol g^{-1}). However, compared to a calcination temperature of 400 °C which yielded a similar CO_2 capture value (0.96 mmol g^{-1}), there is a drastic decrease in the rate of adsorption as determined by fitting

to a pseudo-second-order kinetic model (0.19 and 0.44 mmol g^{-1} min^{-1} respectively). Therefore, 400 °C was deemed the optimal calcination temperature.

By investigating a range of different carbon materials, the best results were obtained with AC@Mg_2Al W (49), exhibiting a capture value of 1.24 mmol g^{-1}, and a rate of adsorption of 0.26 mmol g^{-1} min^{-1}.

Post synthesis modifications of NH_3 treatment and solvent treatment were trialled but did not result in any noticeable improvements in CO_2 capture values or rate of adsorption. From the evidence at hand, these core-shell materials show a promising future as excellent CO_2 sorbents. Further fine-tuning of these methods are needed for this family of compounds to reach its fullest potential. Furthermore, the retarded formation of the spinel structure at high temperatures for these core@shell materials could prove to be vital in catalysis, more studies should be carried out in the area to further investigate the mechanisms behind the improved thermal stability, potentially by using non-conductive carbon materials.

5.11 References

1 R. Ghosh Chaudhuri and S. Paria, *Chem. Rev.*, 2012, 112, 2373–2433.
2 B. Han, G. Cheng, E. Zhang, L. Zhang and X. Wang, *Electrochim. Acta*, 2018, **263**, 391–399.
3 W. L. J. Kwok, D. G. Crivoi, C. Chen, J. C. Buffet and D. O'Hare, *Dalton Trans.*, 2018, **47**, 143–149.
4 Z. Gu, J. J. Atherton and Z. P. Xu, *Chem. Commun.*, 2015, **51**, 3024–3036.
5 A. Malak-Polaczyk, C. Vix-Guterl and E. Frackowiak, *Energy and Fuels*, 2010, **24**, 3346–3351.
6 A. Garcia-Gallastegui, D. Iruretagoyena, V. Gouvea, M. Mokhtar, A. M. Asiri, S. N. Basahel, S. A. Al-Thabaiti, A. O. Alyoubi, D. Chadwick and M. S. P. Shaffer, *Chem. Mater.*, 2012, **24**, 4531–4539.
7 L. K. G. Bhatta, S. Subramanyam, M. D. Chengala, U. M. Bhatta and K. Venkatesh, *Ind. Eng. Chem. Res.*, 2015, **54**, 10876–10884.
8 M. S. Shafeeyan, W. M. A. W. Daud, A. Houshmand and A. Shamiri, *J. Anal. Appl. Pyrolysis*, 2010, 89, 143–151.
9 R. V. Siriwardane, M. S. Shen, E. P. Fisher and J. A. Poston, *Energy and Fuels*, 2001, **15**, 279–284.
10 P. González-García, *Renew. Sustain. Energy Rev.*, 2018, **82**, 1393–1414.

11 S. Shukla, N. K. Kalagatur, V. Mudili, K. Karthick, J. A. Allen, O. Sivaraman Nirmal Ghosh, S. Chandranayaka, V. K. Gupta and K. Krishna, *Front. Pharmacol.*, 2017, **8**, 760.
12 Y. Otake and R. G. Jenkins, *Carbon N. Y.*, 1993, **31**, 109–121.
13 C. O. Ania, J. B. Parra and J. J. Pis, *Adsorpt. Sci. Technol.*, 2004, **22**, 337–351.
14 S. S. Barton, M. J. B. Evans, E. Halliop and J. A. F. MacDonald, *Carbon N. Y.*, 1997, **35**, 1361–1366.
15 M. S. Alhumaimess, I. Hotan Alsohaimi, H. M. A. Hassan, M. Y. El-Sayed, M. S. Alshammari, O. F. Aldosari, H. M. Alshammari and M. M. Kamel, *J. Saudi Chem. Soc.*, 2020, **24**, 321–333.
16 A. W. Burton, K. Ong, T. Rea and I. Y. Chan, *Microporous Mesoporous Mater.*, 2009, **117**, 75–90.
17 A. Faour, V. Prévot and C. Taviot-Gueho, *J. Phys. Chem. Solids*, 2010, **71**, 487–490.
18 C. Chen, A. Wangriya, J.-C. Buffet and D. O'Hare, *Dalton Trans.*, 2015, **44**, 16392–16398.
19 M. Yang, O. McDermott, J.-C. Buffet and D. O'Hare, *RSC Adv.*, 2014, **4**, 51676–51682.
20 K. Ruengkajorn, V. Erastova, J.-C. Buffet, H. C. Greenwell and D. O'Hare, *Chem. Commun.*, 2018, **54**, 4394–4397.
21 B. K. Na, K. K. Koo, H. M. Eum, H. Lee and H. K. Song, *Korean J. Chem. Eng.*, 2001, **18**, 220–227.
22 C. Lu, H. Bai, B. Wu, F. Su and J. F. Hwang, *Energy and Fuels*, 2008, **22**, 3050–3056.
23 R. Van Der Vaart, C. Huiskes, H. Bosch and T. Reith, *Adsorption*, 2000, **6**, 311–323.
24 U. Sharma, B. Tyagi and R. V. Jasra, *Ind. Eng. Chem. Res.*, 2008, **47**, 9588–9595.
25 M. K. Ram Reddy, Z. P. Xu, G. Q. (Max) Lu and J. C. Diniz da Costa, *Ind. Eng. Chem. Res.*, 2006, **45**, 7504–7509.
26 Y. Gao, Z. Zhang, J. Wu, X. Yi, A. Zheng, A. Umar, D. O'Hare and Q. Wang, *J. Mater. Chem. A*, 2013, **1**, 12782.
27 J. Rocha, M. del Arco, V. Rives and M. A. Ulibarri, *J. Mater. Chem.*, 1999, **9**, 2499–2503.
28 J. Guo, H. Lou, H. Zhao, X. Wang and X. Zheng, *Mater. Lett.*, 2004, **58**, 1920–1923.
29 D. Robati, *J. Nanostructure Chem.*, 2013, **3**, 1–6.
30 H. Wang, A. Zhou, F. Peng, H. Yu and J. Yang, *J. Colloid Interface Sci.*, 2007, **316**, 277–283.
31 S. M. Yusuff, O. K. Khim, W. Md Zin Man Yunus, A. Fitrianto, M. Ahmad, N. Ibrahim, F. C. Ros and T. Cc, in *Materials Today: Proceedings*, Elsevier Ltd, 2018, vol. 5, pp. 21948–21955.
32 G. Blanchard, M. Maunaye and G. Martin, *Water Res.*, 1984, **18**, 1501–1507.
33 Y. Xiao, J. Azaiez and J. M. Hill, *Ind. Eng. Chem. Res.*, 2018, **57**, 2705–2709.
34 X. Zhu, C. Chen, H. Suo, Q. Wang, Y. Shi, D. O'Hare and N. Cai, *Energy*, 2019, **167**, 960–969.
35 Y. S. Ho and G. McKay, *Process Saf. Environ. Prot.*, 1998, **76**, 332–340.
36 C.-H. Yu, C.-H. Huang and C.-S. Tan, *Aerosol Air Qual. Res.*, 2012, **12**, 745–769.
37 C. Chen, R. Felton, J. C. Buffet and D. O'Hare, *Chem. Commun.*, 2015, **51**, 3462–3465.
38 J. Przepiórski, M. Skrodzewicz and A. W. Morawski, *Appl. Surf. Sci.*, 2004, **225**, 235–242.

Chapter Six - Study of CO_2 capture during polyurethane synthesis

6.1 Introduction

While heterogeneous capture of CO_2 from the gas phase has been a widely researched field over the past decades, the capture of CO_2 directly from a reaction mixture is still relatively unexplored. An important reaction that releases CO_2 as a by-product is the polymerisation reaction of moisture-cured polyurethane resins (MCPUs).

Polyurethanes (PUs) were first discovered by Bayer *et al.* in 1937 with the initial purpose of exploiting the areas of polymer classes not covered by a patent for polyamides and nylon.[1] They are a family of polymers which, in their monomeric form, possess a varying number of isocyanate and alcohol functional groups (Figure 6.1).[2–4]

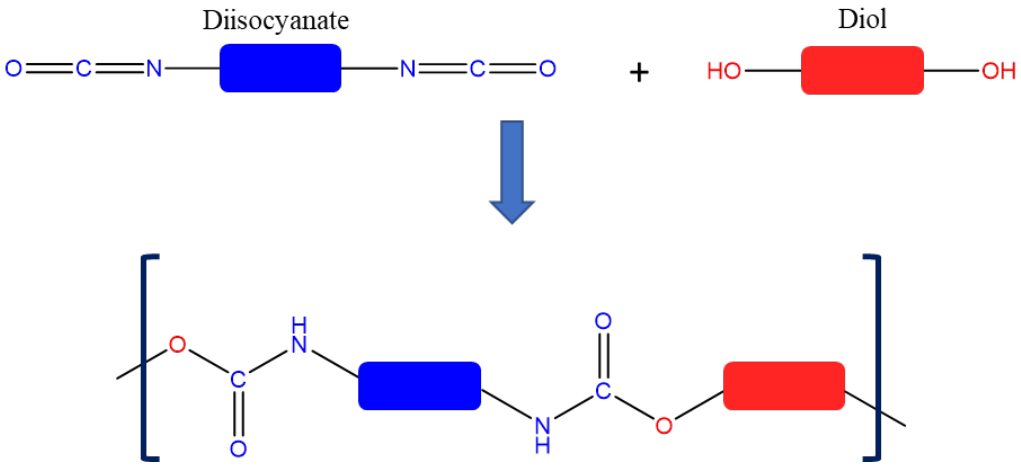


Figure 6.1 - Graphical representation of a general synthesis of polyurethane.

The isocyanates are typically reacted with di-/polyols to form polyurethane linkages and can be facilitated by the presence of UV light or a catalyst.[5,6] Properties of the PUs can be easily modified by altering isocyanate and alcohol containing monomers. A few examples of common starting monomers for PUs are shown in Figure 6.2. A more rigid polymer can be synthesised by incorporating aromatic groups which provides rigid segments within the matrix, while a more elastic product is formed by using long chain polyols.[7] By utilising aromatic polyols, the polymer can display flame retardance properties, while aliphatic polyols improves oxidative stability.[7–9] These tuneable properties make them highly desirable as they can be easily deployed in different applications, from electrical insulation to adhesives and packaging.[10]

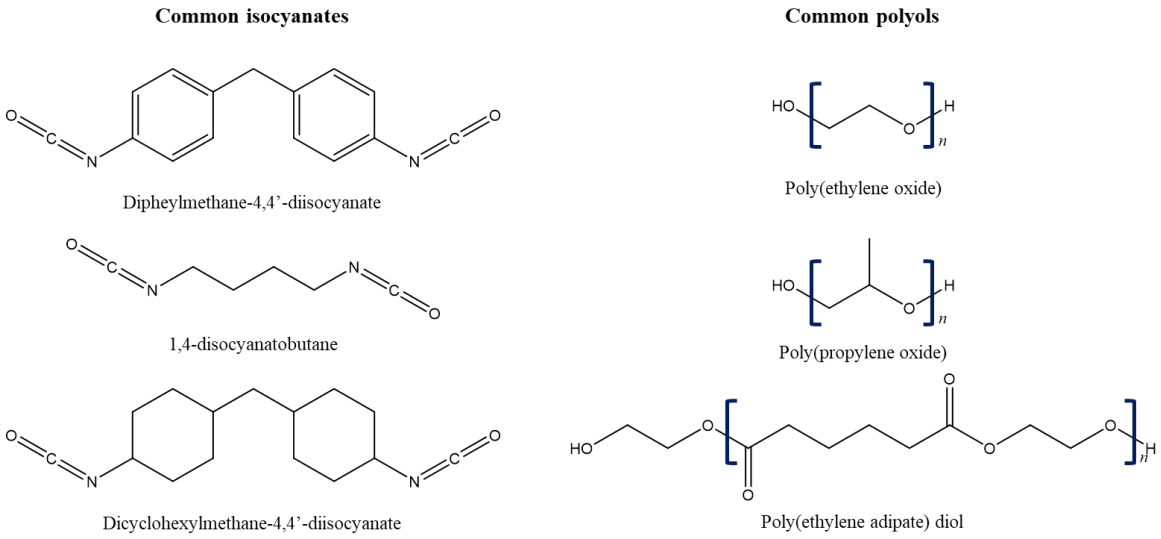
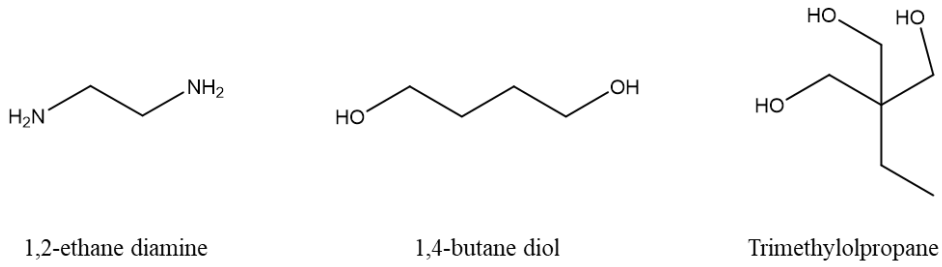


Figure 6.2 - Examples of common starting isocyanates and polyols for PUs.[11]

Additional reagents can be added to the polymerisation mixture to further alter the properties of the resulting PU. Chain extenders and cross-linkers can be added to improve the morphology and strength of the PU.[12] Chain extenders are usually short chain diamines or diols while cross-linkers have 3 or more functional groups (Figure 6.3). They react with the diisocyanates to increase the molecular weight of the polymer and the resulting polymer

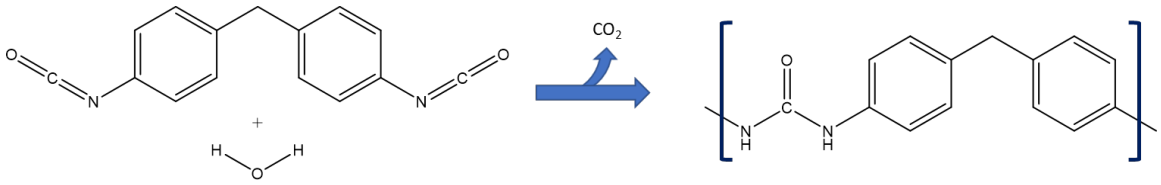
usually displays enhanced structural properties, such as tensile strength, due to improved hydrogen bonding within the structure.[13] The addition of chain extenders is also a route to synthesising degradable PU by choosing degradable extenders, such as diamine amino acids.[14]



1,2-ethane diamine 1,4-butane diol Trimethylolpropane

Figure 6.3 - Examples of common chain extenders and cross-linkers.[11,15]

MCPUs are a one-component class of PUs which reacts isocyanates with H_2O, instead of polyols, to form urea linkages (Scheme 6.1), and results in a heavily cross-linked polymer with higher strength and flexibility compared to traditional two-component PUs.[16,17] This family has a longer natural curing time compared to other PUs as it is dependent on the diffusion of atmospheric moisture through the matrix. During the curing and cross-linking process to form the polymer, CO_2 is released. With normal atmospheric moisture, the curing time is slow enough for the CO_2 to escape and not cause formation of air pockets. However, in countries with high humidity, CO_2 air pockets could form due to the excess moisture. In order to improve curing time, additional water can be added. This increases the curing rate but has the disadvantage of creating CO_2 air pockets within the polymer matrix. This is detrimental in their applications, such as coatings and adhesives. Currently no research has been reported to mitigate the formation of CO_2 air pockets within the polymer matrix. The ability to eliminate CO_2 air pockets while improving curing time would allow for more wide spread use of MCPUs.



Scheme 6.1 - Polymerisation reaction of diphenylmethane-4,4'-diisocyanate moisture-cured PU.

The MCPU used in this study is Desmoseal M280. It is a commercial, one-component, moisture resistant and solvent free monomer based on diphenylmethane-4,4'-diisocyanate, developed for applications as sealants and adhesives.

In this chapter, a preliminary study of the addition of $[Mg_{0.66}Al_{0.34}(OH)_2](CO_3)_{0.17}(H_2O)_{0.95}$ ($Mg_{1.9}Al$ W LDH) and its ethanol treated counterpart ($Mg_{1.9}Al$ E LDH) during the PU curing process is carried out. The addition of water to improve the curing time of the MCPU is also be investigated. The use of layered double oxides (LDOs), calcined at 400 °C with a heating ramp rate of 100 °C min^{-1} for 2 h, as CO_2 sorbent materials within the PU matrices is also be explored. Finally, improvements on PU curing time using LDOs with increasing amounts of water are examined.

6.2 Experimental details

The content of each mixture were added to a plastic mixing container. Holes were created in the lid of the container to allow for a vacuum to form inside. The container was then mounted into an Intertronics THINKY Planetary Vacuum Mixer and spun at 500 rpm for 1 min, then 1000 rpm for 1 min and finally 2000 rpm for 2 min. Pressure was at 100 kPa, 30 kPa and 5 kPa respectively unless specified otherwise. The resulting mixture was placed in a fumehood or 99% humidity box for the amount of time specified in the table below.

The 99% humidity box was created by placing a saturated solution of KNO_3 in an air tight container and the humidity was monitored by a digital hydrometer.

$Mg_{1.9}Al$ W LDH and $Mg_{1.9}Al$ E LDH were synthesised as outlined in Chapter Four.

6.3 Effects of LDH on the curing process of MCPU

5 mL of Desmoseal M280 was cured under different conditions, both with and without the addition of LDHs. The samples were mixed under vacuum to ensure no external factors could cause the formation of air pockets within the sample, and then observed over 3 weeks (Figure 6.4).

Without the addition of water, the sample of Desmoseal M280 cured in a 99% humidity box had a curing time of 3 days while the sample cured in a fumehood presented with a curing time of 4 days. Neither samples produced observable CO_2 air pockets or any discolouration due to the slow rate of curing from the atmospheric moisture allowing for the CO_2 formed within the matrix to escape (Figure 6.4 (a) and (b)).

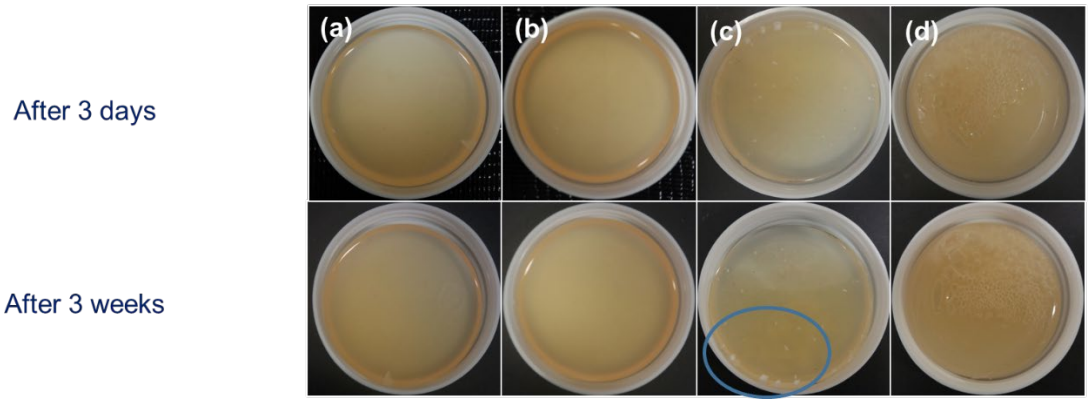


Figure 6.4 - Images of Desmoseal M280 cured after 3 days and 3 weeks (a) in a fumehood, (b) in a 99% humidity box, (c) in a 99% humidity box with 0.5 g $Mg_{1.9}Al$ W LDH and (d) in a 99% humidity box with 0.5 g $Mg_{1.9}Al$ E LDH, without the addition of water. Sections highlighted to show non-dispersed particles.

The addition of 0.5 g $Mg_{1.9}Al$ W LDH and $Mg_{1.9}Al$ E LDH did not affect the curing time of the MCPU and remained at 3 days. $Mg_{1.9}Al$ W LDH was shown to aggregate into large cluster within the PU matrix (Figure 6.4 (c)). The aggregation can be observed in the bottom region of the sample with no addition of water (highlighted in blue). This is due to the

hydrophilic nature of conventional water washed LDHs leading to the lack of dispersibility within the organic polymer matrix.

However, $Mg_{1.9}Al$ E LDH displayed a high level of dispersibility within the matrix and no observable LDH aggregates were present (Figure 6.4 (d)), although the overall appearance became more opaque compared to the sample with $Mg_{1.9}Al$ W LDH. AMO-LDHs have been shown to possess increased surface area and improved organophilicity compared to a conventional water washed LDH.[18] The improved organophilicity could allow for more favourable interactions with the PU matrix which could allow for a more thorough dispersion of the LDH sample (Figure 6.5).

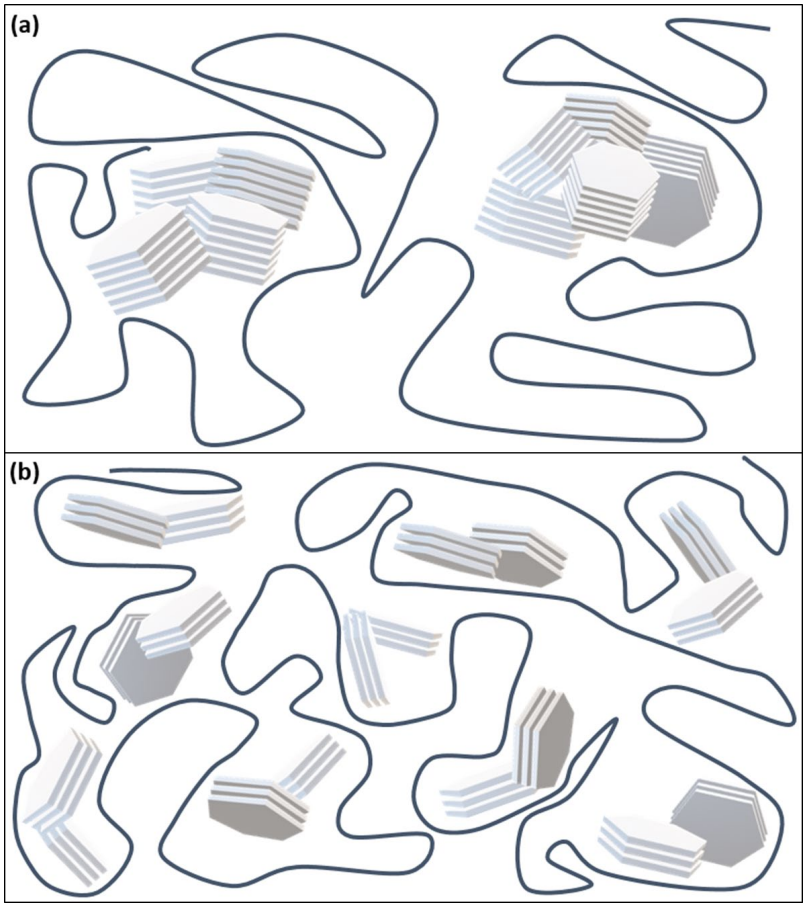


Figure 6.5 - Graphical illustration of proposed dispersion of (a) water washed and (b) solvent treated LDHs in a PU matrix. Blue line represents PU polymer strands.

Although no CO_2 air pockets were observed by eye upon PU curing without the addition of water, microbubbles, *ca*. 2–5 µm in diameter, were observed within the polymer matrix under scanning electron microscopy (SEM) in Figure 6.6 (highlighted in orange).

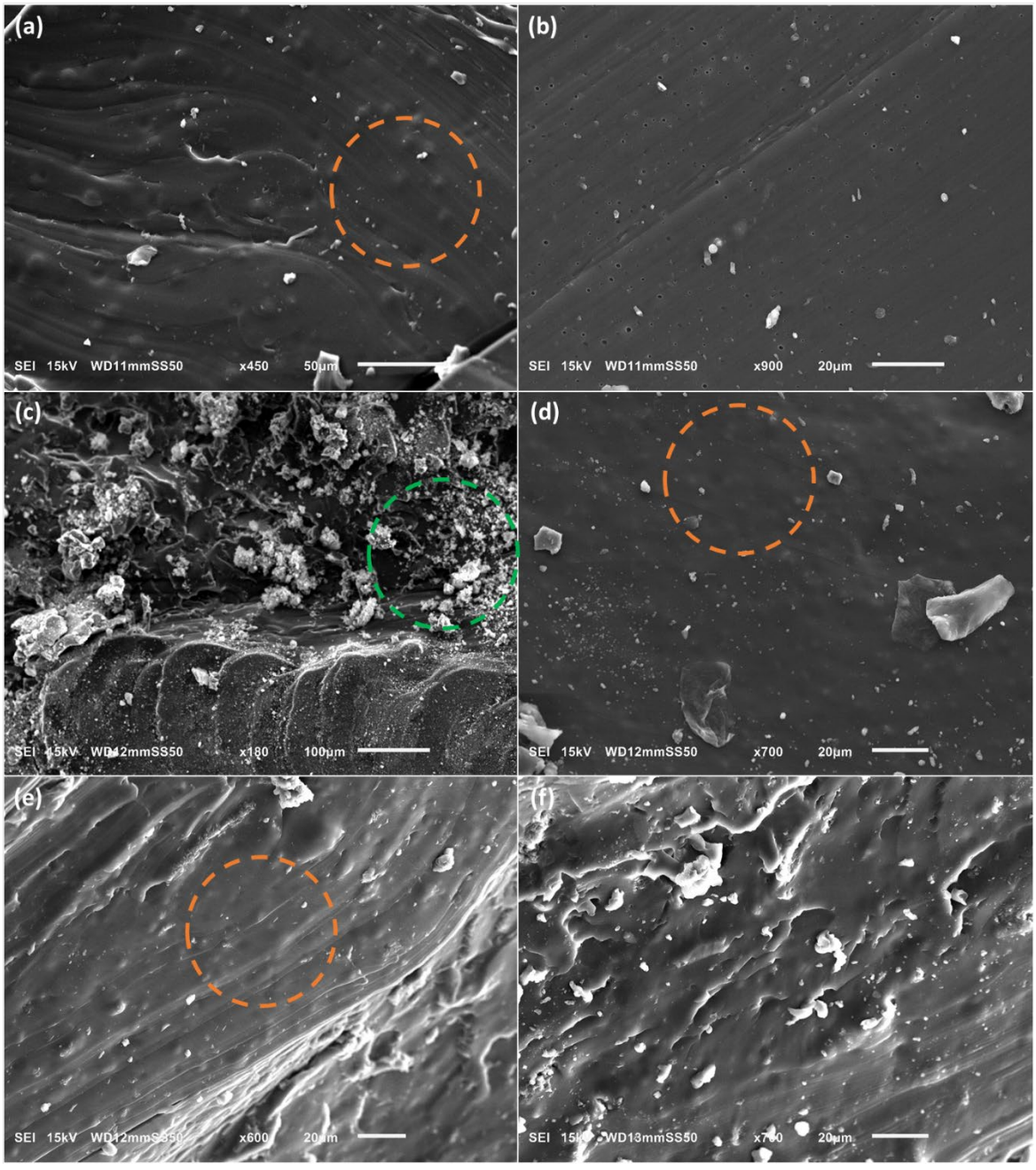


Figure 6.6 - SEM images of (a)–(b) Desmoseal M280 cured in a 99% humidity box, (c)–(d) Desmoseal M280 cured in a 99% humidity box with 0.5 g $Mg_{1.9}Al$ W LDH and (e)–(f) Desmoseal M280 cured in a 99% humidity box with 0.5 g $Mg_{1.9}Al$ E LDH, without the addition of water. Microbubbles formed are highlighted in orange. LDH aggregates are highlighted in green.

The microbubbles are still visible under SEM even with the addition of $Mg_{1.9}Al$ W and $Mg_{1.9}Al$ E LDHs. Large aggregates and clusters of LDHs are observed in the sample with $Mg_{1.9}Al$ W LDH (Figure 6.6 (c), highlighted in green). The $Mg_{1.9}Al$ E LDH aggregates were sufficiently well dispersed that none were visible in the SEM images.

6.4 Effects of water on the curing process of MCPU

To improve the curing time of MCPUs, controlled quantities of water was added. Upon the addition of water, large CO_2 air pockets were formed in the PU samples due to the increased rate of CO_2 release accompanied with the improved curing time. This was also accompanied by a discolouration of the PU matrix to a creamy white colour (Figure 6.7 (b)). The CO_2 air pockets were formed due to the sped up curing and hardening of Desmoseal M280 which trapped the CO_2 released during the curing process, causing the formation of CO_2 air pockets. The addition of water drastically shortened the curing time from 3 days to 2 h. The discolouration, however, disappeared after 3 weeks, resulting in a final product with greater transparency than the samples with no water added. The sample with 0.5 mL H_2O added displayed fewer air pockets due to the slower curing rate of 3 h (Figure 6.7 (a)).

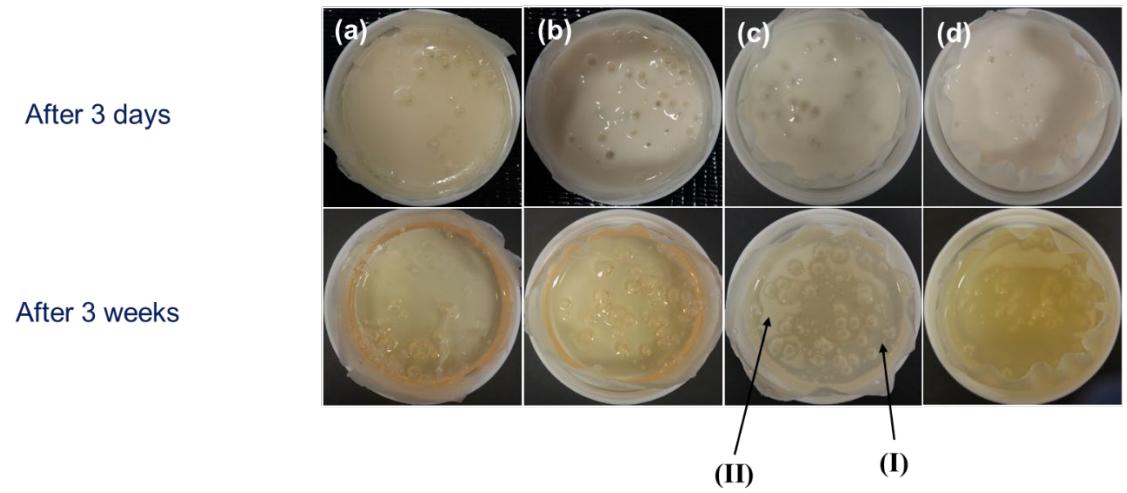


Figure 6.7 - Images of Desmoseal M280 cured after 3 days and 3 weeks with the addition of (a) 0.5 mL water, (b) 1 mL water, (c) 1 mL water with 0.5 g $Mg_{1.9}Al$ W LDH and (d) 1 mL with 0.5 g $Mg_{1.9}Al$ E LDH, in a 99% humidity box.

For the samples containing LDHs, CO_2 air pockets were also observed with the addition of 1 mL water. The curing time also decreased from 3 days to 2 h and the creamy white discolouration was observed after 3 days for both LDH samples. However, after 3 weeks, unlike the sample without LDH, part of the polymer matrix still retained the creamy white discolouration (region (II) in Figure 6.7 (c)). $Mg_{1.9}Al$ E LDH displayed a similar performance: CO_2 was trapped within the matrix and CO_2 air pockets were formed.

The FTIR spectra of the different regions revealed that water remains in region (II) as shown in Figure 6.7 (c), as evident by the OH stretch between 3000–3800 cm^{-1}, and the symmetric bend of H_2O (1650 cm^{-1}) shown in Figure 6.8 (a), and highlighted in Figure 6.8 (b). Both the OH stretch and the symmetric water bend reduced in intensity in region (I), suggesting excess water is able to diffuse out of the PU matrix, but the process appears to be hindered by the introduction of LDH into the structure as the discolouration remains in the product for a prolonged period of time. This could be due to the LDH platelets forming a tortuous pathway within the PU matrix. This could lead to a similar effect observed by Tammaro *et*

al., where upon mixing LDH into poly(ethylene teraphtalate), an increase in barrier properties, such as diffusion and permeability, was observed.[19]

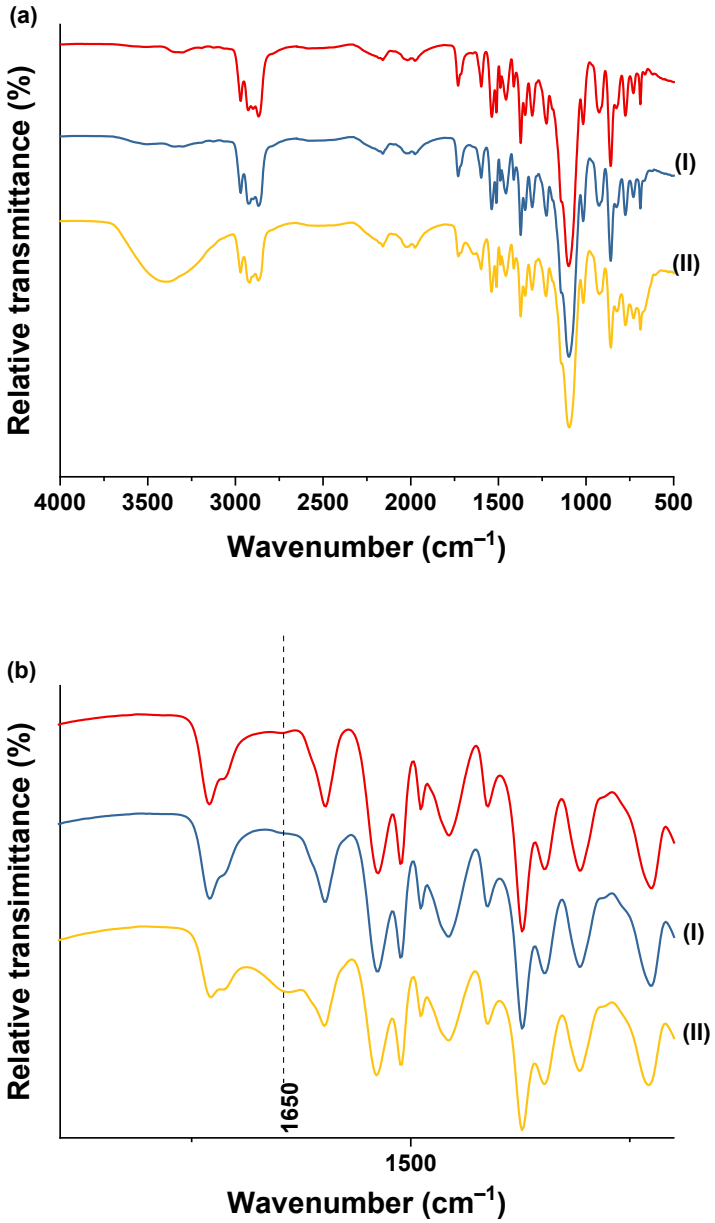


Figure 6.8 - (a) FTIR spectra of pure Desmoseal M280 (red), region (I) and region (II) from Figure 6.7, and (b) zoomed-in range (1100–1900 cm^{-1}) of FTIR spectra (a).

6.5 Solution phase CO_2 capture of LDOs in PU matrices

As discussed in Chapter Four, $Mg_{1.9}Al$ W and $Mg_{1.9}Al$ E with a calcination condition of 400 °C with a heating ramp rate of 100 °C min^{-1} for 2 h (400-2h-100) exhibited excellent CO_2 capture capacity. Therefore these samples were used to test for CO_2 adsorption in solution phase and the results are shown in Figure 5.9.

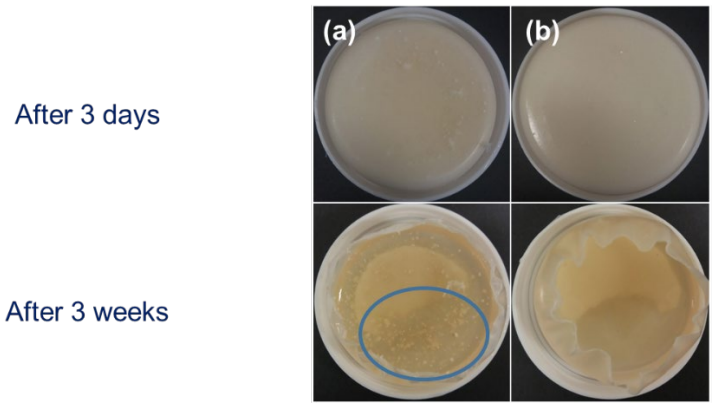


Figure 6.9 - Images of PU cured after 3 days and 3 weeks with the addition of 1 mL water in a 99% humidity box with (a) 0.5 g $Mg_{1.9}Al$ W 400-2h-100 and (b) $Mg_{1.9}Al$ E 400-2h-100 LDOs. Sections highlighted to show non-dispersed aggregates.

Results from previous sections show the low capability of the LDH materials to capture CO_2 during the curing process of the MCPU. However, once both LDHs were calcined at 400 °C with a ramp of 100 °C min^{-1} for 2 h, even with addition of 1 mL water, no visible CO_2 air pockets can be observed (Figure 6.9). This is due to the excellent CO_2 capture ability of the LDOs, as shown in Chapter Three (0.59 and 1.34 mmol g^{-1} for $Mg_{1.9}Al$ W 400-2h-100 and $Mg_{1.9}Al$ E 400-2h-100 respectively). The dramatic improvement in CO_2 air pockets reduction could also be due to the fact that in presence of CO_2, with the addition of water, the LDO could reconstruct and reform LDH, which permanently incorporates the CO_2 as carbonate anions into its structure (Figure 6.11). This is confirmed by the presence of the (110) and (113) Bragg reflections in the XRD patterns in Figure 6.10 (b) and (c), which are characteristic of an LDH structure. The d_{110}-spacing (60.8°) corresponds to a lattice

parameter *a*/*b* of 3.04 Å, which agrees with the value obtained for $Mg_{1.9}Al$ W LDH in Chapter Three.

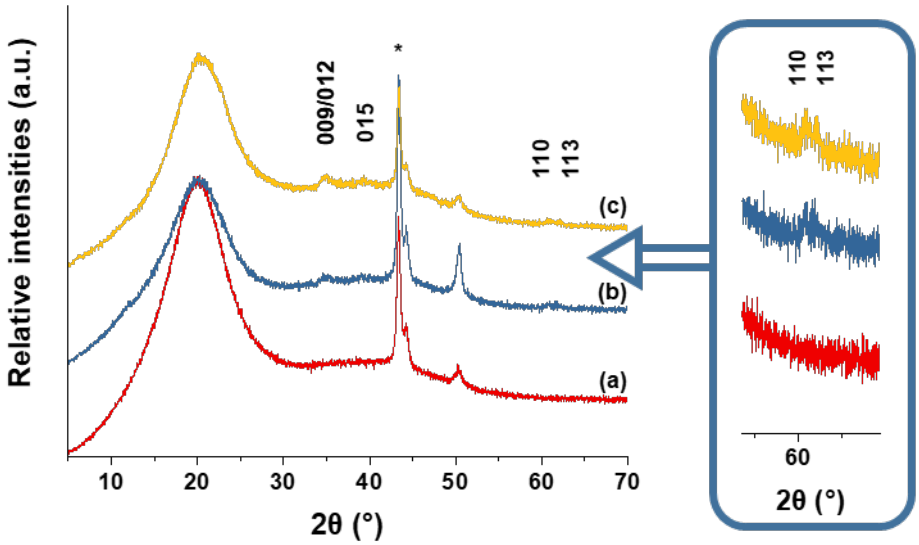


Figure 6.10 - XRD patterns of (a) Desmoseal M280 cured with the addition of 1 mL water in a 99% humidity box and with (b) 0.5 g $Mg_{1.9}Al$ W 400-2h-100 and (c) $Mg_{1.9}Al$ E 400-2h-100 LDOs. (*) denotes sample holder peak.

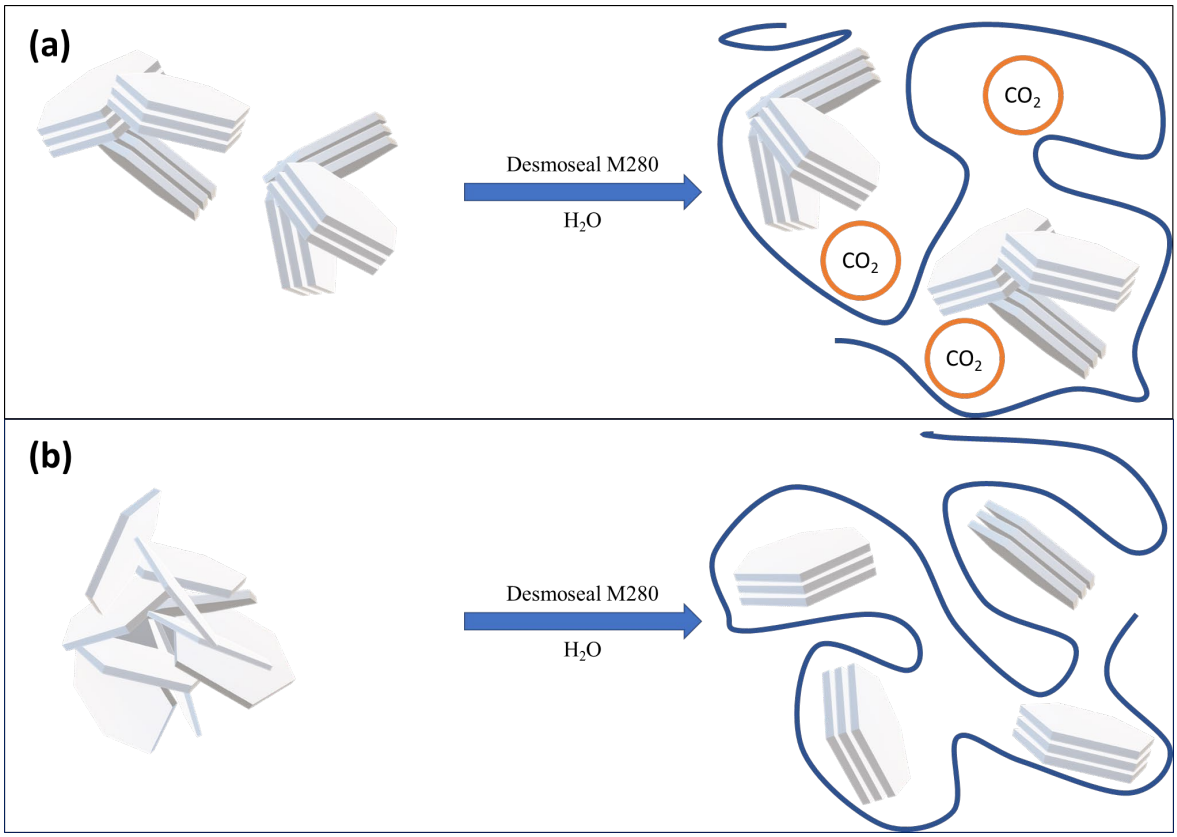


Figure 6.11 - Graphical representation of (a) LDH and (b) LDO during the polymerisation reaction of Desmoseal M280.

Moreover, when comparing the water washed sample to that of the ethanol treated sample, $Mg_{1.9}Al$ E 400-2h-100 retained the dispersibility of the parent LDH. This could be due to the more exfoliated parent LDH allowing for the LDO to be more readily dispersed in within the PU matrix. Despite $Mg_{1.9}Al$ W 400-2h-100 displaying excellent CO_2 capture ability which eliminated all CO_2 air pockets, large LDO clusters still remained visible within the product (highlighted in Figure 6.9 (a)), resulting in uneven distribution of LDO.

Without any addition of LDOs, the SEM images shows the formation of large CO_2 air pockets, with diameters *ca*. 200–300 µm (Figure 6.12 (a) and (b)). No microbubbles were observed upon further magnification, which could be due to the increased curing rate allowing for the microbubbles to merge and form the large CO_2 air pockets shown.

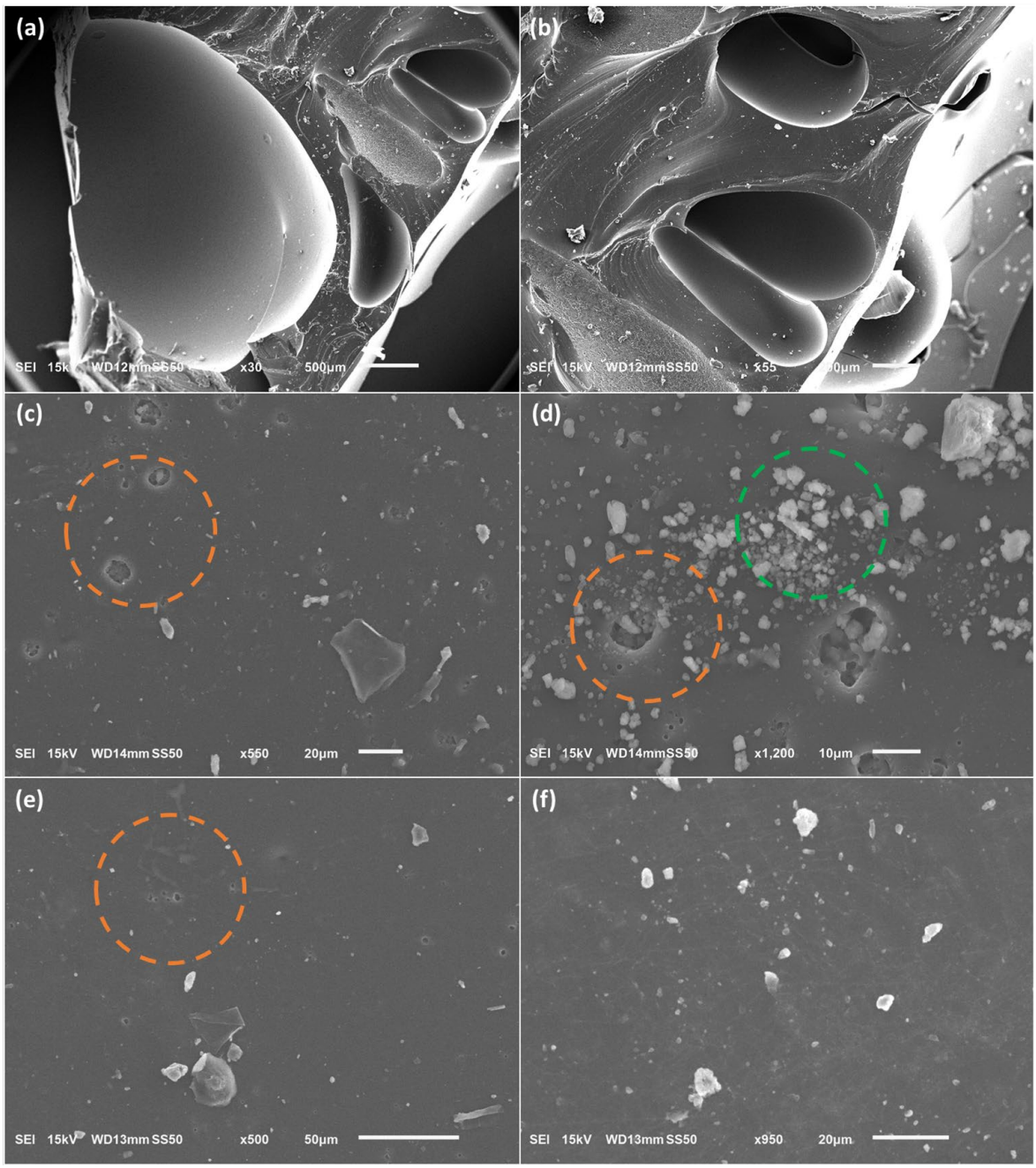


Figure 6.12 - SEM images of (a)–(b) Desmoseal M280 cured with the addition of 1 mL water in a 99% humidity box and with (c)–(d) 0.5 g $Mg_{1.9}Al$ W 400-2h-100 and (e)–(f) $Mg_{1.9}Al$ E 400-2h-100 LDOs. Microbubbles formed are highlighted in orange. LDH aggregates are highlighted in green.

Upon the addition of $Mg_{1.9}Al$ W 400-2h-100, only microbubbles were observed (Figure 6.12 (c) and (d)). The microbubbles exhibit a diameter of *ca.* 10 µm and were observed across the whole sample. However, upon the introduction of $Mg_{1.9}Al$ E 400-2h-100, the microbubbles reduced in size, exhibiting a diameter of *ca.* 2–4 µm (Figure 6.12 (e)).

Furthermore, no microbubbles were observed in the close proximity of the LDO particles (Figure 6.12 (f)). This could be due to the superior CO_2 uptake of the ethanol treated LDO adsorbing the CO_2 in close proximity and therefore eliminating the microbubbles as they are formed.

6.6 Improvement of curing time

In an effort to further reduce curing time, increasing amounts of water was added to a 5 mL PU sample containing 0.5 g $Mg_{1.9}Al$ E 400-2h-100, and the product was cured in a 99% humidity box. As shown in Figure 6.13, the curing time of PU was drastically improved with the increasing amount of water added. From a curing time of 3 days without water, the time decreased to 25 min with the addition of 4 mL water. The production of large CO_2 air pockets was also eliminated by the addition of $Mg_{1.9}Al$ E 400-2h-100.

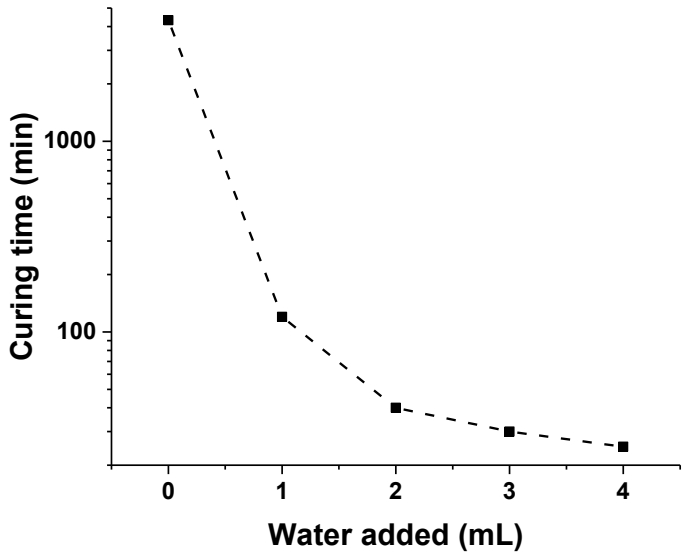


Figure 6.13 - Desmoseal M280 curing time with 0.5 g Mg_2Al E 400-2h-100 with addition of water in a 99% humidity box.

The sample with 4 mL added water presented with the formation of a small amount of air pockets on the surface (Figure 6.14 (d)). This could be due to the rate of CO_2 production during the curing process exceeding the rate of CO_2 capture of $Mg_{1.9}Al$ E 400-2h-100. The appearance of the cured product also becomes less regular. This is also possibly due to the increase in curing rate leading to the hardening of the matrix prior to the mixture fully settling into the container. This improved curing time is comparable to other PU systems studied in literature: Li *el al.* showed complete curing occurred after 40 min for a two component PU system while González-Benito *et al*. demonstrated a curing time of 25 min with a similar system of polyol/NCO by using differential scanning calorimetry to monitor the molar conversion of the PU mixture over time.[20,21] However, these were only achieved at elevated temperatures which is shown to drastically improve curing time.

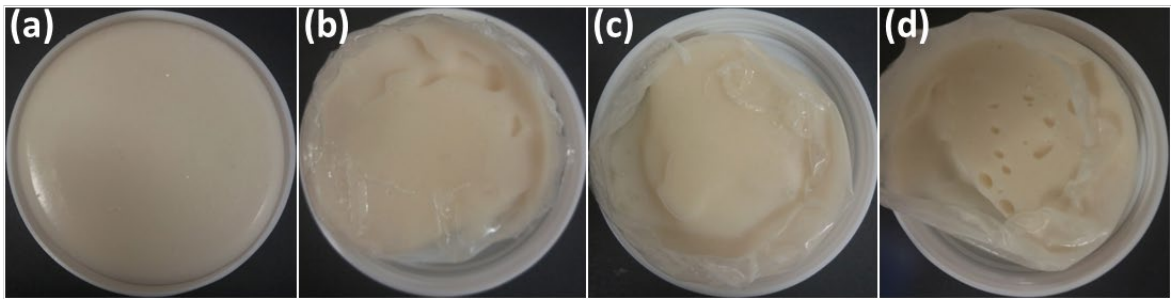


Figure 6.14 - Images of cured Desmoseal M280 with the addition of 0.5 g $Mg_{1.9}Al$ E 400-2h-100 and (a) 1 mL, (b) 2 mL, (c) 3 mL and (d) 4 mL water.

6.7 Conclusion

A preliminary study on the shortening of the curing time of MCPUs have been carried out. Firstly, the effects of an LDH dispersion within Desmoseal M280 were carried out and it was discovered that $Mg_{1.9}Al$ E LDH displayed decreased levels of aggregation within the PU matrix compared to $Mg_{1.9}Al$ W LDH, which allowed for more thorough integration of LDHs, but resulted in a more opaque PU matrix. When examined by SEM, it was observed

that microbubbles (*ca*. 2–5 μm in diameter) were formed during the curing process of PU, which was not eliminated by the addition of LDHs. With the addition of 1 mL of water, the curing time was drastically improved from 3 days to 2 h. However this led to the formation of large CO_2 air pockets within the polymer matrix. The presence of LDH particles within the mixture seemed to have delayed the removal of moisture from within the PU matrix. This is suspected to be due to the tortuous pathway created by the dispersed LDH within the PU matrix.

The LDHs were calcined at 400 °C with a heating ramp rate of 100 °C min^{-1} for 2 h to test their CO_2 capture ability in the solution phase during the MCPU curing process with the addition of 1 mL water. Both $Mg_{1.9}Al$ W and $Mg_{1.9}Al$ E 400-2h-100 displayed the ability to prevent the formation of large CO_2 air pockets during the curing process. However, SEM showed the presence of microbubbles still remained, although not when in close proximity to $Mg_{1.9}Al$ E 400-2h-100 aggregates.

$Mg_{1.9}Al$ E 400-2h-100 was added to the PU mixture with excess water to further improve curing time. The curing time was reduced drastically from 3 days, without the presences of water, to 25 min with the addition of 4 mL water. This improvement was also accompanied by the elimination of internal CO_2 air pockets. The improved curing time is similar to that of two component PUs, which are known in industry as fast curing polymers.

6.8 Outlook

Nanomaterials have been deployed into PU matrices to reinforce the structure by providing extra stiffness and strength. Montmorillonites (MMTs) have been shown to increase the thermostability of the PU matrix by improving the second transition temperature.[22] Their usage as filler materials have also improves gas barrier properties and can be very well

delaminated within the polymer. This increases the interactions between the platelets and PU, which further enhances the improvements.[23–25] LDHs are the anionic analogues of MMTs and could potentially exhibit a similar manner of incorporation into the matrix.

As shown in the studies in Section 5.2, ethanol treated LDH showed improved dispersibility within the MCPU matrix due to the enhanced organophilicity resulting from the solvent treatment method. Other AMO and AIM solvent treated LDHs/LDOs could potentially display different levels of dispersibility within the PU polymer and further improve upon this result.[26,27] High resolution cross-sectional SEM-EDS could be used in the future to investigate the level of incorporation of LDH platelets within the matrices. Furthermore, all solvent treated samples, once calcined, have shown CO_2 capture values greater than the water washed counterpart in Chapter Two, therefore these materials would also aid in the elimination of CO_2 air pockets during the MCPU curing process. *In situ* FTIR and differential scanning calorimetry (DSC) studies could be carried out to more closely monitor the curing process in the presence of inorganic platelets.

Finally, the incorporation of carbon@LDO materials can be investigated as they were shown, in Chapter Four, to possess a higher rate of CO_2 capture with similar CO_2 capture performances. The carbon core could also allow for improved dispersibility within the PU mixture. Stress-strain tests should also be carried out to measure any structural improvements achieved with the incorporation of nanosheets.

6.9 References

1 O. Bayer, *Angew. Chemie*, 1947, **59**, 257–272.
2 A. K. Mishra, D. K. Chattopadhyay, B. Sreedhar and K. V. S. N. Raju, *Prog. Org. Coatings*, 2006, **55**, 231–243.
3 C. P. Christenson, M. A. Harthcock, M. D. Meadows, H. L. Spell, W. L. Howard, M. W. Creswick, R. E. Guerra and R. B. Turner, *J. Polym. Sci. Part B Polym. Phys.*,

1986, **24**, 1401–1439.
4 L. H. Sperling, S. L. Cooper and A. V. Tobolsky, *J. Appl. Polym. Sci.*, 1966, **10**, 1725–1735.
5 J. W. Britain and P. G. Gemeinhardt, *J. Appl. Polym. Sci.*, 1960, **4**, 207–211.
6 W. Dzierża, *J. Appl. Polym. Sci.*, 1978, **22**, 1331–1342.
7 J. O. Akindoyo, M. D. H. Beg, S. Ghazali, M. R. Islam, N. Jeyaratnam and A. R. Yuvaraj, *RSC Adv.*, 2016, 6, 114453–114482.
8 M. Ginic-Markovic, N. R. Choudhury, J. G. Matisons and D. R. G. Williams, *J. Therm. Anal. Calorim.*, 2000, **59**, 409–424.
9 G. Malucelli, A. Priola, F. Ferrero, A. Quaglia, M. Frigione and C. Carfagna, *Int. J. Adhes. Adhes.*, 2005, **25**, 87–91.
10 F. M. de Souza, P. K. Kahol and R. K. Gupta, *Polyurethane Chemistry: Renewable Polyols and Isocyanates*, American Chemical Society, Washington, DC, 2021.
11 T. J. Touchet and E. M. Cosgriff-Hernandez, *Hierarchal structure–property relationships of segmented polyurethanes*, Woodhead Publishing, 2016.
12 S. Yamasaki, D. Nishiguchi, K. Kojio and M. Furukawa, *J Polym Sci Part B Polym Phys*, 2007, **45**, 800–814.
13 J. Blackwell and K. H. Gardner, *Polymer (Guildf).*, 1979, **20**, 13–17.
14 K. Gisselfält, B. Edberg and P. Flodin, *Biomacromolecules*, 2002, **3**, 951–958.
15 H. Mingjie, F. Wei, G. Le, W. Weibing, L. Xinghai and H. Chi, *Polym. Bull.*, 2014, **71**, 2671–2693.
16 D. K. Chattopadhyay, P. S. R. Prasad, B. Sreedhar and K. V. S. N. Raju, *Prog. Org. Coatings*, 2005, **54**, 296–304.
17 H. Ni, A. D. Skaja, R. A. Sailer and M. D. Soucek, *Macromol. Chem. Phys.*, 2000, **201**, 722–732.
18 C. Chen, M. Yang, Q. Wang, J.-C. Buffet and D. O'Hare, *J. Mater. Chem. A*, 2014, **2**, 15102–15110.
19 L. Tammaro, V. Vittoria and V. Bugatti, *Eur. Polym. J.*, 2014, **52**, 172–180.
20 J. González-Benito, F. Mikeš, J. Baselga and H. Lemetyinemm, *Appl. Polym. Sci.*, 2002, **86**, 2992–3000.
21 S. Li, E. Vuorimaa and H. Lemmetyinen, *Appl. Polym. Sci.*, 2001, **81**, 1474–1480.
22 G. H. Hsiue, W. J. Kuo, Y. P. Huang and R. J. Jeng, *Polymer (Guildf).*, 2000, **41**, 2813–2825.
23 J. Zhu, A. B. Morgan, F. J. Lamelas and C. A. Wilkie, *Chem. Mater.*, 2001, **13**, 3774–3780.
24 J. M. Yeh, S. J. Liou, M. C. Lai, Y. W. Chang, C. Y. Huang, C. P. Chen, J. H. Jaw, T. Y. Tsai and Y. H. Yu, *J. Appl. Polym. Sci.*, 2004, **94**, 1936–1946.
25 T. Takeichi and Y. Guo, *J. Appl. Polym. Sci.*, 2003, **90**, 4075–4083.
26 K. Ruengkajorn, V. Erastova, J.-C. Buffet, H. C. Greenwell and D. O'Hare, *Chem. Commun.*, 2018, **54**, 4394–4397.
27 M. Yang, O. McDermott, J.-C. Buffet and D. O'Hare, *RSC Adv.*, 2014, **4**, 51676–51682.

Chapter Seven - Conclusion

7.1 Conclusion

The work described in this thesis is focused on the development, optimisation and application of Mg$_x$Al-layered double hydroxides (LDHs), Mg$_x$Al-layered double oxides (LDOs) and Mg$_x$Al-LDH-based core@shell materials in carbon dioxide (CO_2) capture.

Chapter Three successfully characterised the acidity and basicity of solvent treated LDHs and LDOs (calcined at 450 °C for 12 h with a ramp rate of 5 °C min^{-1}). Combining Hammett indicator and titration techniques, the Brønsted basicity of LDHs and LDOs were quantitatively investigated. It was shown that there was not only an increase in total basic sites when LDHs are transformed into LDOs, a shift to strong basic sites was also observed. Temperature programmed desorption (TPD) was used to probe the Lewis acidity and basicity of the LDOs. While an increase in total basic site was observed, there was no change in the distribution of peaks. However, the acidity was shown change drastically for the solvent treated LDOs: a suppression of the medium acidic sites was observed. This is a novel discovery for AMO and AIM treated LDOs. Combined with ^{1}H and ^{27}Al ssNMR, a hypothesis of solvent molecules bonding to and denying access to tetrahedrally coordinated Al^{3+} centres was proposed. However, no information on the Mg^{2+} centres could be provided due to the lack of access to more sensitive techniques, such as ^{25}Mg NMR or EXAFS. A decrease in acidic and basic site density was also observed, which would suggest the active sites are mainly focused on the edge of the nanosheets, which do not experience an increase

with the increase in surface area. These LDOs were then tested for CO_2 capture and all solvent treated LDOs outperformed their water washed counterpart.

Chapter Four set out to optimise Mg_xAl-LDOs for use as CO_2 sorbents. Conditions for optimal was achieved: 400 °C for 2 h with a ramp rate of 100 °C min^{-1} and a Mg^{2+}/Al^{3+} ratio of 3.4 with an ethanol treatment provided the best CO_2 capture value (2.04 mmol g^{-1}). With the increase in heating ramp rate, which has not been of focus in any literature studies,[1–4] many physical and chemical changes was observed. As the heating ramp rate increased, so did the surface area, pore volume and basic and acidic sites. A novel resonance in the ^1H MAS NMR spectrum could also be observed at $\delta = 7.3$ ppm. This resonance is proposed to arise from an apical proton of a tetrahedrally coordinated Al^{3+} centres, which facilitates a favourable proton transfer to a bound CO_2 molecule, which led to an increase in CO_2 capture performance. For the $Mg_{1.9}Al$ series calcined at 400 °C, it was discovered that the CO_2 capture was dependent on the acid/base ratio of the respective LDO: when the acid/base ratio is low, the corresponding CO_2 capture value is also low. This is due to the reduced OH bonding mode for NH_3 which also contributes to the overall CO_2 uptake through the bicarbonate bonding motif (not captured by CO_2 TPD due to the high adsorption temperature (100 °C) used to avoid reconstruction of LDOs). At high acid/base ratios (> 0.4), the CO_2 capture performance is again reduced. When the ratio was between 0.2 and 0.4, an increase in CO_2 capture performance was observed, with the optimum ratio at 0.37 for $Mg_{1.9}Al$ W 400-2h-100. The calcination conditions optimised agree with the findings in literature.[5–7] However, it is believed that this is the first extensive study into the effect of heating ramp rate on the physicochemical properties of LDOs and the related CO_2 capture performance.

Chapter Five outlined the successful synthesis of carbon@MgAl core@shell materials. The effect of varying wt% LDH in the core@shell was explored and a growth mechanism was proposed. Initially, LDHs nucleate and grow on the surface as large individual platelets at low LDH concentrations. As the LDH% increases, a secondary layer of LDH, which possesses a rosette structure typical of LDH synthesised via the co-precipitation method, then grows atop the first layer of platelets, blocking access to the primary layer. Cabot@Mg_2Al W was studied for their CO_2 capture ability and rate of capture. The rate of adsorption was assess using the pseudo-second-order kinetic model. It was shown that the core@shells displayed improved rates of adsorption when compared to the LDH/LDO counterparts, however they did not exceed that of the carbon material. The CO_2 capture value was also shown to be lower than that of the LDH/LDO. It was also discovered that Cabot@Mg_2Al delayed the formation of the spinel structure upon calcination to beyond 800 °C, which could prove invaluable in catalytic application and regeneration.

Finally, the use of LDOs for CO_2 capture during the curing of Desmoseal M280, a moisture-cured polyurethane (MCPU), was investigated in Chapter Six. It was discovered that by adding a combination of water and $Mg_{1.9}Al$ E 400-2h-100 LDO, the curing of MCPUs could be drastically reduced from 3 days to 25 min without the formation of visible CO_2 air pockets. It is believed this is the first study of its kind where LDHs and LDOs are deployed as CO_2 sorbent materials in the solution phase. It is also the first study to attempt to reduce the curing time of MCPUs while elimination CO_2 air pockets.

To carry on from this work, different solvents should be investigated and their effect on the acidity and basicity of MgAl LDOs should be examined. The change from electron donating solvents to solvents with good leaving groups could result in a change in the basicity of the LDOs, which could lead to different interactions with acidic molecules. Different metal

systems should be optimised for CO_2 capture based on the work carried out in Chapter Four. Literature showed an MgFe LDO possessed a higher CO_2 capture value.[8] Other methods to further modify the LDO should also be explored, such as amine-modification or K-doping. With the combined improvements, this could see CO_2 capture values of LDOs rival that of more widely used materials, such as zeolites, activated carbons and amine solutions. This would result in LDOs becoming a more viable CO_2 capture material option in the near future.

Other carbons should be explored in the next generation of carbon@LDH core@shells to further improve the rate of adsorption and CO_2 capture value. The interesting discovery of the retardation of spinel formation in the core@shell material should be further explored with DFTs or potentially via ^{27}Al NMR if a non-conductive carbon core is used. Understanding this phenomenon could prove invaluable to catalysis. Finally the improved materials mentioned above could be used to further develop the application of LDOs in the MCPU curing process. This would allow MCPUs to experience more diverse applications without limitations imposed by its long curing time.

The full understanding of the acidity and basicity of solvent treated LDHs/LDOs has allowed Kenyon *et al.* to fine tune ethanol treated NiAl LDOs for use as solid supports for polyethylene,[9] where the balance of acid/base ratio is crucial in determining the activity of the supported catalyst. The optimisation of calcination conditions allowed for a facile and cheap method to improve CO_2 capture performance when compared to the more widely used methods, such as the amine-modification utilised by Jung *et al.*.[10] The carbon@LDH core@shell materials expands on the research currently carried out by Shaffer and co-workers.[11–13] The materials developed in the Shaffer focuses on the use of graphene or graphene oxide as the carbon material, which leads to a very low surface area. By using activated carbon as the core material, the core@shell developed in this work exhibited a

drastically higher surface area, which could lead to a higher physisorption value for CO_2 capture. Finally, it is believe that the work carried out in this thesis is the first in deploying LDHs/LDOs in MCPUs to capture CO_2 released during the curing process which also reducing the curing time. This work will hopefully prove to be most invaluable to the future development of MCPUs as top contenders as adhesives.

7.2 References

1 Y. Gao, Z. Zhang, J. Wu, X. Yi, A. Zheng, A. Umar, D. O'Hare and Q. Wang, *J. Mater. Chem. A*, 2013, **1**, 12782.
2 D. A. Torres-Rodríguez, E. Lima, J. S. Valente and H. Pfeiffer, *J. Phys. Chem. A*, 2011, **115**, 12243–12250.
3 X. Zhu, C. Chen, H. Suo, Q. Wang, Y. Shi, D. O'Hare and N. Cai, *Energy*, 2019, **167**, 960–969.
4 E. L. G. Oliveira, C. A. Grande and A. E. Rodrigues, *Sep. Purif. Technol.*, 2008, **62**, 137–147.
5 M. K. Ram Reddy, Z. P. Xu, G. Q. (Max) Lu and J. C. Diniz da Costa, *Ind. Eng. Chem. Res.*, 2006, **45**, 7504–7509.
6 K. Coenen, F. Gallucci, B. Mezari, E. Hensen and M. van Sint Annaland, *J. CO_2 Util.*, 2018, **24**, 228–239.
7 J. M. Silva, R. Trujillano, V. Rives, M. A. Soria and L. M. Madeira, *Chem. Eng. J.*, 2017, **325**, 25–34.
8 X. P. Wang, J. J. Yu, J. Cheng, Z. P. Hao and Z. P. Xu, *Environ. Sci. Technol.*, 2008, **42**, 614–618.
9 P. Kenyon, D. W. J. Leung, M. Lyu, C. Chen, Z. R. Turner, J. C. Buffet and D. O'Hare, *J. Catal.*, 2021, **402**, 94–100.
10 W. Jung, J. Park and K. S. Lee, *Chem. Eng. Sci.*, 2018, **177**, 122–131.
11 A. Garcia-Gallastegui, D. Iruretagoyena, V. Gouvea, M. Mokhtar, A. M. Asiri, S. N. Basahel, S. A. Al-Thabaiti, A. O. Alyoubi, D. Chadwick and M. S. P. Shaffer, *Chem. Mater.*, 2012, **24**, 4531–4539.
12 D. Iruretagoyena, M. S. P. Shaffer and D. Chadwick, *Ind. Eng. Chem. Res.*, 2015, **54**, 6781–6792.
13 M. De Marco, R. Menzel, S. M. Bawaked, M. Mokhtar, A. Y. Obaid, S. N. Basahel and M. S. P. Shaffer, *Carbon N. Y.*, 2017, **123**, 616–627.

Appendix A - Appendices for Chapter Three

A.1 TGA of LDH samples

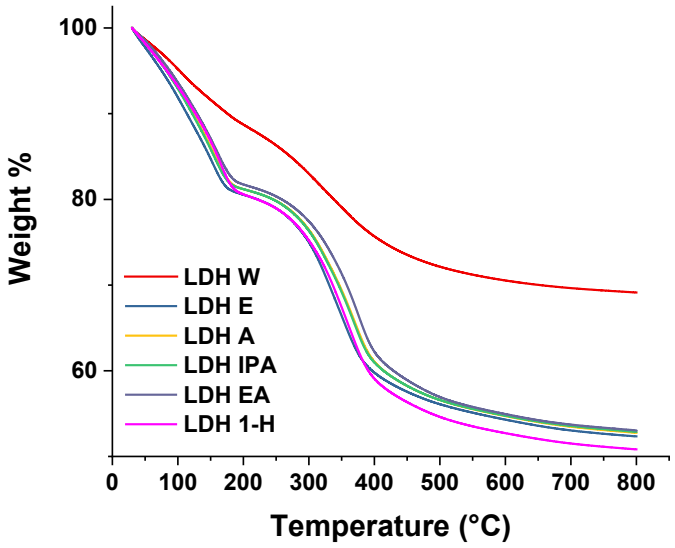


Figure A.1 - TGA of all LDH samples.

A.2 N_2 adsorption-desorption isotherms of LDHs and LDOs

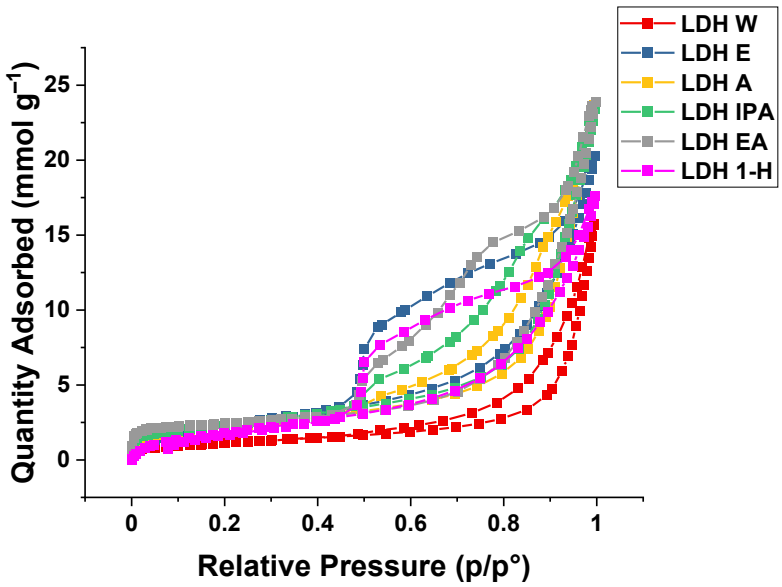


Figure A.2 - N_2 adsorption-desorption isotherms of LDH samples.

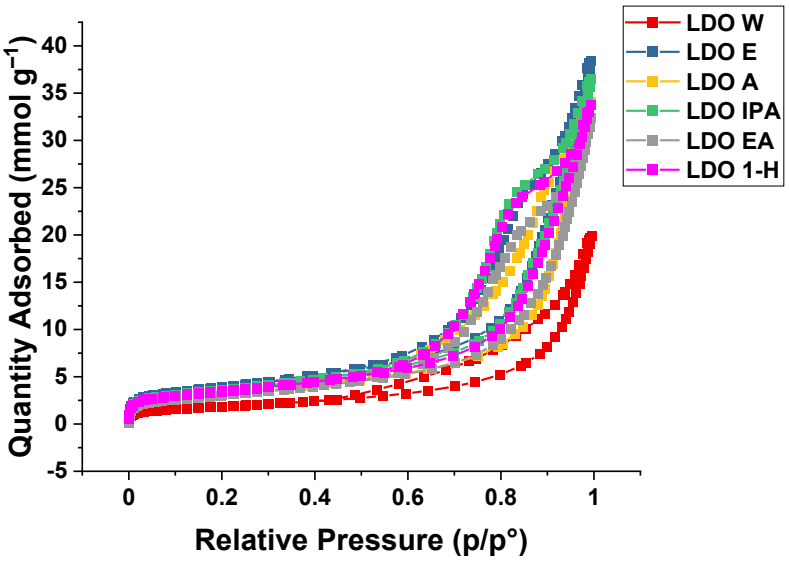


Figure A.3 - N_2 adsorption-desorption isotherms of LDO samples.

A.3 Pore size distributions of LDHs and LDOs

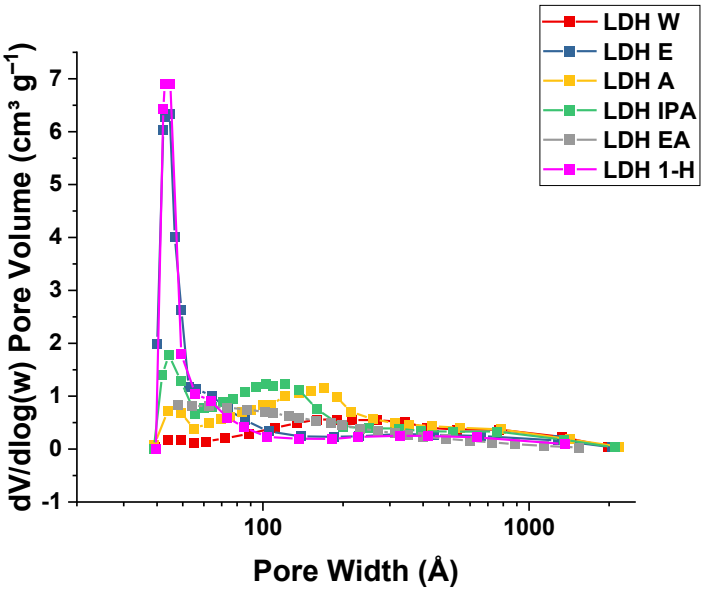


Figure A.4 - Pore size distribution of LDH samples.

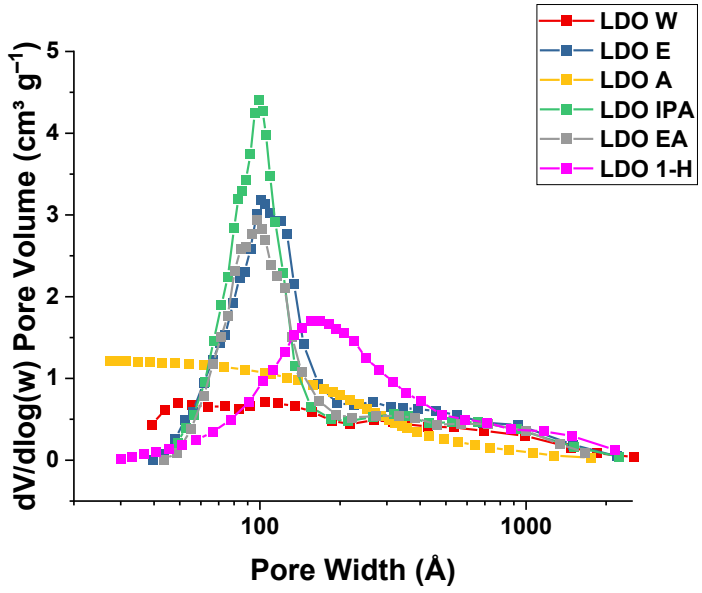


Figure A.5 - Pore size distribution of LDO samples.

A.4 Titration data

Table A.1 - Titration values for LDHs.

Sample	Bromothymol blue (mmol g^{-1})	Error	Phenolphthalein (mmol g^{-1})	error	Clayton yellow (mmol g^{-1})	error
LDH W	0.70	0.01	0.56	0.04	0.33	0.06
LDH E	0.88	0.00	0.34	0.02	0.28	0.04
LDH A	0.86	0.01	0.35	0.04	0.36	0.01
LDH IPA	0.90	0.00	0.56	0.09	0.24	0.01
LDH EA	0.85	0.00	0.40	0.03	0.21	0.01
LDH 1-H	0.92	0.00	0.38	0.02	0.21	0.01

Table A.2 - Titration values for dehydrated LDHs.

Sample (dehydrated)	Bromothymol blue (mmol g^{-1})	Error	Phenolphthalein (mmol g^{-1})	Error	Clayton yellow (mmol g^{-1})	Error
LDH W	0.41	0.06	0.27	0.01	0.25	0.00
LDH E	0.57	0.02	0.29	0.03	0.22	0.01
LDH A	0.57	0.01	0.39	0.05	0.35	0.00
LDH IPA	0.67	0.02	0.42	0.02	0.28	0.02
LDH EA	0.66	0.01	0.30	0.05	0.25	0.01
LDH 1-H	0.67	0.01	0.38	0.03	0.31	0.03

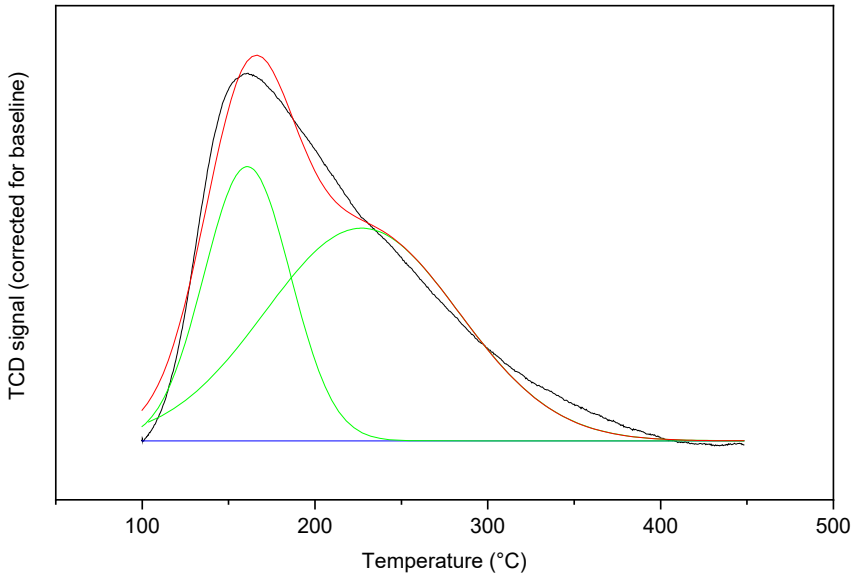
Table A.3 - Titration data for LDOs.

Sample	Bromothymol blue (mmol g^{-1})	Phenolphthalein (mmol g^{-1})	Clayton yellow (mmol g^{-1})
LDO W	0.71	0.63	0.55
LDO E	1.04	1.06	0.78
LDO A	1.00	0.86	0.71
LDO IPA	1.09	1.08	0.99
LDO EA	0.89	0.75	0.81
LDO 1-H	1.58	1.41	0.99

A.5 Deconvolution of TPD data

Peak Analysis

Data Set:[Book1]Sheet1!D"TCD signal (corrected for baseline)" Date:29/03/2021
BaseLine:Constant
Chi^2=2.16119E-06 Adj. R-Square=9.83245E-01 # of Data Points=723
SS=1.54741E-03 Degrees of Freedom=716



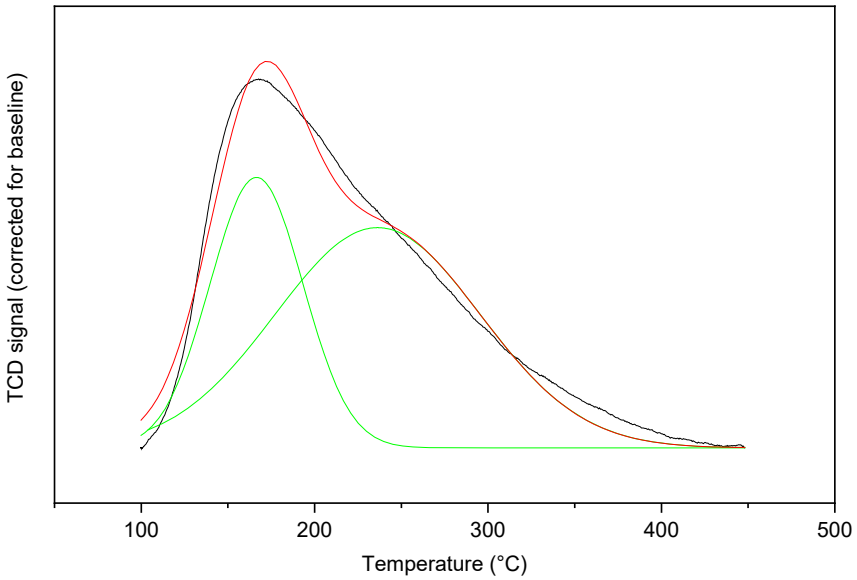
Fitting Results

Peak Index	Peak Type	Area Intg	FWHM	Max Height	Center Grvty	Area IntgP
1	Gaussian	2.68703	131.86653	0.01937	227.06017	63.3486
2	Gaussian	1.55463	58.92818	0.02497	160.80161	36.6514

Figure A.6 - Peak deconvolution of CO_2 TPD of **LDO W**.

Peak Analysis

Data Set:[Book1]Sheet1!B Date:29/03/2021
BaseLine:Line
Chi^2=2.12542E-06 Adj. R-Square=9.83357E-01 # of Data Points=725
SS=1.52818E-03 Degrees of Freedom=719



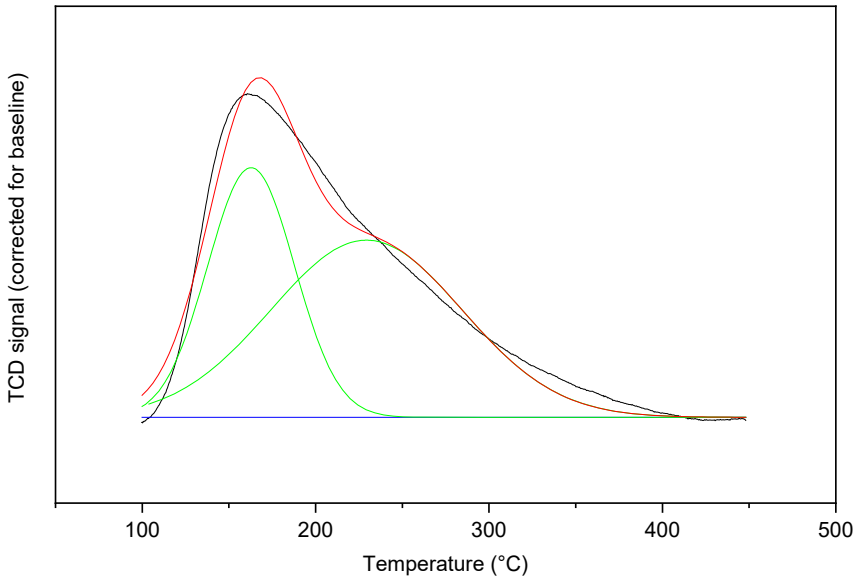
Fitting Results

Peak Index	Peak Type	Area Intg	FWHM	Max Height	Center Grvty	Area IntgP
1	Gaussian	1.63562	63.15267	0.02449	166.48359	35.87968
2	Gaussian	2.923	139.15263	0.01995	236.30563	64.12032

Figure A.7 - Peak deconvolution of CO_2 TPD of **LDO E**.

Peak Analysis

Data Set:[Book1]SubtractedData2!B"TCD signal (corrected for baseline)"Date:29/03/2021
BaseLine:Constant
Chi^2=3.27832E-06 Adj. R-Square=9.81049E-01 # of Data Points=725
SS=2.35384E-03 Degrees of Freedom=718



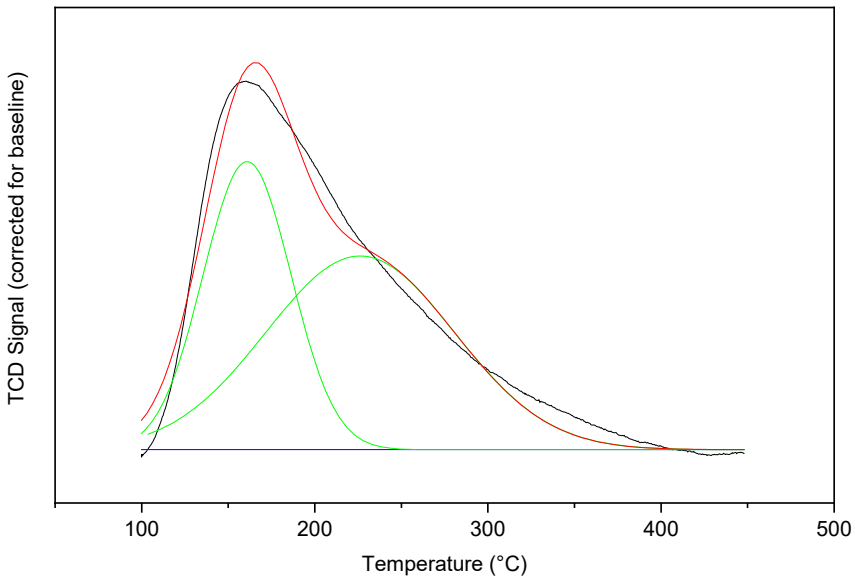
Fitting Results

Peak Index	Peak Type	Area Intg	FWHM	Max Height	Center Grvty	Area IntgP
1	Gaussian	2.92758	129.81301	0.02139	229.2854	60.86018
2	Gaussian	1.88276	59.05152	0.03014	162.76941	39.13982

Figure A.8 - Peak deconvolution of CO_2 TPD of **LDO A**.

Peak Analysis

Data Set:[Book1]SubtractedData2!B"TCD Signal (corrected for baseline)"Date:29/03/2021
BaseLine:Constant
Chi^2=3.11203E-06 Adj. R-Square=9.80211E-01 # of Data Points=724
SS=2.23133E-03 Degrees of Freedom=717



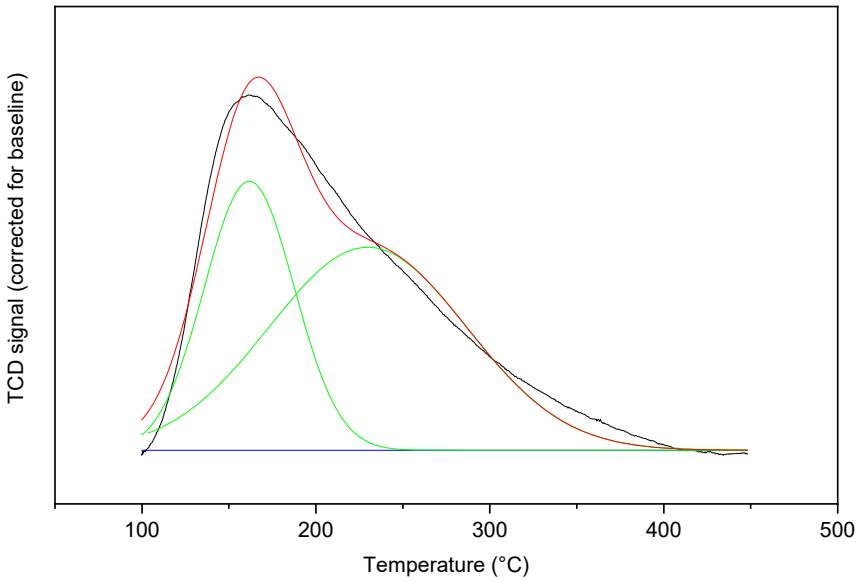
Fitting Results

Peak Index	Peak Type	Area Intg	FWHM	Max Height	Center Grvty	Area IntgP
1	Gaussian	1.83785	59.92102	0.02906	160.89549	41.06846
2	Gaussian	2.63724	128.08231	0.01954	226.17816	58.93154

Figure A.9 - Peak deconvolution of CO_2 TPD of **LDO IPA**.

Peak Analysis

Data Set:[Book1]SubtractedData2!B"TCD signal (corrected for baseline)"Date:29/03/2021
BaseLine:Constant
Chi^2=2.79510E-06 Adj. R-Square=9.80990E-01 # of Data Points=724
SS=2.00409E-03 Degrees of Freedom=717



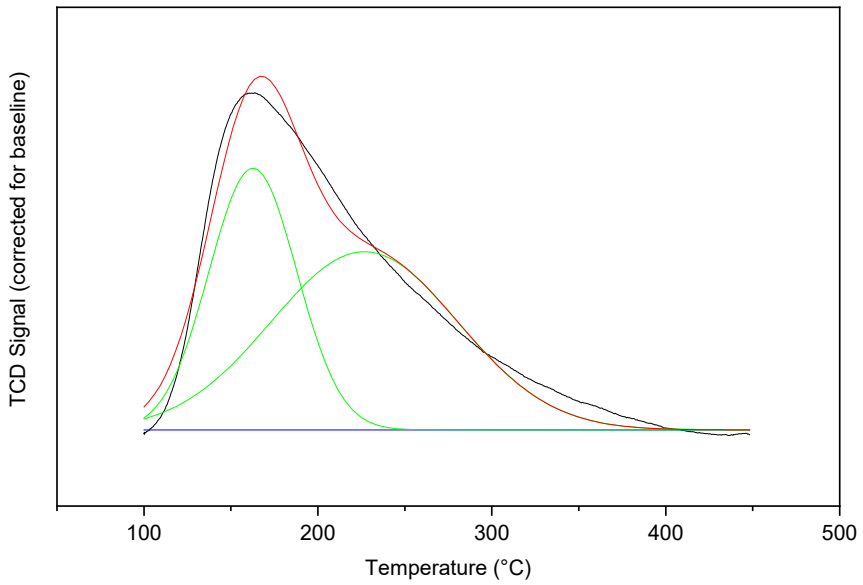
Fitting Results

Peak Index	Peak Type	Area Intg	FWHM	Max Height	Center Grvty	Area IntgP
1	Gaussian	1.73492	60.79722	0.02704	161.69064	37.66263
2	Gaussian	2.87156	133.73735	0.0204	229.82436	62.33737

Figure A.10 - Peak deconvolution of CO_2 TPD of **LDO EA**.

Peak Analysis

Data Set:[Book1]SubtractedData2!B"TCD Signal (corrected for baseline)"Date:29/03/2021
BaseLine:Constant
Chi^2=4.81319E-06 Adj. R-Square=9.81126E-01 # of Data Points=724
SS=3.45105E-03 Degrees of Freedom=717



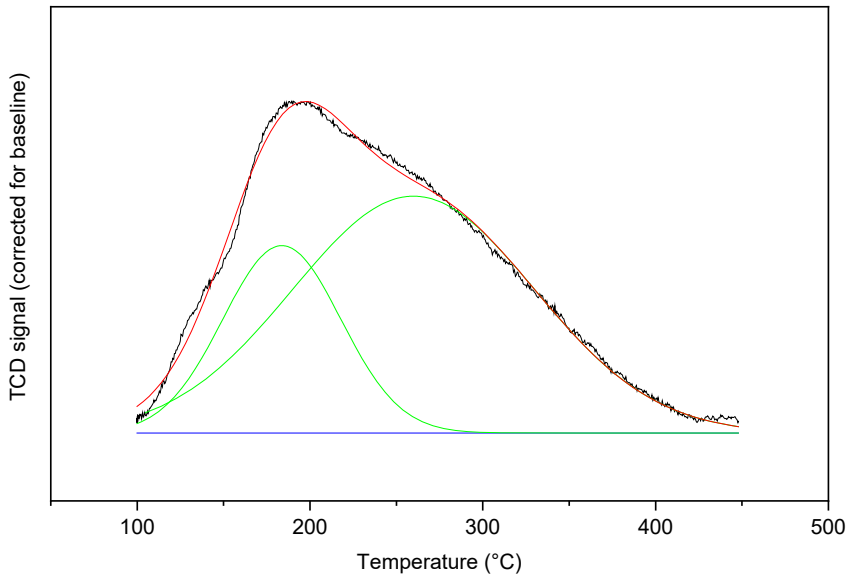
Fitting Results

Peak Index	Peak Type	Area Intg	FWHM	Max Height	Center Grvty	Area IntgP
1	Gaussian	2.30855	59.47545	0.03671	162.65479	40.90522
2	Gaussian	3.33511	126.44747	0.02501	226.72286	59.09478

Figure A.11 - Peak deconvolution of CO_2 TPD of **LDO 1-H**.

Peak Analysis

Data Set:[Book1]SubtractedData1!B"TCD signal (corrected for baseline)"Date:29/03/2021
BaseLine:Constant
Chi^2=5.04396E-08 Adj. R-Square=9.95402E-01 # of Data Points=724
SS=3.61652E-05 Degrees of Freedom=717



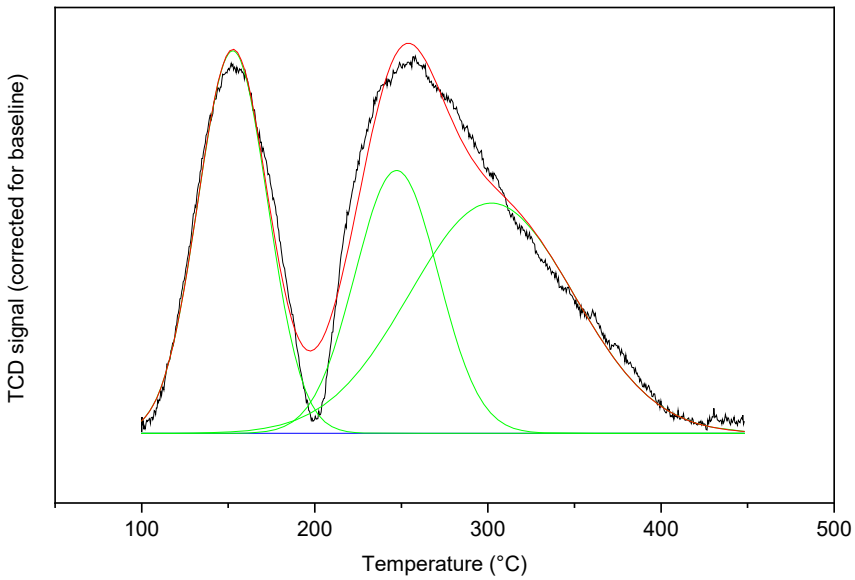
Fitting Results

Peak Index	Peak Type	Area Intg	FWHM	Max Height	Center Grvty	Area IntgP
1	Gaussian	0.48401	80.56444	0.00568	183.69857	28.05676
2	Gaussian	1.2411	164.64085	0.00719	259.95525	71.94324

Figure A.12 - Peak deconvolution of NH_3 TPD of **LDO W**.

Peak Analysis

Data Set:[Book1]Sheet1!D"TCD signal (corrected for baseline)" Date:29/03/2021
BaseLine:Constant
Chi^2=5.38443E-08 Adj. R-Square=9.77576E-01 # of Data Points=723
SS=3.83910E-05 Degrees of Freedom=713



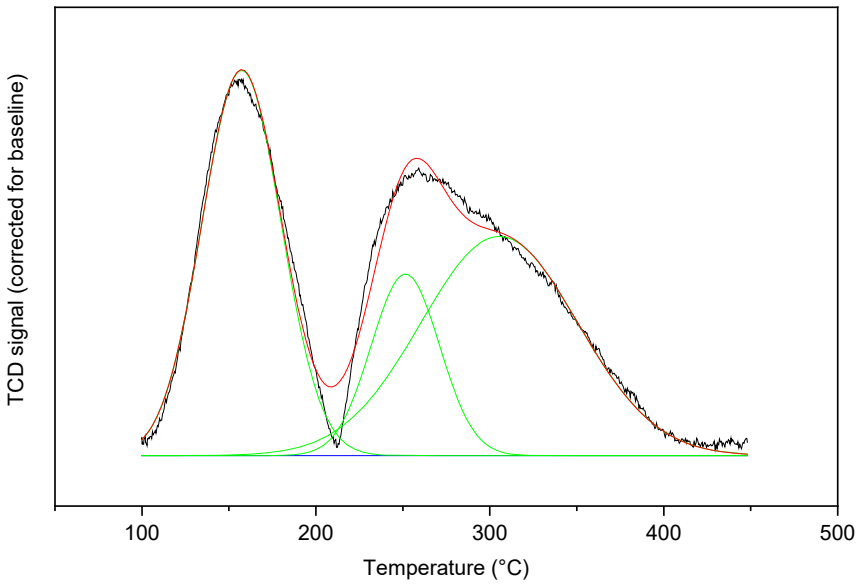
Fitting Results

Peak Index	Peak Type	Area Intg	FWHM	Max Height	Center Grvty	Area IntgP
1	Gaussian	0.23237	47.35095	0.00463	152.60395	30.80705
2	Gaussian	0.1916	56.56029	0.00318	247.26273	25.40148
3	Gaussian	0.33031	111.43214	0.00279	302.06242	43.79146

Figure A.13 - Peak deconvolution of NH_3 TPD of **LDO E**.

Peak Analysis

Data Set:[Book1]Sheet1!D"TCD signal (corrected for baseline)" Date:29/03/2021
BaseLine:Constant
Chi^2=5.10032E-08 Adj. R-Square=9.84343E-01 # of Data Points=723
SS=3.63653E-05 Degrees of Freedom=713



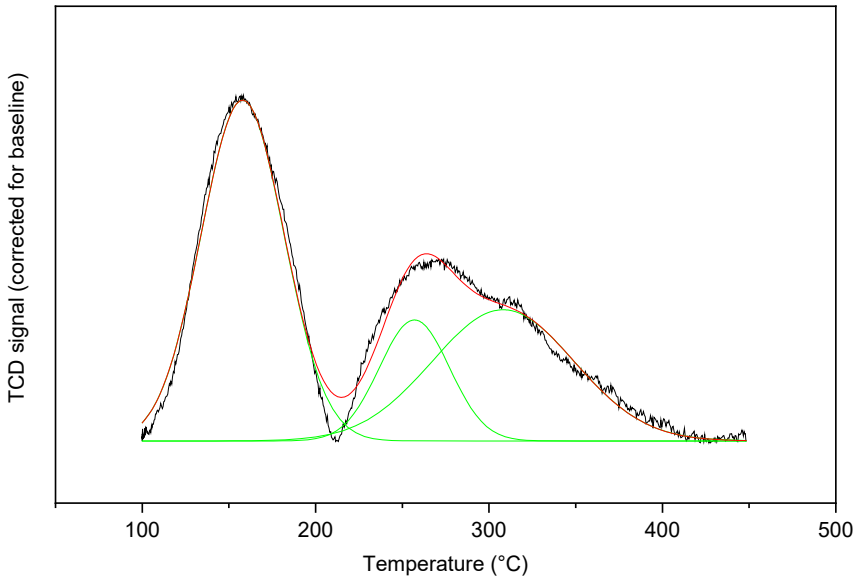
Fitting Results

Peak Index	Peak Type	Area Intg	FWHM	Max Height	Center Grvty	Area IntgP
1	Gaussian	0.34956	53.4823	0.00618	157.25756	39.29084
2	Gaussian	0.14349	46.34014	0.00291	251.45976	16.12826
3	Gaussian	0.39663	106.10679	0.00351	305.45903	44.58091

Figure A.14 - Peak deconvolution of NH_3 TPD of **LDO A**.

Peak Analysis

Data Set:[Book1]Sheet1!B Date:29/03/2021
BaseLine:Line
Chi^2=3.91809E-08 Adj. R-Square=9.83904E-01 # of Data Points=724
SS=2.81319E-05 Degree of Freedom=718



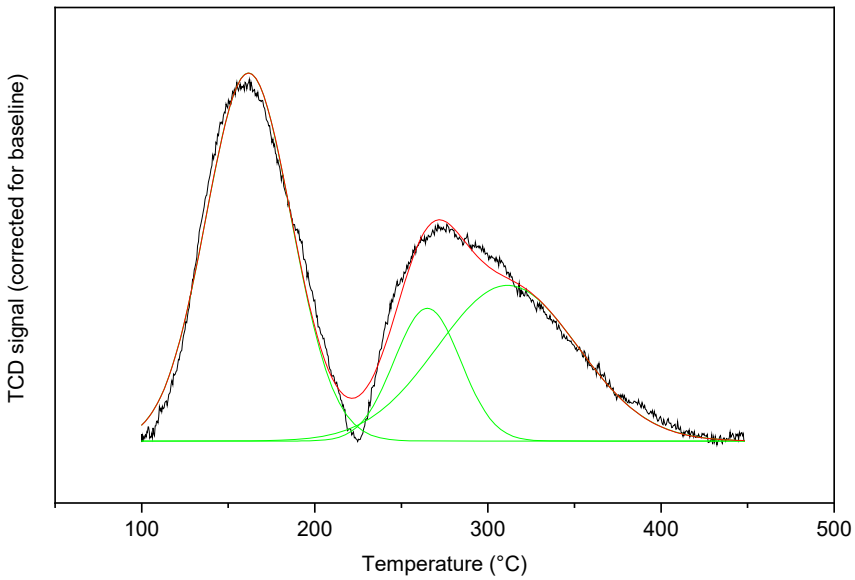
Fitting Results

Peak Index	Peak Type	Area Intg	FWHM	Max Height	Center Grvty	Area IntgP
1	Gaussian	0.32634	56.31974	0.00549	157.87924	50.84358
2	Gaussian	0.09875	47.63005	0.00195	256.9785	15.38577
3	Gaussian	0.21676	96.40426	0.00211	308.11568	33.77065

Figure A.15 - Peak deconvolution of NH_3 TPD of **LDO IPA**.

Peak Analysis

Data Set:[Book1]Sheet1!B Date:29/03/2021
BaseLine:Line
Chi^2=4.62141E-08 Adj. R-Square=9.83735E-01 # of Data Points=724
SS=3.30431E-05 Degree of Freedom=715



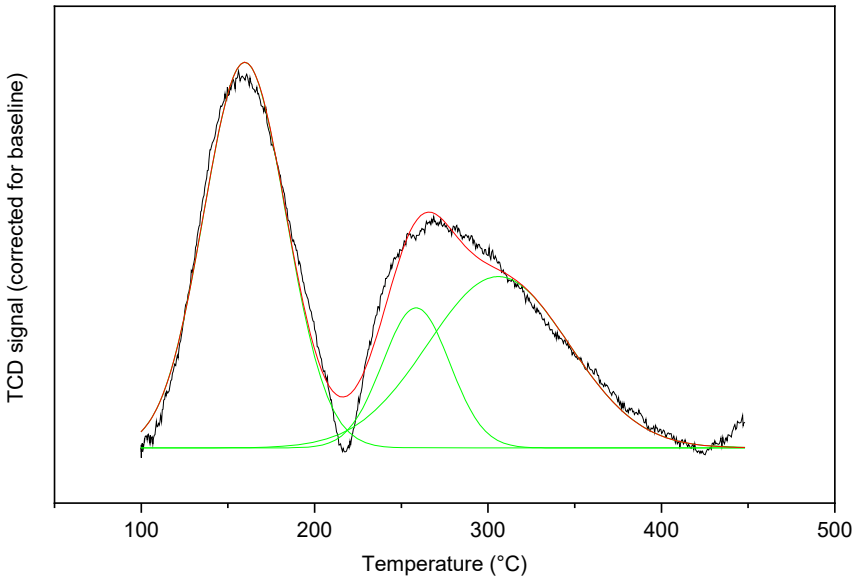
Fitting Results

Peak Index	Peak Type	Area Intg	FWHM	Max Height	Center Grvty	Area IntgP
1	Gaussian	0.36459	58.01665	0.00594	161.71075	50.44777
2	Gaussian	0.10306	45.19688	0.00214	265.03687	14.25976
3	Gaussian	0.25506	95.38065	0.00251	311.38507	35.29247

Figure A.16 - Peak deconvolution of NH_3 TPD of **LDO EA**.

Peak Analysis

Data Set:[Book1]Sheet1!B Date:29/03/2021
BaseLine:Line
Chi^2=7.28795E-08 Adj. R-Square=9.81352E-01 # of Data Points=723
SS=5.20359E-05 Degree of Freedom=714



Fitting Results

Peak Index	Peak Type	Area Intg	FWHM	Max Height	Center Grvty	Area IntgP
1	Gaussian	0.41287	55.89392	0.00698	159.70247	48.40629
2	Gaussian	0.12332	45.68934	0.00254	258.51472	14.45848
3	Gaussian	0.31674	95.94919	0.0031	305.94033	37.13523

Figure A.17 - Peak deconvolution of NH_3 TPD of **LDO 1-H**.

A.6 ^{1}H and ^{27}Al ssNMR spectra of LDH samples

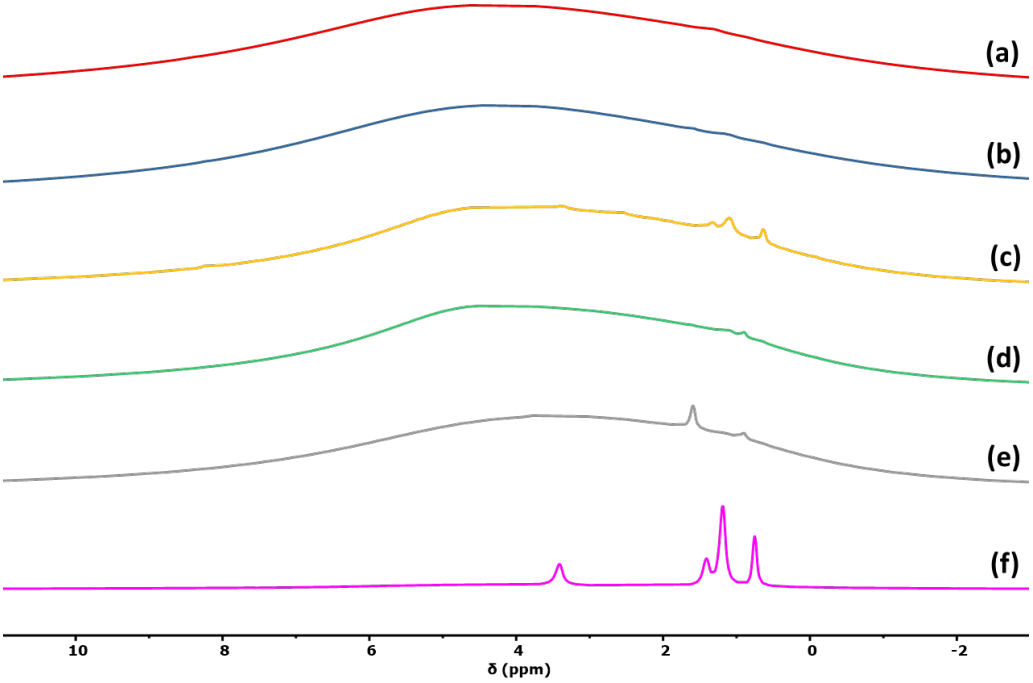


Figure A.18 - ^{1}H MAS ssNMR of LDH samples.

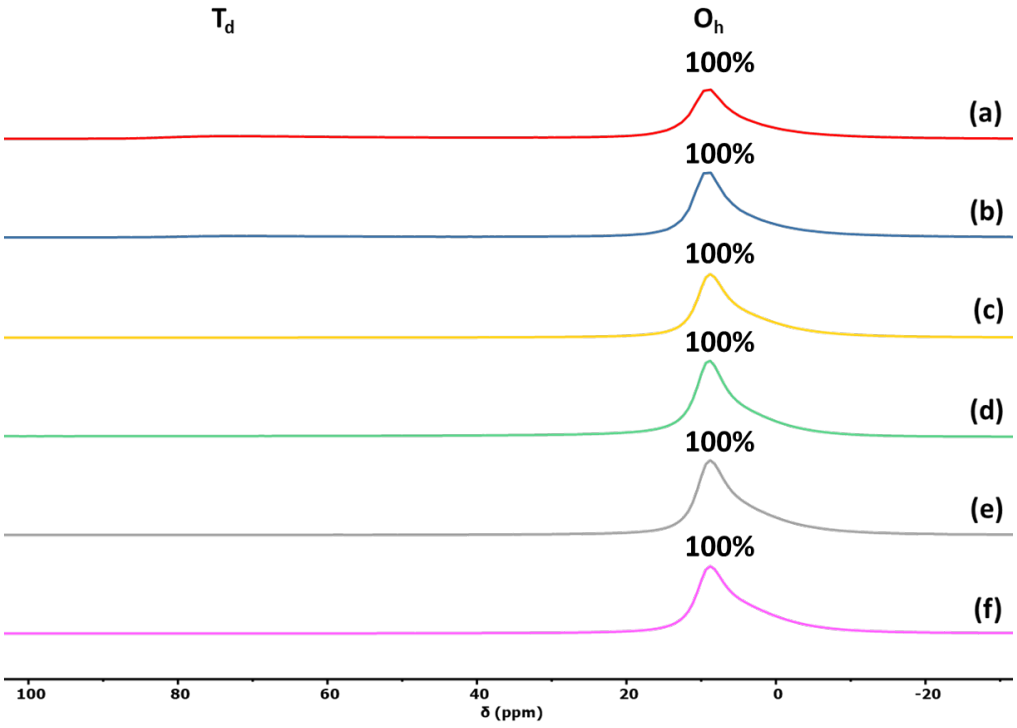


Figure A.19 – ^{27}Al CPMAS ssNMR of LDH samples.

A.7 CO_2 adsorption profiles of LDO samples

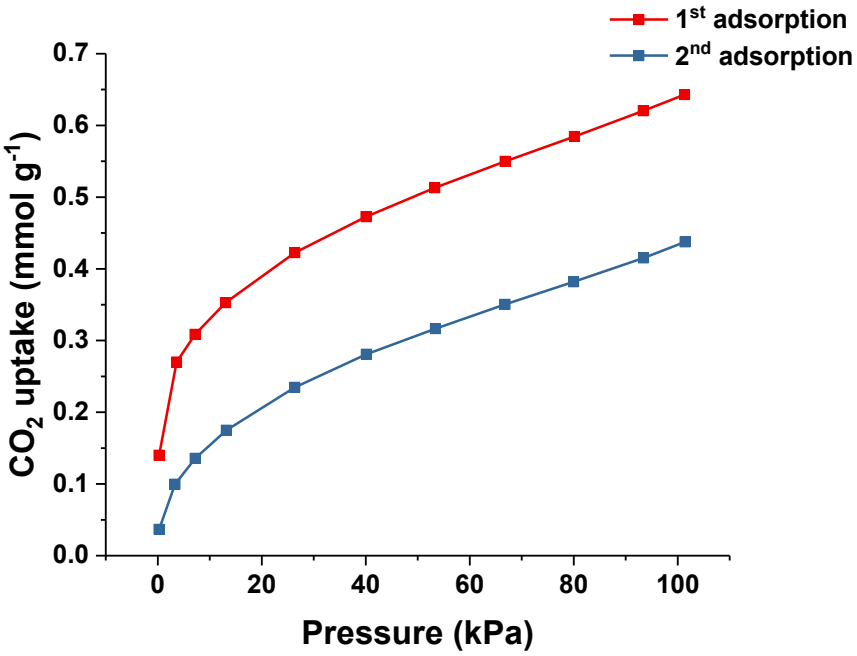


Figure A.20 - 1st and 2nd CO_2 adsorption profiles of **LDO W.**

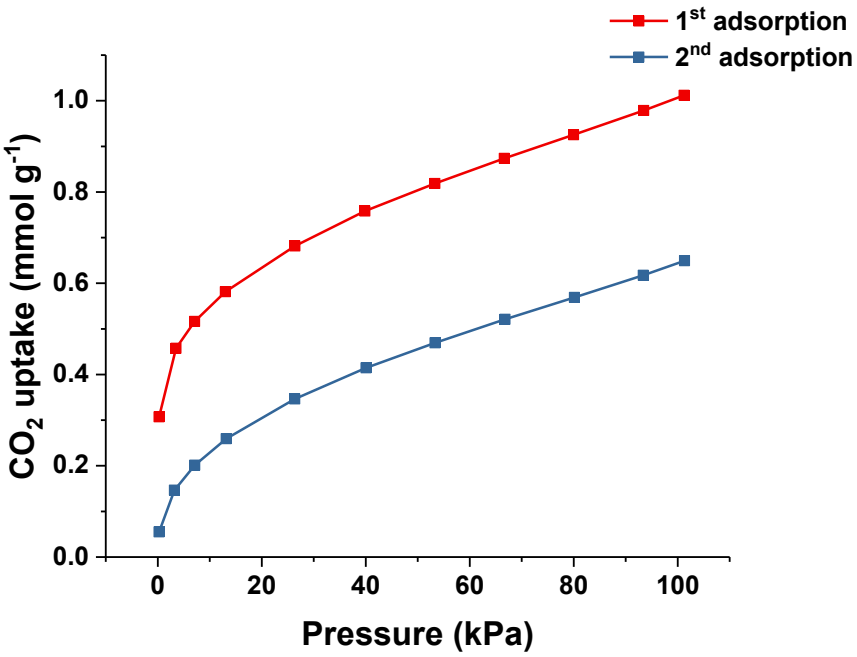


Figure A.21 - 1st and 2nd CO_2 adsorption profiles of **LDO E**.

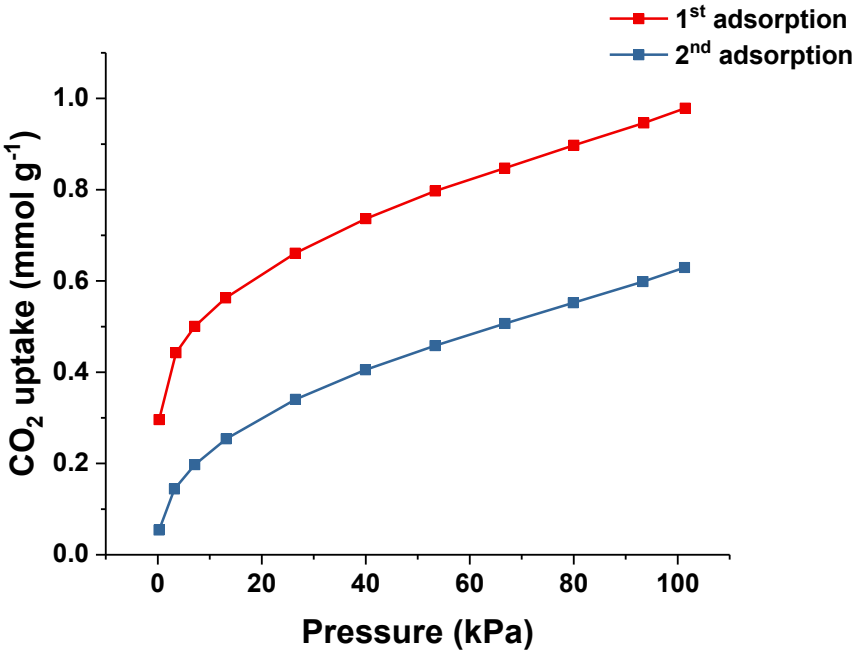


Figure A.22 - 1st and 2nd CO_2 adsorption profiles of **LDO A**.

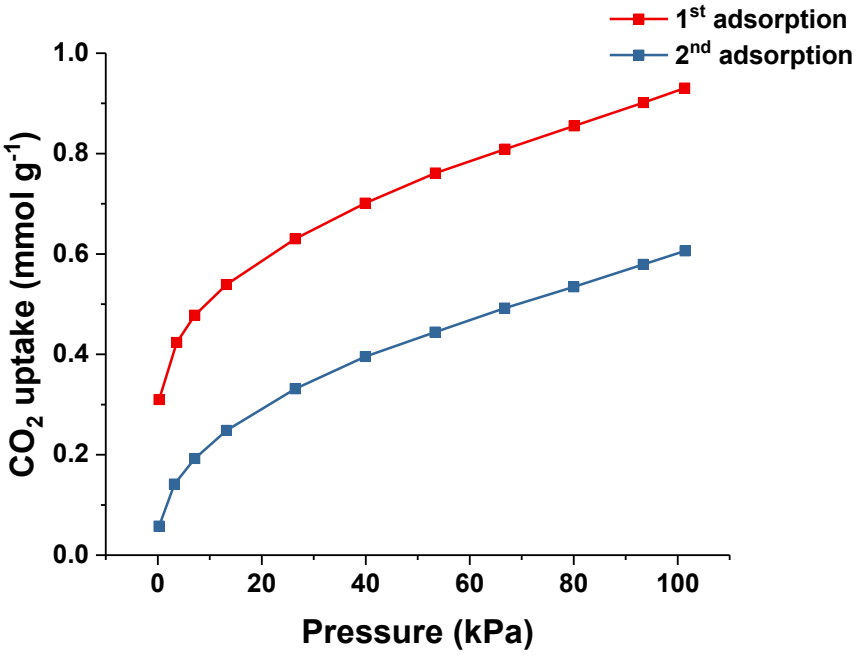


Figure A.23 - 1st and 2nd CO_2 adsorption profiles of **LDO IPA**.

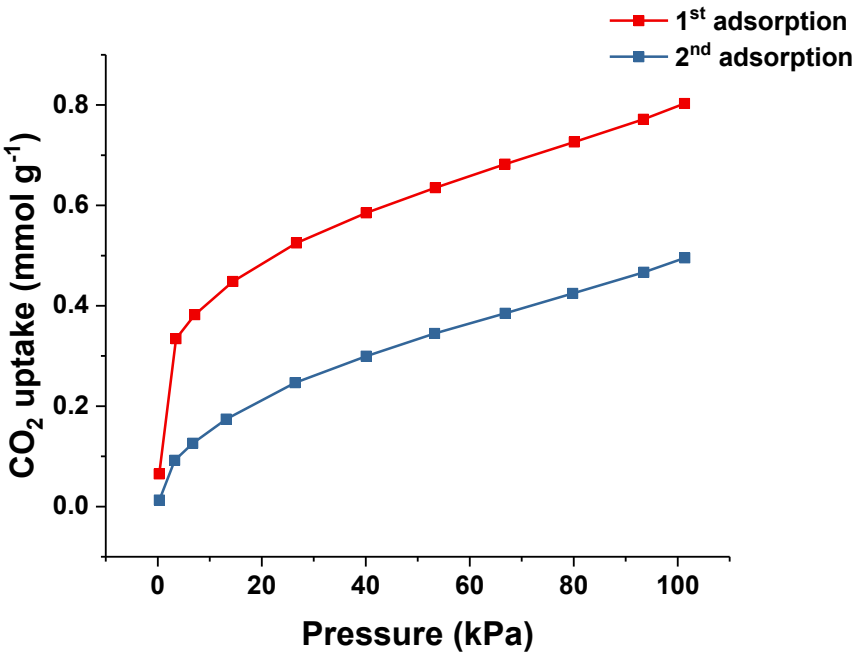


Figure A.24 - 1st and 2nd CO_2 adsorption profiles of **LDO EA**.

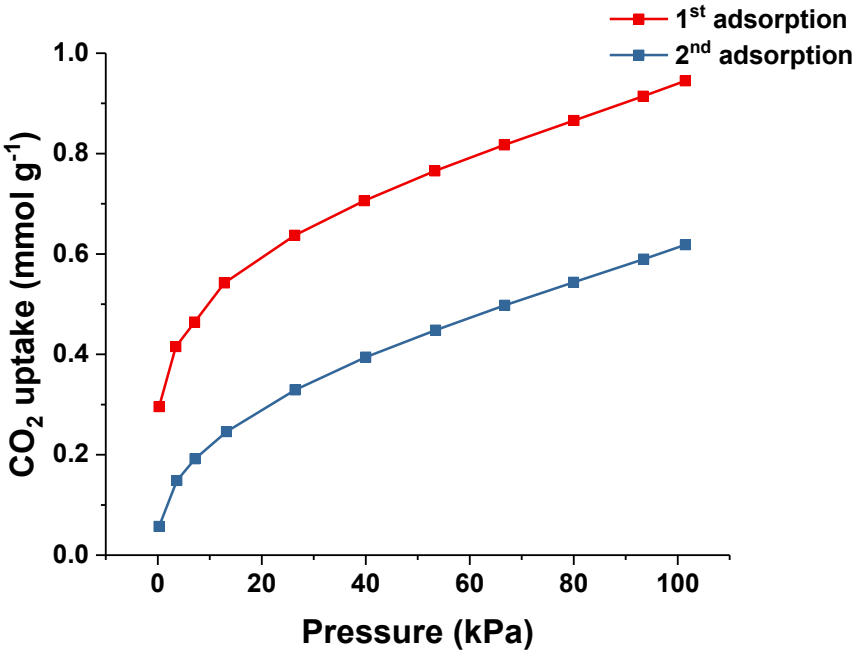


Figure A.25 - 1st and 2nd CO_2 adsorption profiles of **LDO 1-H**.

Appendix B - Appendices for Chapter Four

B.1 N_2 adsorption-desorption isotherms of Mg_xAl LDHs and LDOs

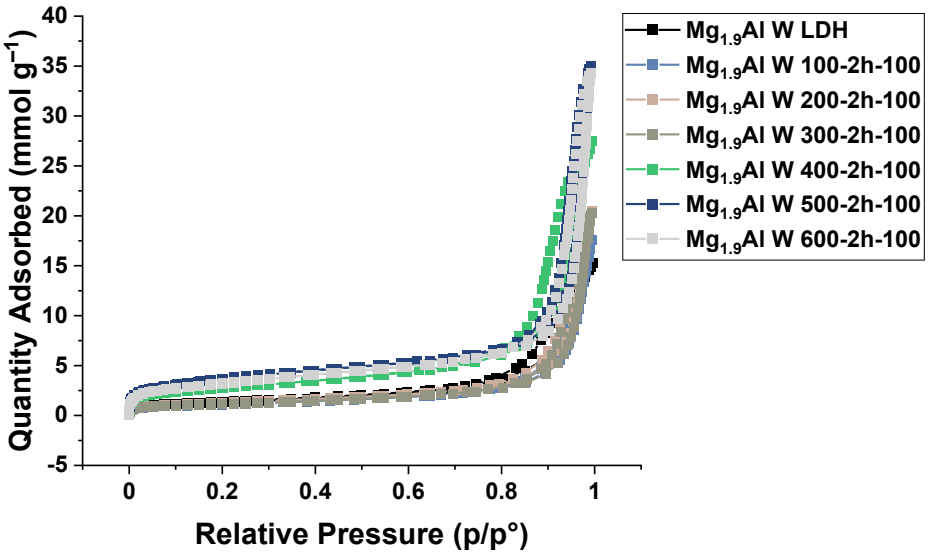


Figure B.1 - N_2 adsorption-desorption isotherms of $Mg_{1.9}Al$ W X-2h-100.

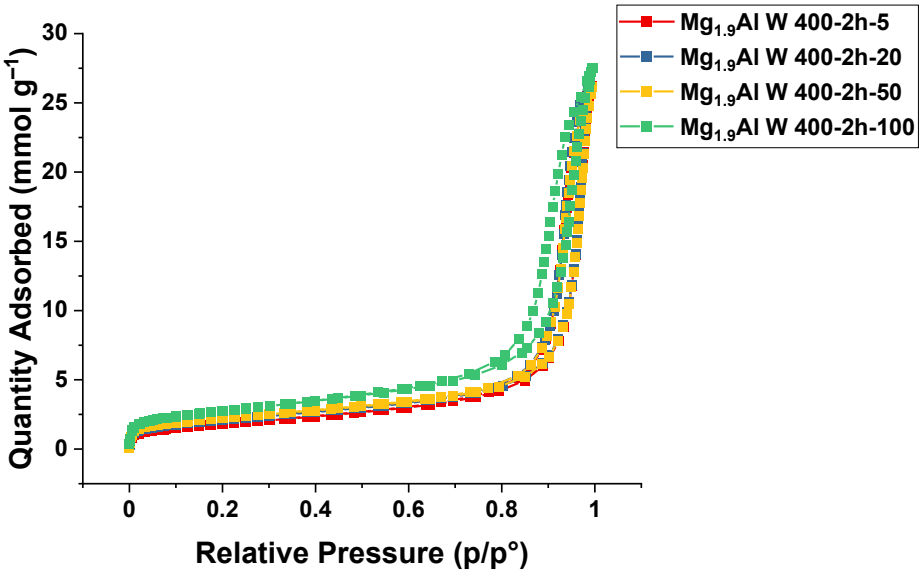


Figure B.2 - N_2 adsorption-desorption isotherms of $Mg_{1.9}Al$ W 400-2h-X.

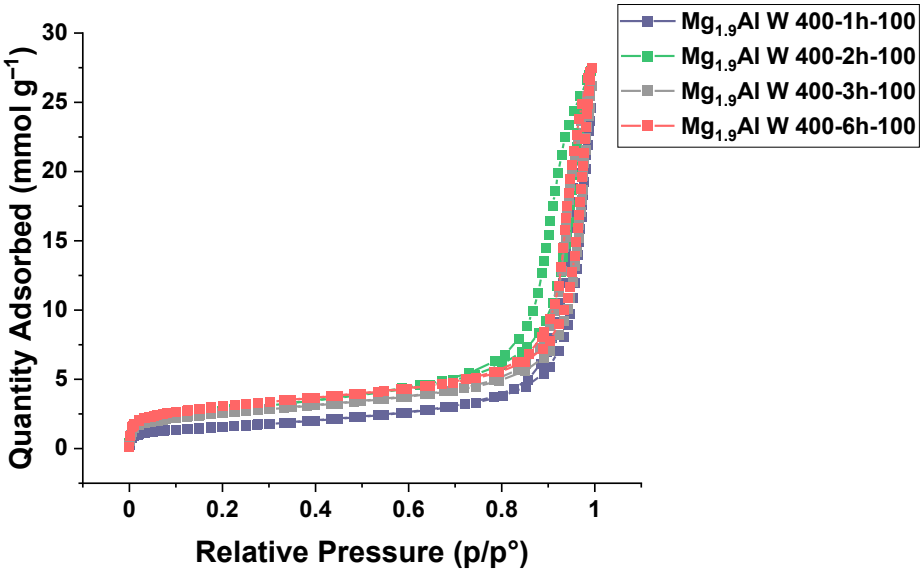


Figure B.3 - N_2 adsorption-desorption isotherms of $Mg_{1.9}Al$ W 400-X-100.

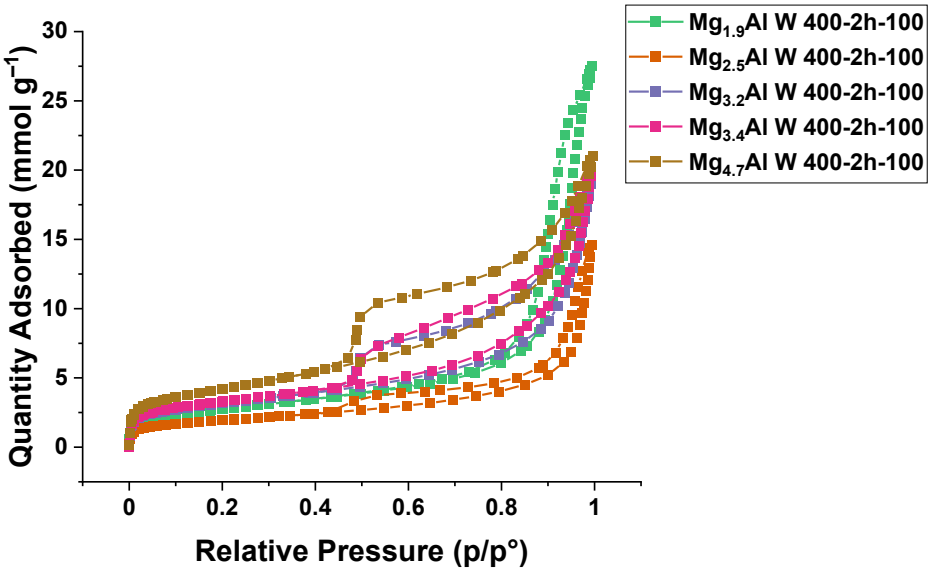


Figure B.4 - N_2 adsorption-desorption isotherms of Mg_xAl W 400-2h-100.

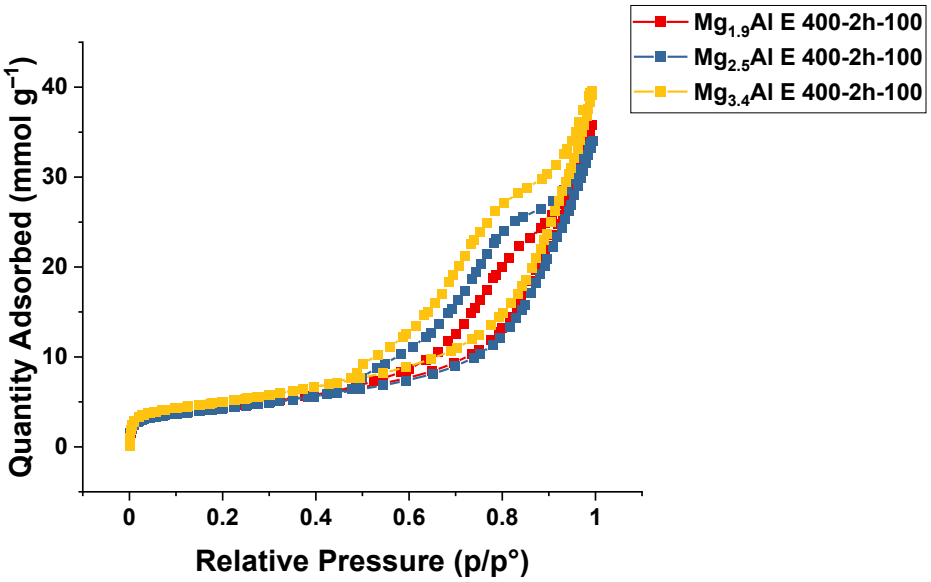


Figure B.5 - N_2 adsorption-desorption isotherms of Mg_xAl E 400-2h-100.

B.2 Pore size distributions of Mg_xAl LDHs and LDOs

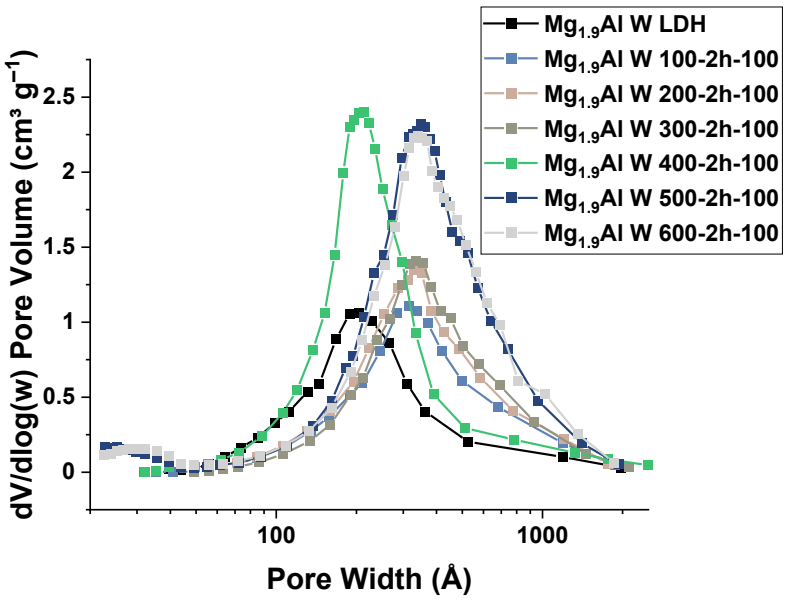


Figure B.6 - Pore size distribution of $Mg_{1.9}Al$ W X-2h-100.

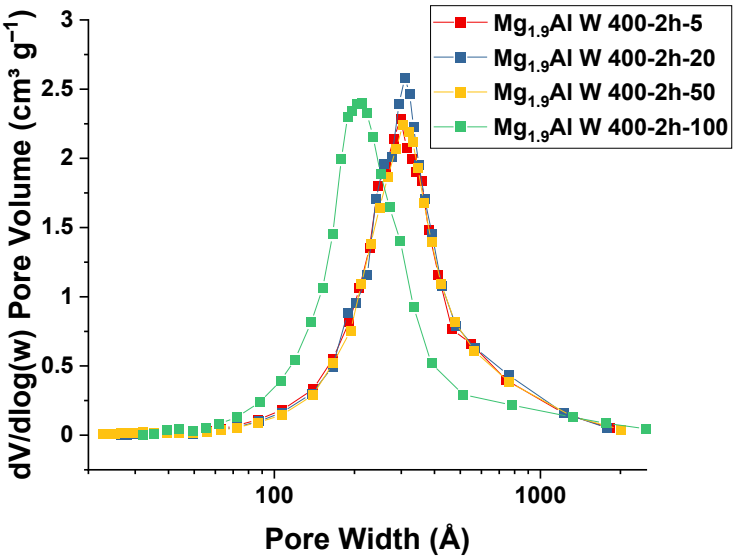


Figure B.7 - Pore size distribution of $Mg_{1.9}Al$ W 400-2h-X.

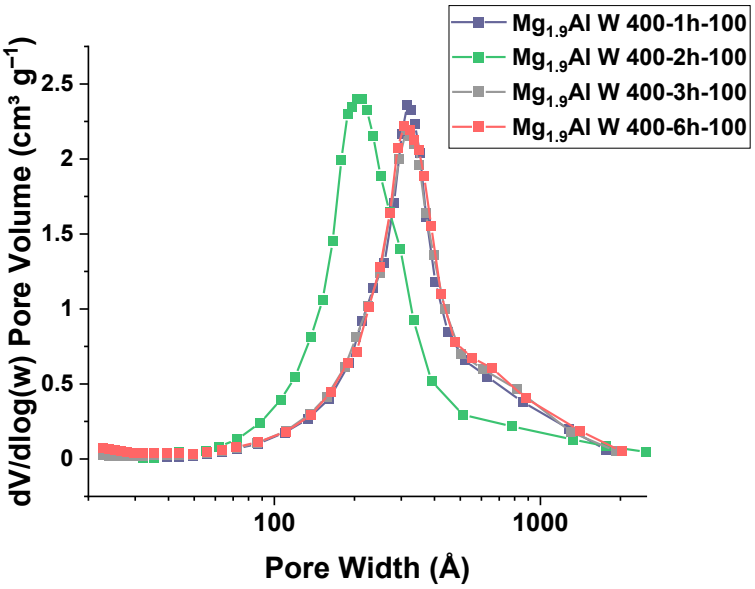


Figure B.8 - Pore size distribution of $Mg_{1.9}Al$ W 400-X-100.

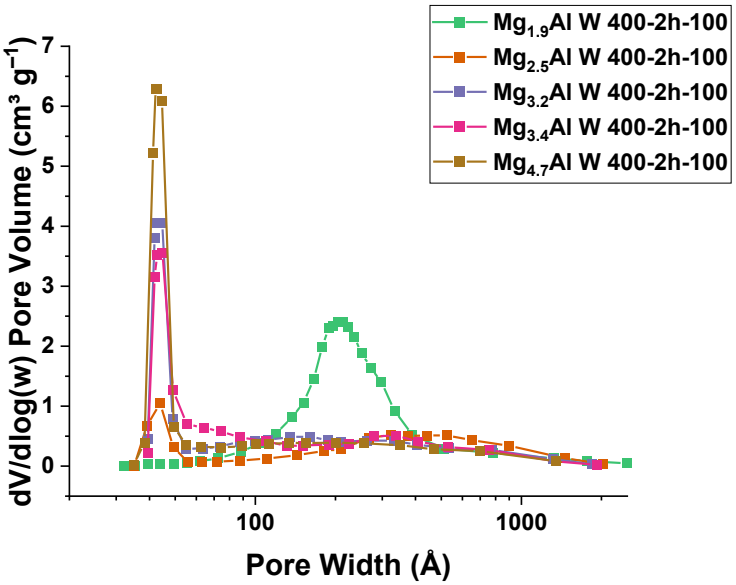


Figure B.9 - Pore size distribution of Mg_xAl W 400-2h-100.

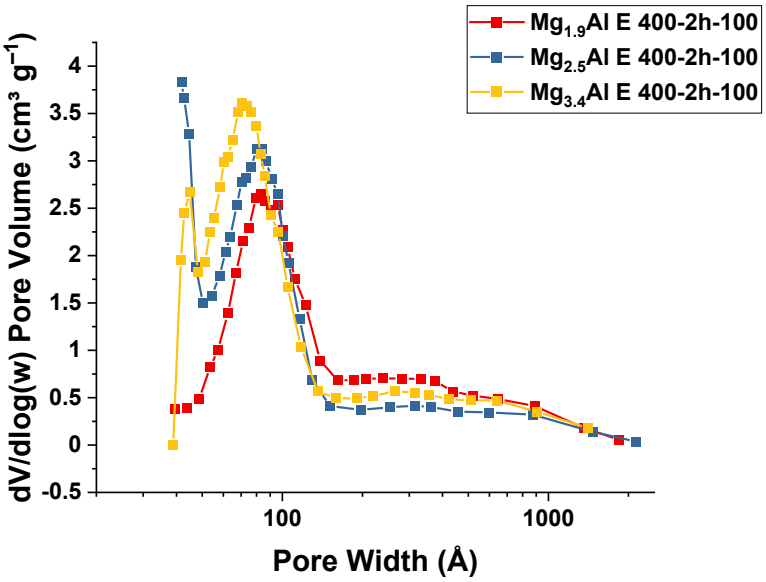
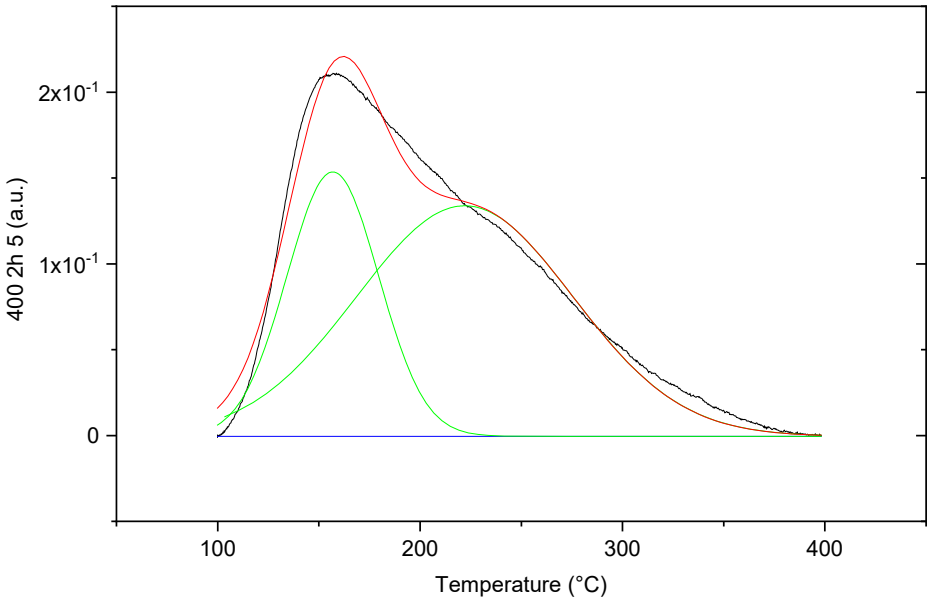


Figure B.10 - Pore size distribution of Mg_xAl E 400-2h-100.

B.3 Deconvolution of TPD data

Peak Analysis

Data Set:[Book3]Sheet1!C"Relative TCD signal" Date:30/04/2021
BaseLine:Constant
Chi^2=8.35984E-05 Adj. R-Square=9.83357E-01 # of Data Points=938
SS=7.78302E-02 Degrees of Freedom=931



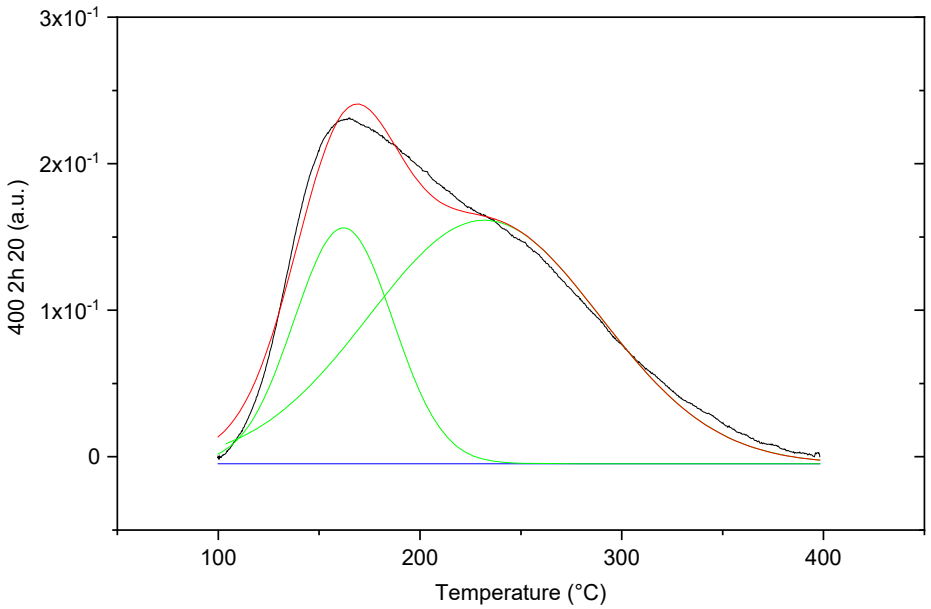
Fitting Results

Peak Index	Peak Type	Area Intg	FWHM	Max Height	Center Grvty	Area IntgP
1	Gaussian	8.69121	53.36726	0.15392	156.87507	32.87446
2	Gaussian	17.74637	125.67188	0.13421	222.07638	67.12554

Figure B.11 - Peak deconvolution of CO_2 TPD of $Mg_{1.9}$ W 400-2h-5.

Peak Analysis

Data Set:[Book3]Sheet1!F"Relative TCD signal" Date:30/04/2021
BaseLine:Constant
Chi^2=7.19262E-05 Adj. R-Square=9.88528E-01 # of Data Points=943
SS=6.73229E-02 Degrees of Freedom=936



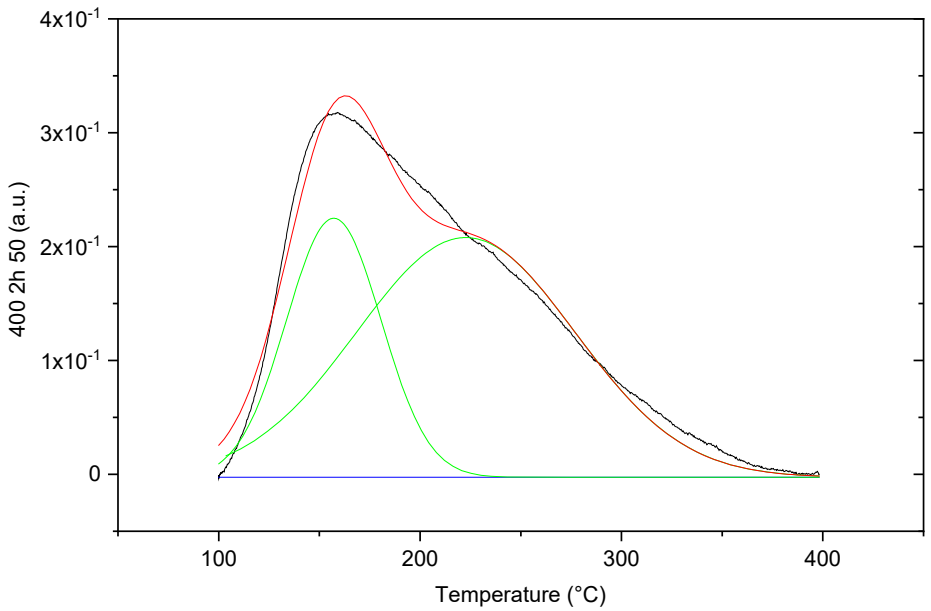
Fitting Results

Peak Index	Peak Type	Area Intg	FWHM	Max Height	Center Grvty	Area IntgP
1	Gaussian	9.85168	57.85903	0.16089	162.09475	29.51285
2	Gaussian	23.52931	134.75415	0.1661	231.87457	70.48715

Figure B.12 - Peak deconvolution of CO_2 TPD of $Mg_{1.9}Al$ W 400-2h-20.

Peak Analysis

Data Set:[Book3]Sheet1!I"Relative TCD signal" Date:30/04/2021
BaseLine:Constant
Chi^2=1.80350E-04 Adj. R-Square=9.84662E-01 # of Data Points=939
SS=1.68086E-01 Degrees of Freedom=932



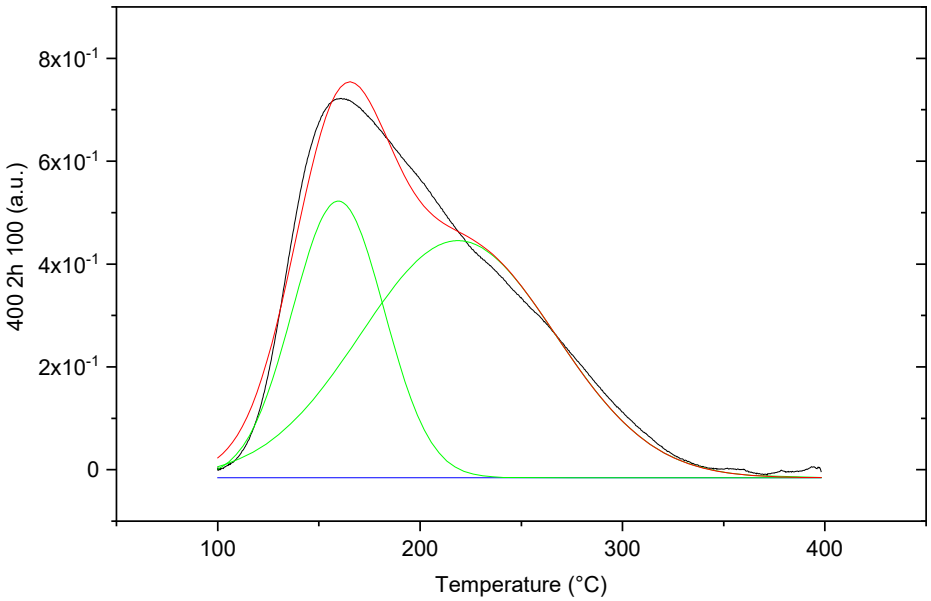
Fitting Results

Peak Index	Peak Type	Area Intg	FWHM	Max Height	Center Grvty	Area IntgP
1	Gaussian	13.30189	55.36167	0.22746	157.14277	32.04751
2	Gaussian	28.2049	127.44546	0.2105	222.68596	67.95249

Figure B.13 - Peak deconvolution of CO_2 TPD of $Mg_{1.9}Al$ W 400-2h-50.

Peak Analysis

Data Set:[Book3]Sheet1!L"Relative TCD signal" Date:30/04/2021
BaseLine:Constant
Chi^2=6.02014E-04 Adj. R-Square=9.90660E-01 # of Data Points=940
SS=5.61679E-01 Degrees of Freedom=933



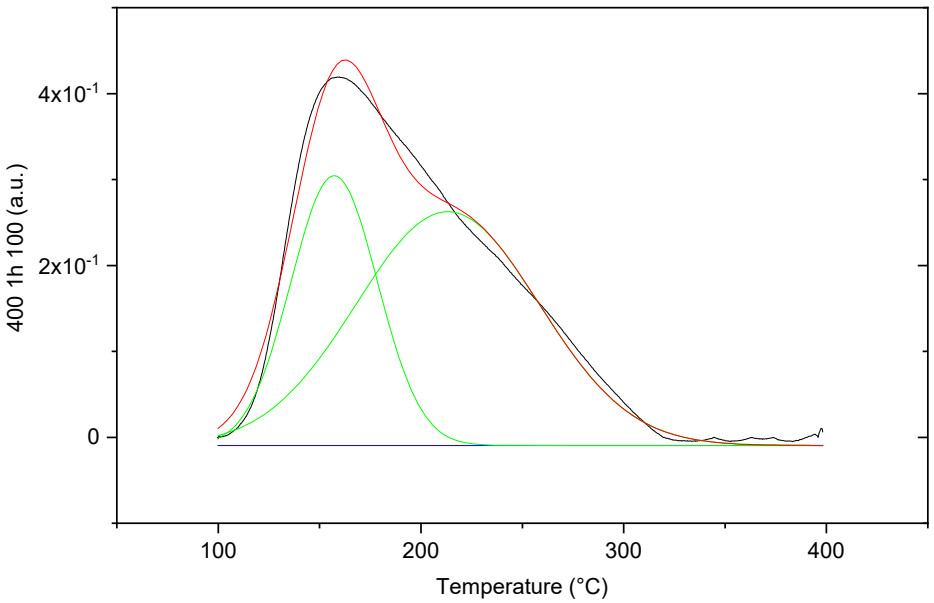
Fitting Results

Peak Index	Peak Type	Area Intg	FWHM	Max Height	Center Grvty	Area IntgP
1	Gaussian	30.42857	53.35247	0.5381	159.64065	35.56863
2	Gaussian	55.12032	113.04553	0.46122	218.68276	64.43137

Figure B.14 - Peak deconvolution of CO_2 TPD of $Mg_{1.9}Al$ W 400-2h-100.

Peak Analysis

Data Set:[Book3]Sheet1!O"Relative TCD signal" Date:30/04/2021
BaseLine:Constant
Chi^2=2.08278E-04 Adj. R-Square=9.90635E-01 # of Data Points=941
SS=1.94532E-01 Degrees of Freedom=934



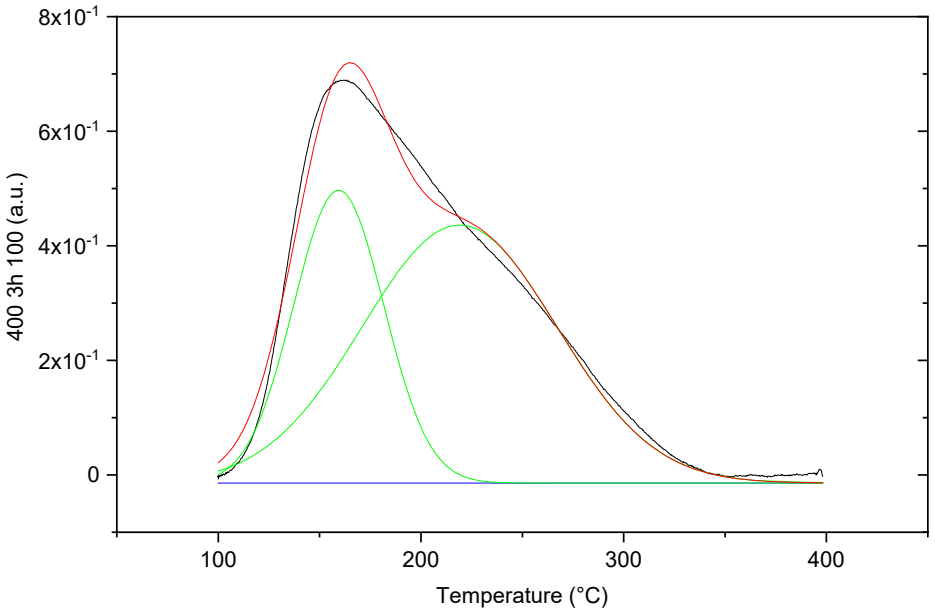
Fitting Results

Peak Index	Peak Type	Area Intg	FWHM	Max Height	Center Grvty	Area IntgP
1	Gaussian	16.74274	50.29374	0.3139	157.23414	35.42701
2	Gaussian	30.51707	105.99963	0.27209	213.20033	64.57299

Figure B.15 - Peak deconvolution of CO_2 TPD of $Mg_{1.9}Al$ W 400-1h-100

Peak Analysis

Data Set:[Book3]Sheet1!R"Relative TCD signal" Date:30/04/2021
BaseLine:Constant
Chi^2=5.36696E-04 Adj. R-Square=9.90866E-01 # of Data Points=943
SS=5.02348E-01 Degrees of Freedom=936



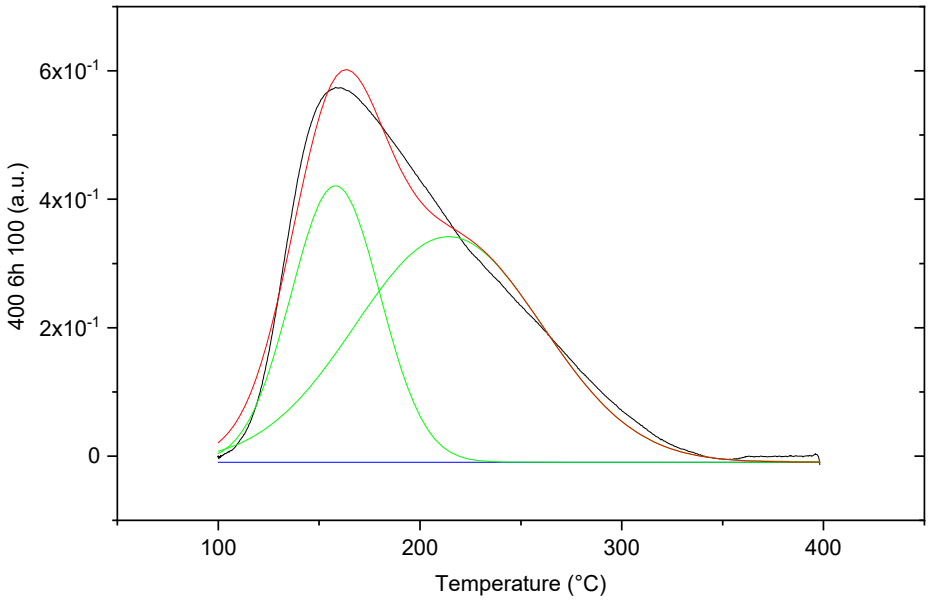
Fitting Results

Peak Index	Peak Type	Area Intg	FWHM	Max Height	Center Grvty	Area IntgP
1	Gaussian	28.41382	52.46441	0.51076	159.43801	34.57307
2	Gaussian	53.77103	112.9803	0.45011	219.03856	65.42693

Figure B.16 - Peak deconvolution of CO_2 TPD of $Mg_{1.9}Al$ W 400-3h-100

Peak Analysis

Data Set:[Book3]Sheet1!U"Relative TCD signal" Date:30/04/2021
BaseLine:Constant
Chi^2=4.31173E-04 Adj. R-Square=9.89325E-01 # of Data Points=942
SS=4.03147E-01 Degrees of Freedom=935



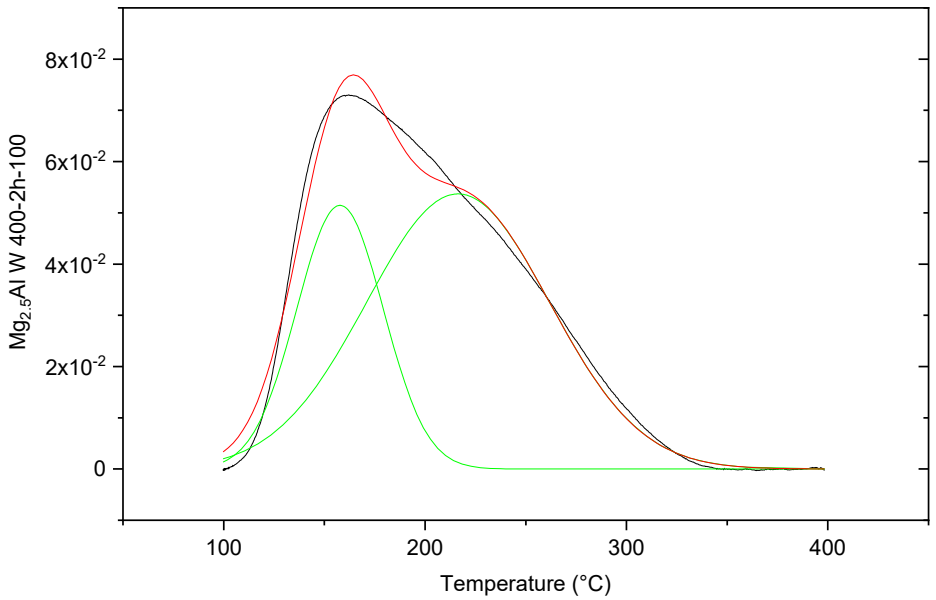
Fitting Results

Peak Index	Peak Type	Area Intg	FWHM	Max Height	Center Grvty	Area IntgP
1	Gaussian	23.73281	52.02823	0.43037	158.13852	36.91259
2	Gaussian	40.56181	109.2654	0.3512	214.16716	63.08741

Figure B.17 - Peak deconvolution of CO_2 TPD of $Mg_{1.9}Al$ W 400-6h-100

Peak Analysis

Data Set:[Book1]Sheet1!B Date:30/04/2021
BaseLine:Line
Chi^2=7.07814E-06 Adj. R-Square=9.90242E-01 # of Data Points=941
SS=6.61806E-03 Degrees of Freedom=935



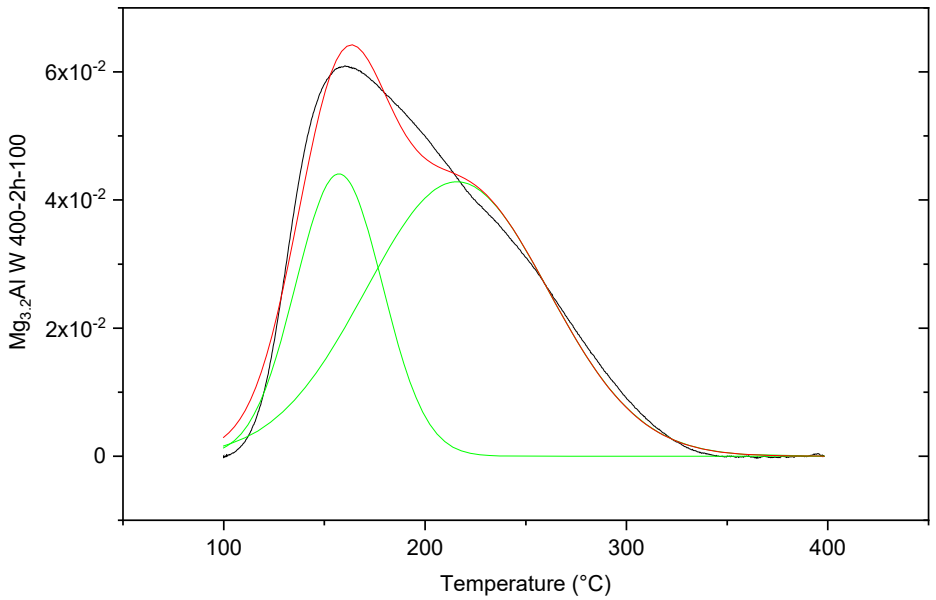
Fitting Results

Peak Index	Peak Type	Area Intg	FWHM	Max Height	Center Grvty	Area IntgP
1	Gaussian	2.7655	50.68119	0.05145	157.75864	31.27101
2	Gaussian	6.07815	106.90524	0.05369	216.37421	68.72899

Figure B.18 - Peak deconvolution of CO_2 TPD of $Mg_{2.5}Al$ W 400-2h-100

Peak Analysis

Data Set:[Book1]Sheet1!D"Relative TCD signal" Date:30/04/2021
BaseLine:Line
Chi^2=5.17406E-06 Adj. R-Square=9.89475E-01 # of Data Points=941
SS=4.83775E-03 Degrees of Freedom=935



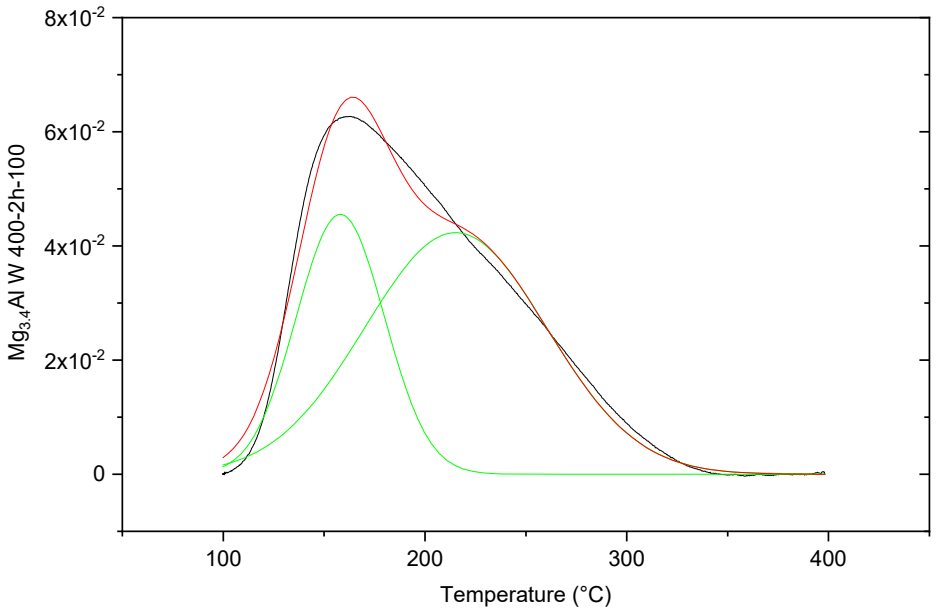
Fitting Results

Peak Index	Peak Type	Area Intg	FWHM	Max Height	Center Grvty	Area IntgP
1	Gaussian	2.37443	50.81571	0.04407	157.27196	32.94434
2	Gaussian	4.83298	106.53693	0.04284	215.81298	67.05566

Figure B.19 - Peak deconvolution of CO_2 TPD of $Mg_{3.2}Al$ W 400-2h-100

Peak Analysis

Data Set:[Book1]Sheet1!F"Relative TCD signal" Date:30/04/2021
BaseLine:Line
Chi^2=5.16317E-06 Adj. R-Square=9.89890E-01 # of Data Points=940
SS=4.82240E-03 Degrees of Freedom=934



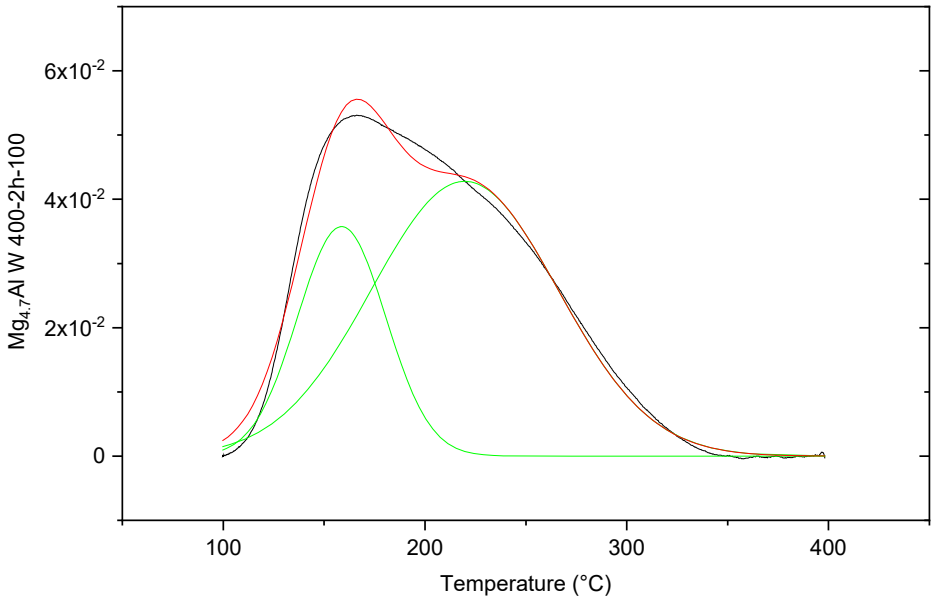
Fitting Results

Peak Index	Peak Type	Area Intg	FWHM	Max Height	Center Grvty	Area IntgP
1	Gaussian	2.48126	51.41223	0.04552	158.06098	34.27671
2	Gaussian	4.75766	106.1633	0.04233	215.18634	65.72329

Figure B.20 - Peak deconvolution of CO_2 TPD of $Mg_{3.4}Al$ W 400-2h-100

Peak Analysis

Data Set:[Book1]Sheet1!B Date:30/04/2021
BaseLine:Line
Chi^2=2.94081E-06 Adj. R-Square=9.92730E-01 # of Data Points=941
SS=2.74966E-03 Degrees of Freedom=935



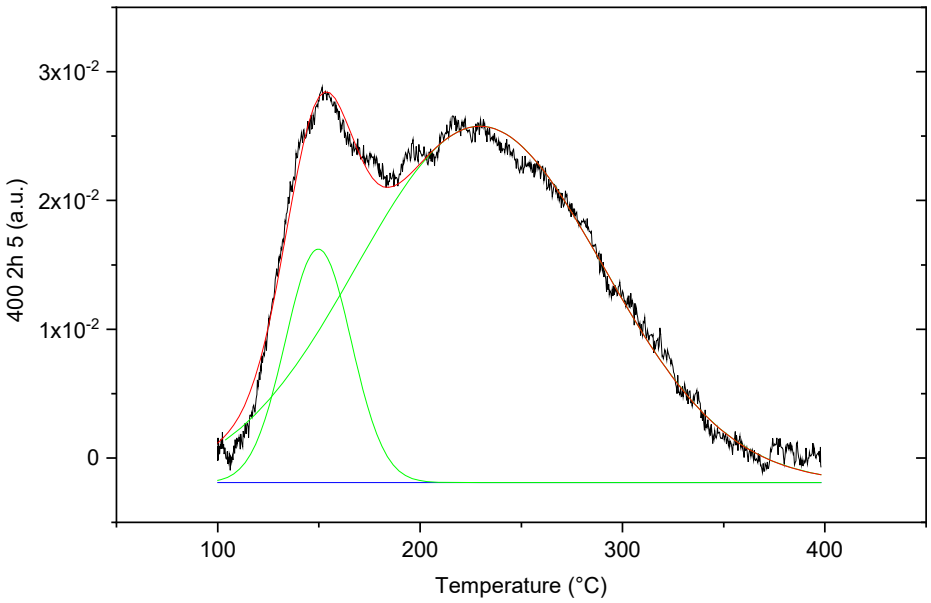
Fitting Results

Peak Index	Peak Type	Area Intg	FWHM	Max Height	Center Grvty	Area IntgP
1	Gaussian	1.9523	51.49879	0.03574	158.69637	28.3597
2	Gaussian	4.93177	108.80518	0.04279	219.67144	71.6403

Figure B.21 - Peak deconvolution of CO_2 TPD of $Mg_{4.7}Al$ W 400-2h-100.

Peak Analysis

Data Set:[NH3]Sheet1!C — Date:30/04/2021
BaseLine:Constant
Chi^2=1.05049E-06 — Adj. R-Square=9.89940E-01 — # of Data Points=939
SS=9.79055E-04 — Degrees of Freedom=932



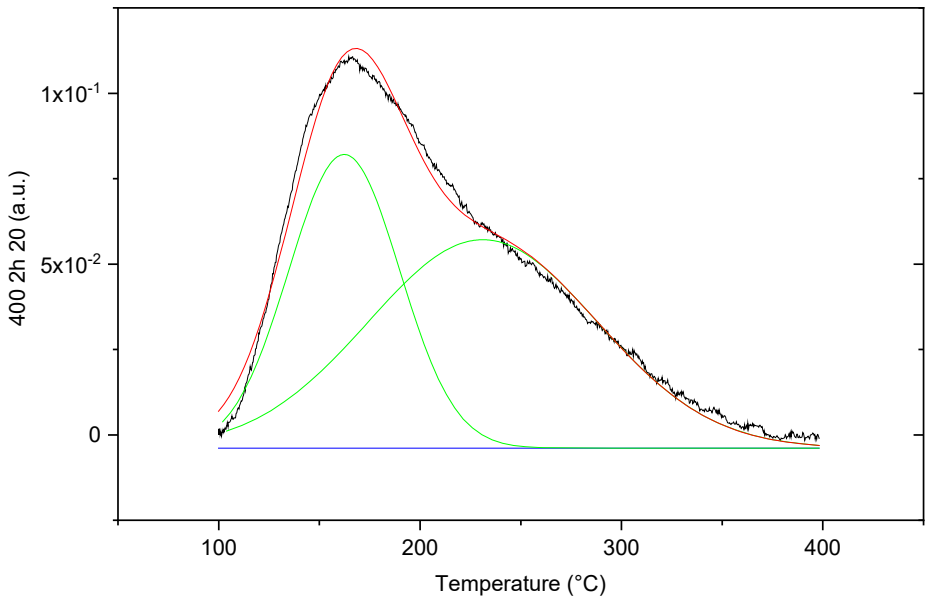
Fitting Results

Peak Index	Peak Type	Area Intg	FWHM	Max Height	Center Grvty	Area IntgP
1	Gaussian	0.7389	38.33646	0.01813	149.7176	15.12161
2	Gaussian	4.14751	143.61839	0.02768	229.53725	84.87839

Figure B.22 - Peak deconvolution of NH_3 TPD of $Mg_{1.9}Al$ W 400-2h-5.

Peak Analysis

Data Set:[NH3]Sheet1!F"Relative TCD signal" Date:30/04/2021
BaseLine:Constant
Chi^2=1.29819E-05 Adj. R-Square=9.90395E-01 # of Data Points=938
SS=1.20862E-02 Degrees of Freedom=931



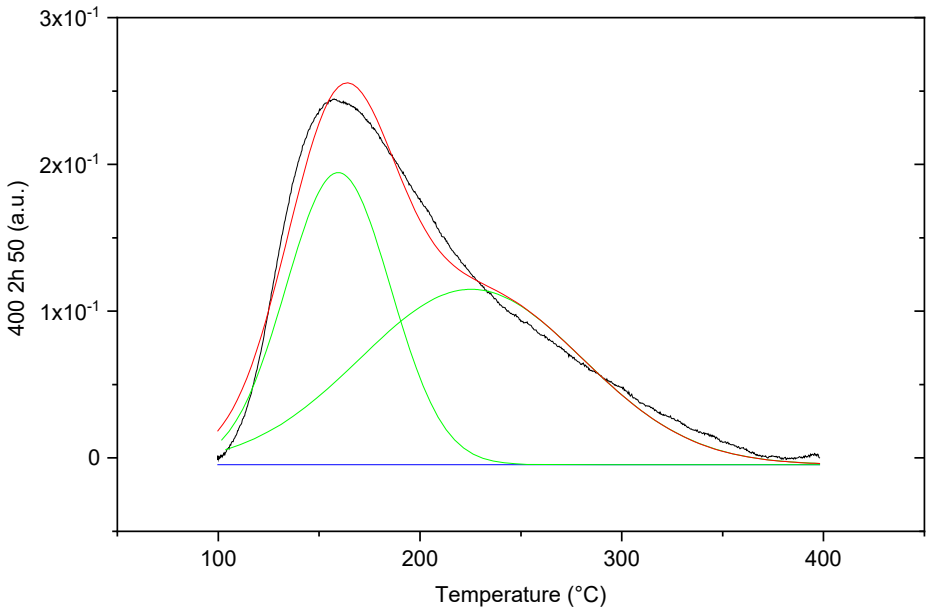
Fitting Results

Peak Index	Peak Type	Area Intg	FWHM	Max Height	Center Grvty	Area IntgP
1	Gaussian	5.85515	64.75204	0.08595	162.34416	40.54935
2	Gaussian	8.58442	133.78958	0.06102	231.15523	59.45065

Figure B.23 - Peak deconvolution of NH_3 TPD of $Mg_{1.9}Al$ W 400-2h-20.

Peak Analysis

Data Set:[NH3]Sheet1!I"Relative TCD signal" Date:30/04/2021
BaseLine:Constant
Chi^2=1.16034E-04 Adj. R-Square=9.82515E-01 # of Data Points=936
SS=1.07795E-01 Degrees of Freedom=929



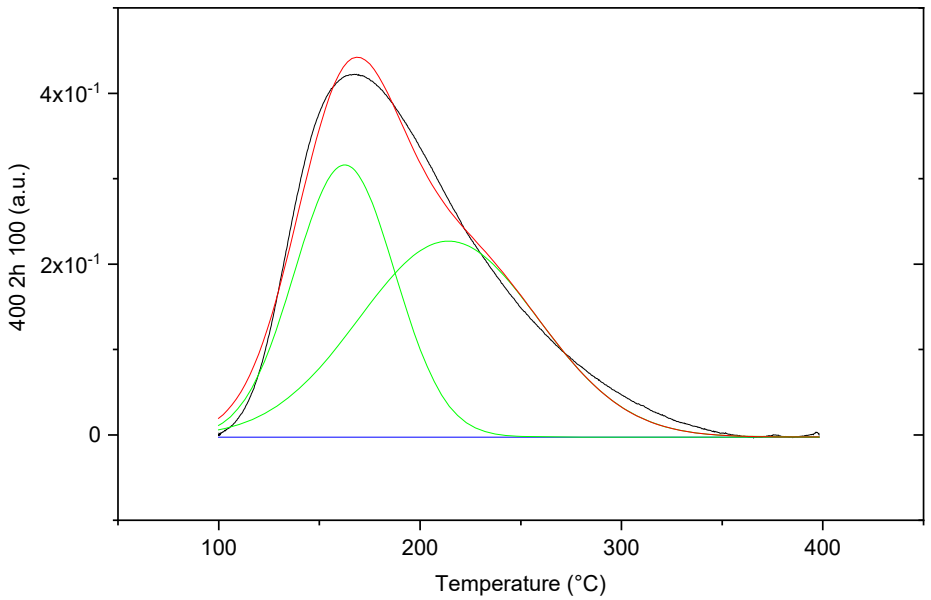
Fitting Results

Peak Index	Peak Type	Area Intg	FWHM	Max Height	Center Grvty	Area IntgP
1	Gaussian	12.82719	61.20229	0.19907	159.48193	44.06588
2	Gaussian	16.28193	129.50969	0.11955	225.36945	55.93412

Figure B.24 - Peak deconvolution of NH_3 TPD of $Mg_{1.9}Al$ W 400-2h-50.

Peak Analysis

Data Set:[NH3]Sheet1!L"Relative TCD signal" Date:30/04/2021
BaseLine:Constant
Chi^2=1.84149E-04 Adj. R-Square=9.91684E-01 # of Data Points=942
SS=1.72179E-01 Degrees of Freedom=935



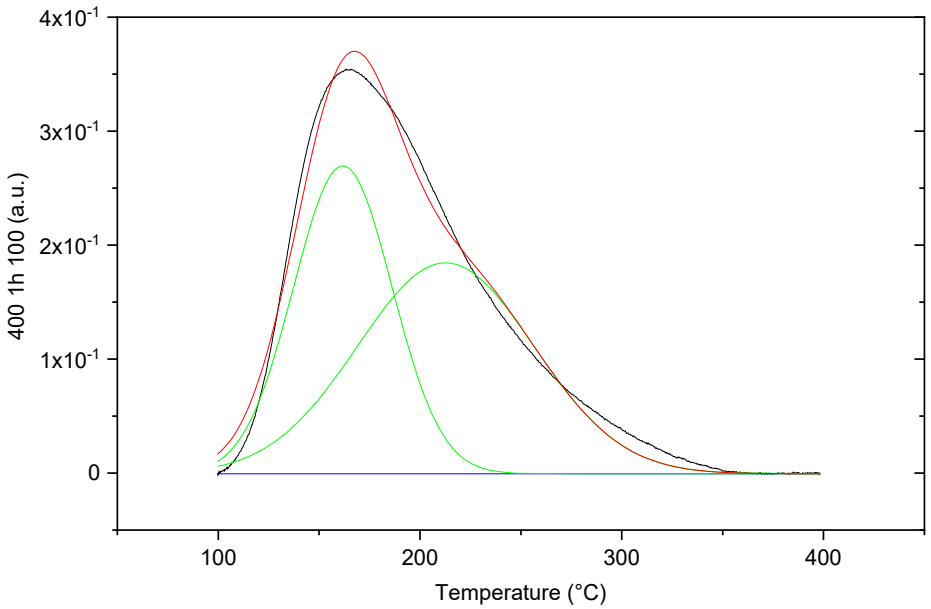
Fitting Results

Peak Index	Peak Type	Area Intg	FWHM	Max Height	Center Grvty	Area IntgP
1	Gaussian	19.77082	58.63985	0.31865	162.56998	43.79818
2	Gaussian	25.36991	104.42877	0.22939	214.09932	56.20182

Figure B.25 - Peak deconvolution of NH_3 TPD of $Mg_{1.9}Al$ W 400-2h-100.

Peak Analysis

Data Set:[NH3]Sheet1!O"Relative TCD signal" Date:30/04/2021
BaseLine:Constant
Chi^2=1.50421E-04 Adj. R-Square=9.90118E-01 # of Data Points=939
SS=1.40192E-01 Degrees of Freedom=932



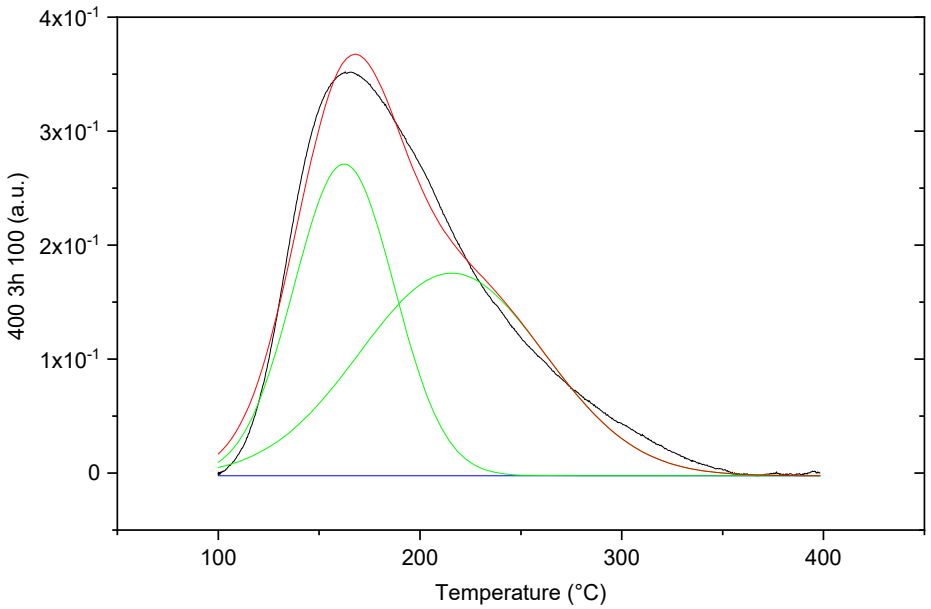
Fitting Results

Peak Index	Peak Type	Area Intg	FWHM	Max Height	Center Grvty	Area IntgP
1	Gaussian	16.43572	57.48814	0.27013	161.73834	44.93731
2	Gaussian	20.13906	102.74773	0.18504	212.71259	55.06269

Figure B.26 - Peak deconvolution of NH_3 TPD of $Mg_{1,9}Al$ W 400-1h-100.

Peak Analysis

Data Set:[NH3]Sheet1!R"Relative TCD signal" Date:30/04/2021
BaseLine:Constant
Chi^2=1.54818E-04 Adj. R-Square=9.89564E-01 # of Data Points=940
SS=1.44445E-01 Degrees of Freedom=933



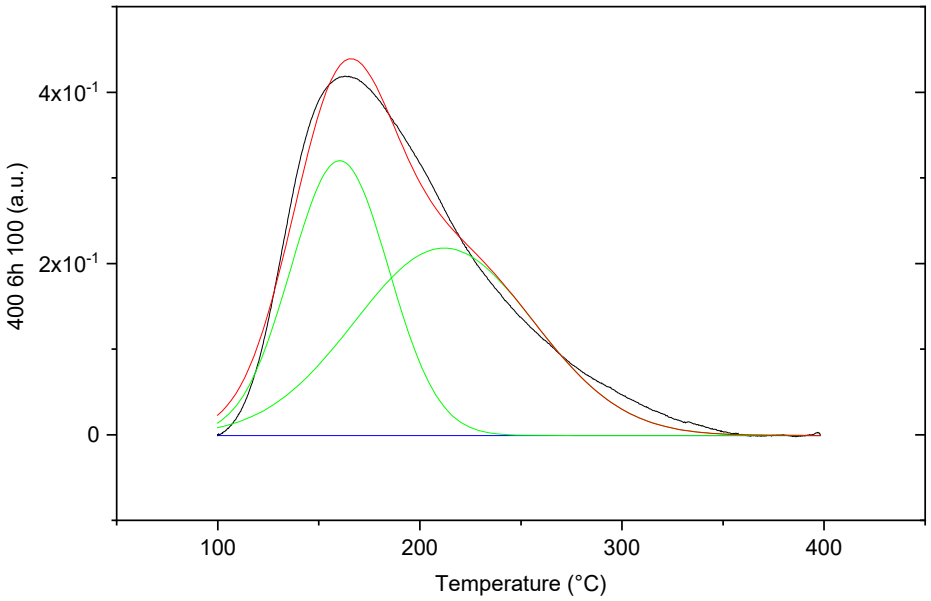
Fitting Results

Peak Index	Peak Type	Area Intg	FWHM	Max Height	Center Grvty	Area IntgP
1	Gaussian	16.97009	58.64098	0.27354	162.40362	45.5481
2	Gaussian	20.28742	107.82284	0.17779	215.74799	54.4519

Figure B.27 - Peak deconvolution of NH_3 TPD of $Mg_{1,9}Al$ W 400-3h-100.

Peak Analysis

Data Set:[NH3]Sheet1!U"Relative TCD signal" Date:30/04/2021
BaseLine:Constant
Chi^2=2.29589E-04 Adj. R-Square=9.89185E-01 # of Data Points=942
SS=2.14665E-01 Degrees of Freedom=935



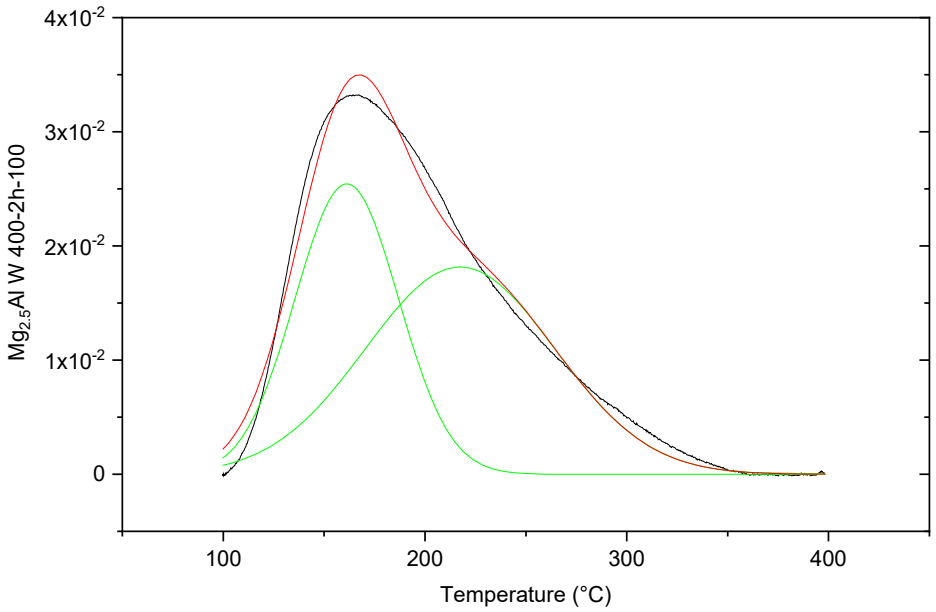
Fitting Results

Peak Index	Peak Type	Area Intg	FWHM	Max Height	Center Grvty	Area IntgP
1	Gaussian	19.39803	57.16236	0.32087	160.34733	44.48876
2	Gaussian	24.20407	104.51501	0.21883	211.99038	55.51124

Figure B.28 - Peak deconvolution of NH_3 TPD of $Mg_{1.9}Al$ W 400-6h-100.

Peak Analysis

Data Set:[Book3]Sheet1!B Date:30/04/2021
BaseLine:Line
Chi^2=1.64702E-06 Adj. R-Square=9.87969E-01 # of Data Points=940
SS=1.53832E-03 Degrees of Freedom=934



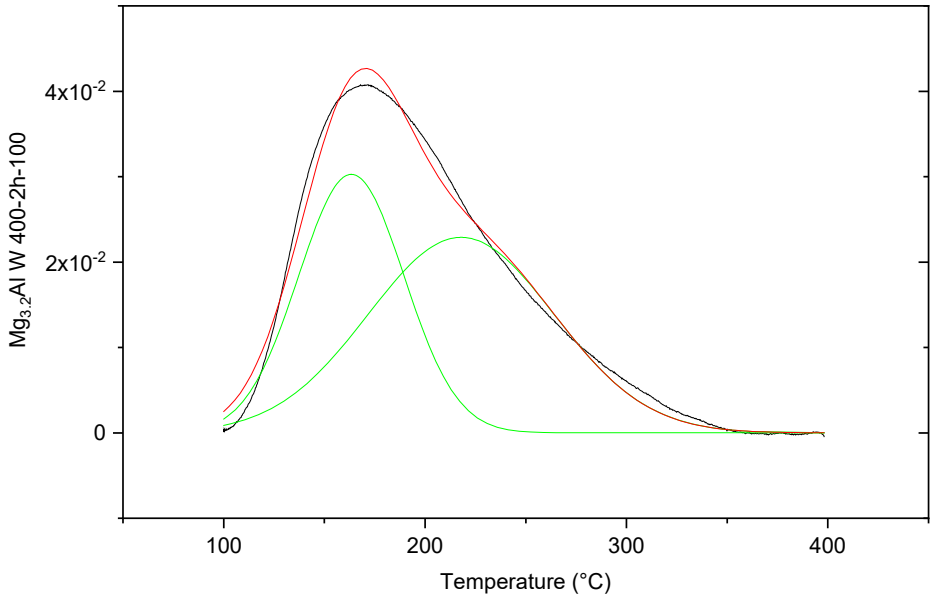
Fitting Results

Peak Index	Peak Type	Area Intg	FWHM	Max Height	Center Grvty	Area IntgP
1	Gaussian	1.61662	60.21667	0.02543	161.25735	43.26564
2	Gaussian	2.11988	110.40729	0.01815	217.36724	56.73436

Figure B.29 - Peak deconvolution of NH_3 TPD of $Mg_{2.5}Al$ W 400-2h-100.

Peak Analysis

Data Set:[Book3]Sheet1!F"Relative TCD signal" Date:30/04/2021
BaseLine:Line
Chi^2=1.91611E-06 Adj. R-Square=9.90847E-01 # of Data Points=940
SS=1.78965E-03 Degrees of Freedom=934



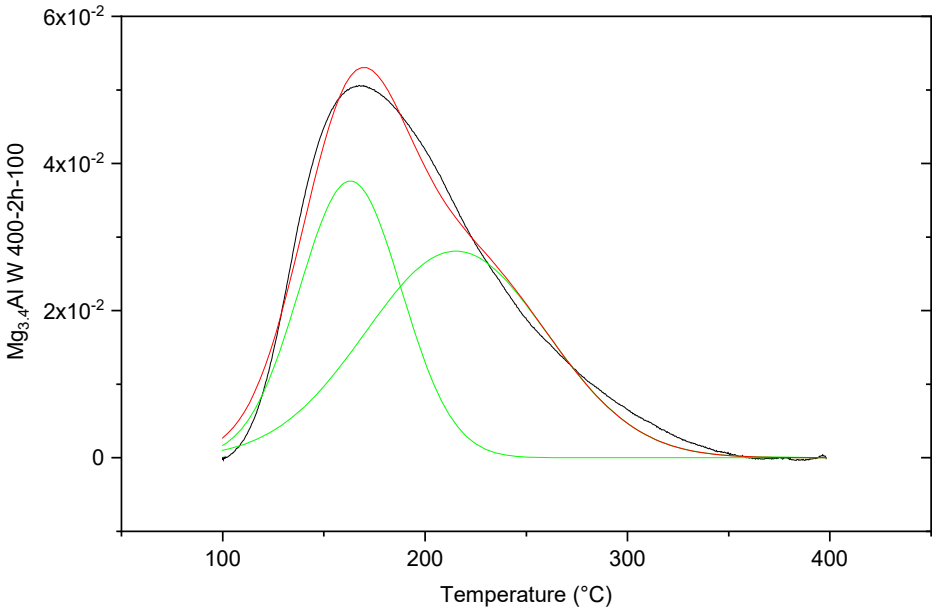
Fitting Results

Peak Index	Peak Type	Area Intg	FWHM	Max Height	Center Grvty	Area IntgP
1	Gaussian	1.9727	61.70301	0.03027	163.37946	42.82953
2	Gaussian	2.63324	108.64199	0.02289	217.89756	57.17047

Figure B.30 - Peak deconvolution of NH_3 TPD of $Mg_{3.2}Al$ W 400-2h-100.

Peak Analysis

Data Set:[Book3]Sheet1!D"Relative TCD signal" Date:30/04/2021
BaseLine:Line
Chi^2=3.26528E-06 Adj. R-Square=9.89843E-01 # of Data Points=940
SS=3.04977E-03 Degrees of Freedom=934



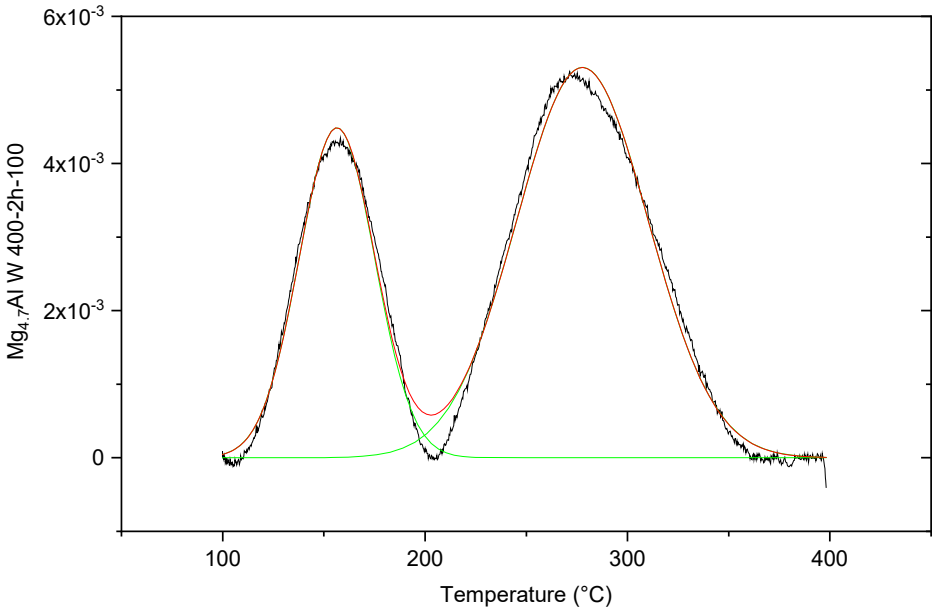
Fitting Results

Peak Index	Peak Type	Area Intg	FWHM	Max Height	Center Grvty	Area IntgP
1	Gaussian	2.36935	59.57066	0.0376	163.10693	43.04979
2	Gaussian	3.1344	105.37795	0.02808	215.24068	56.95021

Figure B.31 - Peak deconvolution of NH_3 TPD of $Mg_{3.4}Al$ W 400-2h-100.

Peak Analysis

Data Set:[Book3]Sheet1!B — Date:30/04/2021
BaseLine:Line
Chi^2=3.96057E-08 — Adj. R-Square=9.87915E-01 — # of Data Points=939
SS=3.69522E-05 — Degrees of Freedom=933



Fitting Results

Peak Index	Peak Type	Area Intg	FWHM	Max Height	Center Grvty	Area IntgP
1	Gaussian	0.20914	43.88367	0.00448	156.44992	32.55627
2	Gaussian	0.43325	76.73368	0.0053	277.73914	67.44373

Figure B.32 - Peak deconvolution of NH_3 TPD of $Mg_{4.7}Al$ W 400-2h-100.

B.4 CO_2 adsorption profiles of LDO samples

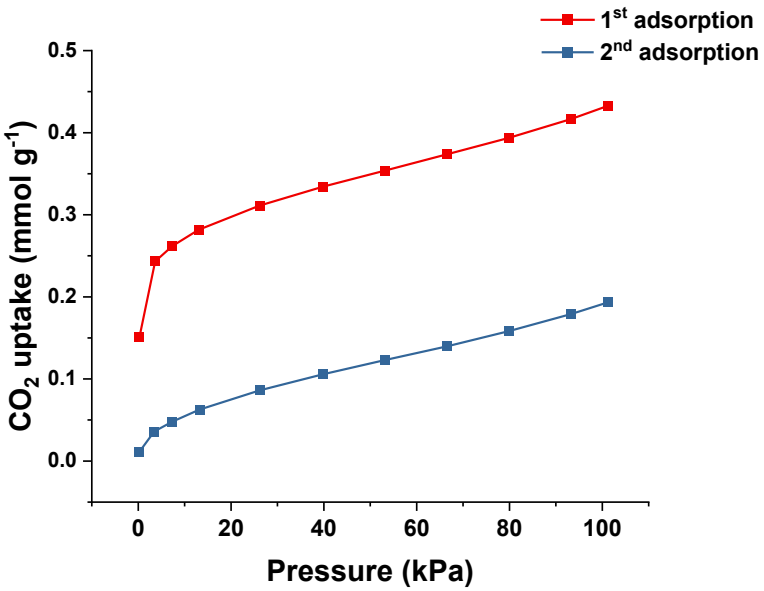


Figure B.33 - 1st and 2nd CO_2 adsorption profiles of $Mg_{1.9}Al$ W 100-2h-100.

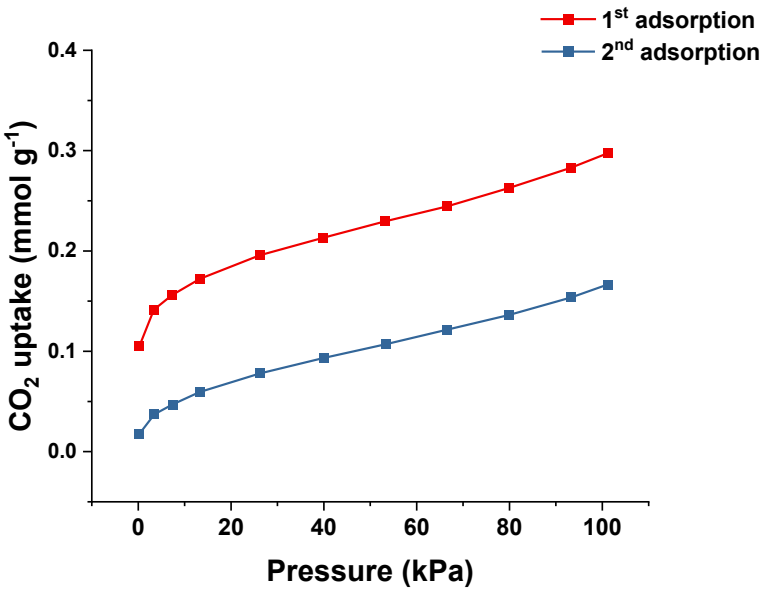


Figure B.34 - 1st and 2nd CO_2 adsorption profiles of $Mg_{1.9}Al$ W 200-2h-100.

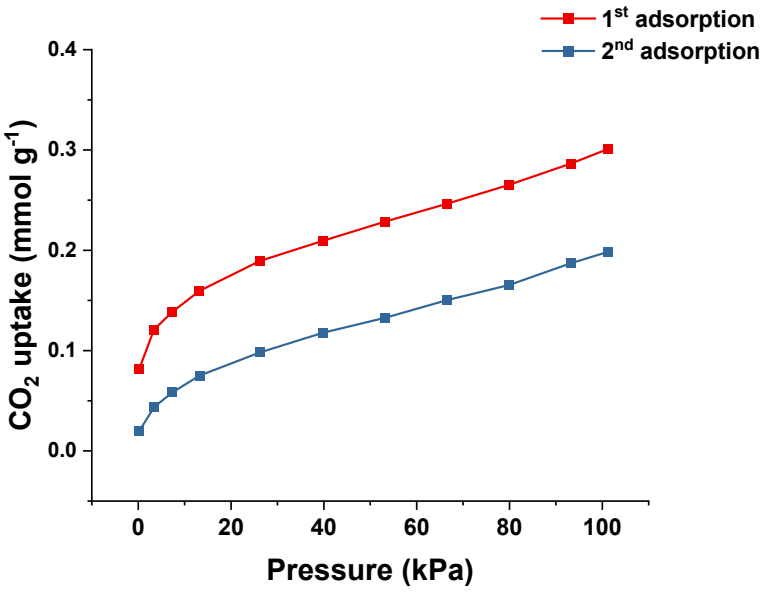


Figure B.35 - 1st and 2nd CO_2 adsorption profiles of $Mg_{1.9}Al$ W 300-2h-100.

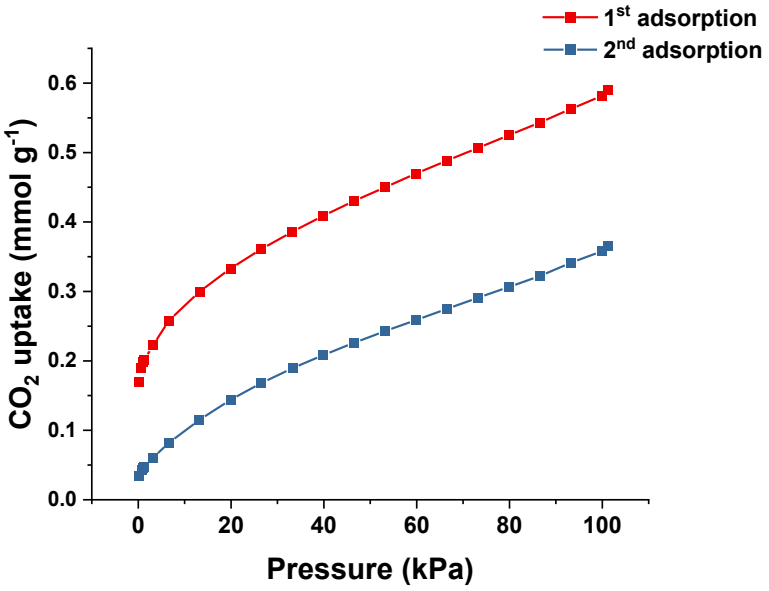


Figure B.36 - 1st and 2nd CO_2 adsorption profiles of $Mg_{1.9}Al$ W 400-2h-100.

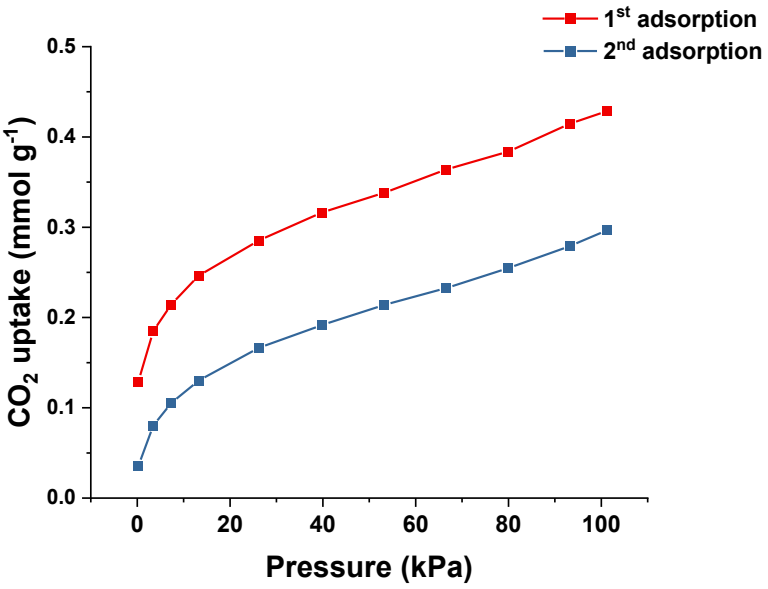


Figure B.37 - 1st and 2nd CO_2 adsorption profiles of $Mg_{1.9}Al$ W 500-1h-100.

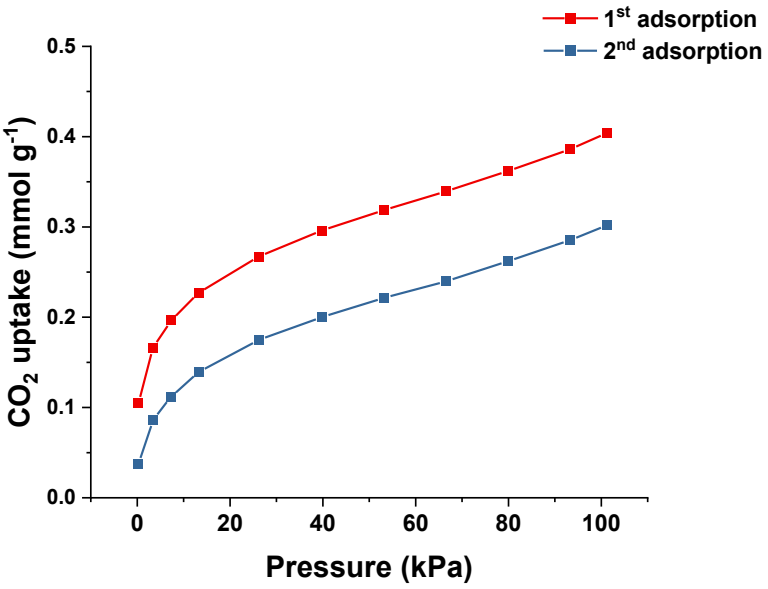


Figure B.38 - 1st and 2nd CO_2 adsorption profiles of $Mg_{1.9}Al$ W 600-2h-100.

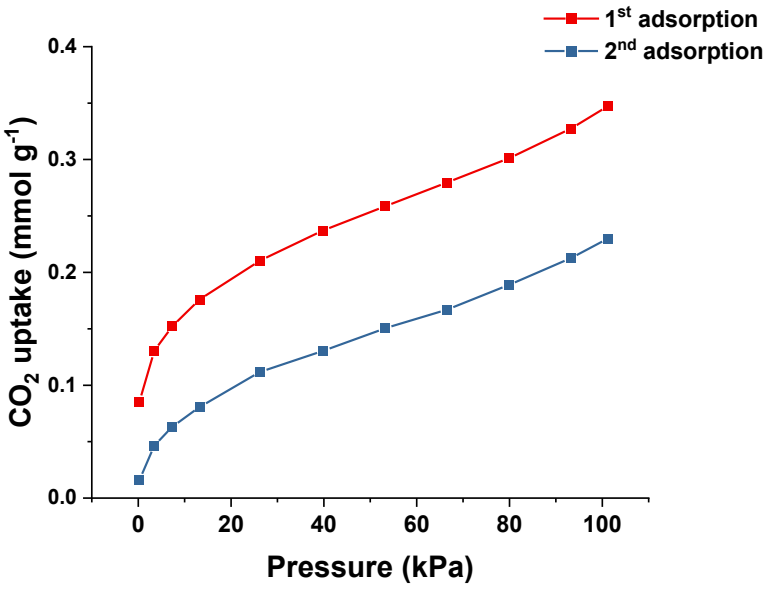


Figure B.39 - 1st and 2nd CO_2 adsorption profiles of $Mg_{1.9}Al$ W 400-2h-5.

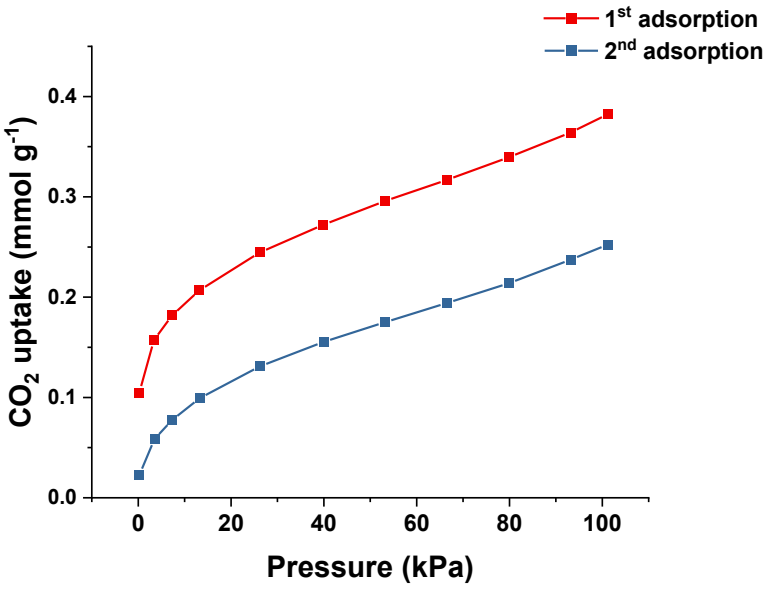


Figure B.40 - 1st and 2nd CO_2 adsorption profiles of $Mg_{1.9}Al$ W 400-2h-20.

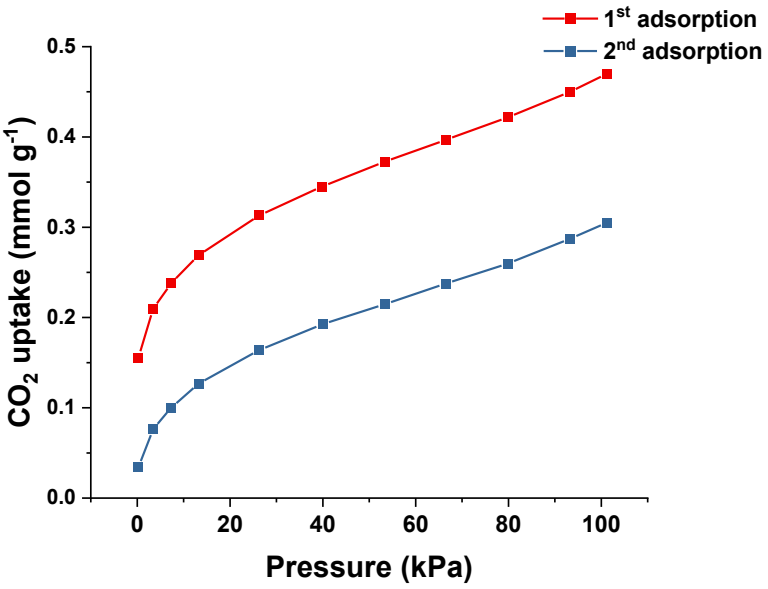


Figure B.41 - 1st and 2nd CO_2 adsorption profiles of $Mg_{1.9}Al$ W 400-2h-50.

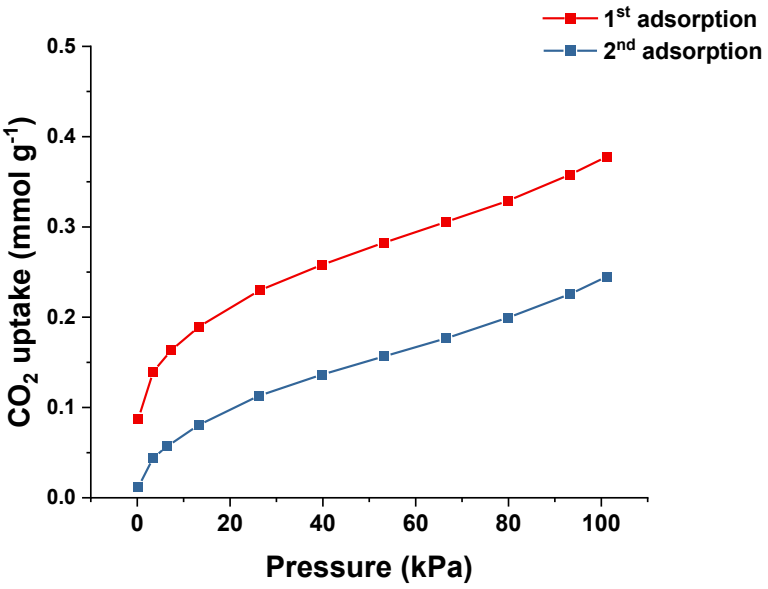


Figure B.42 - 1st and 2nd CO_2 adsorption profiles of $Mg_{1.9}Al$ W 400-1h-100.

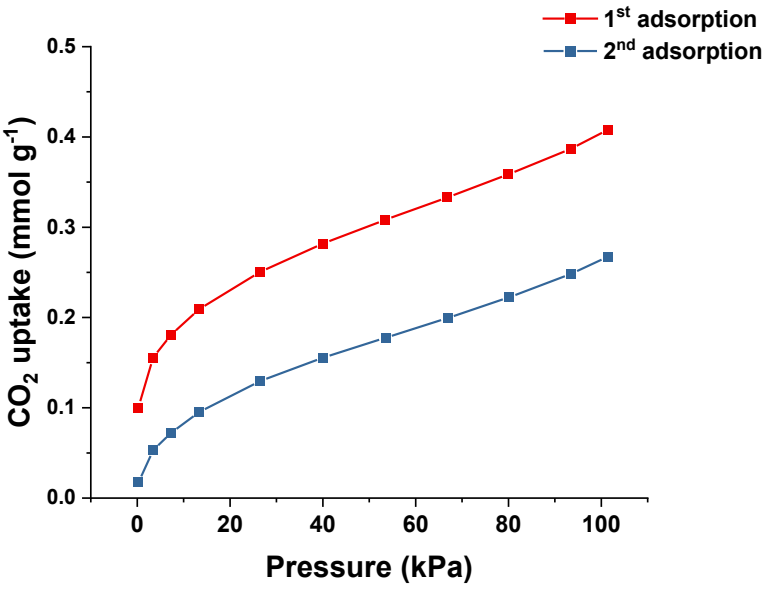


Figure B.43 - 1st and 2nd CO_2 adsorption profiles of $Mg_{1.9}Al$ W 400-3h-100.

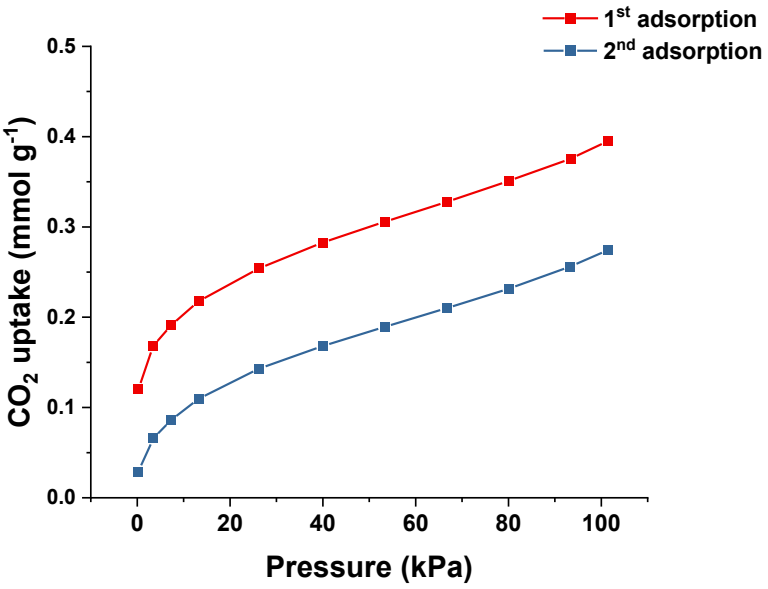


Figure B.44 - 1st and 2nd CO_2 adsorption profiles of $Mg_{1.9}Al$ W 400-6h-100.

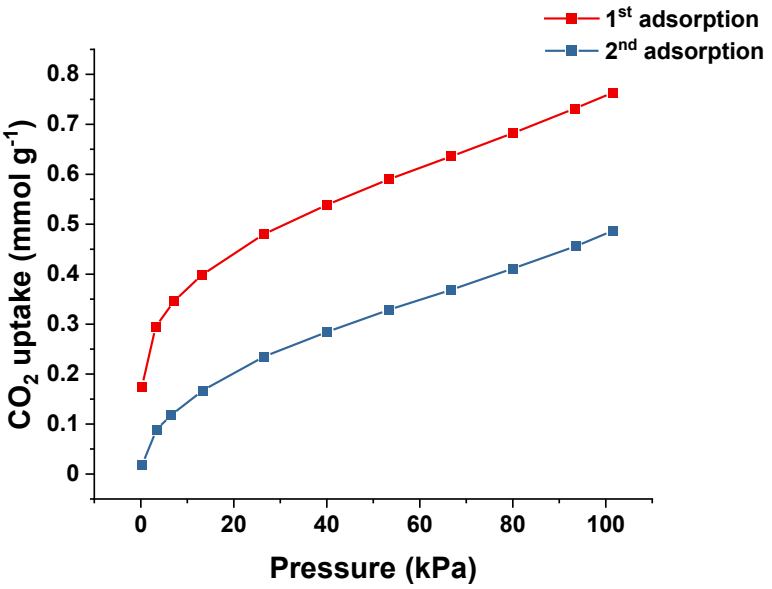


Figure B.45 - 1st and 2nd CO_2 adsorption profiles of $Mg_{2.5}Al$ W 400-2h-100.

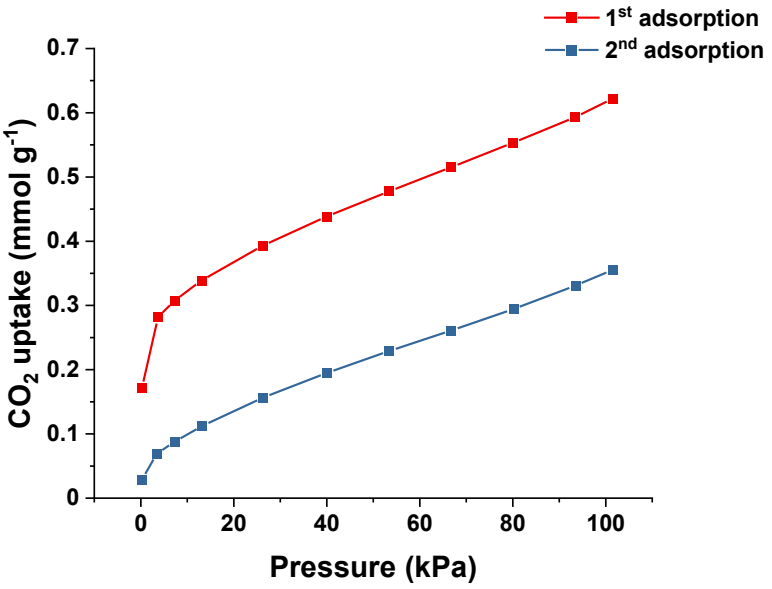


Figure B.46 - 1st and 2nd CO_2 adsorption profiles of $Mg_{3.2}Al$ W 400-2h-100.

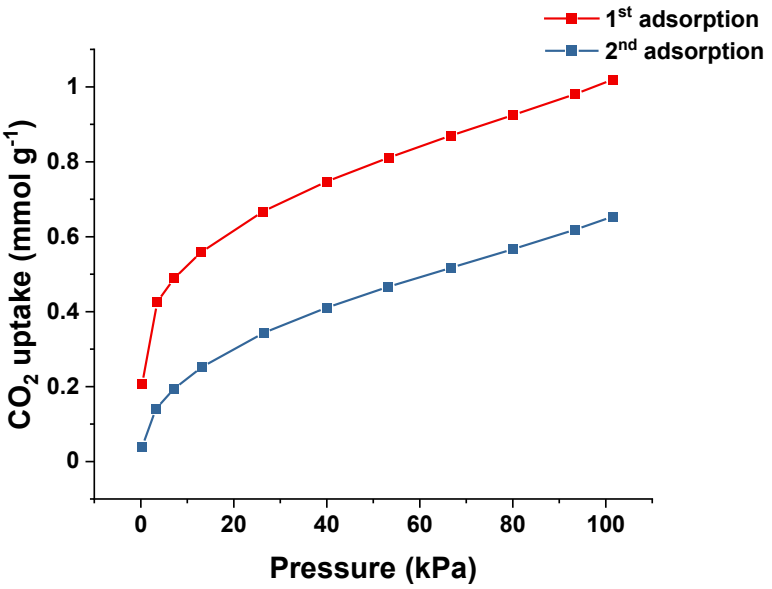


Figure B.47 - 1st and 2nd CO_2 adsorption profiles of $Mg_{3.4}Al$ W 400-2h-100.

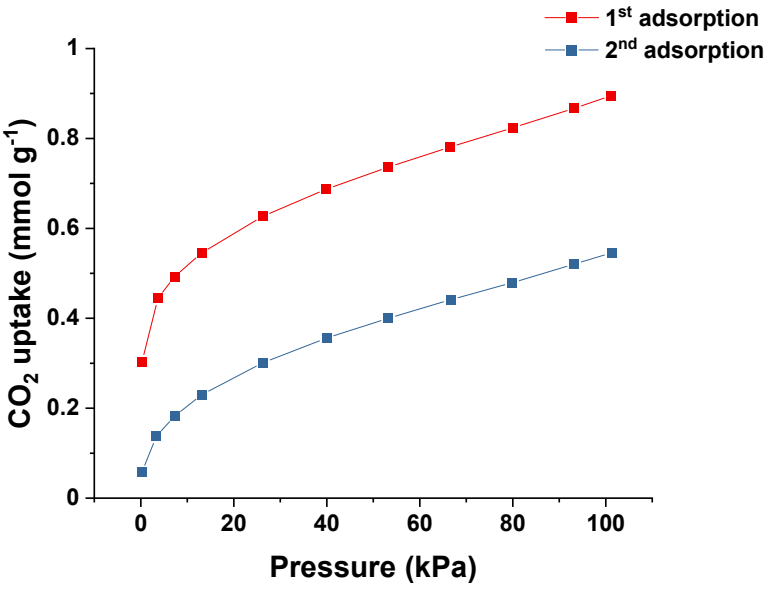


Figure B.48 - 1st and 2nd CO_2 adsorption profiles of $Mg_{4.7}Al$ W 400-2h-100.

Appendix C - Appendices for Chapter Five

C.1 N_2 adsorption-desorption isotherms of carbon and carbon@LDH materials

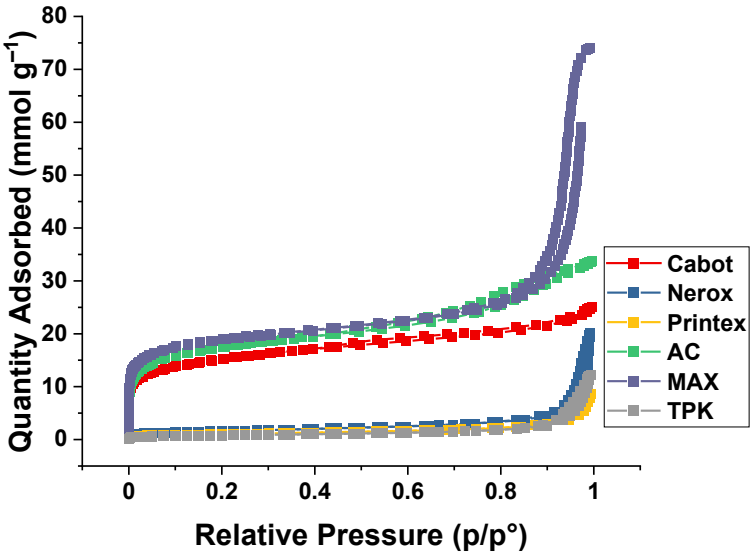


Figure C.1 - N_2 adsorption-desorption isotherms of carbon materials.

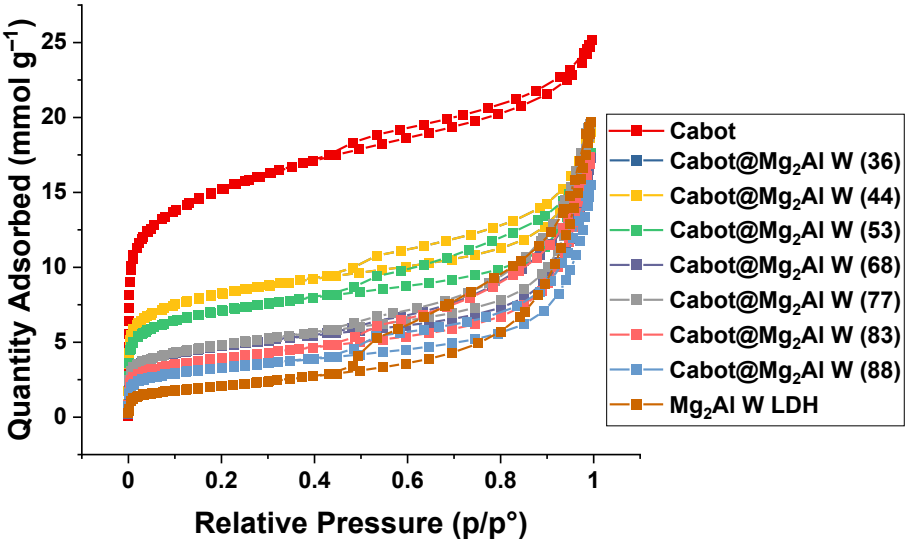


Figure C.2 - N_2 adsorption-desorption isotherms of Cabot@Mg_2Al W LDHs.

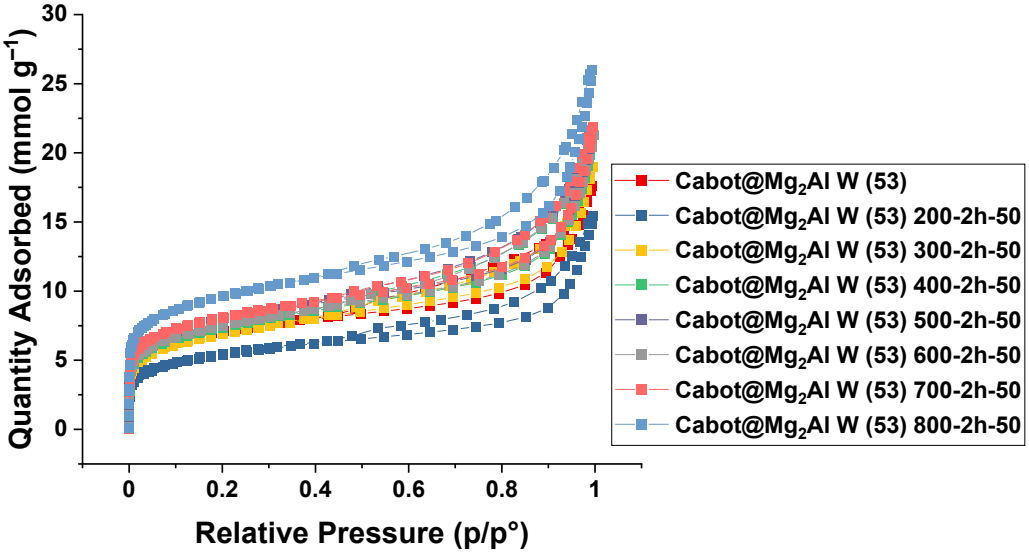


Figure C.3 - N_2 adsorption-desorption isotherms of Cabot@Mg_2Al W (53) LDO calcined at different temperatures for 2 h with a ramp rate of 50 °C min^{-1}.

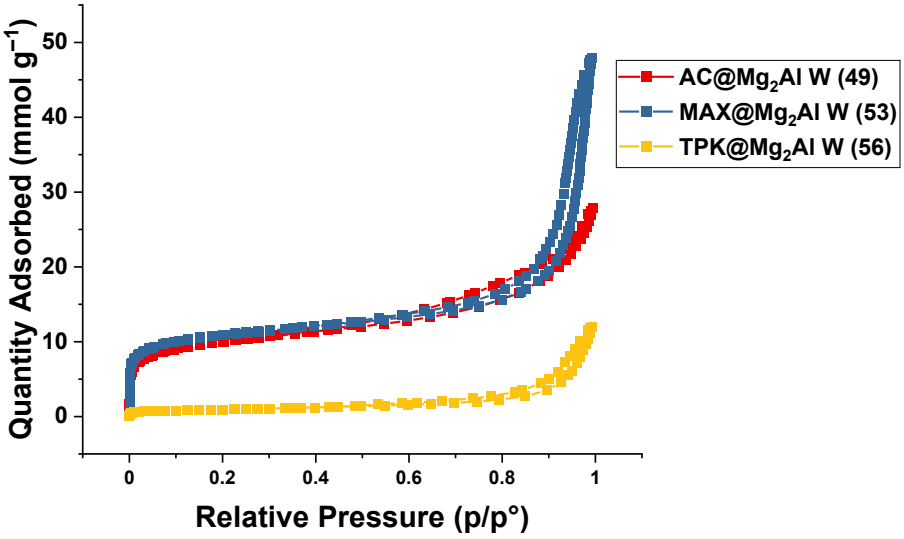


Figure C.4 - N_2 adsorption-desorption isotherms of AC@Mg_2Al W (49), MAX@Mg_2Al W (53) and TPK@Mg_2Al W (56).

C.2 Pore size distributions of carbon and carbon@LDH core@shell materials

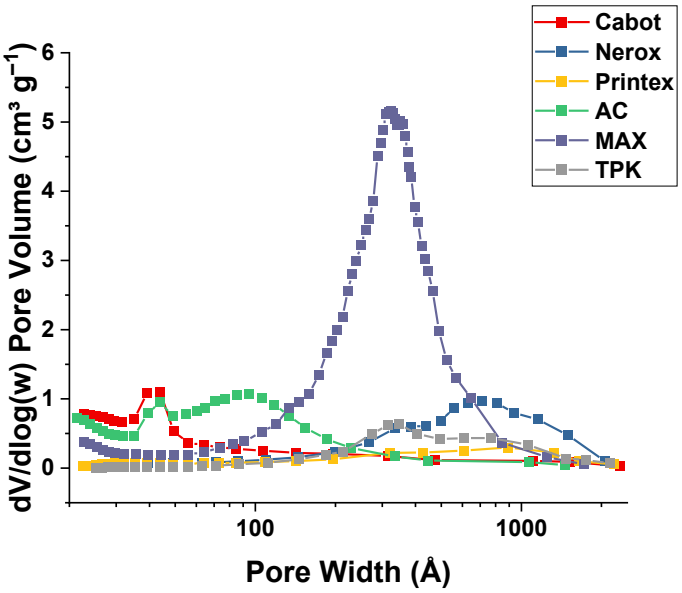


Figure C.5 - Pore size distribution of carbon materials.

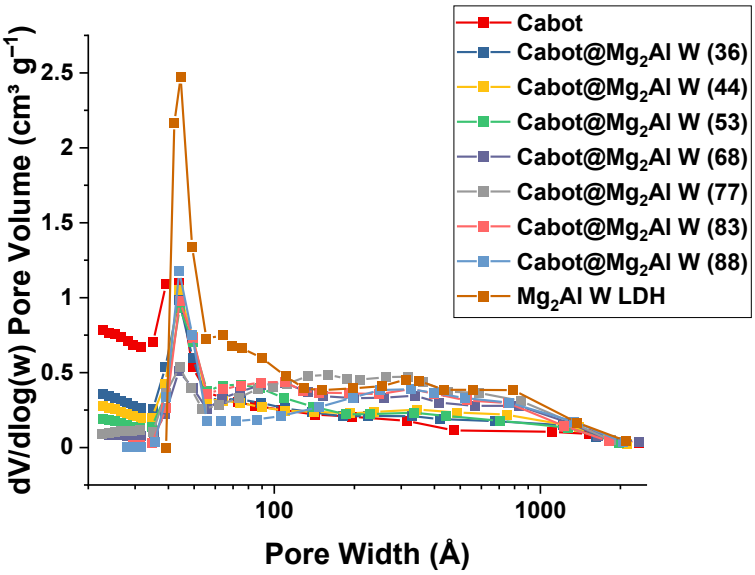


Figure C.6 - Pore size distribution of Cabot@Mg_2Al W LDHs.

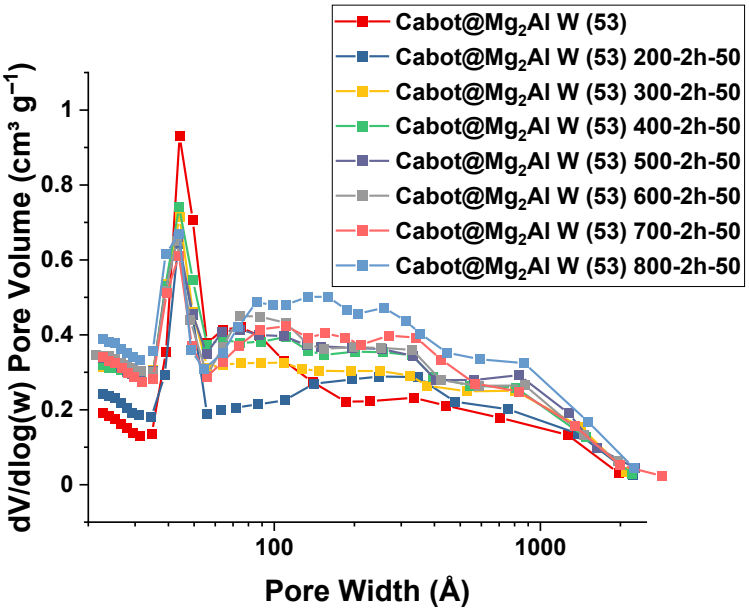


Figure C.7 - Pore size distribution of Cabot@Mg_2Al W (53) LDO calcined at different temperatures for 2 h with a ramp rate of 50 °C min^{-1}.

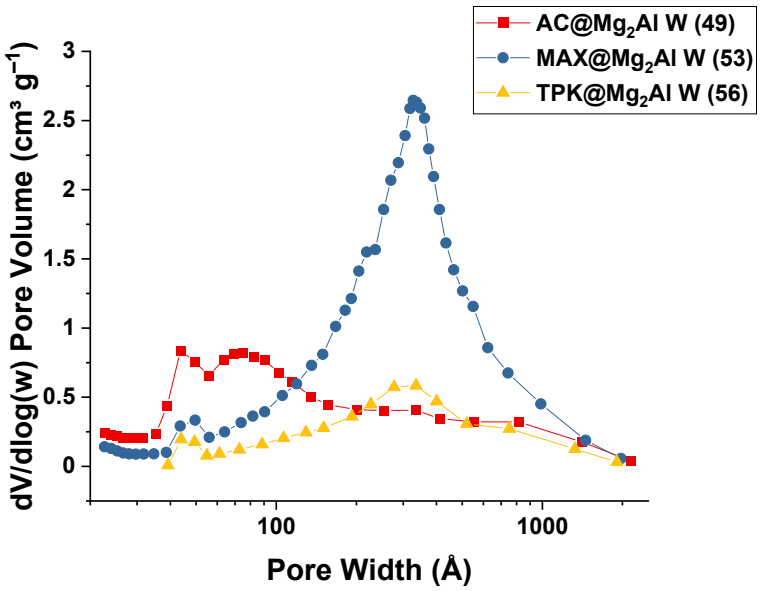


Figure C.8 - Pore size distribution of AC@Mg_2Al W (49), MAX@Mg_2Al W (53) and TPK@Mg_2Al W (56).

C.3 CO_2 breakthrough curves

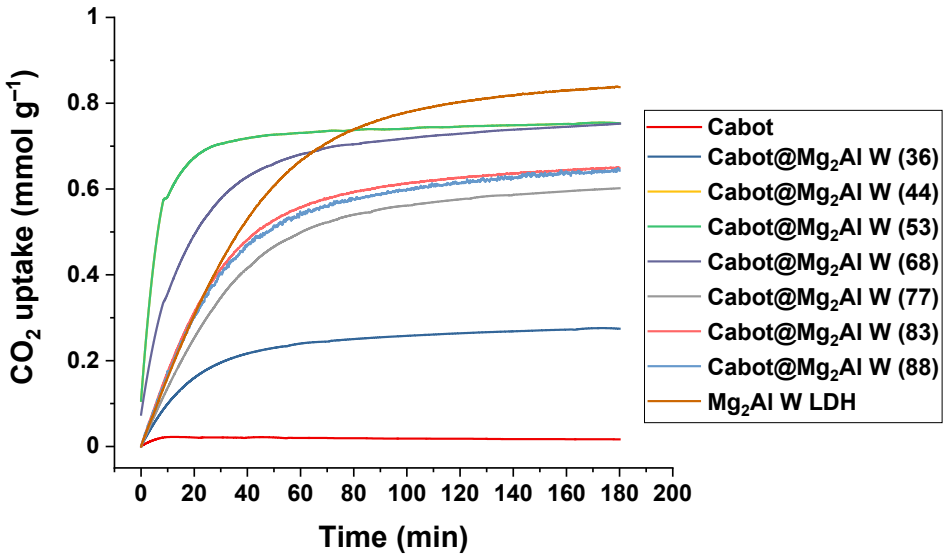


Figure C.9 - CO_2 adsorption breakthrough curves for Cabot@Mg_2Al W core@shell materials. Samples were pre-treated at 100 °C for 30 min at 50 °C min^{-1} ramp rate under N_2 atmosphere. The CO_2 testing atmosphere was 33:67 CO_2:N_2.

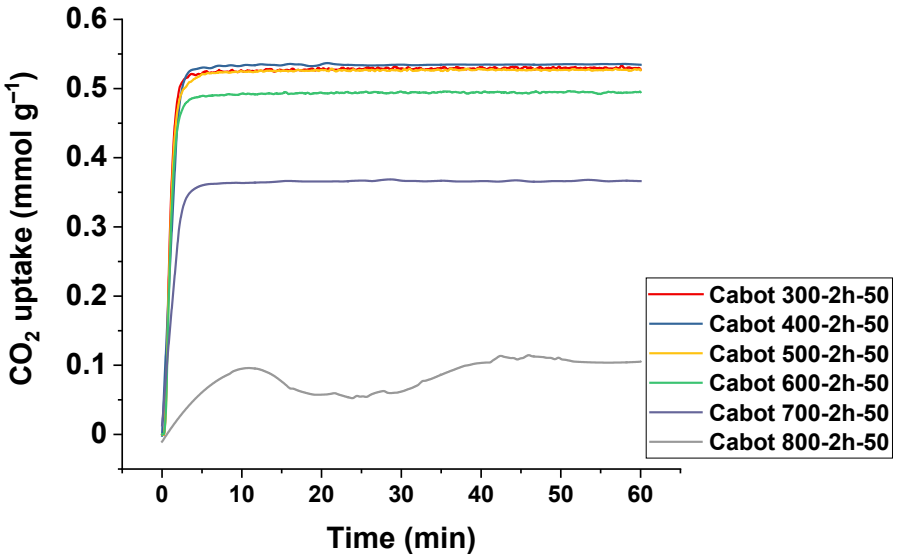


Figure C.10 - CO_2 adsorption breakthrough curves for Cabot calcined at different temperatures for 2 h with 50 °C min^{-1} ramp under N_2 atmosphere. The CO_2 testing atmosphere was 33:67 CO_2:N_2.

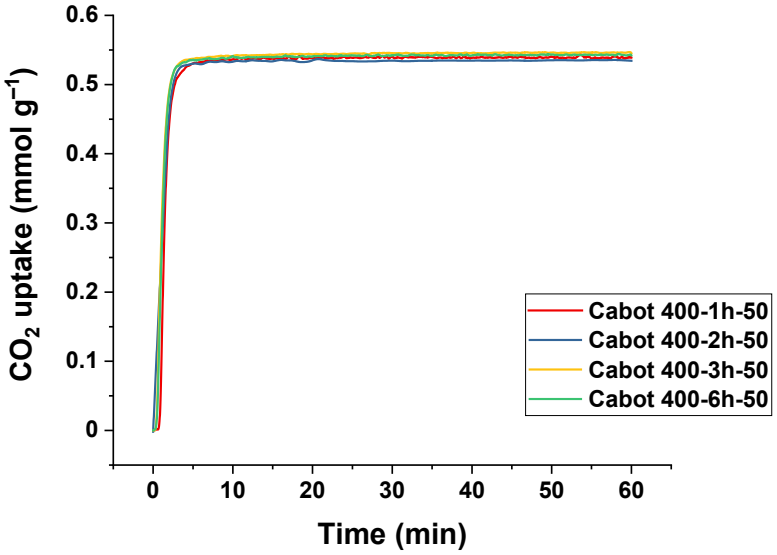


Figure C.11 - CO_2 adsorption breakthrough curves for Cabot calcined at 400 °C 50 °C min^{-1} ramp for various times under N_2 atmosphere. The CO_2 testing atmosphere was 33:67 CO_2:N_2.

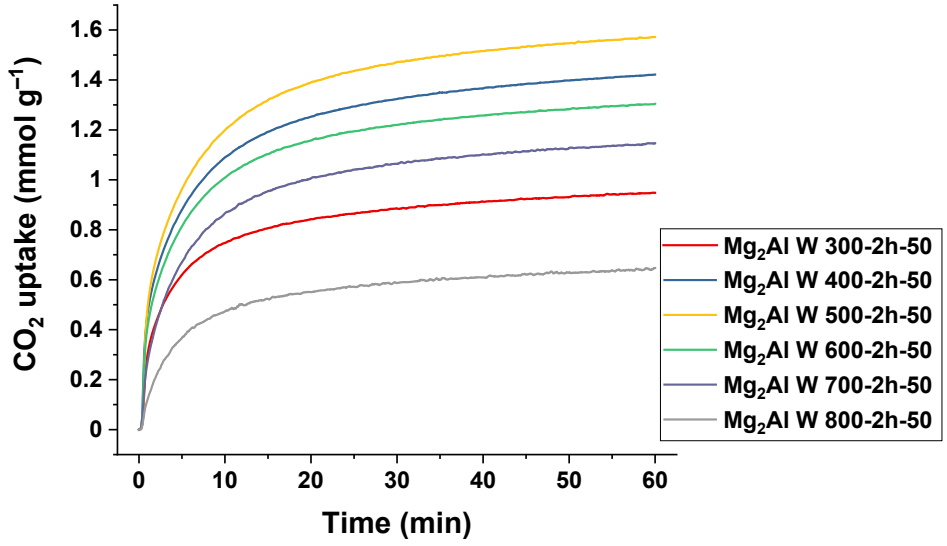


Figure C.12 - CO_2 adsorption breakthrough curves for Mg_2Al W calcined at different temperatures for 2 h with 50 °C min^{-1} ramp under N_2 atmosphere. The CO_2 testing atmosphere was 33:67 CO_2:N_2.

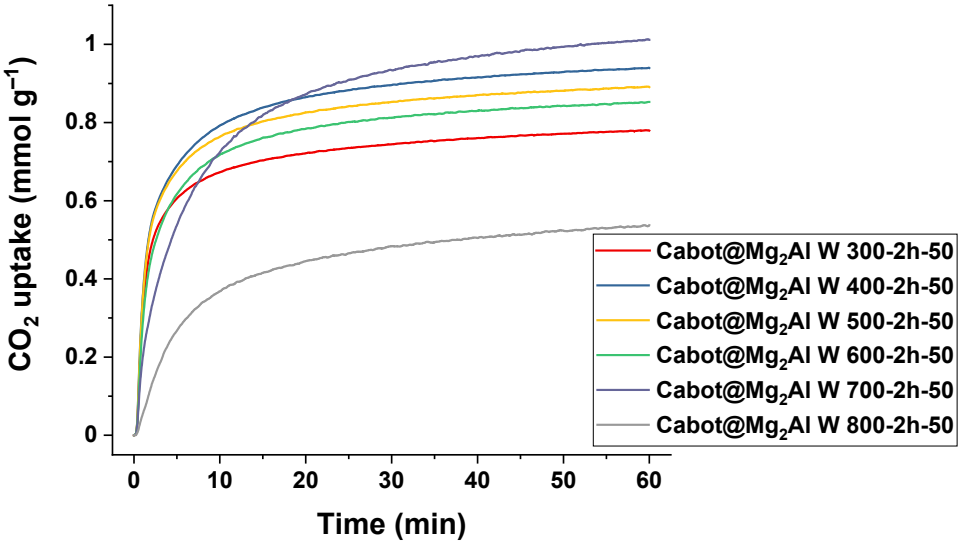


Figure C.13 - CO_2 adsorption breakthrough curves for Cabot@Mg_2Al W (53) calcined at different temperatures for 2 h with 50 °C min^{-1} ramp under N_2 atmosphere. The CO_2 testing atmosphere was 33:67 CO_2:N_2.

C.4 Pseudo-second-order kinetic model fitting of Cabot samples

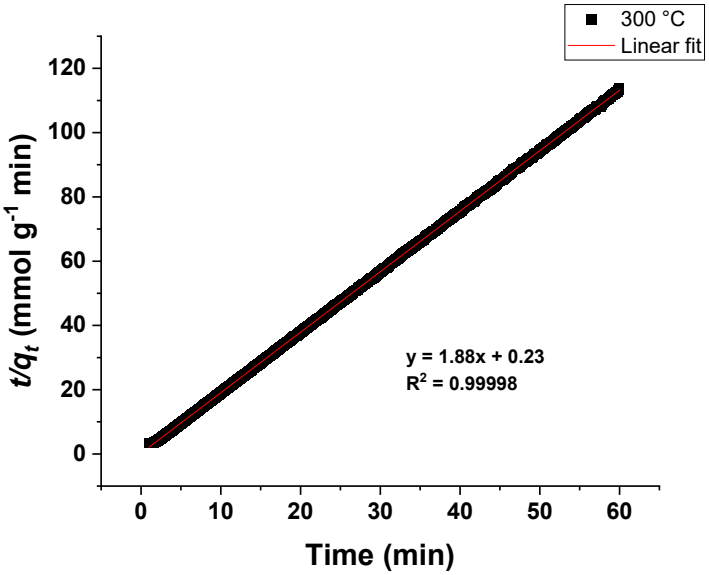


Figure C.14 - Linear fitting of t/q_t against time of Cabot calcined at 300 °C for 2 h with a ramp rate of 50 °C min^{-1}.

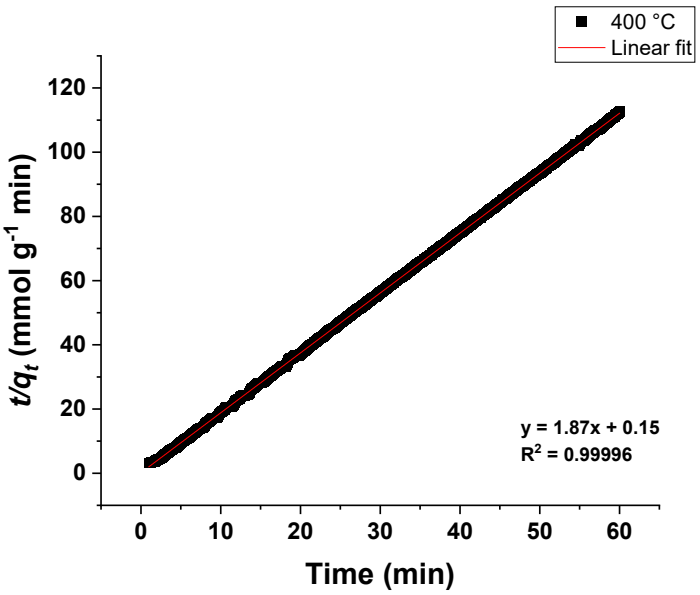


Figure C.15 - Linear fitting of t/q_t against time of Cabot calcined at 400 °C for 2 h with a ramp rate of 50 °C min^{-1}.

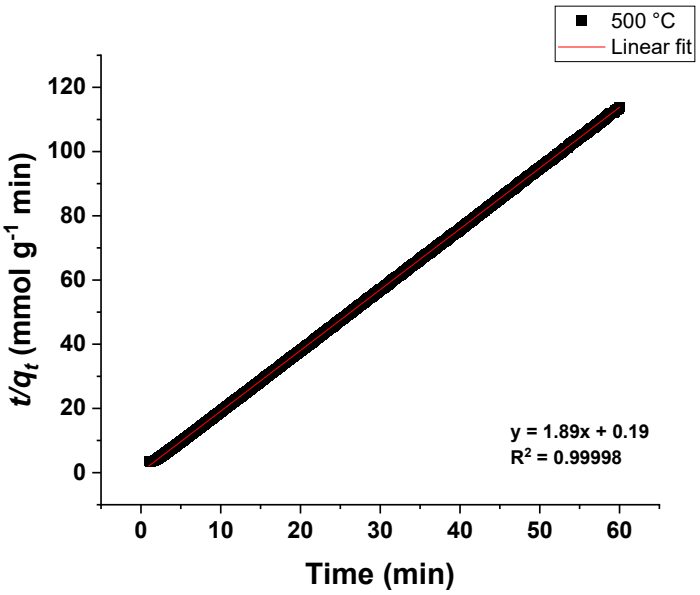


Figure C.16 - Linear fitting of t/q_t against time of Cabot calcined at 500 °C for 2 h with a ramp rate of 50 °C min^{-1}.

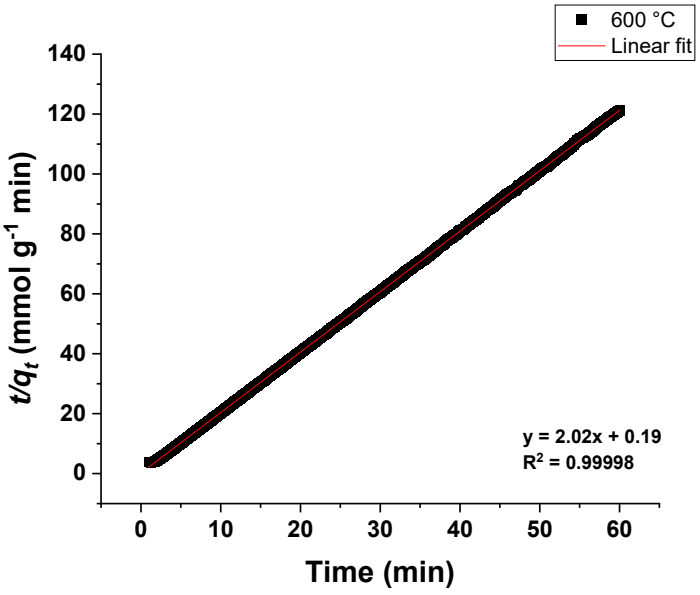


Figure C.17 - Linear fitting of t/q_t against time of Cabot calcined at 600 °C for 2 h with a ramp rate of 50 °C min^{-1}.

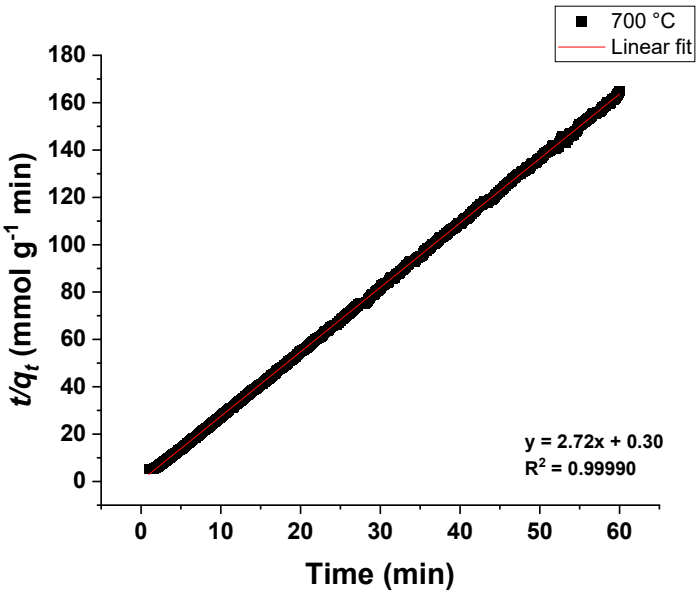


Figure C.18 - Linear fitting of t/q_t against time of Cabot calcined at 700 °C for 2 h with a ramp rate of 50 °C min^{-1}.

C.5 Pseudo-second-order kinetic model fitting of Mg_2Al W samples

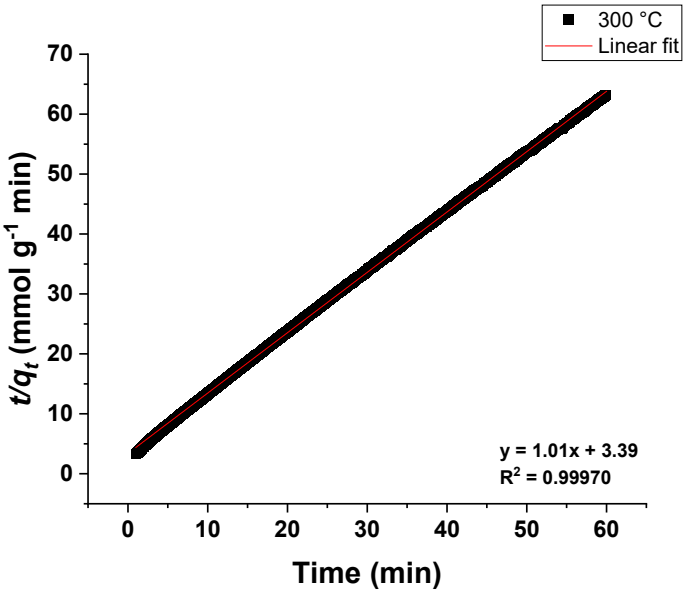


Figure C.19 - Linear fitting of t/q_t against time of Mg_2Al W calcined at 300 °C for 2 h with a ramp rate of 50 °C min^{-1}.

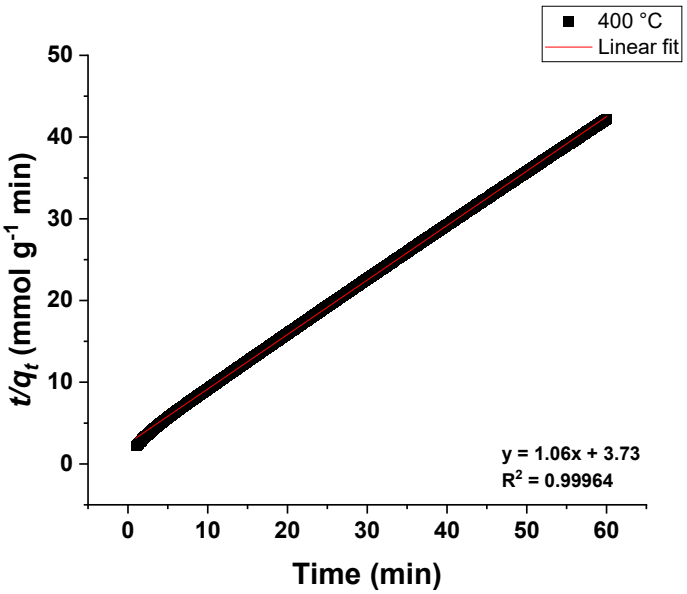


Figure C.20 - Linear fitting of t/q_t against time of Mg_2Al W calcined at 400 °C for 2 h with a ramp rate of 50 °C min^{-1}.

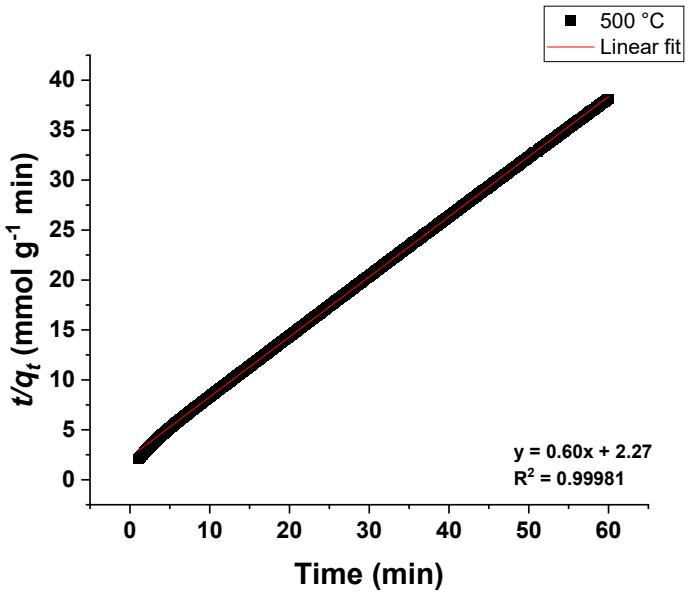


Figure C.21 - Linear fitting of t/q_t against time of Mg_2Al W calcined at 500 °C for 2 h with a ramp rate of 50 °C min^{-1}.

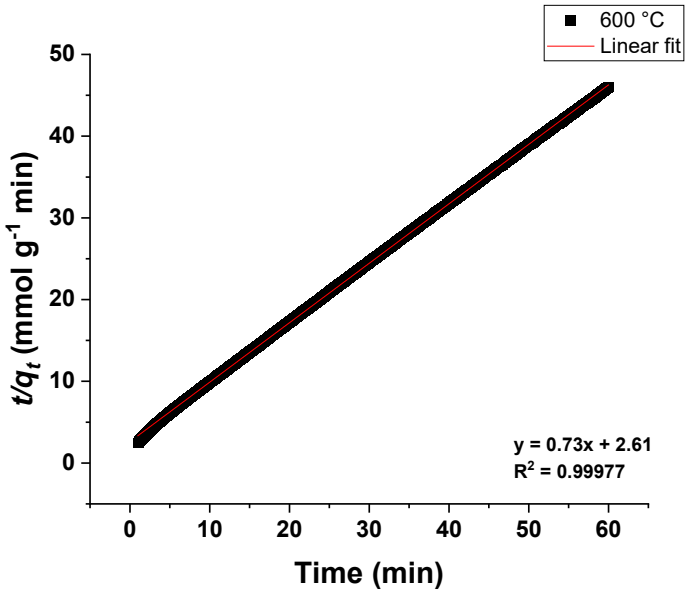


Figure C.22 - Linear fitting of t/q_t against time of Mg_2Al W calcined at 600 °C for 2 h with a ramp rate of 50 °C min^{-1}.

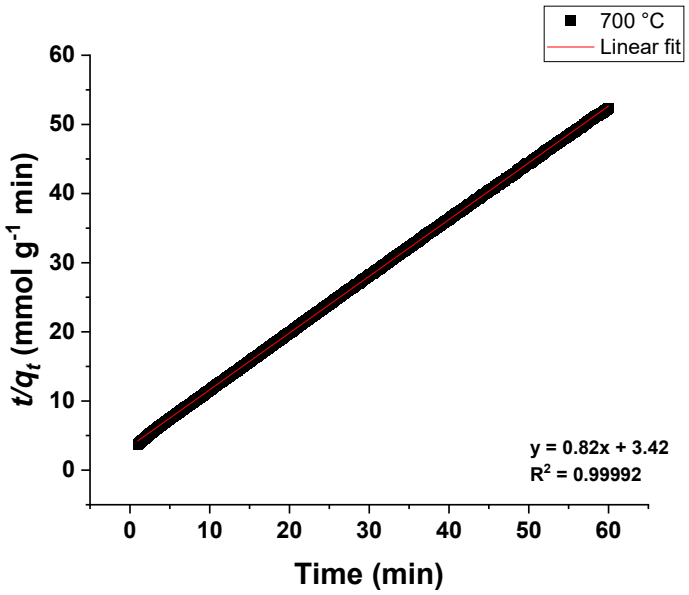


Figure C.23 - Linear fitting of t/q_t against time of Mg_2Al W calcined at 700 °C for 2 h with a ramp rate of 50 °C min^{-1}.

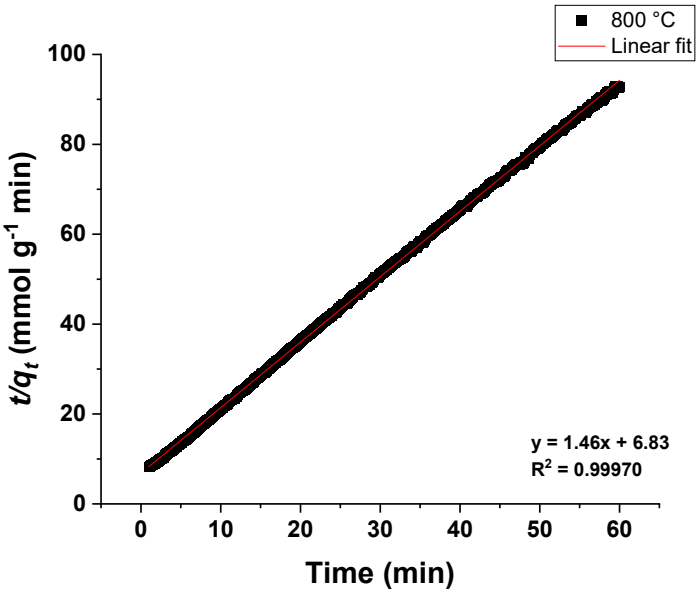


Figure C.24 - Linear fitting of t/q_t against time of Mg_2Al W calcined at 800 °C for 2 h with a ramp rate of 50 °C min^{-1}.

C.6 Pseudo-second-order kinetic model fitting of Cabot@Mg2Al W (53) samples

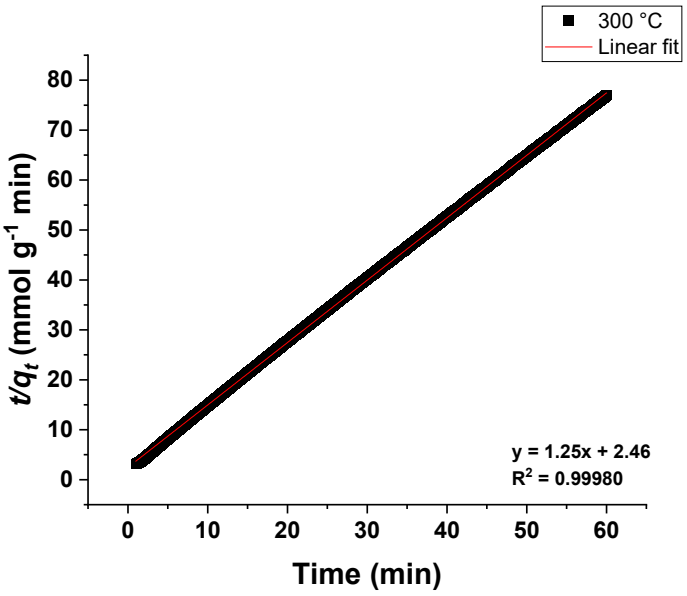


Figure C.25 - Linear fitting of t/q_t against time of Cabot@Mg_2Al W (53) calcined at 300 °C for 2 h with a ramp rate of 50 °C min^{-1}.

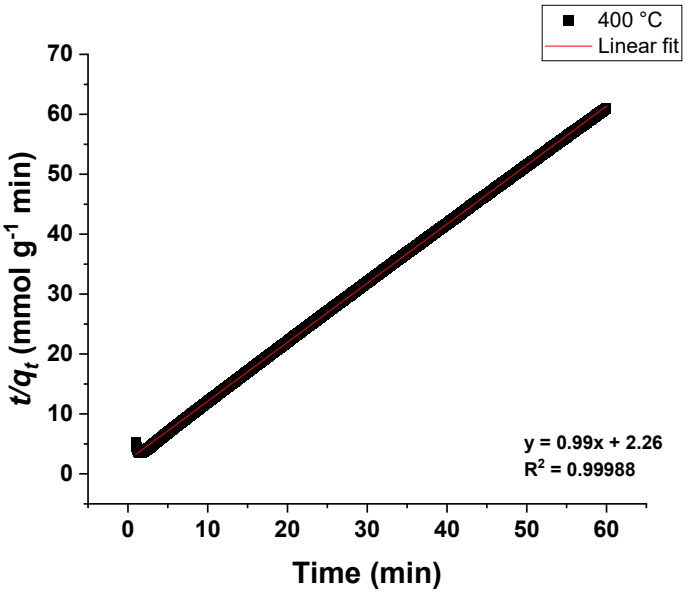


Figure C.26 - Linear fitting of t/q_t against time of Cabot@Mg_2Al W (53) calcined at 400 °C for 2 h with a ramp rate of 50 °C min^{-1}.

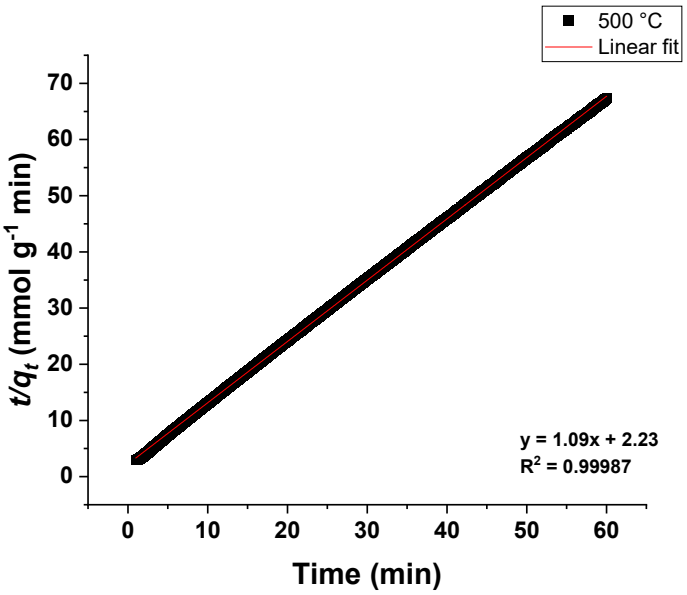


Figure C.27 - Linear fitting of t/q_t against time of Cabot@Mg_2Al W (53) calcined at 500 °C for 2 h with a ramp rate of 50 °C min^{-1}.

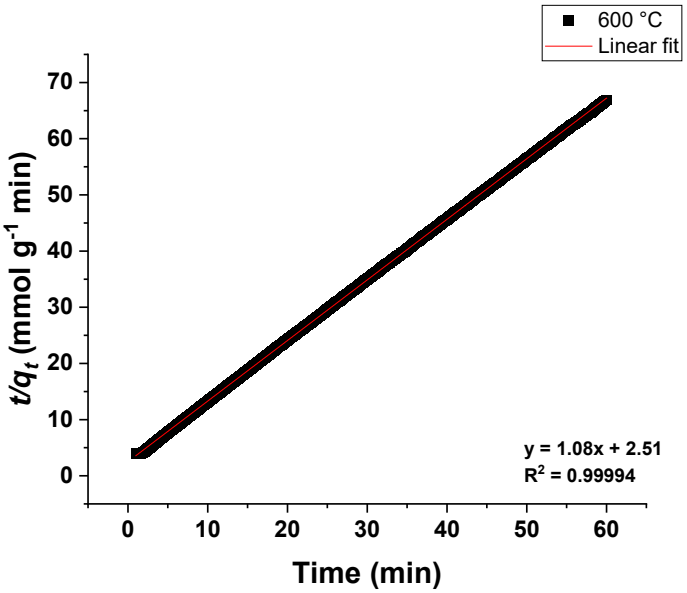


Figure C.28 - Linear fitting of t/q_t against time of Cabot@Mg_2Al W (53) calcined at 600 °C for 2 h with a ramp rate of 50 °C min^{-1}.

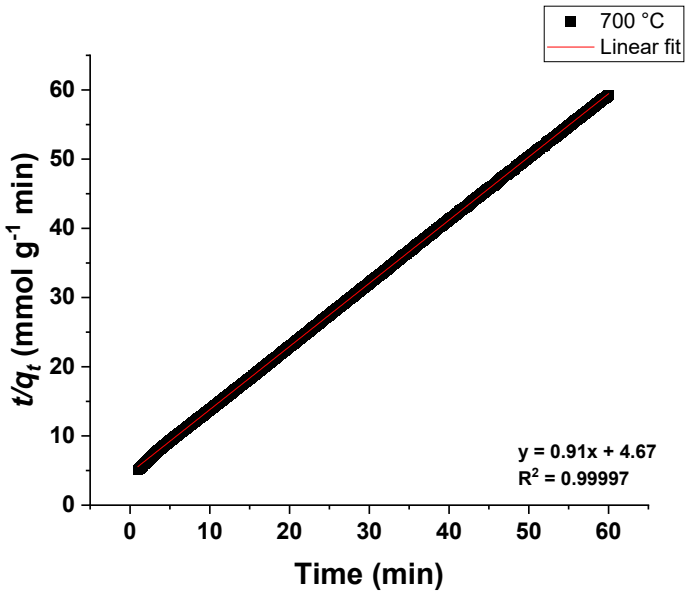


Figure C.29 - Linear fitting of t/q_t against time of Cabot@Mg_2Al W (53) calcined at 700 °C for 2 h with a ramp rate of 50 °C min^{-1}.

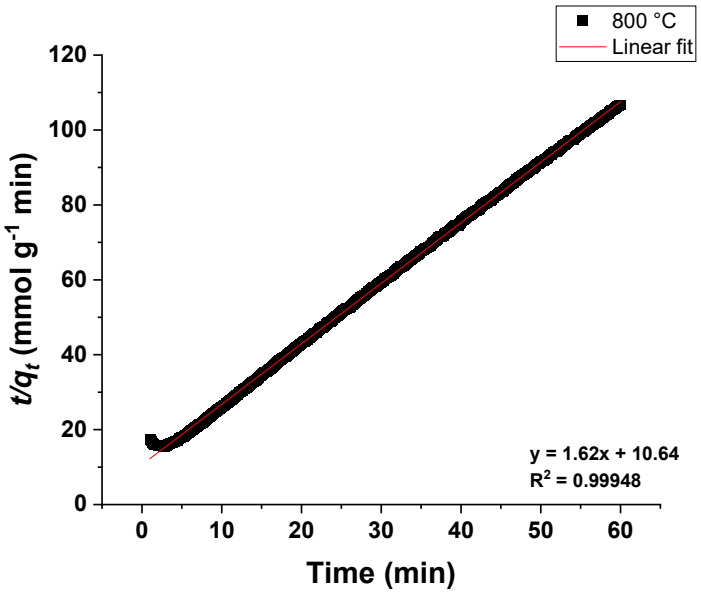


Figure C.30 - Linear fitting of t/q_t against time of Cabot@Mg_2Al W (53) calcined at 800 °C for 2 h with a ramp rate of 50 °C min^{-1}.